THE UNIVERSITY *of* EDINBURGH

Molecular Simulation Studies of Gas Adsorption in Metal–Organic Frameworks

Linjiang Chen

Doctor of Philosophy

The University of Edinburgh

2014

Declaration

I, Linjiang Chen, hereby declare that this thesis has been written by me and has not been written for me, in whole or in part, by any other person; that it is the record of work carried out by me; and that it has not been submitted in any previous application for a degree or qualification. I also certify that wherever contributions of others are involved in the work that I present for examination, every effort has been made to indicate this clearly, with due reference to the literature and acknowledgement of collaborative research and discussions. This thesis has been compiled entirely by me under the supervision of Doctor Tina Düren, at Institute for Materials and Processes, School of Engineering, The University of Edinburgh.

陈林江

Linjiang Chen

Abstract

Using computational tools ranging from molecular simulations – including both Monte Carlo and molecular dynamics methods – to quantum mechanical (QM) calculations (primarily at density functional theory (DFT) level), this work focuses on addressing some of the challenges faced in molecular simulations of gas adsorption in metal–organic frameworks (MOFs). This work consists of two themes: one concerns gas adsorption in MOFs with coordinatively unsaturated metal sites (cus's), and the other one deals with predicting and understanding the breathing behaviour of the flexible MOF MIL-53(Sc).

It has been shown experimentally that incorporation of cus's – also known as "open" metal sites or unsaturated metal centres – into MOFs significantly enhances the uptake of certain gases such as CO_2 and CH_4. As a result of the considerably enhanced, localized guest-molecule interactions with the cus's, it, however, remains a challenge to predict correctly adsorption isotherms and/or mechanisms in MOFs with cus's using grand-canonical Monte Carlo (GCMC) simulations based on generic classical force fields. To address this problem, two multi-scale modelling approaches – which combine GCMC simulations with QM calculations – have been proposed in this work. The first approach is based on the direct implementation of a fluid–framework potential energy surface, calculated by a hybrid DFT/*ab initio* method, in the GCMC simulations. The second approach involves parameterization of *ab initio* force fields for GCMC simulations of gas adsorption in MOFs with cus's. This approach focuses on the generation of accurate *ab initio* reference data, selection of semiempirical model potentials, and force-field fitting through a multi-objective genetic algorithm approach. The multi-scale

simulation strategy not only yields adsorption isotherms in very good agreement with experimental data but also correctly captures adsorption mechanisms, including the adsorption on the cus's, observed experimentally but absent from GCMC simulations based on generic force fields.

The second challenge that this work aims to address concerns the "breathing" phenomenon of MOFs, in which the framework structure adapts its pore opening to accommodate guest molecules, for example. The breathing effect gives rise to some exceptional properties of these MOFs and hence promising applications. However, framework flexibility often poses a challenge for computational studies of such MOFs, because suitable flexible force fields for frameworks are lacking and the effort involved in developing a new one is no less a challenge. Here, an alternative to the force-field-based approach is adopted. *Ab initio* molecular dynamics (AIMD) simulations – which combine classical molecular dynamics simulations with electronic-structure calculations "on the fly" – have been deployed to study structural changes of the breathing MOF MIL-53(Sc) in response to changes in temperature over the range 100–623 K and adsorption of CO_2 at 0–0.9 bar at 196 K. AIMD simulations employing dispersion-corrected DFT accurately simulated the experimentally observed closure of MIL-53(Sc) upon solvent removal and the transition of the empty MOF from the *closed-pore* phase to the *very-narrow-pore* phase with increasing temperature. AIMD simulations were also used to mimic the CO_2 adsorption of MIL-53(Sc) *in silico* by allowing the MIL-53(Sc) framework to evolve freely in response to CO_2 loadings corresponding to the two steps in the experimental adsorption isotherm. The resulting structures enabled the structure determination of the two CO_2-containing *intermediate* and *large-pore* phases observed by experimental synchrotron X-ray diffraction studies with increasing CO_2 pressure; this would not have been possible for

the *intermediate* structure via conventional methods because of diffraction peak broadening. Furthermore, the strong and anisotropic peak broadening observed for the *intermediate* structure could be explained in terms of fluctuations of the framework predicted by the AIMD simulations. Fundamental insights from the molecular-level interactions further revealed the origin of the breathing of MIL-53(Sc) upon temperature variation and CO_2 adsorption.

Both the multi-scale simulation strategy for gas adsorption in MOFs with cus's and the AIMD study of the stimuli-responsive breathing behaviour of MIL-53(Sc) illustrate the power and promise of combining molecular simulations with quantum mechanical calculations for the prediction and understanding of MOFs.

Acknowledgments

Every undertaking such as this one requires sources of inspiration and support; I am fortunate to have found such sources that made the past four years a truly enjoyable and fruitful journey for me. Writing and completing this thesis would not have been possible without the help of numerous mentors, colleagues, friends, and my family. While it is impossible to list everyone who has helped me over the years, the people mentioned will always have my greatest respect and gratitude.

First and foremost, I would like to express my sincerest gratitude to my Ph.D. supervisor, Tina Düren, for her overwhelmingly generous support and tremendously inspirational mentoring all the way along. Her extensive knowledge laid the essential foundation for this thesis, and she has been a constant source of advice, ideas, and encouragement. I am deeply grateful for her academic excellence, warm and open-minded spirit, and enthusiasm, which made my Ph.D. a success. Her endurance of my demanding impatience is also greatly appreciated.

I am heavily indebted to Carole A. Morrison who always has her door open for me. I am immensely grateful to her for mentoring me in quantum chemistry and for helping me to learn about, and cope with, those fascinating and frustrating aspects of the application of quantum mechanics. Without her, it would not have been even half the fun, but certainly many times the effort. I would also like to thank Lev Sarkisov for co-supervising my Ph.D. research and for his constructive guidance, valuable help, and humour.

Furthermore, my heartfelt gratitude goes to all my brilliant collaborators who made significant contributions to the creation and success of this work. In no particular order, I would like to say a special thank-you to Lukáš

Grajciar and Petr Nachtigall (Charles University in Prague), to John P. S. Mowat and Paul A. Wright (University of St. Andrews), and to David Fairen-Jimenez (University of Cambridge). All of these collaborations enriched me with unique experiences of different academic endeavours that broadened my perceptions, and enhanced my knowledge and methodological sills – it will always be greatly appreciated.

There are many other people to whom I owe more than just a thank-you for their presence, support, and friendship. I would like to thank all present and past members of the Düren group for making these years an unforgettable journey. My profound gratitude goes to Ana-Maria Banu, Naomi F. Cessford, Matthew Lennox, and Peyman Z. Moghadam for all the good times that we had. I am grateful to all IMP members whom I not only learned a great deal from but was also able to extend my professional and social network to. I would also like to thank all the administrative and technical support staff at the University of Edinburgh for creating and maintaining a pleasant working environment that enabled me to pursue and accomplish this work. Financial support from the UK Engineering and Physical Sciences Research Council under grant number EP/G062129/1 is gratefully acknowledged.

Finally and most importantly, I want to thank and dedicate this thesis to my parents and my sister. I have received nothing but unwavering support and uncompromising love from you, and I hope this makes you proud. I cannot be grateful enough for the enormous belief and encouragement of you, and none of this would have been possible without you being there. My last lines go to Tianyu Qiu who not only shared the ups but also endured the downs with me. I am wholeheartedly grateful that you have become a sustainable part of my life; I cannot image what this journey would have been like without you there to calm nerves and provide motivation.

Table of Contents

Chapter 1 Introduction

Metal–organic frameworks (MOFs) (Zhou et al., 2012), also known as porous coordination polymers (Kitagawa et al., 2004), are hybrid porous solids that represent an extensive family of crystalline materials realized through modular syntheses from metal centres bridged by organic ligands. These porous coordination polymers are characterized by an infinite network with backbones constructed by metal ions/clusters as connectors and organic ligands as linkers. The infinite net is defined by coordination bonds, which play an important role in the development of synthesis routes to build a variety of spatial structures, while (often) allowing mild conditions to be used, in a chemically self-assembling and self-organizing manner. A key component enabling the so-called rational design of MOFs is that coordination bonds are not as strong as some other intramolecular bonding (such as ionic bonds) and are not as weak as intermolecular bonding (such as hydrogen bonds). Put precisely, the strength and lability of the coordination bond are such that ordered structures can be synthesized owing to the reversibility of these interactions; that is, "errors" in the assembly of a MOF can be readily corrected during the self-assembly so that a periodic three-dimensional structure with crystallographic order can be realized (Kitagawa and Matsuda, 2007). By contrast, in (most if not all) covalently bonded organic polymers "errors" are locked-in once made, hence leading to their much lower periodic ordering. On the other hand, coordination bonds are also strong enough to facilitate the formation of robust materials with high degree of structural integrity and regularity that, in turn, are pivotal for yielding porosities, upon which many applications of MOF materials are based.

Unlike ionic bonding, in which no ion is specifically paired with any single oppositely-charged ion surrounding it in a specific directional bond, metal–ligand coordination bonds are directional, with generally predictable geometries around the metal centre. This directionality of bonding gives rise to the much desired architectural designability of MOFs. In particular, transition metals have been extensively incorporated into MOFs as building blocks to direct a certain framework topology. As most often seen in MOFs, the directionality of coordinative bonding typically affords coordination geometries including linear, trigonal, square-planar, tetrahedral, and octahedral. In other words, transition metals may be used as 2- to 6-way connectors. Put this into context, for each transition metal ion and each of its permitted oxidation states, the possible coordination geometries are well defined so that particular ones can be targeted, allowing structural design to be attempted with certain degree of confidence.

These hybrid inorganic–organic network materials are synthesized by coordination of metal clusters or ions with organic ligands, normally through hydrothermal or solvothermal synthesis routes. Alternative synthesis methods have also been employed, such as microwave-assisted, electrochemical, mechanochemical and sonochemical syntheses (Stock and Biswas, 2012). In constructing MOFs, multi-carboxylate ligands, especially bivalent or trivalent aromatic carboxylate ions, are frequent choices of anions necessary for the charge balanceing to the chosen metal cations. For example, benzene-1,3,5-tricarboxylate anions (btc^{3-}) are used as bridging ligands in the synthesis of a prototypical MOF $[Cu_3(btc)_2(H_2O)_3]$, commonly referred to as CuBTC or HKUST-1 (Chui et al., 1999). The MOF contains dimeric copper units coordinated by btc^{3-} carboxylate ligands in the well-known paddle-wheel structure of copper acetate. It crystalizes with the formation of a

highly porous cubic structure with a three-dimensional pore network. Both the solvent molecules from crystallization and the aqua ligands coordinating the copper atoms can be removed under mild activation procedures without loss of the structural integrity, resulting in the so-called coordinatively unsaturated metal sites (cus's), also known as open metal sites. More generally speaking, coordinatively unsaturated metal sites are commonly realized by the synthesis of solvated MOFs, from which metal-bound solvent molecules – such as water, methanol, *N*,*N*-dimethylformamide – are removed to produce cus's. The vacant coordination sites thus generated within the host MOF may provide strong binding sites for guest molecules, hence enhancing the adsorption performance of the MOF. This is the main subject of this Thesis and is discussed in detail below.

Compared to more traditional porous materials such as zeolites and activated carbons, MOFs afford a higher degree of structural and chemical tunability, which could ultimately facilitate material properties that are optimized for specific applications. For example, by allowing for molecular-level fine-tuning of the thermodynamics of the interaction between CO_2 and the adsorbent, MOFs can be rationally designed for particular types of CO_2 capture such as pre- or post-combustion capture (Sumida et al., 2012). Owing to their well-defined porous structures, high internal surface areas, and the possibility to tailor them with desired chemical functionalities, MOFs are of interest for potential applications not only in carbon capture but also in, for example, adsorptive storage and separation of gases and liquids (Li et al., 2012; Suh et al., 2012; Sumida et al., 2012; Wu et al., 2012), catalysis (Ranocchiari and Bokhoven, 2011; Yoon et al., 2012), sensing (Kreno et al., 2012), and biotechnology (Della Rocca et al., 2011; Horcajada et al., 2012).

Metal–organic frameworks have been reported to be highly promising candidates for various physisorption-based applications. However, their interactions with small gaseous molecules (such as CO_2, CH_4, and H_2) are typically weak, primarily dominated by dispersive and electrostatic forces (while the latter only applies to molecules bearing permanent multipole moments). As a consequence, taking methane storage as an example, these materials function best at low temperatures and their use as storage media in vehicles would require cryogenic cooling. There have been different approaches devised to increase the MOF affinity toward guest molecules. To enhance the van der Waals contacts with the target guest molecules, the size of the MOF pores may be tailored; for example, see Collins and Zhou (2007) and references therein. It has also been well established that coordinatively unsaturated metal sites embedded within MOFs can participate directly in the binding of guest molecules, ranging from apolar CH_4 to polar CO_2 and H_2 and to unsaturated hydrocarbons (Li et al., 2012; Suh et al., 2012; Sumida et al., 2012; Wu et al., 2012). Recently, a number of MOFs with cus's were demonstrated to exhibit extraordinary capabilities of quantum sieving deuterium from hydrogen (FitzGerald et al., 2013; Oh et al., 2013).

In addition to the aforementioned pore-size control and cus incorporation approaches, MOF structural flexibility has also been well exploited to achieve the desired host–guest chemistry. Dynamic structural transformations of flexible MOFs have been identified as an important feature for applications that can benefit from the material ability to control pore size as a function of guest-molecule pressure or concentration. Such ability has rendered these MOFs highly selective chemical sensors, gas separation compounds, or drug nanocarriers (Kitagawa and Uemura, 2005; Férey, 2012; Horcajada et al., 2012). Furthermore, dynamically responding MOFs can fine-tune their

structures in accordance with guest-molecule uptake. Upon these stimuli-responsive framework changes, selective adsorption may be achieved in conjunction with changes in luminescence to the MOF, allowing for detection techniques that would be otherwise not possible for nominally rigid MOFs (Cui et al., 2012).

In comparison with zeolites and activated carbons, it is easier to tailor the pore structures and the chemical compositions of MOFs, a critical advantage that endows considerable opportunities to optimize the materials for applications. However, there are also challenges, such as synthesis cost and material stability, which have to be addressed before MOFs can be used in practical applications. MOFs generally show good thermal stability ranging from 250° to 500° C, because of their strong constituent bonds (e.g., C–C, C–H, C–O, and metal–O) (Furukawa et al., 2013). Synthesizing chemically stable MOFs is, however, a challenge often due to their susceptibility to breaking of the metal–ligand coordination bonds upon exposure to water or organic solvents over extended periods of time (Liu et al., 2012). Additionally, the stability of MOFs toward acidic vapours (such as SO_x and NO_x), and the stability of MOFs toward storage, thermal regeneration and cyclic processing are a few other existing challenges requiring further efforts in order to enhance their performance and to extend their applications to industrial processes.

As mentioned above, one of the various attributes that make MOFs promising for a variety of applications is their structural diversity. The number of existing and potential MOFs is virtually limitless, as simple changes in the combinations of linkers and metal nodes can produce novel MOFs with distinct properties. The possibility of realizing new MOF

structures is further enhanced by catenation of a known framework topology or post-synthesis functionalization through, for example, introduction of functional groups to the linkers. This suggests that computational tools – which are much less dependent on extensive "trial and error" that is often required by experimental methods – can be powerful and efficient in helping to investigate and elucidate the diverse properties that MOFs now can offer.

Indeed, computational studies on MOFs have accompanied the experimental efforts since the very beginning. Numerous literature simulation studies on different length and/or time scales have showcased the ability of theoretical investigations to complement and to guide experiments in furthering the understanding of MOFs (Düren et al., 2009; Keskin et al., 2009; Tafipolsky et al., 2010). To exploit the synergistic relationship that exists between simulation and experiment has undoubtedly become an indispensable strategy in studying and characterizing MOFs. Here, Chapter 6 gives one such example, in which computer simulations come into play and provide unique insight to complete the story that is told only partially by experimental measurements on their own.

In a more specific context of applying computer simulations to study gas adsorption in MOFs, molecular simulations, particularly grand-canonical Monte Carlo (GCMC) simulations, have received enormous attention and constitute an important part of the *in silico* materials design that aims to allow experimental efforts to be focused on promising candidate MOFs for specific applications. To be precise, several seminal literature reports (Dubbeldam et al., 2012; Lin et al., 2012; Wilmer et al., 2012) have demonstrated how optimal structures (and sometimes synthesis targets) may be identified computationally by using large-scale *in silico* screening of

(hypothetical) MOF structures or, more generally, porous frameworks such as zeolites and covalent–organic frameworks (Dubbeldam et al., 2012; Lin et al., 2012). The core of those studies is to find correlations between gas storage/separation performances and various structural and chemical characteristics of MOFs (sometimes explicitly termed as structure–property relationship analyses), ultimately aiming at guiding the design of MOFs for individual applications. Much of the emphasis of such large-scale screening studies is usually placed on the importance of investigating a large enough collection of framework structures, in order to ensure the diversity of the screened structures in the possible porous materials space. For example, in the case of low-pressure carbon capture, Snurr and co-workers have pointed out that while a linear correlation between CO_2 uptake and heat of adsorption can be clearly established based on a set of a few tens of MOFs (Bae and Snurr, 2011), a more complex relationship (possessing a maxima and multi-dimensional features) is observed instead when expanding the screening set to include over 130 000 MOFs (Wilmer et al. 2012).

Another equally (if not more) important and more fundamental aspect of a computational screening study is the simulation method chosen to evaluate the performances (e.g., CO_2 uptake) of the training set of MOFs. The limitations of the underlying physical models (i.e., the force fields, partial atomic charges, etc.) used in those large-scale screening studies (Dubbeldam et al., 2012; Lin et al., 2012; Wilmer et al., 2012) were explicitly mentioned and critically discussed by the authors for special situations such as MOFs containing coordinatively unsaturated metal sites (cus's). Whereas GCMC simulations based on generic classical force fields (which were used by those screening studies) provide good predictions of adsorption isotherms in many MOFs, they fail to do well in MOFs with cus's. The main reason is that such

generic force fields cannot correctly capture the considerably enhanced, localized guest-molecule interactions with cus's. However, little has been done to address such challenges. At first glance, this might not pose a problem – although it is well-known that these "off-the-shelf", generic force fields are only approximation, their use can be well-justified for high-throughput, large-scale analyses. In other words, *in silico* screening is usually aimed at identifying a small number of promising target structures that are then to be investigated with more sophisticated methods. However, relaxing the fundamental physical constraints imposed by the simulation model is as important as increasing the structural diversity of the screening database. Put simply, it is crucial to rigorously validate and to improve (when needed) the fundamentals of chosen simulation models. Failing to predict a known top-performing MOF (let alone a class of them as discussed below) for a particular application is going to undermine the screening methodology (arguably) to a greater extent than being unable to suggest a (hypothetical) structure with the greatest potential. Figure 1.1 illustrates one such example, where the simulation model clearly fails to describe a class of MOFs.

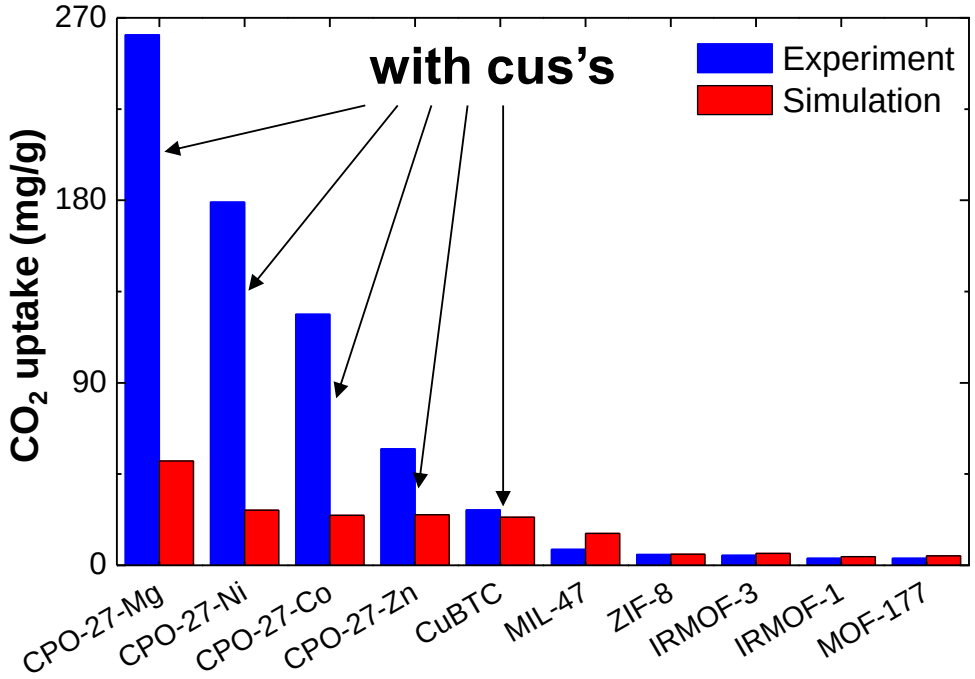

Figure 1.1. Comparison of CO_2 uptakes at 0.1 bar at 298 K for a variety of MOFs. GCMC simulation results were based on generic force fields; experimental data were taken from the report by Yazaydın et al. (2009). "Cus's" stands for coordinatively unsaturated metal sites.

Figure 1.1 clearly shows that experimentally MOFs with cus's remarkably outperform their counterparts without cus's for adsorption of CO_2 at 0.1 bar at 298 K, relevant to post-combustion carbon capture from flue gases. Also obvious is that while GCMC simulations based on generic force fields do very well for MOFs without cus's, they cannot capture the considerably enhanced CO_2 uptakes in MOFs with cus's, indicating that certain information is missing from the physical models adopted. Moreover, CPO-27-Mg, the experimentally best-performing MOF in Figure 1.1, (almost) certainly will not be one of the target structures coming out of the computational screening protocol proposed by Wilmer et al. (2012) for flue gas separation applications (at a CO_2 pressure of 0.1 bar and at 298 K). Their "adsorbent evaluation criteria" suggest that a promising material will have a helium void fraction of 0.3–0.4, the largest pore diameter should be smaller than ca. 12 Å, and the heat of adsorption should be ca. 33 kJ mol^{-1}. The

corresponding values for CPO-27-Mg, however, are 0.72, 11.5 Å, and 26.7 kJ mol^{-1} according to GCMC simulations based on generic force fields. This means that CPO-27-Mg will be discarded by the screening, although it has been reported experimentally to be one of the best MOFs for selective removal of CO_2 under typical flue gas conditions (Britt et al., 2009; Yazaydın et al., 2009; Remy et al., 2013). Furthermore, the other MOFs with cus's in the CPO-27 family (see Figure 1.1) are also unlikely to be identified as promising adsorbents according to the evaluation criteria of Wilmer et al. (2012), suggesting a systematic error in the simulation model used.

It has been known for some time that the presence of the cus's in CPO-27-Mg (over)compensates the low framework density (i.e., a large void fraction) and the lack of small pores (Dietzel et al., 2009; Yazaydın et al., 2009). Both have been repeatedly identified as important structural characteristics of MOFs for capture of CO_2 at low pressures by screening studies; for example, see Lin et al. (2012), Wilmer et al. (2012), and Wu et al. (2012). Another well-known problem for computational screening is that simulated heat of adsorption is very sensitive to the simulation model used. For CPO-27-Mg, generic force fields yield a value of 26.7 kJ mol^{-1} that is substantially lower than the experimental one, which is typically reported to be ca. 40 kJ mol^{-1} (e.g., Dietzel et al. (2009)), resulting in that CPO-27-Mg is falling out of the "selection domain" (ca. 33 kJ mol^{-1}) as defined in the screening approach by Wilmer et al (2012). It is worth noting that despite the fundamental physical constraints imposed by the simulation models, those screening studies have provided invaluable and insightful guide to experimental synthesis, especially when specific interactions (such as guest-molecule interactions with cus's) are not present or do not play the predominant role, for example, in high-pressure gas storage applications.

Put together, there is an urgent need to improve standard, "off-the-shelf" physical models in order to address the difficulties faced in molecular simulations of gas adsorption in MOFs with cus's. In this respect, new computational procedures for GCMC simulations of gas adsorption in MOFs with cus's are presented in Chapters 3–5. Two modelling protocols are proposed and they, in a nutshell, combine standard GCMC simulation technique (dealing with system thermodynamics) with *ab initio* calculations (providing accurate energetic and geometric information). This work introduces a robust and systematic multi-scale simulation strategy for correctly predicting gas adsorption in MOFs with cus's, from which future gas adsorption simulations and (presumably) screening studies will benefit.

The other theme (Chapter 6) in this Thesis deals with using molecular simulations to understand the dynamic structural flexibility, or precisely the "breathing" behaviour, of the MOF MIL-53(Sc) (Mowat et al., 2011). In general, MOFs that can "breathe" exhibit reversible transitions between two (or more) structural phases resulting from the expansion or contraction of the three-dimensional porous framework. The breathing effect gives rise to numerous intriguing properties of such MOFs as described, for example, by Férey et al. (2011) and Horcajada et al (2012). Theoretical investigations are certainly of great importance in studying breathing MOFs, not least because an adaptable framework makes it (more) difficult to probe and understand the nature of the host–guest chemistry by experimental methods alone.

There are a great deal of computational tools and simulation techniques proposed and described in the literature for studying breathing MOFs, and a short overview of them is given in Chapter 6. Up to the completion of this Thesis, most reported molecular dynamics simulation studies of breathing

MOFs used flexible force fields tailor-made for the frameworks. In contrast, this work focuses on investigating the applicability of *ab initio* molecular dynamics (AIMD) simulations (Car and Parrinello, 1985; Kirchner et al., 2012) to capturing the breathing phenomena of MOFs. The so-called AIMD method develops the system dynamics with forces obtained directly from electronic-structure calculations "on the fly", thus removing the necessity of a flexible force field for the framework. In this work, not only are some appealing and advantageous aspects of the AIMD method demonstrated, but several technical issues regarding simulation settings to ensure computational accuracy are also discussed.

In passing, two points are noteworthy. First, throughout this Thesis the phrase "*ab initio*" is referred to in the sense that chemical engineers and materials scientists would normally use it. That is, DFT methods are labelled as "*ab initio*" or "first-principles" methods, although computational chemists do not normally call DFT methods "*ab initio*". The second point concerns the use of the term "force field" in this Thesis. Molecular mechanics is based on a view of molecules as balls held together by springs. The total potential energy of a molecule is then written as a Taylor expansion involving bonds, bends, torsions, non-bonded interactions, and so on. This expansion, including both bonded and non-bonded contributions, is referred to as a force field. Giving the terms in the expansion explicit mathematical forms constitutes devising a force field; giving actual numbers to the constants in the mathematical expressions constitutes parameterizing a force field. The term "force field" arises because the first-order derivative of the potential energy determines the force acting on the particle; a force field, as a function of spatial coordinates of atoms, can be differentiated to give the force on each atom. Throughout this Thesis, however, the term "force field" is almost

exclusively used in the way that it only refers to the non-bonded part of a complete force field. To be precise, all of the force fields proposed and parameterized in Chapters 4 and 5 are *inter*-molecular force fields that have been used to describe the gas–MOF interactions studied in this work. The force fields only involve non-bonded interactions (i.e., dispersive and electrostatic interactions) and do not include parameters associated with bonded interactions (e.g., bond stretching, angle bending, etc.). Furthermore, in all of the gas adsorption simulations performed here the MOF structures were kept rigid; thus, no *intra*-molecular interactions within the MOFs needed to be modelled. By contrast, when studying the MOF structural flexibility reported in Chapter 6, a quantum mechanical method was adopted to describe the *intra*-molecular interactions of the systems; i.e., no force field was used for the purpose.

Publications and Presentations

Parts of the work presented in this Thesis have been reported in the following journal publications and conference presentations:

L. Chen, J. P. S. Mowat, D. Fairen-Jimenez, C. A. Morrison, S. P. Thompson, P. A. Wright, and T. Düren; "Elucidating the Breathing of the Metal–Organic Framework MIL-53(Sc) with *ab initio* Molecular Dynamics Simulations and in Situ X-ray Powder Diffraction Experiments"; *Journal of the American Chemical Society*, DOI: 10.1021/ja403453g, in press.

L. Chen, C. A. Morrison, and T. Düren; "Improving Predictions of Gas Adsorption in Metal–Organic Frameworks with Coordinatively Unsaturated Metal Sites: Model Potentials, *ab initio* Parameterization, and GCMC Simulations"; *Journal of Physical Chemistry C*, 116 (35), 18899 (**2012**).

L. Chen, L. Grajciar, P. Nachtigall, and T. Düren; "Accurate Prediction of Methane Adsorption in a Metal–Organic Framework with Unsaturated Metal Sites by Direct Implementation of an *ab initio* Derived Potential Energy Surface in GCMC Simulation"; *Journal of Physical Chemistry C*, 115 (46), 23074 (**2011**).

L. Chen and T. Düren; "Molecular simulation studies of gas adsorption in metal–organic frameworks" (talk); *UK Adsorption Research Industrial Consortium Annual Meeting*; Edinburgh, UK (**2012**).

L. Chen, L. Grajciar, C. A. Morrison, P. Nachtigall, and T. Düren; "Improving predictions of gas adsorption in metal–organic frameworks with coordinatively unsaturated metal sites" (poster); *3rd International Conference on Metal–Organic Frameworks and Open Framework Compounds*; Edinburgh, UK (**2012**).

L. Chen and T. Düren; "*Ab initio* aided molecular simulation studies of adsorption in MOFs with open metal sites" (talk); *35th Annual British Zeolite Association Meeting*; Chester, UK (**2012**).

Chapter 2 Simulation Methodologies

The underlying information needed in simulations of MOFs (and the guest molecules inside their pores) is molecular interactions involved in the system of interest, which intrinsically determine the reliability and accuracy of simulation results. Theoretical approaches to quantifying molecular interactions broadly fall into two categories: one is based on classical Newtonian physics and the other one is based on quantum mechanics (QM).

The classical approach gives rise to molecular mechanics that provides the foundation for (classical) molecular simulations, which is also known as force-field methods. The fundamental assumption here is that atoms are large enough to be treated as classical objects; that is, they are modelled as spheres connected by bonds that are treated as springs. Electrons cannot be modelled classically and are therefore ignored. A general form for the total energy of a molecule in an additive force field consists of bonded (intra-molecular) and non-bonded (inter-molecular) terms, where the bonded term includes bond stretching, bond bending, and torsional interactions, and the non-bonded term has van der Waals and electrostatic interactions.

The quantum mechanical approach explicitly takes into account electrons, although the treatment of the behaviour of the electrons in a molecule can be based on either *ab initio* molecular orbital theory or density functional theory (DFT). Both levels of theory yield the ground-state electronic configuration of the molecule by finding solutions to the Schrödinger equation. A principle difference between the two branches lies in that DFT does not calculate a conventional wavefunction (which the *ab initio* approach does), but rather

expresses the total energy as a function of the electron distribution that in turn is a spatially dependent function for the electron density. Since the electrons are modelled explicitly, QM methods of either kind allow for calculations of (in theory at least) any molecular properties of interest. This, however, comes at a cost: QM calculations are computationally much more demanding than the force-field-based counterparts.

This Chapter aims to provide a (really) brief overview of the computational tools that have been used in this work. The reader is referred to standard textbooks in the subjects for methodological details, for example, the books by Frenkel and Smit (2002) for molecular simulation techniques, Jensen (2006) for a general introduction to computational chemistry, Schwabl (2006) for statistical mechanics theories and applications, and Lewars (2011) for a comprehensive description of molecular and quantum mechanics. Details about the particular modelling techniques and simulation settings used here are provided where appropriate in the following, respective Chapters.

2.1 Molecular Simulation

2.1.1 Statistical mechanics

Molecular simulations allow for studying properties of many-body systems, with the help of statistical mechanics (or statistical thermodynamics) that provides a physical framework for relating the microscopic properties and interactions of individual entities (i.e., the atoms, molecules, etc. in the system) to the macroscopic properties of systems. For example, a molecular dynamics simulation yields instantaneous positions and velocities of all

constituent particles. It is the application of statistical mechanics that allows for deriving macroscopic observables, in which one is usually interested, from the microscopic distributions and motions of the particles in the system.

In the language of statistical mechanics, the macroscopic thermodynamic quantities (such as temperature, pressure, and internal energy) of a system consisting of many particles are interpreted based on probability distributions. The Boltzmann distribution is one of the most important distribution laws (or probability measures) that are concerned with the distribution of the states of a system. For example, in a system that can exchange energy, but not particles or volume, with its environment (i.e., the canonical (*NVT*) ensemble), the Boltzmann distribution gives the probability that the system is found in a particular state *i* having an energy of U_i as

$$P(i) = \frac{\exp\left(-\frac{U_i}{k_B T}\right)}{\sum_j \exp\left(-\frac{U_j}{k_B T}\right)} = \frac{\exp\left(-\frac{U_i}{k_B T}\right)}{Q} \tag{2.1}$$

where k_B is the Boltzmann constant, T is the temperature, and the sum in the denominator is performed over all states. In the last part of Equation 2.1, the (canonical) partition function Q is defined, and the knowledge of it allows one to derive thermodynamic variables such as internal energy, free energy and entropy (Frenkel and Smit, 2002). The Boltzmann distribution also says that high energy states are markedly less probable than low energy ones; that is, $n_i \propto \exp\left(-\frac{U_i}{k_B T}\right)$, where n_i is the number of configurations that appear as different possible ways the system can achieve the state *i*.

A microstate is a specific microscopic configuration (or a snapshot during the simulation) of the system, which contains complete information about the positions and momenta of all particles in the system. In contrast, a macrostate, which refers to the macroscopic properties of a system, is characterized by a particular set of thermodynamic constraints that in turn define a certain statistical ensemble. The concept of statistical ensembles is of fundamental importance for the formulation of statistical mechanics. In thermodynamic equilibrium, macroscopic observables can be measured by statistical averages of the ensemble, as it consists of all possible states of the system and the corresponding probabilities of realizing them. In order of increasing extent of contact with the external environment of the system, some important ensembles include: microcanonical (isolated), canonical (in thermal equilibrium with the outside), and grand-canonical (in exchange of energy and particles with the outside) ensembles.

The ergodic theorem, originally proposed by Boltzmann, provides a justification for the description of macroscopic systems in terms of statistical ensembles (Schwabl, 2006). It basically states that in the long run a system's trajectory in the phase space on a surface of constant energy will visit each region of that surface equally frequently. This essentially results in that a time average (the molecular dynamics approach) is equal to an ensemble average (the Monte Carlo approach), if the system is ergodic. Furthermore, for sufficiently long (molecular dynamics) trajectories, the time-averaged properties become independent of the initial conditions. The assumption that this statement holds – i.e., time averages can be replaced by ensemble averages and vice versa – is called ergodic hypothesis. There are, of course, circumstances in which the ergodic hypothesis does not hold (such as for glassy systems and metastable phases), but it is strongly believed that most

many-body systems are ergodic and it is simply assumed in molecular simulations (Frenkel and Smit, 2002).

Even if a system is formally ergodic, its behaviour during a computer simulation may resemble those of nonergodic systems. This means that the system does not properly explore phase space; therefore, the calculated statistical averages are likely to exhibit strong dependence on the initial conditions. This phenomenon is called quasi-nonergodicity. The appearance of quasi-nonergodicity can be caused by (for example) high energy barriers separating different volumes in phase space, which prevents transitions between these volumes from happening during a simulation or leads to transitions happening so infrequently that accurate estimates of statistical averages cannot be obtained. Ensuring ergodicity of the simulation (of an ergodic system) is of paramount importance, although this can be a nontrivial task. There are studies, in the literature, dedicated to the subject; for example, see Frantz et al. (1990), Thirumalai and Mountain (1990), Kuchta (2003), and Frédéric et al. (2009).

2.1.2 Monte Carlo simulation

In a Monte Carlo (MC) simulation of the Metropolis type (Metropolis et al., 1953), a Markov chain of configurations/states is constructed and the probability of finding any particular configuration in this chain is given by the Boltzmann distribution. A Markov chain is a sequence of trials that attempt to generate a new configuration through a variety of random moves such as translation, rotation, insertion, and deletion. The moves are accepted or rejected according to an appropriate acceptance rule, which can be derived from the rules of detailed balance (Frenkel and Smit, 2002):

$$\mathrm{acc}(o \to n) = \min(1, \exp\{-\beta[U(n) - U(o)]\}) \quad (2.2)$$

where $\beta = 1/(k_B T)$. Equation 2.2 states that the probability of accepting or rejecting a trial move depends on the energy difference between the new (n) and the old (o) states of the system. A move is always accepted unconditionally (acceptance = 100%) if the new configuration results in a lower energy. Otherwise, the move has a probability of less than 1 to be accepted; the higher the energy of the new state is, the smaller the probability of it being accepted becomes.

One attractive aspect of the MC approach is that it is a stochastic method, in which only energies (rather than forces) are evaluated during configurational sampling. The system in a MC simulation does not have to (and usually does not) follow the natural path. A new configuration can be generated by unphysical motions (e.g., "jumping" from one position to another) in such a way that energy barriers in any senses are ignored, thus significantly improving simulation efficiency in reaching thermodynamic equilibrium.

MC simulations are particularly suited to studying thermodynamic properties of adsorption of gases and their mixtures in MOFs. For example, adsorption isotherms are typically calculated using grand-canonical Monte Carlo (GCMC) simulations. In the GCMC method, the chemical potential, volume and temperature are kept fixed while the number of gas molecules in the adsorbed phase is allowed to fluctuate so that the chemical potentials of the adsorbed phase and the bulk gas reservoir are equal. The input of a GCMC simulation includes the temperature and the chemical potential of the gas molecules in the reservoir, and the output of the simulation is the average number of adsorbed molecules. This is analogous to an adsorption

experiment, in which the temperature and the bulk pressure of a gas are specified and the corresponding uptake is measured. The chemical potential (as used in GCMC simulations) can be related to the gas phase pressure (as specified in experiments) by an equation of state. Detailed description of the GCMC simulation method can be found, for example, in the book by Frenkel and Smit (2002). Multiple comprehensive reviews in the subject exist; a few examples are given by Düren et al. (2009), Keskin et al. (2009), and Getman et al (2012).

2.1.3 Molecular dynamics simulation

Molecular dynamics (MD) simulation is a deterministic computational technique that has been routinely used to study, for example, diffusion of guest molecules in MOFs (Keskin et al., 2009). An MD simulation mimics the natural pathway of molecular motion to sample successive configurations, following the classical Newtonian mechanics. At a given temperature, the initial velocities of the atoms in a system are assigned according to the Maxwell–Boltzmann distribution. The force exerted on each of the atoms is given by the negative gradient of the potential energy function with respect to the position of the atom. Once these forces are known, the Newtonian equations of motion are solved numerically with a time step, and the positions and velocities of the atoms are updated. This procedure can be repeated until a sufficiently long MD trajectory is obtained, from which the desired thermodynamic and kinetic properties of the system can be extracted.

MD simulations can be performed in different ensembles, similar to the MC approach. In order to use an isothermal ensemble such as the canonical (*NVT*) or the isothermal–isobaric (*NPT*) ensemble, the system may be coupled to a

thermostat that can maintain the average temperature close to a pre-defined value. The Nosé–Hoover (Nosé, 1984; Hoover, 1985) and the Berendsen (Berendsen et al., 1984) thermostats are commonly used. In the case of the *NPT* ensemble, a barostat is needed to adjust the size and shape of the simulation cell in order to maintain the desired average pressure. The Parrinello–Rahman (Parrinello and Rahman, 1981) barostat, and many others, can accomplish this task. The MD method has been discussed in detail, for example, by Frenkel and Smit (2002), and its applications in the field of MOFs have been reviewed by, for example, Keskin et al. (2009).

2.2 Quantum Mechanical Calculation

There are obvious reasons and advantages to use classical molecular simulations (based on molecular mechanics). For example, when appropriate force fields are available for calculations of molecular interactions, the MC and MD simulation techniques described above can be used to study systems containing 1000s of atoms on a single CPU. There are, however, also disadvantages to classical simulations, the most fundamental of which is that electrons are completely ignored. A direct consequence of this simplification is that chemical processes, in which knowledge of the electronic structure of the system is important, cannot be simulated (e.g., photochemical reactions) or at least not with a high accuracy. One example that marks the entrance of quantum mechanics (QM) calculations into this work is that commonly used generic classical force fields cannot describe guest-molecule interactions with coordinatively unsaturated metal sites (cus's) in MOFs. The main reason lies

in that significant electron overlap (at equilibrium separation) of the adsorbate–cus complex cannot be captured by such force fields.

Here, an introductory level overview of two specific aspects of quantum chemistry is given, primarily from a computational perspective.[1] There are many books on the principles of quantum mechanics/chemistry, such as the one by Atkins and Friedman (2011). The review articles by Tafipolsky et al. (2010) and Yang et al. (2013), for example, provide excellent overviews of applications of QM methods in the field of MOFs.

2.2.1 *Ab initio* molecular orbital theory

The term "*ab initio*" indicates that the simulator tells the computer programme "everything" about atoms but nothing about molecules, and the programme has to work out molecular properties "from scratch". Central to this is the *ab initio* molecular orbital theory approach to finding solutions to the Schrödinger equation. Other methods exist, such as the density functional theory approach described in Section 2.2.2. The non-relativistic, time-independent Schrödinger equation is given by

$$\hat{H}\Psi = \frac{-\hbar^2}{2m}\nabla^2\Psi + V\Psi = E\Psi \,. \tag{2.3}$$

Here, Ψ is the wavefunction, which describes the quantum state of a particle and how it behaves. $\hat{H}$ is the Hamiltonian operator, which characterizes the total energy (E) of any given wavefunction. $\hbar$ is the reduced Planck constant,

[1] This Section closely follows the (online) lecture notes on quantum mechanics/chemistry by Doctor Carole A. Morrison (The University of Edinburgh), Professor David Sherrill (http://vergil.chemistry.gatech.edu/notes/), and from Chemistry Department at MIT (http://ocw.mit.edu/courses/chemistry/).

m is the particle mass, ∇^2 is the Laplace operator, and V is the potential energy of the particle. Equation 2.3 essentially states that total energy equals kinetic energy ($\frac{-\hbar^2}{2m}\nabla^2$) plus potential energy; its terms, however, take complex forms (compared to classical mechanics). In this equation, the system kinetic energy results from all of the nuclei and electrons; while the system potential energy comprises the nucleus–nucleus repulsion, electron–electron repulsion, and nucleus–electron attraction. This equation is an eigenvalue function; the Hamiltonian operator ($\hat{H}$) acts on the wavefunction (Ψ) to yield the permitted energy levels (E) of the molecule.

The Schrödinger equation can only be solved exactly for one-electron systems. The electron–electron potential energy term is impossible to solve for multi-electron systems, because the electron motion is correlated: the electrostatic field of one electron will influence the position of a second, and so on. Part of the solution is the Born–Oppenheimer approximation, which makes the assumption that the electronic motion and the nuclear motion in a molecule can be separated. In other words, it allows the total wavefunction of a molecule to be broken into its nuclear and electronic components, i.e., $\Psi_{\text{total}} = \psi_{\text{nuclear}} \times \psi_{\text{electronic}}$. In what follows, the kinetic energy of the nuclei is set to zero, as they move much slower than the electrons and can be considered stationary in the viewpoint of the electrons. Thus, the nucleus–nucleus potential energy becomes a constant. The electronic wavefunction depends on the positions of the nuclei but not on their velocities, and the nuclear motion (rotation, vibration) "sees" a smeared-out potential from the speedy electrons.

So far, all of the nucleus–nucleus and nucleus–electron interactions have been taken care of. To deal with electron–electron interactions, another approximation, known as Hartree theory, needs to be introduced. Hartree theory was devised to allow for ignoring electron–electron correlation (i.e., how the motion of one electron affects all the others), by assuming that each electron moves in a uniform field generated by the other electrons present. As a result, an insoluble *N*-electron problem is replaced by a soluble $N \times$ one-electron problem, which is solved one electron at a time. In addition, electron exchange needs to be modelled. Electron exchange concerns the pairing-up of two opposite-spin electrons in one atomic orbital; that is, each atomic orbital can accommodate a maximum of two electrons, provided that they are of opposite spin (denoted as alpha ↑ and beta ↓). Electron exchange can be handled by Fock theory, which makes use of an anti-symmetric wavefunction – swapping the coordinates of the two electrons in one atomic orbital gives rise to sign change.

Combining Hartree theory (which takes care of electron correlation by ignoring it) and Fock theory (which provides an exact amount of electron exchange) gives the simplest *ab initio* method, the Hartree–Fock (HF) theory, which does surprisingly well for certain systems. The missing correlation energy, however, leads to a serious deficiency of the method in treating, for example, dispersion-dominant systems, as dispersive forces arise from the electron correlation effect in interacting molecules. A number of approaches to this weakness, collectively known as post-Hartree–Fock methods, have been devised to improve upon HF theory by adding additional terms to include electron correlation to the multi-electron wavefunction. Some of these approaches (in order of increasing complexity) include Møller–Plesset perturbation theory, coupled cluster, and configuration interaction.

In summary, within the Born–Oppenheimer approximation, the "stationary" nuclei enter the problem only as generators of an electric potential field in which the electrons move, thus the total molecular Hamiltonian becomes a Hamiltonian of electrons only. Ultimately, the (electronic) Hamiltonian is concerned with modelling the interactions (correlation and exchange) between electrons. There are various ways to construct a Hamiltonian operator for a particular system, giving rise to different levels of theory.

The Schrödinger equation (Equation 2.3) states that the Hamiltonian operator acts on the wavefunction to obtain the permitted energy levels for the molecule. $\hat{H}$, as discussed above, describes how electrons interact with one another, whereas it is the Ψ that describes the region of space in which the electrons are allowed to "live". In other words, Ψ is a mathematical description of a molecular orbital. The concept of orbitals came into being, following on from Heisenberg's uncertainty principle, which says that it is impossible to define both the energy and the position of an electron. This means that if the energy is uniquely defined, then there is an uncertainty in the position of the electron, thus "creating" an orbital.

In a practical QM calculation, the simulator specifies a set of pre-defined basis functions (a basis set) that describe the atomic orbitals, from which the computer programme is to construct the molecular orbitals using the rules of molecular orbital theory. Most commonly, a molecular orbital ϕ_i is written as a linear combination of n atomic orbitals χ_μ:

$$\phi_i = c_{1i}\chi_1 + c_{2i}\chi_2 + c_{3i}\chi_3 + \cdots + c_{ni}\chi_n \quad \text{or}$$
$$\phi_i = \sum_{\mu=1}^{n} c_{\mu i}\chi_\mu \tag{2.4}$$

where c_μ are weighting coefficients, each of which expresses the relative importance of that particular atomic orbital in construction of the molecular orbital. By changing the values of c_μ, different orbitals (or wavefunctions) can be constructed for the molecule.

It is possible to create any number of different molecular wavefunctions using Equation 2.4. Therefore, a procedure is needed to find the right one – the one that corresponds to the ground-state electronic structure of the molecule. This is achieved on the basis of the variational principle, which states that the energy calculated from an approximation to the true wavefunction will always be greater than the true energy. Put differently, the best wavefunction is the one that yields the lowest energy for the molecule. Again, $\hat{H}$ acts on Ψ to give E (the Schrödinger equation), meaning each trial wavefunction can be mapped to a particular energy. A self-consistent loop is set up, in which the weighting coefficients c_μ are altered until the molecular wavefunction that gives the lowest energy is found.

Put together, this Section shows the very basics of one possible approach to solving the Schrödinger equation. From a practical perspective, the Hamiltonian operator can be approximated using a chosen level of theory (e.g., HF theory), while the molecular wavefunction can be approximated using a basis set such as 6-31+G*, a Pople-type Gaussian basis set.

2.2.2 Density functional theory

The Hamiltonian operator (in the Schrödinger equation) of a many-electron system can be constructed alternatively in accord with density functional theory (DFT). With this theory, the properties of a many-electron system can

be determined on the basis of the electron density (of the system) that depends on only three spatial coordinates.

The foundation of DFT is the Hohenberg–Kohn theorem, which states that the external potential (of a system) is a functional of the ground-state electron density. It implies that given an external potential, the wavefunction and the electron density that correspond to it are uniquely determined; conversely, given an electron density, only one potential and one wavefunction correspond to that density. In other words, one can in principle calculate all molecular properties of a system based on the knowledge of the electron density.

In DFT, the (total) energy functional is split into kinetic energy, potential energy, (classical) Coulomb electrostatic repulsion energy, and exchange–correlation energy. This process is in principle exact; however, the "true" form of the exchange–correlation energy functional is not known. As a result, different approximate solutions, giving rise to different exchange–correlation functionals, have been developed, making use of the so-called Kohn–Sham orbitals. The most commonly used functionals can be (very) broadly categorized into three classes: Local Density Approximation (LDA), Generalized Gradient Approximation (GGA), and hybrid functionals.

LDA is the simplest approximation to the exchange–correlation energy functional. With it, the electron density is treated locally as a uniform electron gas; that is, the exchange–correlation energy at each point in space is the same as that of a uniform electron gas having the same density. LDA is a fairly good model for systems where the electron density does not change drastically, such as some metallic systems. Conceivably, it does not work

well for molecular systems that are typically characterized by rapidly varying electron densities. On the other hand, GGA-based DFT functionals take into account additional information on the gradient of the electron density. Compared to LDA-derived functionals, they can therefore better cope with rapidly changing electron densities. Examples of GGA-type functionals include BLYP, PBE, and PW91. In all DFT functionals (of either LDA- or GGA-type), both electron exchange and electron correlation are approximated.

Hybrid DFT functionals incorporate a portion of exchange from Hartree–Fock theory with a DFT exchange and a DFT correlation. This Hartree–Fock-type exchange, commonly referred to as the exact exchange, is calculated from the Kohn–Sham orbitals rather than the electron density. In other words, the exchange is "exact" in the sense that the exchange energy for a given pair of electron spin densities is yielded by a unique Slater determinant of Kohn–Sham orbital. The rationale behind this admixing of an exact exchange and a density functional is that the KS-DFT methods, being either LDA or GGA, are known for systematic errors such as the incomplete cancellation of the self-Hartree energy for each orbital, known as the self-interaction error. Since the self-interaction error is primarily caused by the poor description of the exchange interaction by the (semi)local approximation of DFT, the error is remedied by the incorporation of exact exchange. Compared to pure DFT or the HF method, hybrid DFT functionals generally provide much improved descriptions of, for example, the atomization energies, bond lengths, and vibration frequencies for most molecules. This is a result of how the different techniques deal with electron exchange and electron correlation as summarized in Table 2.1.

Table 2.1. Treatments of electron exchange and correlation in the different levels of theory.

	electron exchange	electron correlation
HF theory	exact	ignored
pure DFT	approximate	approximate
hybrid DFT	approximate + exact	approximate

One of the most popular hybrid functionals is the so-called B3LYP functional. The "3" in the name says that three different levels of theory – namely, HF, LDA, and GGA – were mixed to create the functional. The weights of the various contributions to the mix (the total exchange–correlation energy) were obtained by fitting to reference data for a training set of molecules.

Both the Hartree–Fock theory and density functional theory have long been known to account poorly for the long-range correlation effect of dispersion. This type of weak interaction is, however, of paramount importance in the host–guest chemistry investigated in this Thesis. To achieve an accurate description of the dispersion interaction of interest, this work has made use of the empirically dispersion-corrected DFT methods, termed as DFT-D, of Grimme and co-workers (Grimme, 2006; Grimme et al., 2010). In addition, a double-hybrid density functional – namely, B2PLYP (Grimme, 2006) – has also been used extensively. The method adds nonlocal electron correlation effects to a standard hybrid DFT functional by second-order perturbation theory. For the sake of clarity, more detailed discussions on these methods are provided in the respective Chapters.

2.3 Physical Adsorption at the Gas–Solid Interface

Adsorption occurs when a solid surface is exposed, in this case, to a gas; the phenomenon is marked by an increase in the density of the gas in the vicinity of an interface. Molecules of the gas undergo interactions with the solid, temporarily departing from the gas phase; those in the condensed phase formed at the solid surface remain for a period of time, and then return to the gas phase. The duration of this stay is dependent on many factors, such as the nature of the adsorbing surface and that of the adsorptive gas, the temperature, and so on. In contrast with chemisorption (in which new chemical compounds are formed) and absorption (in which gas molecules penetrate into the bulk of the solid), physical adsorption (or physisorption) is brought about by the weak interactions between the solid and the molecules in the fluid phase. The forces responsible are predominantly the attractive dispersion forces, as well as short-range repulsive forces. In addition, electrostatic forces are also involved in the adsorption of polar molecules. A physisorbed molecule keeps its identity (in the adsorbed phase) and upon desorption returns to the fluid phase in its original form.

2.3.1 Gas–solid adsorption models

An adsorption isotherm describes the mass-transfer equilibrium, at a given temperature, between a reservoir and a solid surface on which molecules can be adsorbed. The general relation takes the form:

$$n_{\mathrm{ad}} = f(\mu) \tag{2.5}$$

where n_{ad} is the amount of molecules adsorbed, and μ is the chemical potential of the adsorptive in the reservoir. If the gas reservoir can be considered as made up of ideal gases, then its chemical potential is given by

$$\mu = \mu_0(T) + k_B T \ln(P/P_0) \tag{2.6}$$

where P is the vapour pressure, P_0 is the saturation pressure, and $\mu_0(T)$ is the chemical potential at saturation. Since at a given temperature the chemical potential is only dependent on P, adsorption isotherms are often expressed as $n_{ad} = f(P)$.

The Langmuir adsorption model, which considers adsorption of an ideal gas onto an idealized surface, relates the coverage or adsorption of gas molecules on a solid surface to the gas pressure above the surface at a fixed temperature. Assuming that the adsorbent surface has a total of M adsorption sites, then the central question to answer is: how many of these M sites will be occupied when the adsorbent is brought into contact with a gas reservoir with chemical potential μ at temperature T? Broadly speaking, two parts constitute an answer to the question. First, using the fundamental principles of statistical mechanics, the chemical potential of the adsorbed phase, μ_{ads}, can be obtained – by taking the derivative of the Helmholtz free energy with respect to the number (N) of molecules adsorbed – and is given by

$$\mu_{ads} = u_{ads} + k_B T \ln\left(\frac{N}{M-N}\right). \tag{2.7}$$

The chemical potential has two contributions: the first, u_{ads}, is energetic and the second is entropic. It is clear that the chemical potential diverges for $N \rightarrow M$ and for $N \rightarrow$ zero; that is, the molecules tend to be desorbed when $N \approx M$ but tend to be adsorbed when $N \approx$ zero. It is noteworthy that the entropic

term is proportional to $k_B T$, the thermal energy. This means that at finite temperature, thermal fluctuations enable a molecule to move to a state of higher energy by taking the missing energy in a reservoir in the form of heat.

Second, for the surface with N adsorbed molecules (having chemical potential μ_{ads}) in mass-transfer equilibrium with a reservoir of chemical potential μ_{res}, the equilibrium condition is that $\mu_{ads} = \mu_{res}$. In other words, if the surface defined by Equation 2.7 is put in contact with the reservoir defined by Equation 2.6, then molecules get transferred between the gas phase and the adsorbed phase until the equilibrium is reached. This (i.e., $\mu_{ads} = \mu_{res}$) leads to

$$\frac{N}{M} = \frac{Kx}{1+Kx} \tag{2.8}$$

where K is a constant (at a given temperature), given by

$$K = \exp\left[\frac{\mu_0(T) - u_{ads}}{k_B T}\right] \tag{2.9}$$

and x is the partial vapour pressure given by $x = P/P_0$. In the limit of low vapour pressure (i.e., $Kx \rightarrow$ zero) Equation 2.8 reduces to a simple proportionality law (sometimes referred to as Henry's law):

$$\frac{N}{M} \approx Kx. \tag{2.10}$$

For adsorption experiments carried out up to 1 bar, it can usually be assumed that the gas phase behaves like an ideal gas. As the pressure increases, this becomes less and less acceptable. A satisfactory calculation of either the amount left in the gas phase or its density requires taking into account the molecular interactions and the limiting volume of the molecules

when under compression. To this end, a number of equations (collectively known as equations of state) have been proposed to relate the pressure P to the temperature T and the gas molar volume V_m. Among them (except the ideal gas law), perhaps, the van der Waals equation is the simplest, given by

$$(P + a/V_m^2)(V_m - b) = RT \tag{2.11}$$

where the van der Waals constants a (allowing for the molecular interactions) and b (corresponding to the limiting molar volume) are independent of temperature and only dependent on the nature of the gas. They are calculated from the critical temperature T_c and critical pressure P_c, as

$$a = (R^2 T_c^2)/(64P_c); b = (RT_c)/(8P_c). \tag{2.12}$$

There exist many other more elaborate equations, which are only of slightly greater complexity but of much higher accuracy, such as the Peng–Robinson equation of state. The interested reader is referred to the original article by Peng and Robinson (1976).

2.3.2 Grand-canonical Monte Carlo simulation of adsorption

In adsorption studies, one is interested in obtaining information on the average number of molecules adsorbed as a function of the pressure and temperature of the reservoir with which the adsorbent is in contact. The grand-canonical ensemble is a natural choice for simulation of adsorption. In a grand-canonical Monte Carlo (GCMC) simulation, the chemical potential, volume, and temperature are kept fixed while the number of gas molecules in the adsorbed phase is allowed to fluctuate so that the chemical potential of the adsorbed phase is the same as that of the gas reservoir. The microscopic

configurations of the system are generated by creating random Monte Carlo moves – such as translation, rotation, insertion, deletion, etc. – according to statistical mechanics. The grand canonical partition function, $Q_{\mu VT}$, is the following sum over microstates:

$$Q_{\mu VT} = \sum_i \exp[(N_i\mu - E_i)/(k_\mathrm{B}T)] \tag{2.13}$$

where each microstate i has a total of N_i particles and a total energy of E_i. The probability (p_i) to find the system in state i is then given by

$$p_i = \frac{1}{Q_{\mu VT}} \exp[(N_i\mu - E_i)/(k_\mathrm{B}T)]. \tag{2.14}$$

To impose a constant chemical potential, fluctuations in the number of particles are required, achieved by random particle insertions and deletions. The insertion of a particle at a random position is accepted with a probability

$$\mathrm{acc}(N \to N+1) = \min\left[1, \frac{V}{\Lambda^3(N+1)} \exp\{\beta[\mu - E(N+1) + E(N)]\}\right]. \tag{2.15}$$

The deletion of a randomly selected particle is accepted with a probability

$$\mathrm{acc}(N \to N-1) = \min\left[1, \frac{\Lambda^3 N}{V} \exp\{-\beta[\mu + E(N-1) - E(N)]\}\right]. \tag{2.16}$$

Here, $\beta = 1/(k_\mathrm{B}T)$ and Λ is the de Broglie thermal wavelength.

Monte Carlo simulations require separate equilibration and production runs, which also applies to molecular dynamics simulations. Initial configurations of the system may be chosen in a variety of ways, but it is important to allow the system to lose memory of them as it approaches equilibrium. This corresponds to the Markov chain approaching long-term behaviour where it

reaches the imposed stationary distribution of states. The number of MC cycles required for equilibration (normally) is not known *a priori*; thus, it should be probed by test runs, from which (for example) the system density can be plotted against the MC cycle number to help determine the equilibration period needed. It is also commonplace to discard a large number of early MC cycles for the purpose of equilibration. The average of any quantity from a Monte Carlo simulation is then accumulated after this equilibration run. As these averages are subject to statistical errors, it is important to provide error estimates for such quantities. The error represents the deviation from the average value over the post-equilibration run. If the error estimate is large it may indicate that the equilibrium has not been reached or that the simulation is subject to errors in the setup/code or suffers from actual physical limitations (e.g., correlation-length induced fluctuations at the critical point). Errors can be estimated in various ways; for example, from independent simulations with different initial configurations or from a single simulation by dividing the production run into several blocks. In this work, the latter approach has been chosen. To be explicit, the error estimates reported in this Thesis are computed in the following procedure. First, the production run of a GCMC simulation is divided into 20 blocks, for each of which the average of the quantity of interest is calculated. Then, the standard deviation of the 20 averages is calculated. Last, the reported error estimates (or error bars) are determined as the 95% confidence interval (assuming a normal distribution).

2.4 Free Energy Calculation

To understand comprehensively the vast majority of chemical processes, it is often necessary to examine their underlying free energy behaviour. This is certainly the case, for instance, in understanding and/or predicting first-order phase transitions of a given substance; free energy is an important and useful concept when the relative stability of several phases is of interest. The thermodynamic free energy is the amount of work that a thermodynamic system can perform; it is the internal energy (U) of a system minus the amount of energy that cannot be used to perform work. The unusable energy is given by the entropy (S) of a system multiplied by the temperature of the system. If a system is in contact with a heat bath, such that its temperature T, volume V, and number of particles N are fixed, then the Helmholtz free energy $F \equiv U - TS$ is at a minimum in equilibrium. Analogously, for a system of N particles at constant pressure P and temperature T, the Gibbs free energy $G \equiv U + PV - TS$ is at a minimum in equilibrium. By comparing the Helmholtz free energies of different phases, for example, it is straightforward to establish which of the phases is stable under the given conditions. However, it is not (always) possible to measure free energy directly in simulations (or experiments). The reason is that free energy (or entropy) is not simply averages of functions of phase space coordinates of the system; instead, it is directly related to the volume in phase space available to the system. In statistical mechanics, the Helmholtz free energy F is proportional to the logarithm of the partition function $Q(N,V,T)$ for the canonical ensemble; that is:

$$F = -k_{\mathrm{B}} T \ln Q(N, V, T). \tag{2.17}$$

Since free energies cannot be measured directly, what are normally determined in simulations or experiments are derivatives of the free energy, such as the derivative with respect to volume V or temperature T:

$$\left(\frac{\partial F}{\partial V}\right)_{NT} = -P; \left(\frac{\partial F/T}{\partial 1/T}\right)_{NV} = E. \tag{2.18}$$

As pressure P and energy E are mechanical quantities, they can be determined in a simulation. To compute the free energy of a system at given temperature and density, one therefore only needs to find a reversible path in the V–T plane that links the state under consideration to a state of known free energy. The change in F along this path can then be evaluated by thermodynamic integration; that is, integration of Equation 2.18. There are only very few thermodynamic states for which the free energy of a substance is known. One such state is the ideal gas phase, which, for example, can be used as the reference state in the calculation of the free energy of a liquid through integration of the equation of state. For determining the free energy of a dense liquid, a reversible path to a very dilute gas phase may be used; it is not always necessary to reach the ideal gas phase. This reference phase should, however, be sufficiently dilute to ensure accuracy in the free energy calculation. To compute the free energy of a solid, the ideal gas reference state is rarely useful and other approaches are necessary. For example, within the framework of thermodynamic integration, in order to compute the Helmholtz free energy of an atomic solid, the solid is transformed reversibly into an Einstein crystal. The basic idea is that the atoms are coupled harmonically to their lattice sites; if the coupling is sufficiently strong, the solid behaves as an Einstein crystal, for which the free energy can be determined exactly.

In addition to thermodynamic integration, many other methodological frameworks and techniques have been widely employed, such as free energy perturbation, methods based on probability distributions and histograms, and methods based on calculating free energy from nonequilibrium dynamics. There are also various methods that were proposed for more specific systems. For example, the so-called lattice-switch Monte Carlo method of Wilding and co-workers is a technique devised to study phase transitions of solid-state crystals (Bruce et al., 1997). The method has been used to evaluate the difference between the free energies of two structural phases of a crystal. By making use of a biased sampling of atomic displacements to favour configurations of one structure that can be replaced by corresponding configurations of the other through a Monte Carlo switch of the lattice, the method can efficiently deal with comparing the statistical weights of two regions of configuration space. For more complete discussions on free energy calculations, the reader is referred to standard text books, such as the one by Chipot and Pohorille (2007).

Although the theoretical aspects described in this Chapter for the various modelling methodologies are elementary, they provide the foundations for the molecular simulations and QM calculations performed in this work. In the reminder of this Thesis, GCMC simulations and first-principles DFT calculations are used to study gas adsorption in MOFs with coordinatively unsaturated metal sites, while DFT-based MD simulations are performed to investigate and elucidate the structural changes of a flexible MOF in response to temperature variation and variable sorbate uptake.

Chapter 3 Gas Adsorption in MOFs with Coordinatively Unsaturated Metal Sites

3.1 Introduction

The incorporation of coordinatively unsaturated metal sites (cus's), also known as open metal sites or unsaturated metal centres, into MOFs has been shown to enhance significantly the uptake of certain gases such as CO_2 (Caskey et al., 2008; Llewellyn et al., 2008; Dietzel et al., 2009; Yazaydın et al., 2009), CH_4 (Dietzel et al., 2009; Getzschmann et al., 2010), and H_2 (Zhou et al., 2008; Sumida et al., 2011), especially at low loadings when fluid–framework interactions play the predominant role.

Because of the considerably enhanced, localized interaction between the guest molecule and the cus, it remains a challenge to predict correctly adsorption isotherms and/or mechanisms in MOFs with cus's using GCMC simulations based on generic classical force fields such as UFF (Rappe et al., 1992), DREIDING (Mayo et al., 1990), and OPLS-AA (Jorgensen et al., 1996). These force fields fail to describe guest-molecule interactions with cus's correctly as the equilibrium distance between the metal atom and the adsorbate molecule at a cus is often considerably smaller than the combined hard-sphere diameter defined by the force fields (Getzschmann et al., 2010; Wu et al., 2010; Queen et al., 2011). Take CO_2 adsorption in the MOF CPO-27-Mg (Dietzel et al., 2009) as an example. The distance observed experimentally between the magnesium cus and the nearby oxygen of the adsorbed CO_2 molecule is ca. 2.30 Å (Queen et al., 2011), which is markedly smaller than the value of 2.87 Å for the Lennard–Jones parameter $\sigma_{Mg–O(CO_2)}$ (i.e., 0.5 ×

(σ_{Mg} + $\sigma_{O(CO_2)}$) = 2.87 Å) given by the combination of UFF for Mg and TraPPE (Potoff and Siepmann, 2001) for O(CO_2). As a result, GCMC simulations making use of these (and most likely other) generic classical force fields are unable to reproduce adsorption on the cus's when compared to experiment. A few examples are the reports of Yazaydın et al. (2009), Getzschmann et al. (2010), Chen et al. (2011), and Chen et al (2012).

In contrast to the difficulties faced by generic classical force fields in describing correctly the guest-molecule interactions with cus's, it has been clearly demonstrated in the literature that *ab initio* methods can deal with interactions of this kind with a high level of accuracy, which is of crucial importance for obtaining accurate predictions of adsorption in MOFs with cus's (Fischer et al., 2010; Chen et al., 2011; Chen et al., 2012; Fischer et al., 2012). The associated computational cost, however, increases drastically with system size, allowing only the description of small systems (less than 100s atoms, rather than 1000s by force-field-based molecular simulations). Although DFT methods allow for treatment of larger systems on a sound first-principles basis, they are still too expensive to be carried out routinely and, more importantly, are prone to underestimate some contributions to the intermolecular interaction – e.g., dispersive or van der Waals (vdW) (Kristyán and Pulay, 1994; Cohen et al., 2011; Klimes and Michaelides, 2012). Moreover, when the whole adsorption isotherm is of interest, no QM method on its own is practically adequate for the goal.

Since both molecular simulation and QM approaches have strong advantages together with critical disadvantages, a multi-scale strategy that allows for computation on large systems with high accuracy seems a promising and somewhat natural solution for answering the challenges faced in simulating

adsorption and diffusion in MOFs with cus's. The fundamental principle behind the proposed multi-scale modelling strategy in this Thesis is to implement accurate energetic and geometric information – which concerns a particular fluid–framework system – provided by a chosen QM method into GCMC simulations, which handle description of the thermodynamic behaviour of the system and produce results that are directly comparable to experiments. To demonstrate this strategy, two modelling approaches have been developed and are described in detail in this and the following Chapters (Chapters 3 and 4).

3.2 Direct Implementation of an *ab initio* Derived Potential Energy Surface in GCMC Simulations of CH_4 adsorption in the MOF CuBTC

The first proposed modelling approach combines *ab initio* methods with classical GCMC simulations by implementing an *ab initio* derived fluid–framework potential energy surface (PES) into GCMC simulations and thus removing the ambiguities and inaccuracies resulting from the use of generic force fields. During a GCMC simulation of this kind, the fluid–framework interactions are taken directly from the *ab initio* PES constructed *a priori* and are not calculated using force fields. An especially appealing aspect of this approach, from a fundamental viewpoint, is that the various intermolecular interactions – such as exchange, electrostatics, induction, and dispersion – as captured by the chosen *ab initio* method are included in GCMC simulations by means of a single fluid–framework potential map.

To illustrate this method, the adsorption of methane in the MOF CuBTC (Chui et al., 1999) at 77 K was studies. This particular system was chosen for the following three reasons. Firstly, the importance of cus, even for non-polar fluids such as methane, has been observed experimentally (Dietzel et al., 2009; Getzschmann et al., 2010; Wu et al., 2010; Guo et al., 2011). Secondly, methane is a nearly spherical molecule, so the orientation dependence of the methane–framework potential energy can be neglected, which significantly reduces computational costs. Thirdly, Getzschmann et al. (2010) studied deutero-methane (CD_4) adsorption in CuBTC at 77 K using high-resolution *in situ* neutron diffraction and reported detailed information about the localization of methane molecules inside the framework. Preferential adsorption sites and a sequential pore-filling mechanism were identified in their experiments. Moreover, the cus's in the CuBTC framework were demonstrated to play an important role in the adsorption mechanism, since they were found to be the primary adsorption sites for methane at 77 K. In contrast, the GCMC simulations based on generic force fields carried out in the same work could not capture correctly the methane–cus interaction, ultimately leading to a different adsorption mechanism being predicted as compared to the experimental findings (Getzschmann et al., 2010). The lack-of-representation of generic force fields in describing the CH_4–Cu(II) interaction, together with the computational feasibility enabled by neglecting the orientation dependence of fluid–framework interactions, makes the CH_4 – CuBTC system an ideal test case for the modelling approach proposed here.

The notations for the pores and adsorption sites in CuBTC used in this Thesis are the same as those specified by Getzschmann et al (2010). In brief, the CuBTC framework contains three types of pores: S1, with a diameter of 4.9 Å – which was calculated as the diameter of the largest sphere that could fit

into the cavity without overlapping with the framework atoms (Gelb and Gubbins, 1999) – and centre at (0.25, 0.25, 0.25) (Wyckoff notation); L2, with a diameter of 10.5 Å and centre at (0.5, 0.5, 0.5); and L3, with a diameter of 12.2 Å and centre at (0.0, 0.0, 0.0). In total nine adsorption sites were identified from neutron diffraction experiments, as shown in Figure 3.1. Their crystallographic positions can be found in the work of Getzschmann et al (2010). In particular, the distance observed experimentally between CD_4 and the copper ion is 3.075 Å. As this distance is considerably smaller than the Lennard–Jones hard-sphere parameter σ_{CH_4-Cu} [$0.5(\sigma_{CH_4} + \sigma_{Cu})$ = 3.422 Å], it is clear that the UFF-based GCMC simulation cannot reproduce CH_4 adsorption on the cus's.

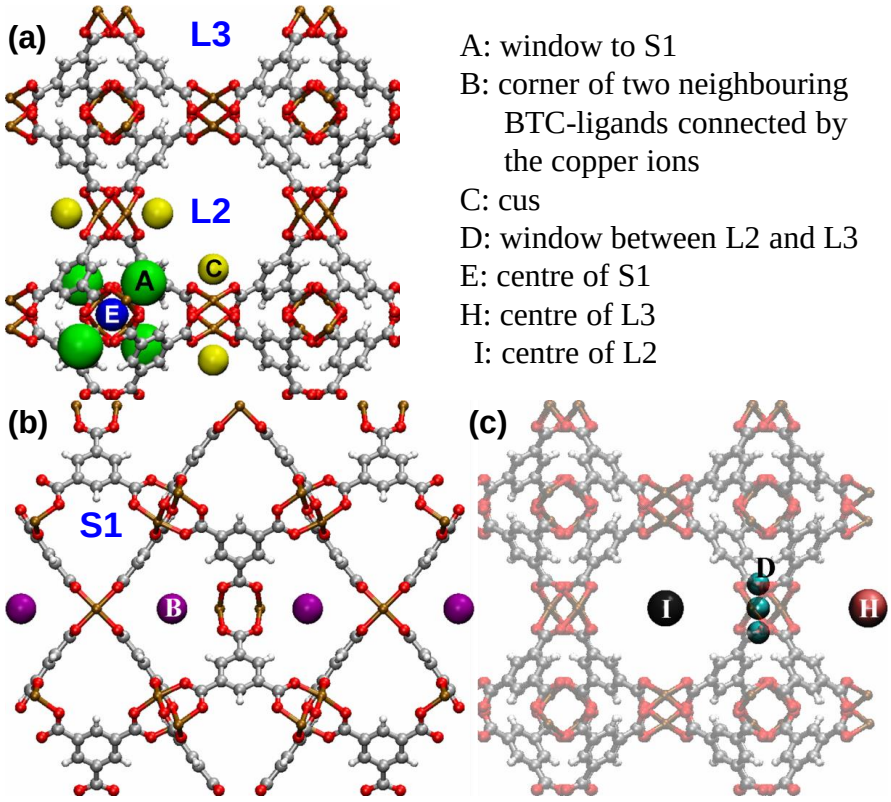

Figure 3.1. Structure of CuBTC viewed from the (a, c) front and (b) side: white, hydrogen; grey, carbon; red, oxygen; and brown, copper. Pores S1, L2, and L3 are described in the text. Experimental adsorption sites are represented by coloured spheres, with definitions given in the figure. Two secondary adsorption sites G and F (not shown) are close to sites A and D, respectively.

3.2.1 Building a DFT/CC PES for CH_4 – CuBTC

The *ab initio* CH_4–CuBTC interaction potential was described by a hybrid DFT/*ab initio* method, named DFT/CC (Bludský et al., 2008; Rubeš et al., 2010; Zukal et al., 2010). Note that all of the DFT/CC calculations were carried out by the group of Professor Petr Nachtigall at Charles University in Prague. The DFT/CC method has been demonstrated to provide accurate descriptions of guest-molecule interactions with not only the cus's but also all the other sites in CuBTC for a number of sorbate molecules, such as H_2O (Grajciar et al., 2010), CO_2 (Grajciar et al., 2011), CO (Rubeš et al., 2012), and C_3 hydrocarbons (Rubeš et al., 2013). In the case of constructing a CH_4–CuBTC PES, the carbon atom of a single methane molecule was placed in a random configuration on specific grid points (inside the framework), and the CH_4 interaction energies with the CuBTC framework were then evaluated by DFT/CC calculations. The potential energy grid thus obtained was used to determine the CH_4–CuBTC interactions in the GCMC simulations.

The CH_4–CuBTC PES was represented by a precalculated three-dimensional Cartesian grid neglecting the orientation dependence of the interaction potential (which is small, as methane is a nearly spherical molecule) and keeping the CuBTC framework rigid. The fluid–framework potential energy was calculated at the DFT/CC level as

$$E_{\text{int}} = E(\text{CH}_4 \cdots \text{CuBTC}) - E(\text{CH}_4) - E(\text{CuBTC}) + \Delta E_{\text{DFT/CC}} \tag{3.1}$$

where $E(CH_4 \cdots CuBTC)$, $E(CH_4)$, and $E(CuBTC)$ are the total energies of the $CH_4 \cdots CuBTC$ system, an isolated CH_4 molecule, and the CuBTC framework, respectively, calculated at the Perdew–Burke–Ernzerhof (PBE) (Perdew et al., 1996) level of theory with the periodic model (see Appendix A1 for details).

$\Delta E_{DFT/CC}$ is the DFT/CC correction described in detail in Appendix A1. The frozen monomer approximation was adopted, employing the CCSD(T)/AVQZ-optimized geometry of CH_4 and the experimental geometry of CuBTC (Chui et al., 1999). "AVQZ" denotes a mixed basis set of aug-cc-pVQZ-PP (Peterson and Puzzarini, 2005) for Cu and aug-cc-pVQZ (Thom H. Dunning, 1989) for the other atoms (likewise for AVXZ and VXZ, hereafter).

The CH_4–CuBTC interaction potential was first evaluated on the equally spaced 2.0-Å grid with the exclusion of the grid points in close contact with the framework (less than 1.5 Å from the framework atoms). Based on these values, a refinement of the grid was performed, introducing a denser grid especially in the vicinity of adsorption sites A, B, C and E (Figure 3.1). The grid was constructed from about 2000 grid points for which the interaction potential was explicitly evaluated with the DFT/CC method. By taking into account the symmetry of the individual sites, the number of grid points was increased to a few tens of thousands. Finally, to obtain the equally spaced 0.25-Å grid used in the GCMC simulations, a three-dimensional linear interpolation was used to determine the potential energy between a methane molecule and the CuBTC framework.

For completeness, a short description of the DFT/CC method in the context of constructing a PES for the CH_4 – CuBTC system is given in Appendix A1. It should be emphasized again that all of the DFT/CC calculations were done by Lukáš Grajciar and Professor Petr Nachtigall. Methodological details about DFT/CC can be found in the literature (Bludský et al., 2008; Rubeš et al., 2010; Zukal et al., 2010), while the application of DFT/CC to describing the CH_4 – CuBTC system is reported by Chen et al (2011).

3.2.2 GCMC simulations

Methane adsorption in CuBTC was studied using GCMC simulations implemented in the multipurpose simulation code MUSIC (Gupta et al., 2003). The atomistic representation of the CuBTC framework was constructed from the experimental crystallographic data (Chui et al., 1999), with all of the framework atoms kept fixed at their positions during the simulations. In the DFT/CC-PES GCMC simulations, the CH_4–CuBTC interaction was determined from the pretabulated potential determined by DFT/CC as described above. For comparison, GCMC simulations were also performed using three generic classical force fields for the framework – namely, UFF, DREIDING, and OPLS-AA. The model used for CH_4 was derived by Goodbody et al.(1991), using a united-atom (denoted as UA) description of the CH_4 molecules – one CH_4 molecule is represented by a single sphere (σ_{CH_4} = 3.73 Å, ε_{CH_4}/k_B = 148.00 K). All CH_4–CH_4 interactions and all generic-force-field-based CH_4–CuBTC interactions were modelled using the standard (12–6) Lennard–Jones (LJ) potential. The Lorentz–Berthelot combining rules were used to calculate the LJ cross-parameters. Interactions beyond 18.650 Å were neglected. Each simulation consisted of an equilibration period of 2.0×10^7 iterations, followed by a production run of further 2.0×10^7 iterations, carefully ensuring that equilibrium was reached.

The amounts of guest molecules adsorbed that are obtained from a GCMC simulation correspond to total amounts, also called "*absolute*" amounts, of the adsorptive inside the pores of the adsorbent. More generally, however, in experiment it is the surface "*excess*" amount of the adsorptive that is measured. Therefore, to compare simulation results with experiment, the absolute amount adsorbed from a GCMC simulation was converted to the

excess amount adsorbed using the method of Myers and Monson (2002). The excess amount of methane adsorbed, n_{excess}, is given by

$$n_{\text{excess}} = n_{\text{abs}} - \frac{pV_{\text{pore}}}{\text{ZR}T} \tag{3.2}$$

where n_{abs} is the absolute amount adsorbed, p is the bulk pressure, V_{pore} is the pore volume, Z is the compressibility factor, R is the ideal gas constant, and T is the temperature. The Peng–Robinson equation of state was used to estimate Z. The accessible pore volume, V_{pore}, was taken to be equal to the experimentally determined value of 0.72 $cm^3\ g^{-1}$ (Getzschmann et al., 2010).

The isosteric heat of adsorption, Q_{st}, was calculated as the difference in the partial molar enthalpy of the sorbate between the bulk phase and the adsorbed phase, given by

$$Q_{st} = \text{R}T - \frac{\langle VN \rangle - \langle V \rangle \langle N \rangle}{\langle N^2 \rangle - \langle N \rangle^2} \tag{3.3}$$

where V is the potential energy of the system and N is the number of adsorbed CH_4 molecules.

3.2.3 Results and discussion

Adsorption isotherms. The DFT/CC-PES GCMC modelling approach is assessed by comparing simulation results with the experimental data from the work of Getzschmann et al (2010). In that work, not only adsorption isotherms were measured but also adsorption sites were determined, and the UFF-based GCMC simulations in the same work highlighted the

shortcomings of using parameters from the generic UFF for describing the adsorption mechanism.

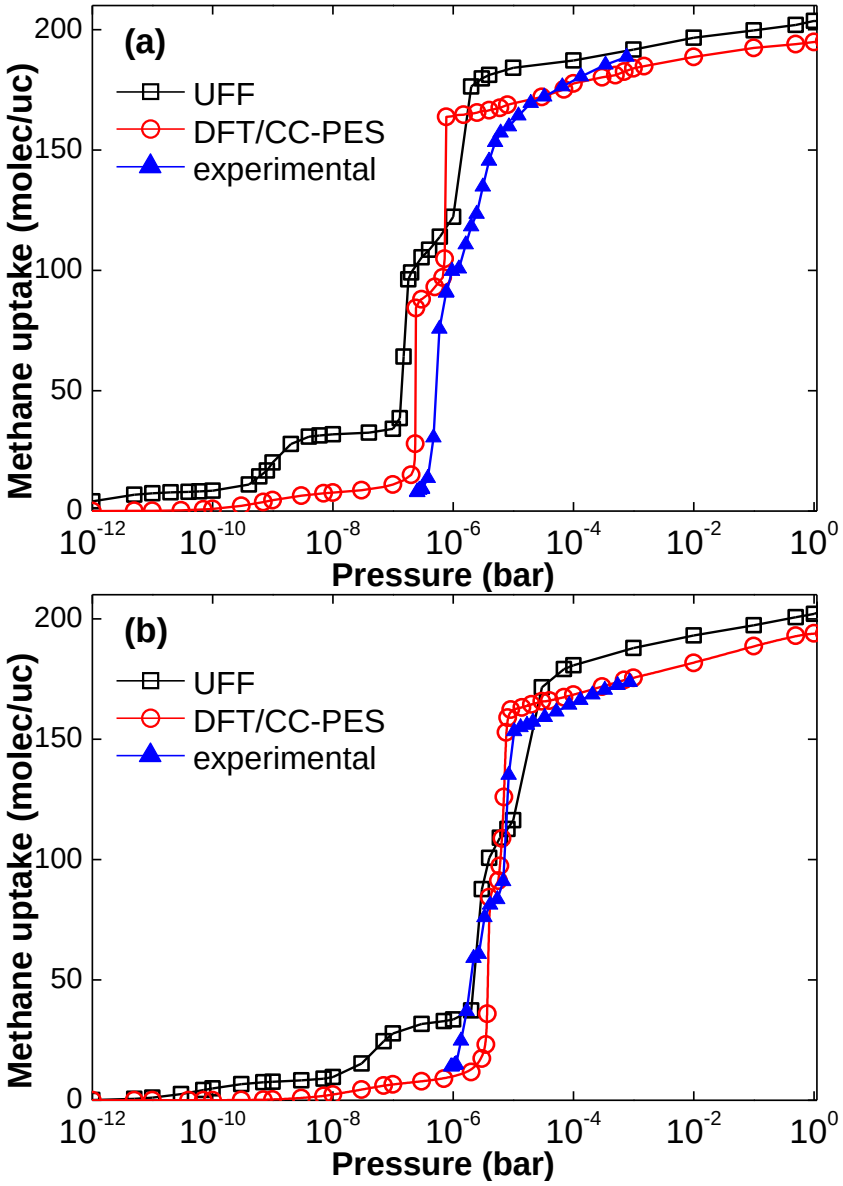

Figure 3.3. CH_4 adsorption isotherms for CuBTC at (a) 77 and (b) 87 K. Experimental data were taken from the work of Getzschmann et al (2010). Note that the isotherms are represented on a logarithmic pressure axis to better show the adsorption behaviour at low pressures and the lines were added to guide the eye. It is further noted that the error estimates, obtained considering a 95% confidence interval, are all within ±0.5% of the corresponding uptake values reported here; they are all smaller than the symbols and thus omitted for clarity.

Methane adsorption isotherms obtained from DFT/CC-PES- and UFF-based GCMC simulations at 77 and 87 K are shown in Figure 3.3. Experimentally, it was determined that one unit cell (uc) of the CuBTC framework contains 88 favourable adsorption sites for CH_4 (Figure 3.1): 40 are located in the small S1 pores – one at the centre (site E) and one at each of the four triangular-shaped windows (site A) of the eight S1 pores – and 48 are located at the cus's (site C). A marked feature of the experimental CH_4 adsorption isotherms shown in Figure 3.3 is the "step" at 85 CH_4/uc, which is clearly observable at both 77 and 87 K. Rietveld refinement of the neutron diffraction data further attributed the uptake of 85 CH_4/uc to the filling of the 88 primary adsorption sites; that is, sites A, C, and E (Getzschmann et al., 2010).

The UFF-simulated isotherms are in fair agreement with experiment (Figure 3.3). On the one hand, the two isotherms obtained at 77 and 87 K display a step at ca. 95 CH_4/uc, which tentatively points to the capturing of the experimental adsorption mechanism (i.e., the step at 85 CH_4/uc). On the other hand, an additional step at very low pressures is observed in the UFF-based isotherms at both temperatures; an uptake of 40 CH_4/uc is predicted at ca. 10^{-8} bar at 77 K, for example. A close inspection on the molecular-level sitings of the adsorbed CH_4 molecules inside the framework reveals that the uptake of 40 CH_4/uc corresponds to the filling of the eight S1 pores (sites A and E). The UFF-based simulations fail to capture any CH_4 adsorption on the cus's, in contradiction with the experimental observations described above. Moreover, the seemingly good reproduction of the 85-CH_4/uc step in the experimental isotherm (at 77 K) by the UFF-based simulations was found to originate from a different adsorption mechanism compared to the experimental one, which is discussed in detail below. Note that the UFF-based GCMC simulations

performed here predict CH_4 uptakes in qualitative agreement with the simulation results reported by Getzschmann et al (2010). The discrepancies were found to stem from different force-field parameters being used for the CuBTC framework: scaled UFF parameters were used by Getzschmann et al. (2010), whereas this work used the (unmodified) LJ parameters directly taken from the UFF to allow for comparison with the other generic force fields.

Despite the good agreement, discrepancies between the DFT/CC-PES-based GCMC simulation results and the experiments are obvious (Figure 3.3). Many factors could have contributed to the differences. In (perhaps) the most general terms, one could argue that simulations use the perfect, fully activated crystal structures, thus yielding predictions for the idealized situations. In contrast, the quality of the experimental sample is dependent on (for example) the synthesis and activation procedure, most likely having an imperfect structure with possible incomplete removal of solvents, contamination with interpenetrated phases, or partial framework collapse (Düren et al., 2009). Similarly, another frequently given explanation is that the rigid-framework assumption, inherent to GCMC simulations, contributes to the differences. However, this is not the case for the system studied here (i.e., ignoring framework flexibility is not responsible for the differences), as it has been well established that the CuBTC MOF does not undergo any significant structural changes upon adsorption of small gases such as CH_4 and CO_2. Often, but undesirably, simulation setups can also have an influence on the quality of the simulation results, giving rise to, for example, finite size effect, quasi-nonergodicity, etc. With this in mind, the simulation setup used here was carefully checked to remove such adverse effects. Explicitly, to check for any possible finite size effects, the simulation box was doubled in each of the x, y, and z directions. The GCMC simulation results

thus obtained (with all the other settings unchanged) were found to be almost identical to the ones obtained using the original simulation box, thus confirming that the system did not suffer from finite size effects. To ensure an ergodic behaviour of the simulations and hence the quality of the results, five independent GCMC simulations (with different random numbers) were performed in parallel for each adsorption isotherm. It was then confirmed that in all cases the five resulting isotherms were quantitatively identical. Moreover, with the DFT/CC PES, desorption simulations were carried out following the corresponding adsorption simulations. Again, the adsorption and desorption isotherms were found to be the same; the desorption isotherms were not included in Figure 3.3, as they would overlay the adsorption ones precisely. More specific to the adsorption of methane at 77 and 87 K studied here, one should be aware of the potential freezing transitions (i.e., crystallization of methane), from which complications such as quasi-nonergodicity may rise. To this end, the above described desorption simulations can be useful, providing evidence to support that the simulated systems were ergodic. A further discussion on adsorbate freezing in a confined environment is given below in Chapter 6 (Section 6.4.2), together with a listing of commonly used criteria for assessing freezing.

In passing, it is worth noting that the failure to reproduce correctly the CH_4 adsorption isotherm in CuBTC at 77 K is not unique to UFF but applies to two other commonly adopted generic force fields, namely DREIDING and OPLS-AA. It is shown in Figure 3.4 that the DREIDING force field simulates an adsorption isotherm that is very similar to the one based on UFF. The OPLS-AA force field, however, yields remarkably more pronounced over-predictions of the methane uptakes in CuBTC as compared to the other two generic force fields. On the molecular level, none of the three generic force

fields predicts any CH_4 adsorption on the cus's. This is not surprising, considering the copper atoms of CuBTC were described by UFF in all of the three GCMC simulations. Methane was also modelled explicitly as a five-atom molecule according to the TraPPE-EH force field (Chen and Siepmann, 1999) in one GCMC simulation, where UFF was used for the framework (Figure 3.4). It is clear that using the more sophisticated model for methane cannot help to capture the adsorption on the cus's – a sensible solution, almost certainly, lies in correctly describing the CH_4–Cu interactions.

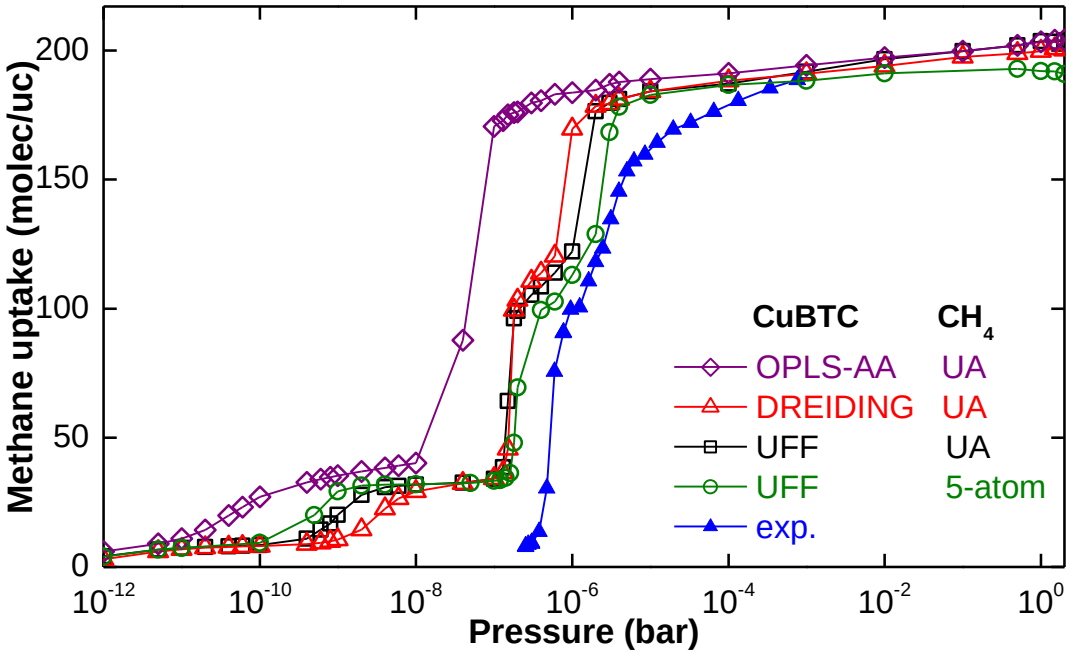

Figure 3.4. Comparison of CH_4 adsorption isotherms at 77 K simulated using different force fields that are given in the legends. Experimental results were taken from the work of Getzschmann et al (2010). The lines were added to guide the eye.

In contrast, the DFT/CC-PES-based GCMC simulations yield remarkably good agreement with experiment at both 77 and 87 K (Figure 3.3). The shape of the experimental isotherms is reproduced very well – both the step at 85 CH_4/uc and the maximum uptake are captured to a high accuracy. Moreover, in the very low pressure range (< 10^{-7} bar), the DFT/CC-PES-based GCMC

simulations predict that the CuBTC framework does not adsorb significant amounts of CH_4 molecules (as opposed to the predicted uptake of 40 CH_4/uc from UFF), in line with the experimental results. These observations provide the first evidence that the experimentally identified adsorption mechanism is captured correctly by the GCMC simulations based on the DFT/CC derived CH_4–CuBTC interactions. In addition, Figure 3.5 shows that the isosteric heats of adsorption calculated from the DFT/CC-PES-based simulations at 77 K are in very good agreement with the experimental adsorption enthalpies from microcalorimetric measurements made on the system (Llewellyn, unpublished data). Larger values for isosteric heat of adsorption were obtained from the UFF-based simulations (Figure 3.5), corroborating the larger methane uptakes predicted, especially at low pressures (Figure 3.3).

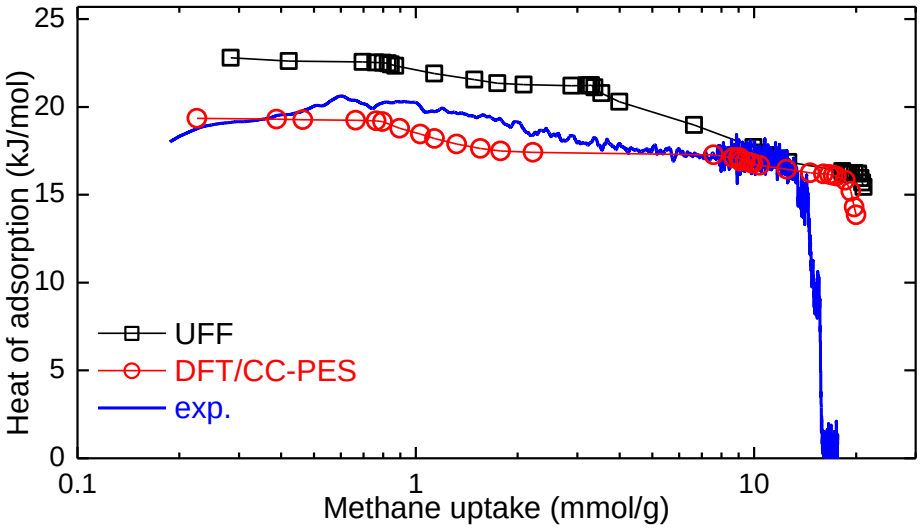

Figure 3.5. Heat of adsorption for CH_4 in CuBTC at 77 K as a function of loading. The simulation results were calculated using Equation 3.3, while the experimental ones were measured by microcalorimetry experiments. The lines were added to guide the eye.

DFT/CC-PES GCMC simulations were further performed for CH_4 adsorption in CuBTC at temperatures up to 373 K with pressures up to 200 bar. Again, good agreement between simulated and experimental isotherms was obtained and can be clearly seen in Figure 3.6, confirming the accuracy of the

DFT/CC-PES GCMC simulations in predicting CH_4 adsorption in the CuBTC MOF over a wide range of temperatures and pressures.

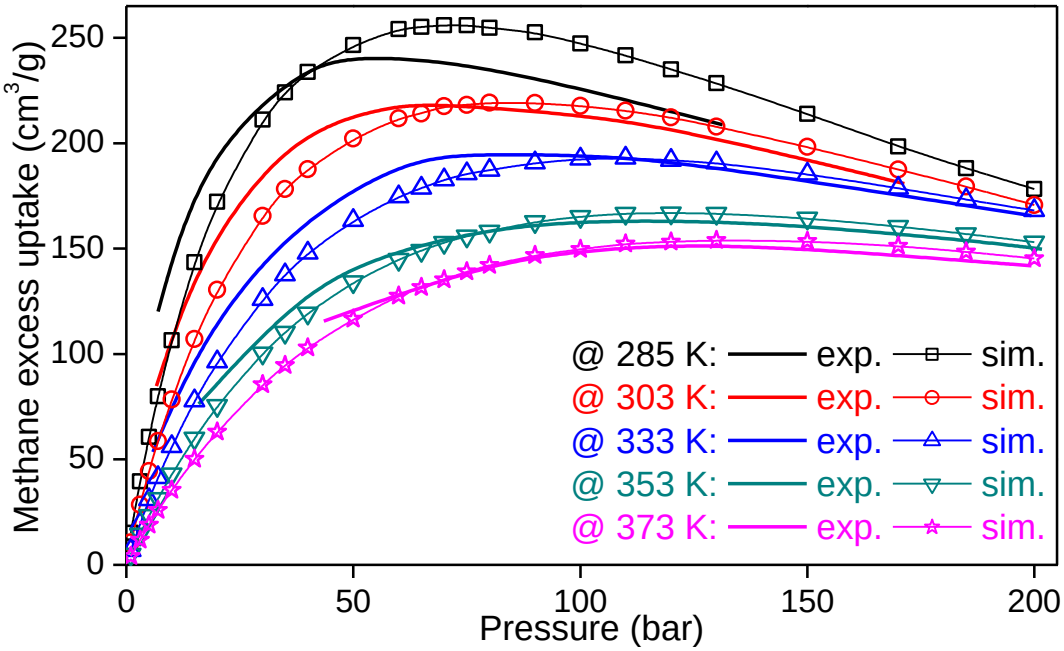

Figure 3.6. Comparison of high-pressure CH_4 adsorption isotherms measured in the temperature range 285–373 K between the DFT/CC-PES-based simulation results and the experimental data of Getzschmann et al (2010). The lines were added to guide the eye.

Molecular-level adsorption mechanisms – energetics and sitings. To illustrate the difference between the CH_4–CuBTC potential energy derived from UFF and DFT/CC, contour plots for the (200) planes (Miller indices) are given in Figure 3.7. Note that the lower (i.e., more negative) the potential energy, the stronger the interaction.

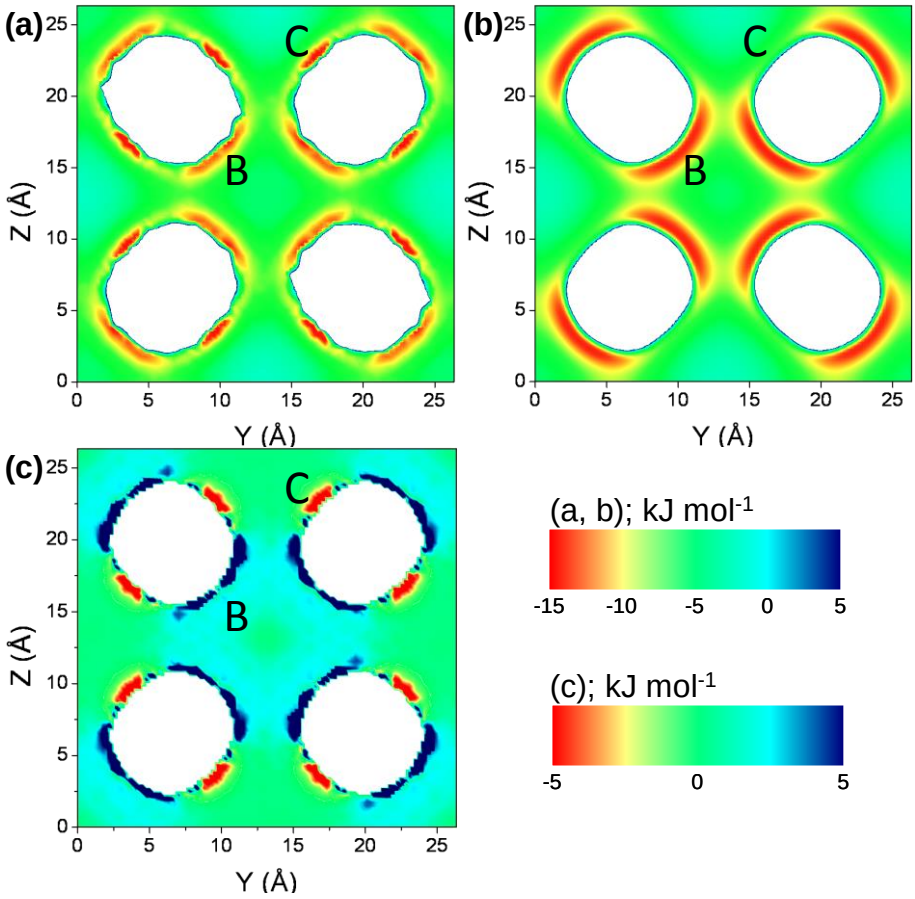

Figure 3.7. Contour plots of the potential energy between a CH_4 molecule and the CuBTC framework on the (200) plane for (a) DFT/CC-PES, (b) UFF, and (c) the difference, $\Delta E = E_{\text{DFT/CC-PES}} - E_{\text{UFF}}$. Adsorption sites B and C (cus's) are labelled. The white space corresponds to the CuBTC framework.

The differences are clearly observable. Site C, the adsorption site determined experimentally for the cus's, is characterized by a very strong, attractive CH_4–CuBTC interaction according to the DFT/CC derived PES, whereas such interaction is completely absent from the PES derived from UFF. The latter is a direct result of the fact that at site C ($r_{\text{Cu-site C}} = 3.08$ Å) the CH_4 molecule is "experiencing" a considerable repulsive interaction with the Cu atom as the combination of UFF (for CuBTC) and UA (for CH_4) gives a value of 3.422 Å for $\sigma_{CH_4\text{–Cu}}$. Another remarkable difference – which also can be expected to have a significant impact on the adsorption mechanism – is that site B, the main adsorption site inside the L2 and L3 pores, is characterized by a

markedly weaker CH_4–CuBTC interaction in the DFT/CC PES as compared to the one based on UFF. This under-prediction of the CH_4–CuBTC interaction energy on the cus's by UFF and its over-prediction at site B are illustrated in Figure 3.7 (c), which contains the energy differences between the CH_4–CuBTC PES's based on DFT/CC and UFF.

As a consequence of the different interactions resulting from the DFT/CC method and the generic UFF, distinct preferential sitings of CH_4 inside the CuBTC framework have been observed over the courses of the GCMC simulations. To illustrate the different adsorption mechanisms predicted and, more importantly, to confirm that the DFT/CC-PES-based GCMC simulations result in a correct description of the adsorption mechanism, the loading of CH_4 molecules at each of the adsorption sites was determined for three uptakes – namely, 8, 88, and 176 CH_4/uc – corresponding to the uptakes at the steps in the experimental adsorption isotherm at 77 K (Figure 3.3 (a)). For the last uptake (176 CH_4/uc) but not the other two, experimental data concerning the localization of CD_4 molecules inside the CuBTC framework are available from the work of Getzschmann et al (2010). Table 3.1 reports the simulated loadings at the experimental adsorption sites for the three uptakes and a comparison to experiment for the 176-CH_4/uc one, together with the CH_4–CuBTC potential energies at the sites given by the DFT/CC and UFF PES's.

In order to determine the loadings of the different adsorption sites, a sphere of radius R = 0.316 Å (R^2 = 0.1 Å^2 was actually used) was defined around each experimental adsorption site. Any CH_4 molecule falling into this sphere during the simulation was counted towards the loading of the corresponding site. Larger values for R were found to result in the same CH_4 molecule being

assigned to two different experimental adsorption sites, especially for the secondary sites G and F, which are close to sites A and D, respectively. Note that for each of the three uptakes the adsorption-site loadings were obtained by analysing the centre-of-mass probability density of the adsorbed CH_4 molecules over the duration of the GCMC simulation. It is, perhaps, worth emphasising that Table 3.1 reports the simulated guest-molecule sitings for the particular adsorption sites as identified by experiment. These numbers were generated by assigning every adsorbed CH_4 molecule, in every accepted configuration of one GCMC simulation (production run only), to one experimental adsorption site. Combining the ratio thus obtained (for the sites) with the CH_4 uptake from the GCMC simulation resulted in the reported uptakes for the individual sites. The errors in these values (for the sites) are therefore proportional to (and are a fraction of) the error in the total CH_4 uptake from the corresponding GCMC simulation. For the loadings of 8, 88, and 176 CH_4/uc reported in Table 3.1, the error estimates are ±0.05, ±0.26, and ±0.35 CH_4/uc, respectively.

Table 3.1. Potential energy and loading (in molecules per unit cell) of CH_4 molecules identified for each adsorption site at different uptakes.

	E (kJ mol^{-1})[a]		8 CH_4/uc		88 CH_4/uc		176 CH_4/uc		
site	DFT/CC	UFF[b]	DFT/CC	UFF[b]	DFT/CC	UFF[b]	DFT/CC	UFF[b]	exp.[c]
A	-14.20	-17.49	1.12	1.21	31.37	31.12	22.38	20.57	24.76
B	-10.45	-12.66	0.00	0.00	1.88	38.25	47.62	48.00	48.00
C	-13.23	N/A	0.00	0.00	46.75	0.00	46.25	0.00	44.63
D	-8.05	-10.88	0.00	0.00	0.00	10.88	29.12	32.13	27.80
E	-18.70	-22.70	6.88	6.79	8.00	2.63	8.00	8.00	6.39
F	-7.90	-10.04	0.00	0.00	0.00	2.12	4.87	19.88	4.00
G	-12.59	-16.33	0.00	0.00	0.00	0.00	10.12	12.15	11.76
H	-1.50	-2.02	0.00	0.00	0.00	0.00	3.52	31.27	4.00
I	-3.36	-4.04	0.00	0.00	0.00	3.00	4.12	4.00	d

[a] Potential energy between a CH_4 molecule and the CuBTC framework. [b] Results from the UFF-based simulations done in this work. [c] Experimental results taken from Getzschmann et al. (2010), where 171.21 of 176 CH_4/uc were resolved. Note that this is the only loading for which occupancies were reported by Getzschmann et al. (2010). [d] Not reported in the work of Getzschmann et al (2010).

It is clearly demonstrated in Table 3.1 that the DFT/CC-PES-based GCMC simulation is able to reproduce quantitatively the adsorption-site loadings determined experimentally for the 176-CH_4/uc uptake. The agreement between simulation and experiment is very good for all of the adsorption sites, including the cus's (site C). To be specific, the DFT/CC-PES-based simulation predicts 46.25 of the 48 cus's (per unit cell) being occupied by methane, which is in very good agreement with the experimental value of 44.63. Moreover, the average simulated distance between a CH_4 molecule and the Cu(II) cus is 3.097 Å, in excellent agreement with the corresponding experimental distance of 3.075 Å (Getzschmann et al., 2010). Combining these very good predictions of the CH_4 sitings with the very good reproductions of the experimental isotherms (Figure 3.3), the accuracy of the DFT/CC-PES

GCMC simulation in providing a correct description of the adsorption mechanism of CH_4 in CuBTC at 77 K can be affirmed.

It is worth pointing out that the characteristic steps in the simulated adsorption isotherms (Figure 3.3) are a direct consequence of the differences in the CH_4–CuBTC potential energies for the main adsorption sites. To elaborate on this, the adsorption mechanism predicted from the DFT/CC PES is further contrasted with the one predicted using UFF for two lower loadings (Table 3.1). At the very low loading of 8 CH_4/uc, the two methods predict the same adsorption mechanism; that is, on average, ca. 7 of the 8 S1 centres are each occupied by a CH_4 molecule. This simulated localization of CH_4 molecules is in accordance with the calculated CH_4–CuBTC potential energies for the different sites (Table 3.1). That is, the centre of the S1 pore (site E) is the most attractive site for methane because of the enhanced dispersion interaction in the small cavities. The other site that becomes occupied at this loading – but to a much lesser extent – is site A, the centre of the window to the S1 pore, of which 32 are present in one unit cell of the CuBTC framework. Again, this site takes up CH_4 molecules at very low pressures because of the strong CH_4–CuBTC interaction present, the second largest (in absolute value) among all of the adsorption sites (Table 3.1).

At higher loadings, the differences in the adsorption mechanisms predicted by the two methods become apparent. Take the sitings of methane in the framework at an uptake of 88 CH_4/uc as an example (Table 3.1). Both methods agree with each other in terms of the almost identical values predicted for the loading at site A, the centre of the window to the small S1 pore. The DFT/CC-PES simulations, however, show that the next adsorption sites to be occupied are the cus's (site C) and not sites B and D, the sites in the

L2 and L3 pores, as predicted by the UFF-based simulations. Furthermore, the UFF-based predictions completely fail to capture the adsorption of methane on the cus's for all of the three uptakes investigated, whereas the DFT/CC-PES-based simulations indicate that the cus's start being populated at uptakes as low as 25 CH_4/uc. Interestingly, in the case of methane adsorption in CuBTC, the cus's are not the first sites to be occupied. After the S1 pores and the cus's have been saturated, the larger L2 and L3 pores start being filled by methane.

It is worth noting that Getzschmann et al. (2010) reported that experimentally refining the CuBTC framework loaded with small amounts of CD_4 molecules (i.e., 8 and 104 CD_4/uc) was difficult due to the dilution of scattering density at certain sites and also likely as a result of an incomplete equilibration of the filling operation. Consequently, the simulation predictions discussed above for the uptakes of 8 and 88 CH_4/uc cannot be validated by experiment. Nevertheless, the sequential filling of the S1 pores, cus's, and large pores – which is identified by the DFT/CC-PES GCMC simulations – is supported by the reports of Getzschmann et al. (2010) and Wu et al (2010) who identified the same pore-filling sequence through a combined experimental and theoretical investigation.

Despite not capturing the CH_4 adsorption on the cus's, the UFF-based simulations provide surprisingly good predictions for higher CH_4 loadings. This can be rationalized by the fact that the CH_4–CuBTC potential energies determined by UFF are consistently lower (i.e., more attractive) than the corresponding DFT/CC values in the L2 and L3 pores (except for the cus's in the L3 pore), especially at site B, as illustrated in Figure 3.7 (c). This leads to the L2 and L3 pores (sites B, D, and F) being heavily populated starting from

relatively low pressures, which is the reason for the step in the UFF-simulated isotherm at a loading of 104 CH_4/uc (Figure 3.3). Towards saturation, site H, the centre of the L3 pore, starts playing a pivotal role in accommodating CH_4 molecules in the UFF-based simulations, where CH_4 molecules were observed to reorder themselves to be extremely close-packed (Getzschmann et al., 2010). Only 4 of the 171.21 CH_4 molecules resolved were assigned to site H experimentally, whereas as many as 31.27 of the 176 CH_4 molecules were predicted at site H by the UFF-based simulation. These artefacts largely compensate for the missing strong adsorption sites at the cus's. This could very well explain the generally good agreement between simulation based on generic force fields and experimental results at higher temperatures, when the isotherms are much less sensitive to the precise description of the adsorption mechanism. In contrast, the correct prediction of CH_4 adsorption at 77 K, especially at low loadings, requires an accurate description of the CH_4 interactions with the various adsorption sites including the cus's. Put together, adsorption isotherms on their own are, in general, not adequate for validating a modelling approach. Instead what is required to assess whether molecular simulations capture the adsorption mechanism correctly is high-quality adsorption data, ideally measured at low temperatures, and *in situ* data that reveal the localization of adsorbates inside the framework.

Adsorption isotherms obtained from DFT and DFT-D(2, 3) PES's. It needs to be emphasized that the choice of *ab initio* method has a critical influence on the accuracy of predictions of CH_4 adsorption in CuBTC at 77 K. None of the PES's derived using pure DFT, DFT-D2 (Grimme, 2006), or DFT-D3 (Grimme et al., 2010) method (DFT = PBE) results in a correct reproduction of the experimental adsorption isotherm, as illustrated in Figure 3.8.

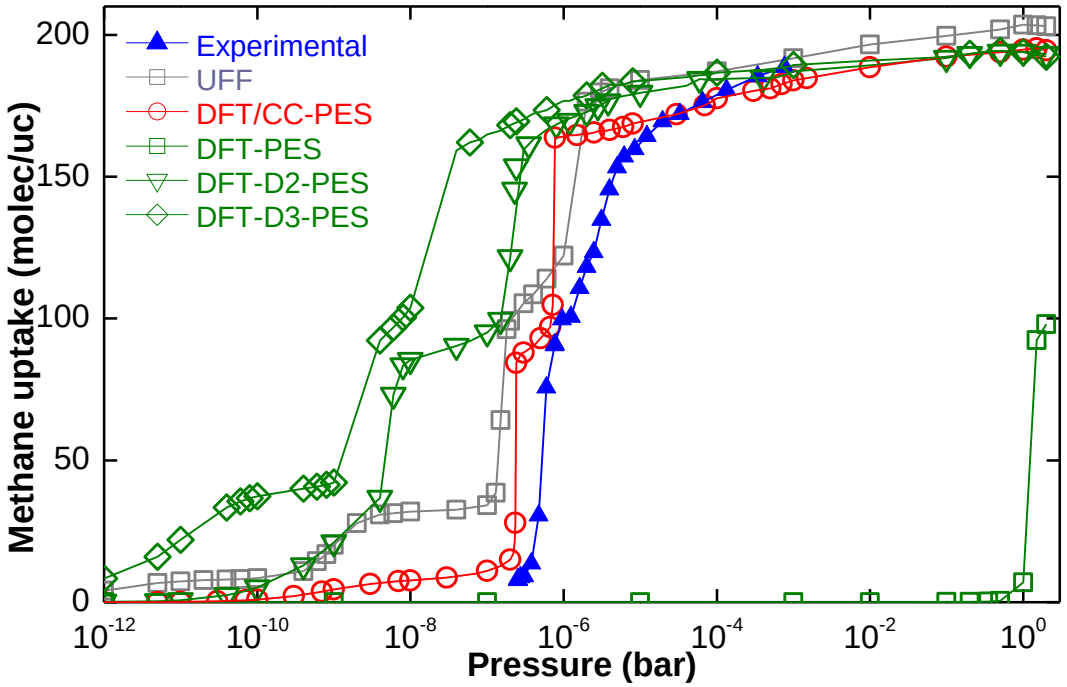

Figure 3.8. Comparison of CH_4 adsorption isotherms for CuBTC at 77 K calculated by GCMC simulations based on potential energy surfaces derived from different *ab initio* methods with the experimental data of Getzschmann et al. (2010). The UFF-simulated isotherm was included for comparison and the lines were added to guide the eye.

The adsorption isotherm obtained from the (pure) DFT derived CH_4–CuBTC interaction potential is completely wrong (Figure 3.8). This is conceivable rather than surprising, as the most important contribution to the CH_4–CuBTC potential energy is the dispersive interaction, which is known to be accounted for poorly by common DFT functionals (including PBE) (Kristyán and Pulay, 1994; Cohen et al., 2011; Klimes and Michaelides, 2012). The two PES's obtained using semiempirically dispersion-corrected DFT-D methods yield significantly better agreement with experiment compared to the one based on the pure DFT. Nevertheless, the adsorption isotherms obtained from the GCMC simulations based upon DFT-D-type PES's are far less accurate than the ones simulated using the generic force fields (compare Figures 3.8 and 3.4). At the first sight this may be surprising, as the DFT-D methods of Grimme have generally been found to perform (very) well for

many systems dominated by dispersion interactions. However, in terms of reproducing the experimental CH_4 adsorption isotherm at 77 K they appeared to do worse than the generic UFF, as shown in Figure 3.8. The reason for this is twofold. On the one hand, the seemingly good CH_4 uptake predictions from UFF are, in fact, due to error cancellations. The GCMC simulation based on UFF predicted no adsorption on the cus's at all for the whole pressure range and over-predicted the uptakes at the other adsorption sites, leading, as a whole, to the observed "qualitative" agreement with the experiments. On the other hand, the GCMC simulations based on the DFT-D2 and DFT-D3 methods yielded CH_4 uptakes at the cus's but, unfortunately, overestimated the CH_4–CuBTC interactions for the other sites (especially, sites E and B; Figure 3.1) where dispersion energies are large. On the whole, the DFT-D-based simulations significantly overestimated the uptakes in the low pressure range (up to 10^{-7} bar). The DFT-D methods of Grimme have been known to overestimate binding energies for some other systems; for example, see Vydrov and Van Voorhis (2012).

This comparison provides a strong demonstration for the promise of the DFT/CC method. The thus-established understanding that neither DFT nor DFT-D method is a suitable choice for the CH_4–CuBTC system demonstrates that the lack of accounting for dispersion is only part of the problem. The DFT/CC method "inexplicitly" corrects the errors of a chosen DFT method by referencing to the corresponding results obtained from the much higher level-of-theory CCSD(T)/CBS method. In addition, it has been shown that standard exchange–correlation functionals fail to describe properly electron density distribution between anionic organic linkers and transition-metal cations (Grajciar et al., 2010). It should therefore be stressed again that an accurate description of the guest-molecule interactions with the open-shell

transition-metal cus's requires more involved methods than just standard DFT or DFT-D approaches. These findings, to a certain extent, motivated the choice of a double-hybrid density functional (having a perturbative second-order correlation term in the total energy expression) for parameterization of intermolecular force fields for studying gas adsorption in MOFs with cus's, as discussed in the following Chapters.

3.3 Conclusions

In this Chapter, it has been shown that GCMC simulations based on generic classical force fields – although doing surprisingly well for predictions of adsorption isotherms in many MOFs, especially at higher temperatures – fail to describe correctly the adsorption mechanism in MOFs with cus's at low temperatures, even for nonpolar fluids such as methane. To address this problem, a new modelling procedure has been proposed, in which an *ab initio* CH_4–CuBTC potential energy surface derived using the DFT/CC method (by the group of Professor Petr Nachtigall) was used within standard GCMC simulations to predict the adsorption of CH_4 in CuBTC. A comparison with previously published *in situ* experiments has demonstrated that this new approach not only quantitatively predicts adsorption isotherms for a wide range of temperatures and pressures but also provides the correct description of the adsorption mechanism, including the adsorption on the cus. Importantly, the methane interactions with the cus's are correctly described in the GCMC simulations based on the DFT/CC PES, which cannot be achieved by using any of the classical force fields investigated here. It has also been shown that care must be taken when selecting the *ab initio* method

to be coupled with GCMC simulations to obtain accurate predictions. Although it is well-known that DFT on its own is not capable of accurately describing dispersion-dominant systems, even the commonly adopted semiempirically dispersion-corrected DFT-D methods of Grimme et al. appear to need a careful justification when in use.

The proposed simulation approach is not restricted to the CH_4–CuBTC system studied here and can be applied to other MOFs with (or without) coordinatively unsaturated metal sites, as well as other fluids. In terms of the latter, work has already been started to implement a DFT/CC derived Ar–CuBTC PES into GCMC simulations for studying adsorption of argon in the CuBTC framework. The computational procedure employed in the case of the Ar–CuBTC system almost exactly followed the one described in this Chapter. Preliminary results indicate that the DFT/CC-PES-simulated Ar adsorption mechanism in CuBTC at low temperatures (87–143 K) is, not surprisingly, very different from the predictions based on the generic force fields (namely, UFF and DREIDING). As can be expected, substantial adsorption of Ar on the cus's is predicted by the DFT/CC PES, as opposed to the complete absence of Ar molecules in the vicinities of the cus's in the UFF-based simulations. This work, however, is still in the very early stage, mainly because the available experimental adsorption data were found to be not good enough for benchmarking, especially not adequate for assessing the different adsorption mechanisms predicted by the different simulation methods. The search for a high-quality CuBTC sample to be used for adsorption and *in situ* experiments is in progress.

Chapter 4 *Ab initio* Parameterized Force Fields for Predictions of Gas Adsorption in MOFs with Coordinatively Unsaturated Metal Sites

4.1 Introduction

Molecular simulations, allowing for calculations on large systems consisting of thousands of atoms at an affordable computational cost, usually rely on force fields which are aimed at approximating the total interaction potential of the system with simple analytical functional forms. The review articles by Düren et al. (2009) and Getman et al. (2012), for example, discuss the versatile applications of molecular simulations in the field of MOFs. To date, most molecular simulation studies use the Lennard–Jones (LJ) potential with parameters usually taken from generic force fields such as UFF (Rappe et al., 1992), DREIDING (Mayo et al., 1990), and OPLS-AA (Jorgensen et al., 1996). Although these force fields do surprisingly well for describing adsorption in many MOFs, their applicability has been criticized for describing the guest-molecule interactions with cus's in MOFs – see Yazaydın et al. (2009), Fischer et al. (2010), Chen et al. (2011), Chen et al. (2012), and Fischer et al. (2012) for a few examples.

In Chapter 3, the direct implementation of a potential energy surface (PES) calculated by a hybrid DFT/*ab initio* method in GCMC simulations was demonstrated by the successful predictions of methane adsorption in the MOF CuBTC. Not only were the amounts adsorbed correctly predicted, but the adsorption mechanisms were also accurately captured when compared to available experimental results. More importantly, the guest-molecule

interactions with the cus's were correctly described, which cannot be achieved by any generic classical force fields investigated. While such a direct implementation of an *ab initio* PES in GCMC simulations removes most of the ambiguities introduced by approximating the fluid–framework potential energy with semiempirical model potentials (e.g., Lennard–Jones (LJ) (Jones, 1924), Morse (Morse, 1929), etc.), force fields using simple analytical representations for the potential are more convenient to use and ideally are transferable to other systems, thus removing the necessity of expensive *ab inito* calculations to determine the PES of every new combination of fluid and MOF of interest. Therefore, this Chapter focuses on the development of *ab initio* force fields for improving predictions of gas adsorption in MOFs with cus's.

In order to achieve quantitative predictions of adsorption isotherms in MOFs with cus's when generic force fields fail to do well, some studies in the literature resorted to manually scaling or calibrating force-field parameters from generic force fields or partial charges of the framework to match simulation results with experiments (Castillo et al., 2008; Lucena et al., 2011). This parameterization strategy is purely empirical and results in an effective model that is able to reproduce the experimental results to which it has been fitted. The danger of using such 'unphysical' parameters was carefully investigated in a theoretical study (McDaniel et al., 2011), which pointed out that the ability (of the empirical scaling approach) to correctly capture the underlying physics of the system as well as the transferability of the parameters to other systems is questionable. Therefore, simulation strategies that are heavily reliant on human intuitions are not pursued in this work.

To accurately describe specific fluid–framework interactions, which is not restricted to but is essential for guest-molecule interactions with cus's, considerable effort has been made to develop *ab initio* based force fields (Fu and Sun, 2009; Fischer et al., 2010; McDaniel et al., 2011; Chen et al., 2012; Fischer et al., 2012; Li et al., 2012; Yu et al., 2012). In the development of these force fields, QM calculations yielded accurate reference data for parameterization of the chosen potential functional forms. In most of these studies, finite-size cluster models were adopted to represent the whole frameworks in the QM reference data calculations. This approximation gives rise to lower computational costs and allows for use of higher level of theory methods (e.g., second-order Møller–Plesset perturbation theory (MP2) (Møller and Plesset, 1934; Head-Gordon et al., 1988)), which is crucial when describing intermolecular interactions. Recent reports on the development of *ab initio* force fields for CO_2 adsorption in zeolites and for CH_4 adsorption in CuBTC (detailed in Section 4.4 in this Chapter) demonstrated how such a multi-scale simulation strategy can also be realized using the periodic structure (Chen et al., 2012; Fang et al., 2012). While these *ab initio* force fields do share some common ground, they differ in the potential functional forms adopted for describing non-bonded intermolecular interactions. Because of their simplicity, the LJ and Morse potentials are widely used (Fu and Sun, 2009; Fischer et al., 2010; Yu et al., 2012). On the other hand, more sophisticated, physically motivated but also more complicated potential energy expressions have emerged (Li et al., 2012; McDaniel and Schmidt, 2013). The additive terms involved in these intermolecular potentials were fitted explicitly to the decomposition of the corresponding *ab initio* potential energy whenever and wherever possible. Thus, these force fields can be expected to provide a more in-depth interpretation of the physics involved in

the system. It, however, remains to be seen to what extent the additional information issued from the detailed decomposition of total energy can enhance the prediction from molecular simulation based upon these force fields.

In this Chapter, several well-established semiempirical model potentials are firstly described and compared, highlighting the function-dependent behaviour of the potential energy curve with respect to the intermolecular separation. Thereafter, the adopted force-field parameterization strategy – which is based on a combination of genetic algorithm and multi-objective optimization – is discussed. Finally, the *ab initio* parameterized force fields for CH_4 and CO_2 adsorption in cus-containing MOFs are presented, together with the corresponding computational details about the *ab initio* calculations as well as force-field validation and performance.

4.2 Semiempirical Model Potentials

Model potentials, in this context, are simple analytical representations of potential energy. Their parameters can be determined from experiment or computation, while their mathematical forms are based on the theoretical concepts of intermolecular theory selecting only the most important contributions to different types of intermolecular interactions. For example, the Lennard–Jones potential represents dispersion interaction using only the first term, proportional to $(1/R)^6$ (R: interatomic separation), of the multipole expansion for dispersion energy.

In all *ab initio* force fields proposed here, the interatomic potential energy (E_{int}) is approximated by the sum of electrostatic interaction (E_{es}) and van der Waals interaction (E_{vdW}) that are calculated in a pairwise additive way as

$$E_{\text{int}} = E_{\text{es}} + E_{\text{vdW}} \tag{4.1}$$

The electrostatic interaction is modelled in the simplest way, which is the atom-centred charge–charge Coulomb interaction, defined as

$$E_{\text{es}} = \frac{1}{4\pi\varepsilon_0}\frac{z_i z_j \text{e}^2}{r_{ij}} \tag{4.2}$$

where r_{ij} is the distance between atoms i and j, z_i and z_j are the fractional charges, e is the elementary charge, and ε_0 is the vacuum permittivity. By definition, the van der Waals interaction is the sum of the repulsive and attractive forces between two molecules (or between parts of the same molecule), excluding those forces due to covalent bonds, the hydrogen bonds, or the electrostatic interaction involving ions. Throughout this Thesis, the term "van der Waals" is used, however, when referring to a combination of all the contributions to the weak intermolecular interaction other than the electrostatic contribution as given by the Coulomb potential (Equations 4.1 and 4.2). In other words, the "van der Waals" interaction, in this context, includes both short-range repulsive and long-range dispersive contributions, as well as any non-explicitly defined ones.

The decomposition of the total energy defined in Equation 4.1 means that the quality of the partial atomic charges is of crucial importance to achieve a high quality parameterization of the force-field parameters that describe vdW

interactions. The performances of some of the most widely used partial charge derivation schemes (e.g., CHelpG, MK, RESP, etc.) have been critically reviewed in the literature, for example, by Spackman (1996) and Sigfridsson and Ryde (1998). Taking into account the findings by Sigfridsson and Ryde (1998), point charges reported in this work were derived using the Merz–Kollman (MK) method (Singh and Kollman, 1984; Besler et al., 1990), unless explicitly stated otherwise. In order to eliminate the undesirable rotational dependence observed for the original MK sampling scheme, denser grids were used by setting the internal options in the Gaussian 09 program (Frisch et al., 2009), via IOp(6/41, 6/42, 6/43), carefully ensuring the number of sampling points per atom exceeds the recommended density of 2000 points per atom by Sigfridsson and Ryde (1998).

The choice of the functional form for fitting the vdW contribution to the *ab initio* potential energy was found to be of vital importance and is discussed in detail in the latter Sections for individual cases. In general, the following model potentials were considered during the development of the force fields.

The ***Lennard–Jones potential*** is widely adopted by generic classical force fields, e.g., UFF and DREIDING, and its so-called (12–6) form is written as

$$E_{\mathrm{vdW}}^{\mathrm{LJ}}(r_{ij}) = 4D_{eq}\left[\left(\frac{\sigma}{r_{ij}}\right)^{12} - \left(\frac{\sigma}{r_{ij}}\right)^{6}\right] \tag{4.3}$$

where D_{eq} is the potential-well depth and σ is the position at which the potential is zero. The attractive term, proportional to $(1/r_{ij})^6$, corresponds to the dipole–dipole component of dispersion energy. The repulsion, approximated by the power term with an order of 12, has limited physical

meaning and was historically chosen by the motivation of computational convenience.

The ***Mie potential*** (Mie, 1903; Jones, 1924) is a LJ-type potential with adjustable repulsive (λ_r) and attractive (λ_a) exponents and is given by

$$E_{\mathrm{vdW}}^{\mathrm{Mie}}(r_{ij}) = \Omega D_{eq}\left[\left(\frac{\sigma}{r_{ij}}\right)^{\lambda_r} - \left(\frac{\sigma}{r_{ij}}\right)^{\lambda_a}\right]$$
$$\text{with}\,\Omega = \left[\frac{\lambda_r}{\lambda_r - \lambda_a}\left(\frac{\lambda_r}{\lambda_a}\right)^{\lambda_a/\left(\lambda_r - \lambda_a\right)}\right]. \qquad (4.4)$$

Ω ensures that the minimum of Equation 4.4 has a value of $-D_{eq}$. The Mie potential becomes identical to the LJ potential when $\lambda_r = 12$ and $\lambda_a = 6$ ($\Omega = 4$). λ_r and λ_a control the steepness of the repulsion and the range of the attraction of the interatomic potential, respectively. This functional form exhibits a greater degree of flexibility than the LJ potential, which can give rise to a better fit to reference data. The additional flexibility of the Mie potential, however, comes at the expense of the better theoretical justification of the LJ potential: i.e., a value of λ_a other than 6 can be difficult to be justified from a theoretical standpoint. The reason is that the leading term in the multipole expansion for dispersion energy is proportional to $(1/r_{ij})^6$. This indicates, for example, a fitted λ_a value of 7 (for a Mie potential describing a particular interaction) can only be considered effective in reproducing the reference data rather than be considered physically justified.

The ***Morse potential***, on the other hand, involves no power series but rather consists of two exponential terms:

$$E_{\mathrm{vdW}}^{\mathrm{Morse}}(r_{ij}) = D_{eq}\left\{\exp\left[\alpha\left(1-\frac{r_{ij}}{R_{eq}}\right)\right]-2\exp\left[\frac{\alpha}{2}\left(1-\frac{r_{ij}}{R_{eq}}\right)\right]\right\} \tag{4.5}$$

where R_{eq} is the location of the minimum potential (D_{eq}) and α characterizes the steepness of the exponential repulsion. Compared to the LJ and Mie potentials, the exponential description of short-range repulsion is more realistic from a physical point of view. This understanding has its roots in the exchange perturbation theory of intermolecular forces (Buckingham et al., 1988). That is, very briefly, the short-range valence repulsion term – in an exchange perturbation formulation – can be well represented by exponentials of interatomic separation, because the electronic wavefunctions decay exponentially with distance. Moreover, because of the "softer" repulsion resulting from the exponential function, the Morse potential has been suggested, in the literature, to be more suitable than the LJ potential for developing a force field for studying gas adsorption in porous frameworks (Fischer et al., 2010; Han et al., 2012).

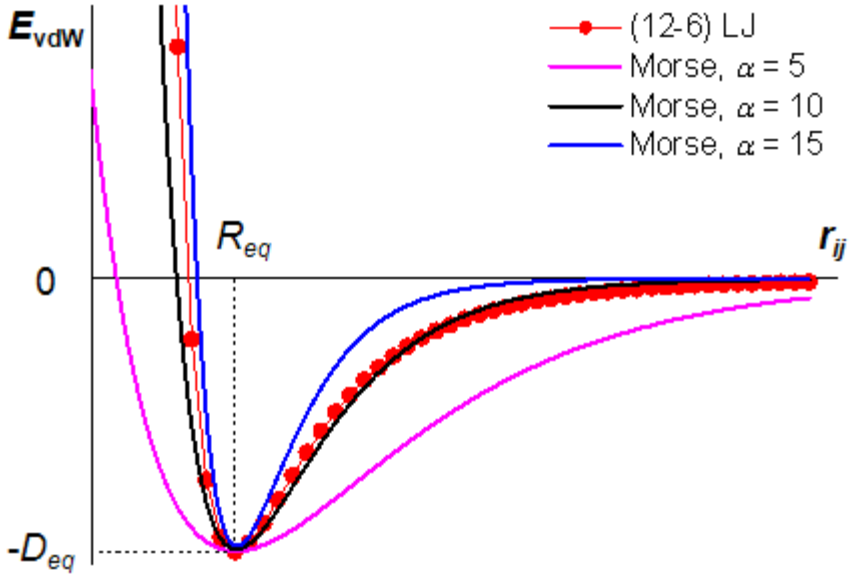

Figure 4.1. Potential energy curves were plotted against the interatomic separation, using the LJ potential and the Morse potential with the different values for parameter α in Equation 4.5. All potential curves were plotted for the same values for R_{eq} and D_{eq} to illustrate the different behaviours of the different potential functions.

The Morse potential does not behave as well as the LJ potential at moderate to large separation distances, because interatomic interactions in this range are better described by a power law of the inverse interatomic distance (i.e., $(1/r_{ij})^6$, etc.) (Buckingham et al., 1988). In addition, regardless of actual values of the parameters the Morse potential has a finite value at $r_{ij} = 0$, which is not correct either (e.g., see the potential curve with $\alpha = 5$ in Figure 4.1). Most relevant to the force-field development in this work is that the "softness" in the repulsive part of the Morse potential is intrinsically associated with a slow decaying behaviour in the attractive region. This feature is illustrated in Figure 4.1 through comparison of the different behaviours of the potential curves determined by the Morse potential functions with the different values for parameter α. The Morse potential was found, in this study, to be unable

to adequately describe the guest-molecule interactions with cus's, which is discussed in detail below.

The ***Buckingham potential*** (Buckingham, 1938) incorporates the repulsive term approximated by an exponential function with the attractive term due to the dipole-dipole ($\sim r_{ij}^{-6}$) dispersion interaction:

$$E_{\mathrm{vdW}}^{\mathrm{Buck}}(r_{ij}) = Ae^{-\alpha r_{ij}} - \frac{C_6}{r_{ij}^6} \tag{4.6}$$

where A and C_6 are constants with the latter commonly called dispersion constant. The Buckingham potential is theoretically better justified than the LJ and Morse potentials, since both the exponential repulsion and the power-term attraction are physically motivated.

The original form of the Buckingham potential (Equation 4.6) cannot be applied to small separation distances, because it has a false maximum at some small distance, $R_{\max}$, and the potential drops to -∞ when r_{ij} approaches zero. The common way to correct this behaviour in molecular simulation is to introduce a hard-sphere potential at small r_{ij}, i.e., $E_{\mathrm{vdW}} = +\infty$ when $r_{ij} \leq R_{\max}$. Alternatively, modifications of the Buckingham potential have been proposed in the literature, aiming at correcting the function behaviour at small r_{ij}; for example, Carra and Konowalow (1964) and Ahlrichs et al. (1977) proposed different modifications. In this work, one of the simpler modifications has been chosen for the force-field development, primarily in order to keep the number of adjustable parameters as small as possible.

The ***Carra–Konowalow potential*** (Carra and Konowalow, 1964), a modified Buckingham potential denoted as Buck-CK hereafter, is given by

$$E_{\mathrm{vdW}}^{\mathrm{Buck-CK}}(r_{ij}) = D_{eq}\left(\frac{\beta+6}{\beta}\right)\left(\frac{R_{eq}}{r_{ij}}\right)^{6}\left\{\left(\frac{6}{\beta+6}\right)\exp\left[\beta\left(1-\frac{r_{ij}}{R_{eq}}\right)\right]-1\right\} \qquad (4.7)$$

where β characterizes the steepness of the exponential repulsion. The Buck-CK potential corrects the wrong behaviour of the (original) Buckingham potential at small r_{ij} by multiplying the exponential repulsive term by $(1/r_{ij})^6$, thus preventing the attraction term from dominating at small r_{ij}. It has been found, in this work, that a uniform, concise potential function, such as the Buck-CK potential, is more convenient in the force-field parameterization process to avoid possible complications arising from defining $R_{\max}$ *a priori*.

Finding an appropriate potential functional form for fitting to the *ab initio* data for the cus's is challenging. The relatively strong binding affinity of the adsorbate–cus complex can be explained by enhanced electrostatic interaction as a result of the local electric field effect of the open metal sites (Wu et al., 2010; Park et al., 2012). There is also clear experimental evidence that the adsorbate–cus distances are considerably smaller than the sum of the corresponding vdW radii (Getzschmann et al., 2010; Queen et al., 2011), indicating that the enhanced interactions at cus's originate from the overlap of electrons. From these two observations follows that the specific interaction with cus's is not only strong but also short-ranged, which suggests a correct approximation (by the chosen potential functional form) for this interaction should comprise a deep potential well at the equilibrium separation as well as a rapid convergence to a dispersion-dominated behaviour. Each of the model potentials discussed above, however, has been shown to work well

only in a certain range of separation distances. Therefore, in order to achieve a more adequate description of the interactions at cus's with the desired flexibility (in a chosen potential function), the *ab initio* force fields developed in this work use a combined potential with each "piece" presented by some model potential that works well in the assigned range of distances.

The MMSV (***Morse–Morse–spline–van der Waals***) and ESMSV (exponential–spline–Morse–spline–van der Waals) potentials are typical examples of such piecewise model potentials that have found wide applications; for example, see Siska et al. (1971), Parson et al. (1972), Pack et al. (1984) and Aziz et al (1991). In this work, the MMSV potential has been chosen for describing the guest-molecule interactions with cus's, which is given by

$$E_{\mathrm{vdW}}^{\mathrm{MMSV}}(r_{ij}) = \begin{cases} D_{eq}\left\{\exp\left[\alpha_1\left(1-\dfrac{r_{ij}}{R_{eq}}\right)\right]-2\exp\left[\dfrac{\alpha_1}{2}\left(1-\dfrac{r_{ij}}{R_{eq}}\right)\right]\right\} \\ \qquad\qquad \text{for } 0 \le r_{ij} \le R_{eq} \\ D_{eq}\left\{\exp\left[\alpha_2\left(1-\dfrac{r_{ij}}{R_{eq}}\right)\right]-2\exp\left[\dfrac{\alpha_2}{2}\left(1-\dfrac{r_{ij}}{R_{eq}}\right)\right]\right\} \\ \qquad\qquad \text{for } R_{eq} \le r_{ij} \le R_1 \\ b_1+\left(r_{ij}-R_1\right)\left\{b_2+\left(r_{ij}-R_2\right)\left[b_3+\left(r_{ij}-R_1\right)b_4\right]\right\} \\ \qquad\qquad \text{for } R_1 \le r_{ij} \le R_2 \\ -C_6 r_{ij}^{-6} \\ \qquad\qquad \text{for } R_2 \le r_{ij} < \infty \end{cases} \tag{4.8}$$

where α_1 and α_2 are the stiffness parameters. The joining points R_1 and R_2, and the spline-function parameters b_1 to b_4 can be obtained algebraically – as opposed to being adjusted independently in the fitting procedure – according to the following rules. R_1 is the inflection point (maximum force) of

the Morse function (with α_2), and R_2 can be fixed at some certain value such as $1.4 \cdot R_{eq}$ to $1.6 \cdot R_{eq}$, following common practices (Siska et al., 1971; Keil and Parker, 1985). Relaxing this constraint on R_2 adds one more variable (for each MMSV potential) to the parameterization and, more importantly, was not found to yield any significant improvement in the fitting. The spline-function parameters b_1 to b_4 can be fixed by smoothness conditions at the joining points, i.e., Equation 4.8 and its first derivatives are continuous at every point. The exact expressions to determine the values of R_1 and R_2 and b_1 to b_4 are given in Table 4.1. The seemingly complicated MMSV potential function thus has only five parameters to be determined in the parameterization, namely D_{eq}, R_{eq}, α_1, α_2, and C_6.

Table 4.1. Formulas for determining the joining points and spline-function parameters of the MMSV model potential.

$$R_1 = R_{eq}\left(1+\frac{2}{\alpha_2}\ln 2\right)$$

$$R_2 = (1.4\ \text{to}\ 1.6)R_{eq}$$

$$b_1 = E_{\text{vdW}}^{\text{MMSV}}(R_1)$$

$$b_2 = \left[E_{\text{vdW}}^{\text{MMSV}}(R_2) - b_1\right] \Big/ \left(R_2 - R_1\right)$$

$$b_3 = -\left[E_{\text{vdW}}^{\text{MMSV}'}(R_1) - b_2\right] \Big/ \left(R_2 - R_1\right)$$

$$b_4 = \left\{\left[E_{\text{vdW}}^{\text{MMSV}'}(R_2) - b_2\right] \Big/ \left(R_2 - R_1\right) - b_3\right\} \Big/ \left(R_2 - R_1\right)$$

Notably, it is known from experiment that the gas adsorption phenomena involved in the systems studied in this Thesis are all fully reversible (Dietzel et al., 2009; Getzschmann et al., 2010; Remy et al., 2013), despite that the

interaction energies at the cus's are high (up to ca. 50 kJ mol^{-1}) and that the equilibrium distances between the two interacting atoms are considerably smaller than the sum of the corresponding vdW radii. From both experiments and computations, it is unambiguous that the adsorbate molecules (CH_4 or CO_2) retain their identities in the adsorbed phase (as they are in the gas phase), and no formation of any covalent bonds is observed (Britt et al., 2009; Wu et al., 2010; Park et al., 2012). From this (i.e., no chemical reactions occur upon gas uptake, hence no *intra*-molecular interactions need modelling) it follows that computing the adsorbate–cus interactions using a purely non-bonded *inter*-molecular force field can be considered a valid approximation.

The two-contribution decomposition of interaction energy (Equation 4.1) needs further clarifying with regard to its validity for representing the guest-molecule interactions with cus's. For interactions between a pair of non-cus atoms the usual meanings of E_{es} and E_{vdW} can be substantiated. While for guest-molecule interactions with cus's as modelled by the MMSV potential here, this simplistic energy decomposition can be justified on the following ground. At small separation distances – i.e., from the "inner-wall" of repulsion to around the equilibrium distance – the Morse functions can absorb (1) any inexplicitly defined contributions to the total energy and (2) any (possible) inadequate representations of the Coulomb potential based on partial atomic charges for the "true" electrostatic potential, especially considering the electron overlap of the adsorbate–cus complex. Put differently, the MMSV potential, together with the Coulomb potential, can be conceived as an effective approach to encompassing all of the contributions to the total energy, instead of adding extra terms (such as induction) to the total energy expression. At larger distances, the combination of electrostatic

and dispersive interactions can be considered as a solid approximation. This justification in turn provides a supporting argument for a piecewise potential to be adopted for describing the interactions with cus's.

4.3 Force-Field Parameterization: a Genetic Algorithm Approach

To fit the chosen model potentials to the *ab initio* reference data, a genetic algorithm (GA) (Holland, 1975) was used because of the non-linear features of these functional forms. In brief, genetic algorithms are heuristic search techniques inspired from the biological process of evolution by means of natural selection. Using mathematical operations that mimic the three biological functions of selection, crossover, and mutation, GAs operate on a dynamic population of potential solutions and generate progressively improved approximations to a solution. GAs can be efficient for function minimization in a complex search landscape with possibly strongly correlated adjustable parameters, which is usually the case in force-field parameterization. The GA solver implemented in the Global Optimization Toolbox of MATLAB® (R2011a, The MathWorks) has been used throughout this work, whereas details about the GA methodology can be found elsewhere, for example, in the book by Goldberg (1989).

The GA implementation in this work is a multi-objective minimization (Deb, 2001) that attempts to create a set of Pareto optima for the two objective functions given by

$$\text{Objective1} = \left[\sum_{i=1}^{n} \text{w}\left(E_i^{\text{ab initio}} \right) \left(E_i^{\text{FF}} - E_i^{\text{ab initio}} \right)^2 \Big/ n \right]^{1/2}$$

$$\text{Objective2} = \left[\sum_{i=1}^{n} \text{w}\left(E_i^{\text{ab initio}} \right) \left(E_i^{\text{FF}} / E_i^{\text{ab initio}} - 1 \right)^2 \Big/ n \right]^{1/2} \qquad (4.9)$$

$$\text{with w}(E) = \frac{1}{\exp[(E-\mu)/k_{\text{B}}T]+1}$$

where $E^{\text{ab initio}}$ and E^{FF} are the interaction energies calculated at the *ab initio* level of theory and determined by the force field, respectively. The weighting function, w(E), restricts the relative importance of high energy (repulsive) configurations on the objective functions. μ and $k_B T$ were set to 3.0 kcal mol^{-1} and 0.6 kcal mol^{-1}, respectively, following the set-up reported by McDaniel et al (2011).

Objective1 is a weighted least-square regression of the absolute error while Objective2 is a weighted least-square regression of the relative error. Minimizing both the absolute and the relative errors simultaneously ensures that the fitted parameters perform well not only around the equilibrium distances (where the potential energy, E, is close to its minimum) but also at larger interatomic separations (where the potential energy is small but a good fit is equally important). Furthermore, this strategy can effectively eliminate possible chance correlations and systematic errors during the fitting procedure.

Force-field parameterization involves finding the global minimum in a multi-dimensional solution space possessing many local minima. To ensure the global minimum can be "visited" during the process and to diminish chance correlations among the many variables to the largest extent, an exhaustive

search procedure has been adopted. A typical procedure for the force-field parameterizations carried out in this work starts with 30 independent GA runs with randomly generated initial populations. In each of these GA runs, every generation consists of three subpopulations, each of which has a size of 10 individuals per adjustable parameter. The fittest individuals (top 10%) of one subpopulation migrate to another by replacing the least fit individuals in that subpopulation after every 30 generations. Upon reproduction of the next generation, a controlled elitism (top 5%) is used to favour not only the individuals with better fitness but also the individuals that can help to increase the diversity of the population (Deb, 2001). In addition, 70% of the children in the next generation are created by crossover operations, with the remaining generated from mutation. The run is terminated by either exceeding the maximum number (200) of generations allowed or reaching the fitness-function tolerance (10^{-5}). The results independently generated from these 30 GA runs are saved and constitute part of the initial population for the final GA run, in which the remaining individuals are created randomly. The force-field parameters reported below are thereby the fittest individuals from the final GA runs.

4.4 GCMC Simulation Details

Gas sorption in the MOFs with cus's was studied using the GCMC simulation method. The simulations were carried out with a locally modified version of the multipurpose simulation code MUSIC (Gupta et al., 2003).

The atomistic representations of the MOFs studied were constructed from the corresponding experimental crystallographic data with all of the

(framework) atoms kept fixed at their positions during the simulation. The force-field parameters derived in this work are reported in the following Sections wherein the particular fluid–framework system is discussed, whereas the UFF and DREIDING parameters used for the MOF atoms are listed in Table 4.2. Partial atomic charges for the MOFs investigated – namely CPO-27-Mg (Dietzel et al., 2009), CPO-27-Co (Dietzel et al., 2005), CuBTC (Chui et al., 1999), and NOTT-140a (Tan et al., 2011) – were calculated and are presented in the corresponding Sections, together with the model clusters for deriving charges. All of the partial charges were calculated at the B3LYP/Def2-TZVPP (Becke, 1993; Weigend and Ahlrichs, 2005) level of theory, and were derived by fitting to the first-principles electrostatic potential using the MK method, within the Gaussian 09 program (Frisch et al., 2009). The van der Waals exclusion radii – which need to be specified for derivation of charges – of all atoms were chosen to be the corresponding values reported in the original DFT-D2 work (Grimme, 2006).

The partial charges and LJ parameters for CO_2 were taken from the TraPPE force field (Potoff and Siepmann, 2001) that was fitted to reproduce the vapour–liquid coexistence curves. The model used for methane was derived by Goodbody et al. (1991) and uses a united-atom description of methane molecules (denoted as UA); that is, one methane molecule is represented by a single sphere. The parameters for CO_2 and CH_4 are presented in Table 4.2. All of the fluid–fluid interactions and all of the fluid–framework interactions determined by generic force fields were modelled using the standard (12–6) LJ potential. The Lorentz–Berthelot combining rules were used to calculate the LJ cross-parameters. Interactions beyond 12.80 Å and 18.65 Å were neglected for CO_2 and CH_4, respectively. Both cutoff values were chosen following common literature practices for GCMC simulations of CO_2 and

CH_4 adsorption in MOFs; for example, the cutoffs were used by Yazaydın et al. (2009) and Getzschmann et al. (2010) for CO_2 and CH_4, respectively. Each simulation consisted of an equilibration period of 2.0×10^7 iterations followed by a production run of further 2.0×10^7 iterations, carefully ensuring that equilibrium was reached.

Table 4.2. Force-field parameters for the MOF, CO_2, and CH_4 atoms.[a]

	UFF		DREIDING	
MOF atom	σ (Å)	ε/k_B (K)	σ (Å)	ε/k_B (K)
H	2.5711	22.1416	2.8464	7.6489
C	3.4309	52.8380	3.4730	47.8561
N	3.2607	34.7221	3.2626	38.9492
O	3.1181	30.1931	3.0332	48.1581
Mg	2.6914	55.8573	n/a	n/a
Co	2.5587	7.0451	n/a	n/a
Cu	3.1137	2.5161	n/a	n/a
	σ (Å)	ε/k_B (K)	q (e)	
$O(CO_2)$	3.0500	79.0000	-0.3500	
$C(CO_2)$	2.8000	27.0000	0.7000	
CH_4(UA)	3.7300	148.0000	n/a	

[a] σ is the position at which the potential is zero and ε is the potential-well depth.

To compare simulation results and experimental results, the absolute amount adsorbed from a GCMC simulation was converted to the excess amount adsorbed using the method of Myers and Monson (2002). The excess amount of guest fluid adsorbed (n_{excess}) is given by

$$n_{excess} = n_{ads} - \frac{PV_{pore}}{ZRT} \tag{4.10}$$

where n_{ads} is the absolute amount adsorbed, P is the bulk pressure, V_{pore} is the pore volume, Z is the compressibility factor, R is the ideal gas constant, and T is the temperature. The Peng–Robinson equation of state was used to

estimate Z. The accessible pore volume (V_{pore}) was taken to be equal to the experimentally determined values of 0.63, 0.50, 0.72, and 1.07 $cm^3\ g^{-1}$ for CPO-27-Mg, CPO-27-Co, CuBTC, and NOTT-140a, respectively (Dietzel et al., 2009; Yazaydın et al., 2009; Getzschmann et al., 2010; Tan et al., 2011).

The isosteric heat of adsorption (Q_{st}) was calculated for each gas as the difference in the partial molar enthalpy of the sorbate between the bulk phase and the adsorbed phase. This is given by

$$Q_{\mathrm{st}} = \mathrm{R}T - \frac{\langle VN \rangle - \langle V \rangle \langle N \rangle}{\langle N^2 \rangle - \langle N \rangle^2} \tag{4.11}$$

where V is the potential energy of the system and N is the number of adsorbed molecules.

4.5 Force Field for CH_4 – CuBTC

4.5.1 Force-field fitting

The *ab initio* CH_4 – CuBTC potential data used for force-field fitting were taken directly from Chapter 3 where the DFT/CC method was used to obtain the potential energy surface for the system. Both the DFT/CC calculations and the force-field fitting were carried out for the whole CuBTC framework with periodic boundary conditions imposed, i.e., no cluster model was used for this system.

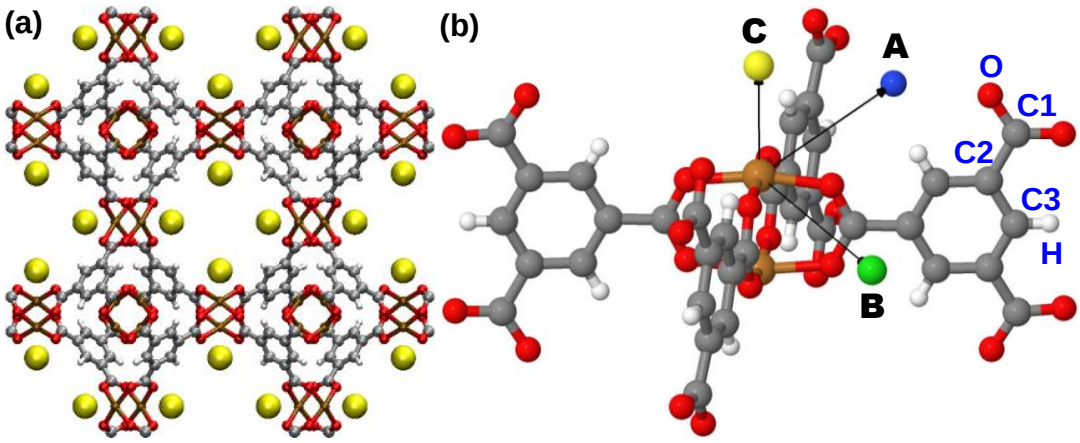

Figure 4.2. (a) CuBTC framework: white, hydrogen; grey, carbon; red, oxygen; and brown, copper. Yellow spheres represent the experimental adsorption sites at the cus's, some of which in adjacent cavities were omitted for clarity. (b) A fragment of the CuBTC framework showing two adjacent copper(II) cus's and four connecting BTC ligands. Atom types defined in the force field are shown except that for copper, which corresponds to the brown spheres. Experimental adsorption sites (Getzschmann et al., 2010) are represented by coloured spheres: site A (blue) is located at the centre of the small-cage window; site B (green) is close to the corner of two neighbouring BTC ligands connected by the copper(II) ions; and site C (yellow) is located close to the open copper(II) site.

The methane molecule was described as a united-atom in the force field; that is, one methane molecule was represented by a single sphere. No electrostatic interaction was taken into account as methane molecule is almost spherical and apolar. The MMSV potential was used for Cu–CH_4 interactions with all of the other framework atoms interacting with a CH_4 molecule described by the Buck-CK potential (Equation 4.7). Six atom types were defined, as shown in Figure 4.2 (b), which results in a total of 20 parameters to be fitted using ca. 1000 *ab initio* data points. A multi-objective GA, in conjunction with the objective functions given in Equation 4.9, was used for the force-field parameterization. The resulting force-field parameters, listed in Table 4.3, yield a very good fit to the whole range of *ab initio* reference data. For the interaction energy ranging from ca. -5 kcal mol^{-1} to +3 kcal mol^{-1}, the root-mean-square deviation (RMSD) between the force-field prediction and the *ab initio* data is only 0.37 kcal mol^{-1}.

Table 4.3. Force-field parameters for CH_4 – CuBTC.

atom type *i*	O	C1	C2	C3	H
			CH_4 [a]		
D_{eq} (kcal mol^{-1})	0.123	0.123	0.115	0.121	0.074
R_{eq} (Å)	3.874	4.062	4.085	4.081	3.372
β	7.300	4.750	4.365	4.197	4.156
			Cu-CH_4 [b]		
D_{eq} (kcal mol^{-1})	R_{eq} (Å)	α_1	α_2	C_6 (kcal mol^{-1} Å^6)	
1.500	3.023	11.098	11.098	246.173	

[a] The Buck-CK potential cross-terms for atom type *i* – CH_4; the methane molecule was modelled as a single sphere using the united-atom approach. [b] The MMSV potential cross-terms for interactions between a copper(II) site and a CH_4 molecule. R_2 was fixed at $1.4 \cdot R_{eq}$.

In spite of the presence of open metal sites in the CuBTC framework, the most attractive adsorption sites for methane at 77 K were determined experimentally (Getzschmann et al., 2010) to be the tight space encapsulated by the four neighbouring BTC (BTC=1,3,5-benzene-tricarboxylate) ligands. It has been shown in Chapter 3 that the correct prediction of CH_4 adsorption at 77 K requires an accurate description of the fluid–framework potential energy associated with the different adsorption sites. Unlike for QM methods that treat interactions in an explicit manner, this is a challenge for force fields using simple functional forms and therefore a very good test of the functional form chosen and the parameters fitted. To illustrate this, the Morse potential (Equation 4.5) and the Mie potential (Equation 4.4) were also used to fit the *ab initio* reference data for CH_4 – CuBTC; that is, the Morse or Mie potential was used for all of the CH_4 – CuBTC interactions including those with the cus's. The reason for using the Mie potential instead of the LJ potential was to make sure the comparisons were done among model potentials that all have certain extent of flexibility in adjusting the repulsive and attractive parts to better fit the *ab initio* data.

To illustrate the difference between the CH_4 – CuBTC potential energy derived from the different methods, contour plots for the (200) planes (Miller indices), which encompass adsorption site C (the cus's) and site B (close to the corner of two neighbouring BTC ligands connected by the copper ions), are given in Figure 4.3. Note that the lower (i.e., more negative) the potential energy, the stronger the interaction. The differences are very apparent. In Chapter 3 it is shown that the strong interaction at cus's (site C) is correctly captured by the DFT/CC method. Moreover, Figure 4.3 (a) demonstrates that the enhanced interaction, arising from the local electric field effects due to the open copper(II) site, is very short-ranged and anisotropic. The origin of this feature can be rationalized by molecular orbital considerations. Briefly, as the electron configuration of copper(II) is d^9, orbital directing effects are present with a preference for a square-planar coordination in the case of four ligating atoms (Bureekaew et al., 2012). In the form of a paddle-wheel unit (as in the CuBTC MOF), each d^9 Cu(II) creates a vacant site, directly above the CuO_4 plane, ready for coordinating an axial ligand. Given the nature of the orbital directing effects, a donor ligand that is too far away from the acceptor Cu(II) or too far off the axial direction of the dimeric copper unit cannot "feel" the attractive interaction from the Cu cus, giving rise to a localized character of the strong interactions with the cus.

In contrast to DFT/CC, the UFF force field, which is based on a (12–6) LJ potential and was chosen here to represent the performance of generic force fields, completely fails to capture the interaction of the cus's. By comparing the differences between Figure 4.3 (b), (d), and (e), the importance of carefully choosing an appropriate functional form to describe CH_4 interactions with cus's is further confirmed. All of the three force fields were fitted independently to the *ab initio* data, and they all reproduce the strong

interaction at the cus's (compared to the UFF one in Figure 4.3 (c), where cus's are completely missed). However, only the force field presented in Table 4.3 is able to preserve the anisotropic features of the potential energy surface around the copper paddle wheels, although this feature is slightly less pronounced using the force-field parameters than in the original DFT/CC data (compare Figure 4.3 (a) and (b)). Notably, the parameters derived using either the Morse potential or the Mie potential result in a much stronger interaction for site B, which is close to the corner of two neighbouring BTC ligands connected by copper(II). This is not surprising given the geometrical arrangements of these sites around the cus (see Figure 4.2 (b): sites A, B and C are ca. 4.8 Å, 5.1 Å, and 3.1 Å from the copper(II) site, respectively). In all of the potential functions examined here, as well as most semiempirical model potentials, the non-bonded monopole–monopole interactions are only distance-dependent. Since no angular dependence of the monomers are considered in these force fields, site B can benefit from two large interactions created by the two deep potential wells surrounding each copper(II) site, though it does not actually face the cus's (Figure 4.2 (b)). In other words, the strong interactions at site B – which were neither observed experimentally nor given by the DFT/CC reference data – are clearly a "by-product" resulting from the large D_{eq} value and the slow-decaying behaviour of the Morse or Mie potential function (see Figure 4.1).

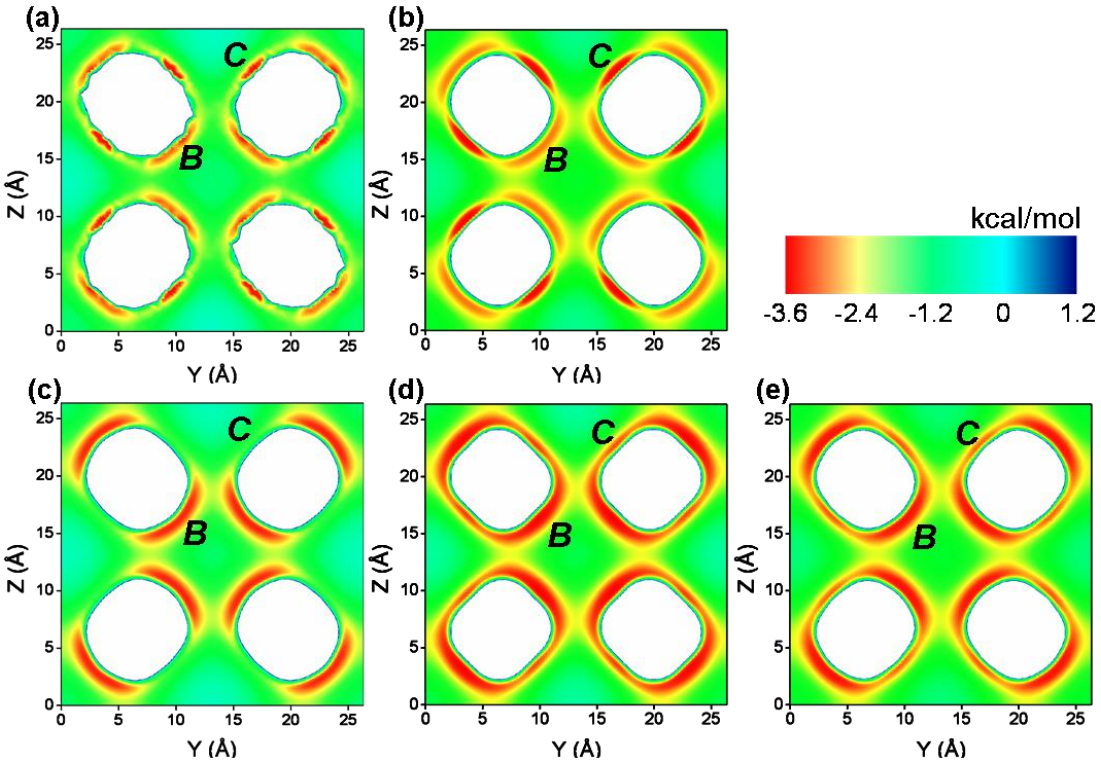

Figure 4.3. Contour plots of the potential energy between a CH_4 molecule and the CuBTC framework on the (200) plane derived from the different methods: (a) DFT/CC, (b) force field presented in Table 4.3, (c) UFF, (d) force field using the Morse potential, and (e) force field using the Mie potential. Adsorption sites B and C (at the cus's) are labelled. The white space corresponds to the CuBTC framework.

4.5.2 GCMC simulations

Methane adsorption isotherms in CuBTC obtained from both DFT/CC-PES and force-field-based simulations at 77 K are shown in Figure 4.4, together with the experimental results (Getzschmann et al., 2010). The most significant feature of the experimental isotherm is the step at 85 molecules per unit cell, which was experimentally determined to be the filling of the 88 favourable adsorption sites of which the cus's constitute 48 (Getzschmann et al., 2010). It is shown in Chapter 3 that the GCMC simulations based on the DFT/CC-PES were able not only to accurately describe the interactions with the cus's, as well as with all other adsorption sites, but also to correctly capture the adsorption mechanisms for a wide range of temperatures and pressures.

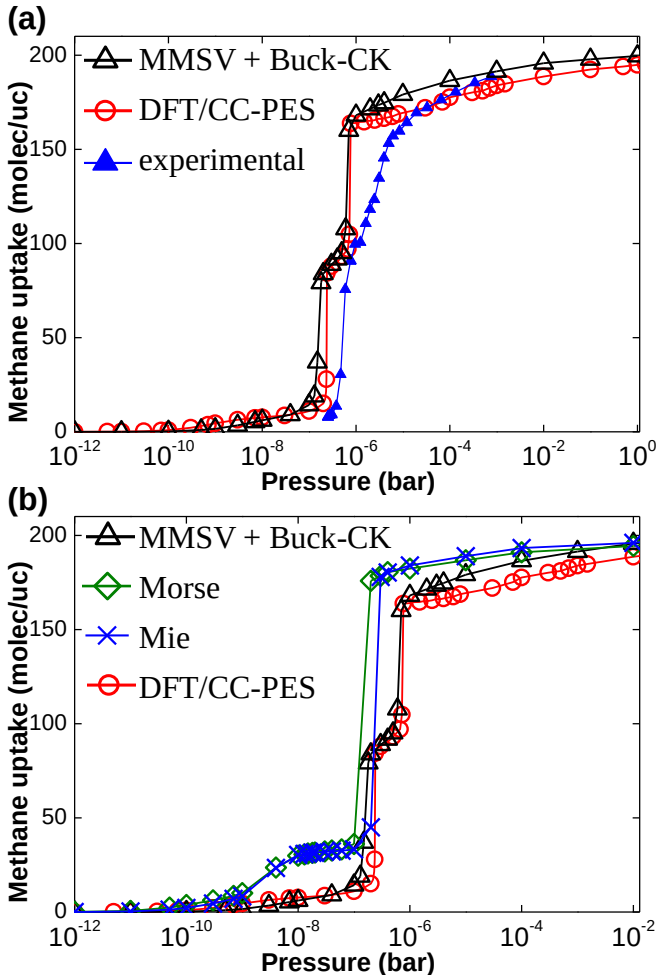

Figure 4.4. Methane adsorption isotherms for CuBTC at 77 K. (a) Comparison of simulated isotherm based on the proposed force field (Table 4.3) with the isotherms from the DFT/CC-PES-based simulation and experiment. (b) Comparison of simulated isotherms using different potential models. Note that the isotherms are represented on a logarithmic pressure axis to better show the adsorption behaviour at low pressure. Experimental data were taken from the work of Getzschmann et al (2010).

In Figure 4.4 (a), an almost quantitative agreement between the isotherms predicted by the DFT/CC-PES and the proposed force field is observed, which confirms the accuracy of the force field (Table 4.3) in reproducing the PES as described by the DFT/CC method. More noteworthy, the significance of the potential functional form chosen is re-emphasised by the comparison of the adsorption isotherms in Figure 4.4 (b). Neither the Morse potential nor the Mie potential results in a correct prediction of the experimental adsorption isotherm. While the strong interaction at the cus's is captured, the

simulations based on these two force fields predict the filling of site B at much lower pressures, leading to a more rapid saturation of methane molecules inside the framework. This should be expected since neither of the two force fields correctly distinguishes the relative strengths of sites B and C (at the cus's), which is evident in Figure 4.3 (d) and (e).

In contrast to standard generic force fields, such as UFF and DREIDING that are generally considered to be transferable, it is unclear *a priori* if force fields developed from *ab initio* calculations on a particular system are transferable to other systems. Methane adsorption isotherms were therefore computed for another Cu-cus-containing MOF, PCN-14 (Ma et al., 2007), at different temperatures using the force-field parameters presented in Table 4.3. Both CuBTC and PCN-14 consist of $Cu_2(OOCR)_4$ paddle wheels, but the two structures differ in the bridging organic ligands – i.e., 1,3,5-benzene-tricarboxylate for CuBTC and 5,5'-(9,10-anthracenediyl)di-isophthalic for PCN-14 – resulting in the different framework topologies. Despite the structural diversity of adsorption sites in PCN-14, the force field parameterized for CuBTC yield CH_4 adsorption isotherms in PCN-14 in very good agreement with the experimental ones (Ma et al., 2007) for all of the temperatures investigated. Figure 4.5 (a) demonstrates that the force field provides a very good description of the interactions between methane and PCN-14, and hence the accurate reproductions of the adsorption isotherms. More encouraging is the significant improvements in prediction of methane adsorption in PCN-14 achieved by using the force field parameterized here when compared to the UFF-based simulation results as shown in Figure 4.5 (b). On the basis of these promising observations, it can be foreseen that, in comparison to generic classical force fields, the proposed force-field parameters may also deliver an improved description of the Cu–CH_4

interaction for other MOFs consisting of $Cu_2(OOCR)_4$ paddle wheels and might do reasonably well for open copper(II) sites in different coordination environments.

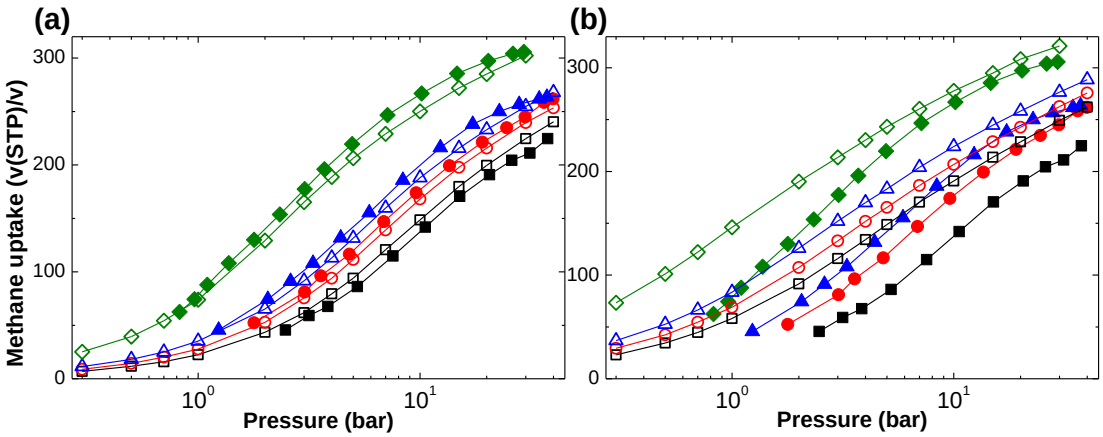

Figure 4.5. Comparison of the absolute methane adsorption isotherms between the force-field-based GCMC simulation results (open symbols) and the experimental results (Ma et al., 2007) (closed symbols) at 240 K (green diamond), 270 K (blue triangle), 280 K (red circle), and 290 K (black square): (a), force field shown in Table 4.3; and (b), UFF.

4.6 Force Field for CO_2 – CPO-27-Mg

CPO-27-Mg [Mg_2(2,5-dioxidoterephthalate)] (Dietzel et al., 2009), also known as Mg\DOBDC or Mg-MOF-74, has been reported to be one of the top-performing MOFs for selective removal of CO_2 under typical flue gas conditions (Britt et al., 2009; Yazaydın et al., 2009). The strong affinities of the cus's toward CO_2 and the high density of cus's present in this MOF (Figure 4.6) are recognized as the main contributors to its outstanding performance. However, large discrepancies between the simulated CO_2 adsorption isotherms based on generic force fields and experimental isotherms were observed for CPO-27-Mg, which were again attributed to the presence of

cus's (Yazaydın et al., 2009), thus making it necessary to develop a new force field for correctly predicting CO_2 adsorption in this MOF.

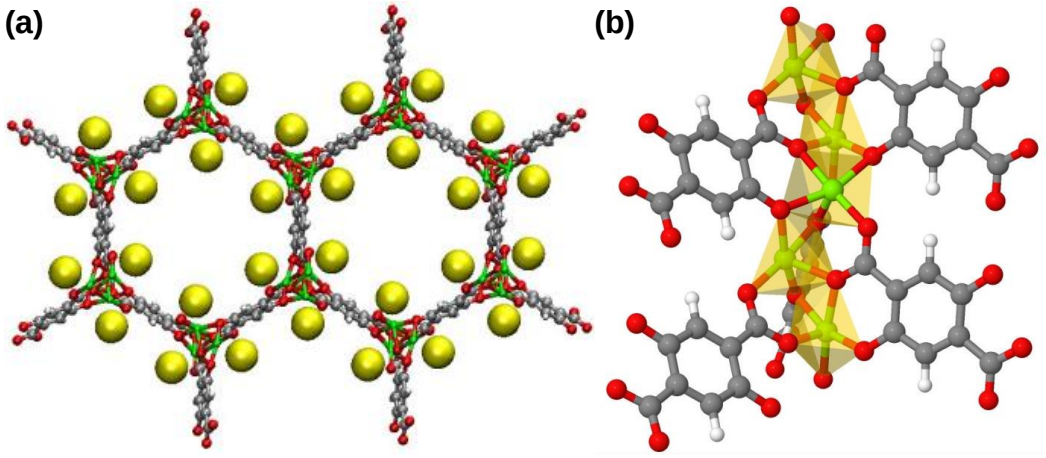

Figure 4.6. (a) The CPO-27-Mg framework, in which the yellow spheres represent the experimental adsorption sites corresponding to the cus's. (b) Repetition of five square-pyramidal cus's along the channel direction. Colour code: white, hydrogen; grey, carbon; red, oxygen; and green, magnesium.

4.6.1 Model cluster construction

To account accurately for the long range correlation effect of dispersion, a high level *ab initio* method (e.g., MP2 or coupled cluster) is preferable to a DFT method with purely empirical dispersion correction (e.g., B97-D of Grimme (2006)) for force-field development. This is currently only achievable for finite-size non-periodic systems. Hence, it is crucial to construct a model cluster that is big enough to represent adequately the most important features of the framework while at the same time ensuring the cluster is small enough to permit manageable computations.

To construct the desired model cluster, the experimental XRD crystal structure of CPO-27-Mg (Dietzel et al., 2009) was first geometry-optimized using periodic DFT with the CASTEP (version 5.501) simulation package

(Clark et al., 2005). All of the periodic DFT calculations, unless stated otherwise, were carried out using the Generalized Gradient Approximation (GGA) based on the Perdew–Burke–Ernzerhof (PBE) (Perdew et al., 1996) exchange–correlation functional. A plane-wave basis set expressed at a kinetic energy cutoff of 600 eV, along with "on-the-fly" ultra-soft pseudopotentials (Vanderbilt, 1990), was used to describe the wavefunction. The geometry-optimization calculations were performed on the hexagonal crystal structure of CPO-27-Mg, amounting to 162 atoms per cell. Because of the large size of this cell, the only k-point sampled in reciprocal space was the Γ-point. During the geometry optimization, both the atomic positions and the lattice parameters were relaxed in accordance with the crystallographic space group constraints. The convergence criterion for self-consistent field (SCF) tolerance was set to 10^{-6} eV per atom. Structures were considered to be optimized when the energy per atom, maximum force, maximum stress, and maximum atomic displacement converged to the values of 10^{-5} eV atom^{-1}, 0.03 eV Å^{-1}, 0.05 GPa, and 0.001 Å, respectively. The minimum energy was obtained for a hexagonal unit cell with lattice parameters $a = b$ = 26.123 Å, and c = 6.954 Å ($\alpha = \beta$ = 90.0 °, and γ = 120.0 °). These values are in very good agreement with the cell constants determined both experimentally ($a = b$ = 25.921 Å, and c = 6.863 Å) (Queen et al., 2011) and in other theoretical studies (Valenzano et al., 2011; Park et al., 2012). The optimized Mg–O bond distances in one 5-coordinated, square-pyramidal cus are 2.075 (-4.5%, compared to experiment), 2.024 (+5.4%), 2.037 (-5.0%), 2.041 (+2.8%), and 2.022 (+0.8%) Å – they are in fair agreement with the corresponding experimental bond distances of 2.174, 1.920, 2.144, 1.986, and 2.006 Å in the bare CPO-27-Mg sample reported by Queen et al (2011).

With the optimized (periodic) structure thus obtained, clusters of different size could be carved out from the periodic framework model. The most relevant feature of CPO-27-Mg is the square-pyramidal coordination environment of the open magnesium(II) sites (Figure 4.6 (b)). Therefore, the primary target in constructing a suitable cluster for *ab initio* calculations was to preserve the electronic structures of the "central", 5-coordinated magnesium(II) site, around which the potential energy surface (PES) was to be sampled. To construct the model cluster, a chain of five consecutive magnesium(II) ions, along with the five connecting dioxidoterephthalate anions, was first carved out from the optimized framework, as shown in Figure 4.7 (a). The structure was further simplified by replacing the five dioxidoterephthalate anions with (1) three 3-oxido-acrylate anions , (2) one acetate anion , and (3) one formate – substitutions are marked by black, pink, and orange circles in Figure 4.7 (a) and (b) for (1), (2), and (3), respectively. Substituting the two magnesium atoms at each end of the chain with two lithium atoms – which is commonly done to cap model clusters carved out from MOFs (Fu and Sun, 2009; Tafipolsky et al., 2010; McDaniel et al., 2011) – and saturating all of the remaining dangling bonds by hydrogen atoms result in the final model cluster (denoted as Model I) as shown in Figure 4.7 (b). Two larger clusters (denoted as Model II and Model III) with two and three 2-oxido-benzoate anions, respectively, were also investigated and are shown in Figure 4.7 (c) and (d).

All of the three clusters were relaxed at the B3LYP/Def2-TZVPP level of theory (Becke, 1993; Weigend and Ahlrichs, 2005), with all of the magnesium and oxygen atoms belonging to the square-pyramidal cus's fixed at the periodic DFT optimized positions. Tight convergence criteria were imposed on these geometry optimizations, where the thresholds for maximum force

and maximum atomic displacement were set to 1.5×10^{-5} a.u. and 6×10^{-5} a.u., respectively. An ultra-fine grid was used for numerical integrations, via Integral(Grid=UltraFineGrid). Cluster calculations were carried out with the Gaussian 09 program (Frisch et al., 2009). Hirshfeld population analyses were performed on the optimized structures of both the periodic framework and the three clusters of different size (i.e., Models I, II, and III). From the comparison shown in Table 4.4, it can be confirmed that even the smallest cluster, Model I, is adequate to reproduce the electrostatic features of the cus. Thus all following *ab initio* calculations discussed are based on Model I.

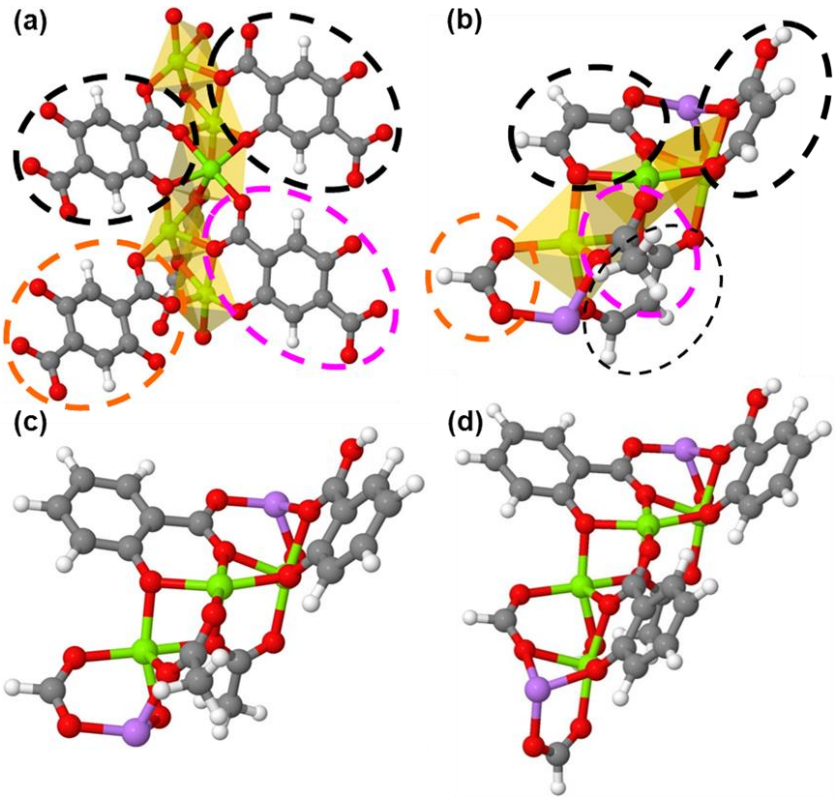

Figure 4.7. Model clusters: white, hydrogen; grey, carbon; red, oxygen; green, magnesium; and purple, lithium. Structures shown in (b), (c), and (d) are denoted as Models I, II, and III, respectively. Anions shown in the coloured, dashed circles in (a) are substituted with the anions marked with circles of the same colour in (b).

Table 4.4. Comparison of the Hirshfeld charges on the 'central', 5-coordinated cus of the periodic framework and the model clusters.

atom	periodic structure	Model III	Model II	Model I
Mg	0.50	0.52	0.52	0.52
O_1(carboxylate)	-0.25	-0.27	-0.26	-0.26
O_2(carboxylate)	-0.26	-0.28	-0.28	-0.27
O_3(carboxylate)	-0.25	-0.26	-0.24	-0.25
O_4(oxido)	-0.28	-0.29	-0.31	-0.31
O_5(oxido)	-0.28	-0.28	-0.29	-0.29

4.6.2 *Ab initio* reference data

To obtain high quality *ab initio* interaction potentials for the Model I···CO_2 complex, a double-hybrid density functional with semiempirical dispersion correction, B2PLYP-D2 (Grimme, 2006; Grimme, 2006), was used in conjunction with a doubly polarized triple-ζ valence basis set, Def2-TZVPP. It is worth noting that the B2PLYP-D2 functional adds non-local electron correlation effects to a standard hybrid functional by second-order perturbation theory; the B2PLYP energy is further augmented by a semiempirical correction to the long-range dispersion interaction (Grimme, 2006; Schwabe and Grimme, 2007). This method has been previously seen to perform very well for dispersion-dominated systems; for example, see the articles of Schwabe and Grimme (2006), Peverati and Baldridge (2008), and Li et al (2012). The frozen monomer approximation was adopted, employing the B3LYP/Def2-TZVPP-optimized geometry of Model I and the experimental geometry of CO_2 (C–O bond length: 1.161 Å; O–C–O angle: 180 °) (Hertzberg, 1945). The wavefunctions were confirmed to have no internal instabilities prior to production of the results. Note that corrections

for basis set superposition error (BSSE) were not applied to the B2PLYP-D2/Def2-TZVPP calculations following arguments presented in the literature (Ducéré and Cavallo, 2007; Peverati and Baldridge, 2008; Li et al., 2012). That is, (1) BSSE effects can be expected to be very small at the B2PLYP-D2/Def2-TZVPP level, and (2) commonly used counter-poise corrections introduce a huge amount of extra computational costs and the method itself is not free of error. The Model I···CO_2 interaction potential (E_{int}) was calculated in the gas phase and is defined as

$$E_{\text{int}} = E(\text{Model I}\cdots\text{CO}_2) - E(\text{Model I}) - E(\text{CO}_2) \tag{4.12}$$

where E(Model I···CO_2), E(Model I), and E(CO_2) are the total energies of the Model I···CO_2 complex, isolated Model I, and isolated CO_2 molecule, respectively.

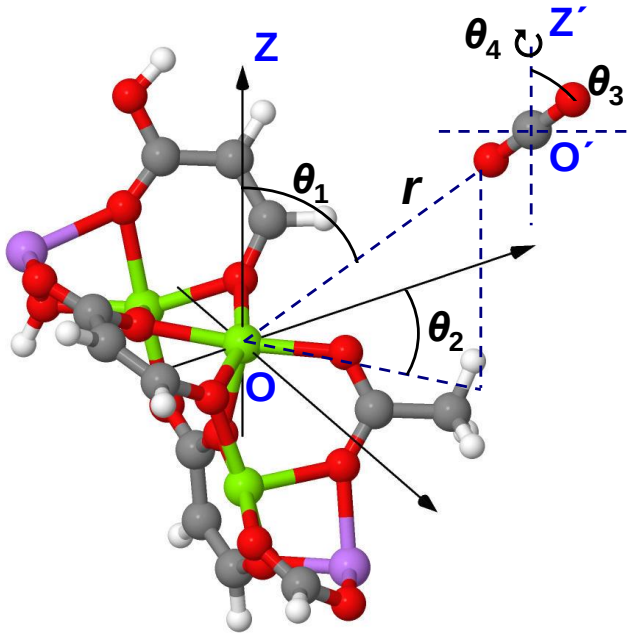

Figure 4.8. Definition of the relative configuration between a CO_2 molecule and the "central" cus of Model I. Colour code: white, hydrogen; grey, carbon; red, oxygen; green, magnesium; and purple, lithium.

A large set of 1158 relative configurations between a CO_2 molecule and Model I were explicitly evaluated by *ab initio* calculations to reproduce the PES in the vicinity of the cus. The sampling scheme depicted in Figure 4.8 – which controls the "approach routes" to the cus – is described by five parameters, *r* and θ_1 to θ_4, and is defined as follows:

1. *r* is the distance between the "central" magnesium(II) ion (origin O) and the centre of the CO_2 molecule (origin O'), and $r \in [2.0\,\text{Å}, 0.2\,\text{Å}, 7.0\,\text{Å}]$, meaning that *r* varies from 2.0 to 7.0 Å with an increment of 0.2 Å;
2. θ_1 is an angle between the OZ axis and OO', and $\theta_1 \in [0°, 25°, 75°]$;
3. θ_2 is a rotational angle of the O'Z' axis around the OZ axis, and $\theta_2 \in [0°, 45°, 360°)$;
4. θ_3 is an angle between the CO_2 and O'Z' axis, and $\theta_3 \in [0°, 30°, 180°)$;
5. θ_4 is a rotational angle of the CO_2 molecule around the O'Z' axis, and $\theta_4 \in [0°, 45°, 360°)$.

At a certain distance *r*, the total configurations that can be generated by varying the four angular parameters (θ_1–θ_4) amount to 1536; out of these 1536 possibilities, 1158 configurations were calculated. Put precisely, the extremely large numbers of possible configurations were reduced by omitting those, in which the CO_2 molecule was in too close contact with the cluster atoms. In particular, any configuration where any atom of the CO_2 molecule was situated less than 4.5 Å from the lithium(I) ions was excluded. The reason for this is twofold. Firstly, the lithium atoms are only used for capping the cluster and it is of little interest to derive new force-field parameters for them since they are not present in the CPO-27-Mg framework. Secondly, given the strong ionic nature of the lithium atoms in Model I, it

was found to be better to exclude these configurations in order not to complicate the fitting of force-field parameters to the *ab initio* data. The sampling scheme described above has a relatively strong focus on the "central" unsaturated magnesium(II) site; therefore, to better explore the PES of Model I some other configurations, mainly with respect to the carbon and hydrogen atoms of Model I, were also considered.

4.6.3 Force-field fitting

In total, 1158 *ab initio* calculations at the B2PLYP-D2/Def2-TZVPP level of theory were carried out with different configurations of Model I···CO_2, and 1065 of them were used in the force-field parameterization, while high-energy (> 5 kcal mol^{-1}) configurations were excluded. The reason for this is that these configurations have negligible influence on adsorption at moderate temperatures (i.e., 278 K, 298 K, and 343 K as being investigated in this work) and at low pressures (i.e., up to atmospheric pressure), which is of interest in this work. This large training set allowed for defining the atom types of Model I in an explicit way (i.e., in accordance to their hybridizations and/or coordination environments) without risking overfitting the model, which can happen when the number of adjustable parameters exceeds (or is too large relative to) the number of data points to be modelled. Eight atom types were defined for Model I, as shown in Figure 4.9.

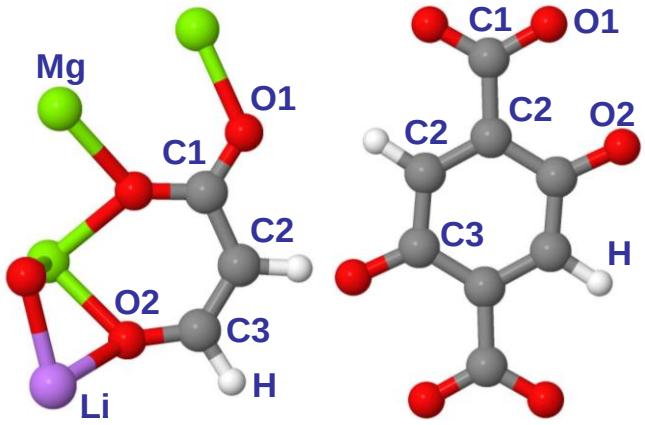

Figure 4.9. Atom types for Model I (left) and their corresponding positions in the organic linker of the CPO-27-Mg framework (right); only fragments of the structures are shown with the rest omitted for clarity.

In fitting the force field, the *ab initio* interaction energy, as defined in Equation 4.12, was approximated by the sum of electrostatic and vdW interactions (Equation 4.1). The electrostatic interactions were calculated according to the Coulomb potential (Equation 4.2), while the partial atomic charges for Model I were calculated at the B2PLYP-D2/Def2-TZVPP level of theory and derived by the MK method. The charges for CO_2 were chosen to be -0.35 for O(CO_2) (i.e., an oxygen atom of the CO_2 molecule), in order to be consistent with the TraPPE (Potoff and Siepmann, 2001) force field used for describing CO_2–CO_2 interactions in the GCMC simulations. To calculate vdW interactions for the Model I···CO_2 complex, the MMSV potential was used for Mg–O(CO_2), with all other interactions calculated by the Buck-CK potential except for those between the CO_2 molecule and the Li atoms (used for capping the dangling bonds in Model I). Since Li atoms are not present in the actual CPO-27-Mg framework and no configurations with CO_2 being close to Li were sampled for the Model I···CO_2 complex, the Li–O(CO_2) and Li–C(CO_2) interactions were calculated using the standard (12–6) LJ potential. In addition, the equilibrium distances (R_{eq}) for the Li–O(CO_2) and Li–C(CO_2) pairs were fixed at the values taken from UFF (using TraPPE for CO_2), while

the potential well depths (D_{eq}) were allowed to vary but acting merely as an error term in the fitting procedure. This definition of intermolecular interactions between Model I and CO_2 gives rise to 46 free parameters to be adjusted in the fitting procedure and the resulting force-field parameters are summarized in Table 4.5.

Table 4.5. Force-field parameters for CO_2 – CPO-27-Mg.

atom type *i*	Mg	O1	O2	C1	C2	C3	H	Li [a]
				C(CO_2) [b]				
D_{eq} (kcal mol^{-1})	0.182	0.099	0.098	0.095	0.096	0.098	0.047	0.034
R_{eq} (Å)	3.252	3.446	3.343	3.618	3.597	3.462	2.965	2.797 [c]
β	6.665	5.614	7.542	7.224	7.501	5.910	5.376	n/a
				O(CO_2) [b]				
D_{eq} (kcal mol^{-1})	n/a	0.102	0.101	0.100	0.101	0.96	0.048	0.062
R_{eq} (Å)	n/a	3.518	3.379	3.452	3.634	3.589	3.067	2.937 [c]
β	n/a	5.175	8.782	5.300	7.855	5.549	5.343	n/a

Mg–O(CO_2) [d]				
D_{eq} (kcal mol^{-1})	R_{eq} (Å)	α_1	α_2	C_6 (kcal mol^{-1} Å^6)
0.777	2.658	10.303	11.888	253.925

[a] Described by the (12–6) LJ potential (Equation 4.3). [b] The Buck-CK cross-terms for atom type *i*–C(CO_2), followed by the cross-terms for O(CO_2). [c] Not fitted and fixed at the UFF+TraPPE values. [d] The MMSV potential cross-terms for interactions between magnesium(II) sites and O(CO_2). R_2 was fixed at $1.4 \cdot R_{eq}$.

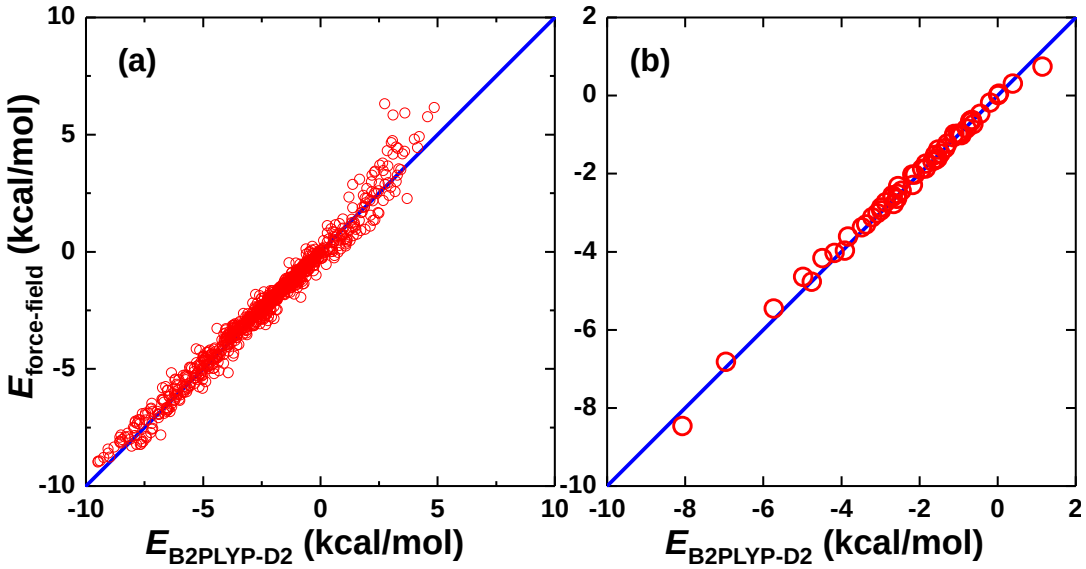

Figure 4.10. Comparison of Model I···CO_2 interaction energies obtained by the B2PLYP-D2/Def2-TZVPP method and the force field (Table 4.5). (a) 1065 configurations in the training set for the force-field parameterization; (b) 50 configurations in the test set, which were generated from an *NVT*-MD simulation and were not included in the fitting of the force.

The force-field parameters presented in Table 4.5 yield a very good fit to the whole range of *ab initio* reference data. Despite the 1065 interaction energies spanning a range from ca. -10 kcal mol^{-1} to ca. +5 kcal mol^{-1}, the RMSD between the force field and the *ab initio* data is only 0.33 kcal mol^{-1} in the whole range and is 0.26 kcal mol^{-1} in the range up to +1 kcal mol^{-1}, which is the most important range to describe adsorption in this MOF. A comparison of the Model I···CO_2 interaction energies given by the B2PLYP-D2/Def2-TZVPP calculations and the corresponding force-field predictions is given in Figure 4.10 (a).

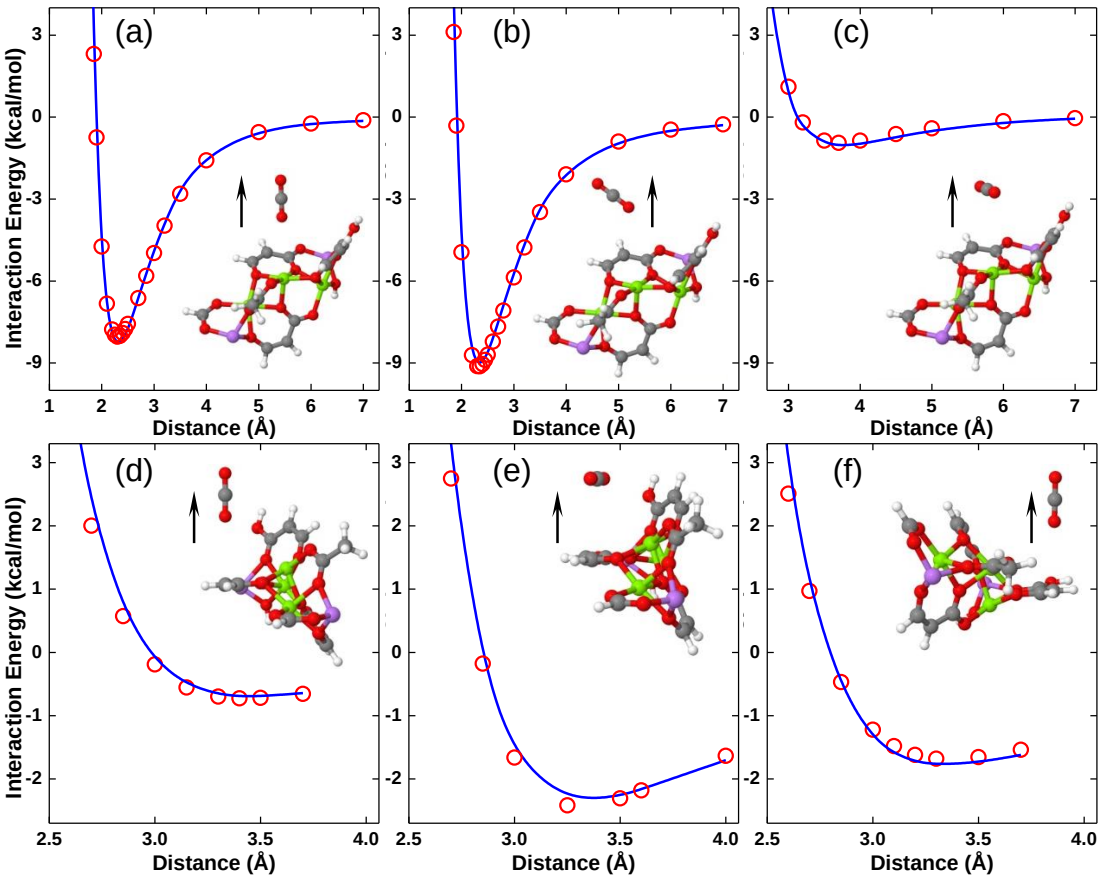

Figure 4.11. Comparison of Model I···CO_2 interaction energies calculated with the B2PLYP-D2/Def2-TZVPP method (red circle) and the force field (blue line) for the different relative configurations shown in the insets. The arrow indicates the direction of the CO_2 molecule moving away from Model I.

A more detailed picture on the performance of the force field can be obtained from Figure 4.11, where (a)–(c) show the approach routes of a CO_2 molecule to the central magnesium(II) site with different CO_2 orientations. In all three cases, the *ab initio* data is very well reproduced. Figure 4.11 (d)–(f) show examples of CO_2 approaching other atoms than Mg, and it can be seen that the force field performs equally well for these configurations.

4.6.4 Force-field validation

The first step taken to validate the force-field parameters (Table 4.5) was the examination on how well the PES obtained from the *ab initio* calculations was

reproduced. To do this, "blind" tests were performed for the Model I···CO_2 complex, wherein MD simulations were used to generate random configurations that were not previously included in the parameterization of the force field. The MD simulations were carried out in an *NVT* (i.e., constant number of particles, volume, and temperature) ensemble at 1000 K, with only one CO_2 molecule and Model I in the simulation box. The UFF and TraPPE force fields were used to describe the intermolecular interactions. In total, 50 relative configurations (between CO_2 and Model I) were generated by taking snapshots of the MD simulations. These configurations were thereafter evaluated by both the B2PLYP-D2/Def2-TZVPP method and the force field (Table 4.5). Again, a very low RMSD value of 0.13 kcal mol^{-1} was obtained for the fit of this set of test configurations, suggesting the force field is able to accurately reproduce the PES of Model I. A comparison of the force-field predicted interaction energies with the corresponding *ab initio* energies is shown in Figure 4.10 (b).

The force-field parameters were further cross-examined by periodic DFT calculations on the whole framework structure to exclude adverse effects that could arise from the cluster approach. The binding energy of CO_2 on the cus's in the CPO-27-Mg framework was calculated using the PBE exchange–correlation functional with the D2 dispersion correction in the CASTEP (version 5.501) simulation package (Clark et al., 2005). The primitive cell of the CPO-27-Mg framework was first relaxed and then one CO_2 molecule was placed adjacent to each magnesium(II) site of the cell (i.e., CO_2 : Mg = 1 : 1), followed by a structural relaxation of the loaded framework. The binding energy per adsorbed CO_2 molecule is given by

$$\Delta E = \frac{1}{n}\left[E\left(\mathrm{CPO-27-Mg}\cdots n\mathrm{CO_2}\right) - E\left(\mathrm{CPO-27-Mg}\right) - nE\left(\mathrm{CO_2}\right)\right] \quad (4.13)$$

where E(CPO-27-Mg···nCO$_2$), E(CPO-27-Mg), and E(CO$_2$) are the total energies of the CO$_2$-loaded framework, isolated framework, and isolated CO$_2$ molecule, respectively; and n = 6 (six magnesium(II) sites are present in the primitive cell of the CPO-27-Mg framework). E(CO$_2$) was calculated by placing a single CO$_2$ molecule in a supercell with the same dimensions as the optimized empty framework. Taking the relative configuration of CO$_2$ on a cus in the PBE-D2-optimized structure of CPO-27-Mg···CO$_2$, the interaction energy according to the force field was then determined with only one CO$_2$ molecule in the periodic framework. The binding energies were found to be -11.21 kcal mol^{-1} and -11.08 kcal mol^{-1} with the PBE-D2 method and the force field, respectively. This very good agreement confirms that the parameters derived from the cluster model do not suffer significant deficiencies when applied to the periodic framework and hence they can be expected to deliver high-quality results in GCMC simulations based upon them.

The PBE-D2 binding energies of CO$_2$ in CPO-27-Mg agree very well with the corresponding values given by the proposed force field that was parameterized by using the high-level *ab initio* B2PLYP-D2 method. Recalling the simulation results for CH$_4$ in CuBTC as shown in Figure 3.8 in Chapter 3, the herein observed good performance of PBE-D2 seems to contradict one of the findings in Chapter 3: that is, PBE-D2 tends to overestimate binding energies. There are, at least, three aspects to be considered when trying to rationalize the different observations. First, two different systems are dealt with in the two Chapters. It is not uncommon to find that a particular modelling method, being either a quantum mechanical level of theory or a

classical force field, performs well for certain systems but fails badly for some others. Second, in Chapter 3 PBE-D2 was compared with the DFT/CC method. The two approaches use very different methodologies (i.e., empirical correction vs. coupled cluster) to account for the missing dispersion interaction in DFT. By contrast, both PBE-D2 and B2PLYP-D2, as compared here, make use of the DFT-D2 method for dispersion calculations, although the latter additionally includes a second-order perturbation contribution. A consistent and potentially more conclusive comparison may be achieved by performing parallel DFT/CC calculations for the CO_2 – CPO-27-Mg system studied in this Chapter. By doing so, the PBE-D2 method can be compared against the DFT/CC method for two different systems; this could be of interest for future research. Last, it has been reported in the literature that a force field developed based on the model-cluster approach can systematically over-predict binding energies for real materials. That is, force-field parameters fitted to gas-phase energetic data may need to be scaled down in order to be used in condensed-phase calculations; for example, see Vanommeslaeghe et al. (2010). One implication of this would be that if PBE-D2 was to be applied to the model cluster used for the B2PLYP-D2 calculations then it might also give larger values for the corresponding binding energies.

4.6.5 GCMC simulations

Partial atomic charges for the CPO-27-Mg framework were calculated at the B3LYP/Def2-TZVPP level of theory with the Gaussian 09 program (Frisch et al., 2009). The MK scheme was used to derive partial charges and internal options, IOp(6/41=15,6/42=27,6/43=15), were set within the Gaussian 09 program to enable a sampling grid of ca. 2000 points per atom for the clusters

shown in Figure 4.12. The resulting partial atomic charges for the CPO-27-Mg framework atoms are reported in Table 4.6.

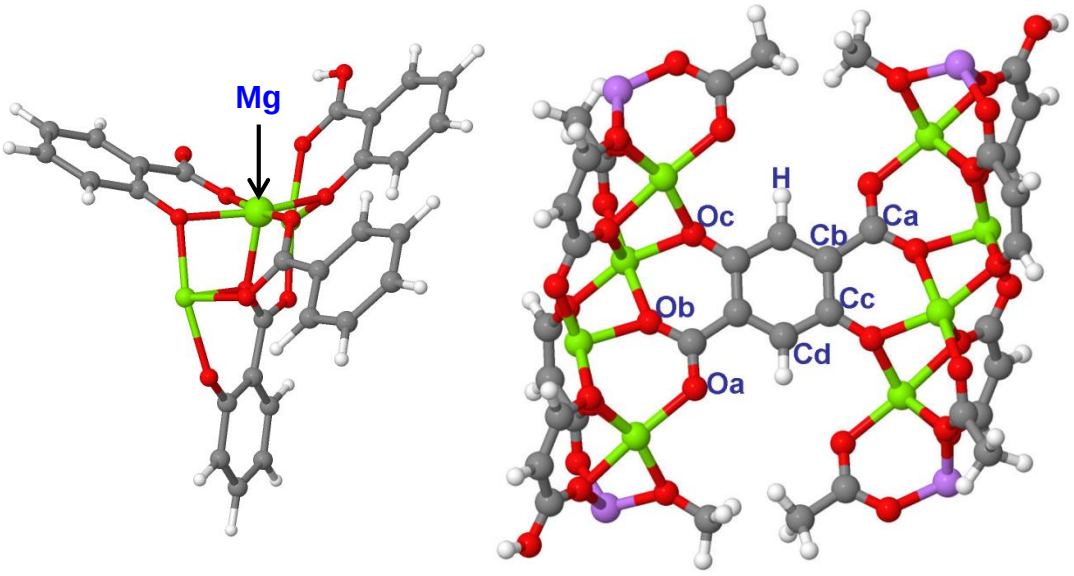

Figure 4.12. Clusters for calculation of partial charges for the CPO-27-Mg framework.

Table 4.6. Partial atomic charges[a, b] and force-field atom types[c] for CPO-27-Mg.

atom	Mg	Oa	Ob	Oc	Ca	Cb	Cc	Cd	H
q (e)	1.6311	-0.7721	-0.8854	-1.0248	0.8820	-0.2735	0.5495	-0.3354	0.2286
type	Mg	O1	O1	O2	C1	C2	C3	C2	H

[a] The vdW exclusion radii for the Mg, O, C, and H atoms are 1.364, 1.342, 1.452, and 1.001 Å, respectively. [b] The charges reported here were derived (using the MK scheme) by fitting them to the electrostatic potential of the cluster as described by the B3LPY/D2-TZVPP method. In contrast, the charges in Table 4.4 were obtained by performing the Hirshfeld population analysis of the electron density distribution of the cluster; i.e., the Hirshfeld charges do not necessarily reproduce the electrostatic potential of the cluster. [c] Force-field atom types as defined in Table 4.5.

With the force-field parameters listed in Table 4.5, CO_2 adsorption in CPO-27-Mg at different temperatures was studied. The simulated CO_2 adsorption isotherms using the parameterized force field and the UFF for comparison are shown in Figure 4.13. Experimentally, the CPO-27-Mg MOF has been

shown to take up impressive amounts of CO_2 at ambient temperatures up to atmospheric pressure (Caskey et al., 2008; Britt et al., 2009; Dietzel et al., 2009; Yazaydın et al., 2009). It is, however, clear from Figure 4.13 (a) that the GCMC simulation based on the UFF cannot correctly predict this significant uptake at the low pressures. Large discrepancies were also observed in the work of Yazaydın et al. (2009), where the DREIDING force field, together with the UFF for Mg atoms, was used. In contrast, the simulations based on the force field derived in this work predict the CO_2 adsorption in good agreement with the experiments. The overestimations may be partly explained by the quality of the experimental sample, as simulations are carried out in infinite, perfect, and fully activated crystals. When the experimental adsorption isotherm at 298 K is scaled by a factor of 1.1 – the ratio between the theoretical (Düren et al., 2007) surface area of 1733 $m^2\ g^{-1}$ (using a nitrogen probe with a diameter of 3.681 Å) and the experimental BET surface area of 1542 $m^2\ g^{-1}$ (Dietzel et al., 2009) – almost quantitative agreement between simulation and experiment can be observed in Figure 4.13 (a).

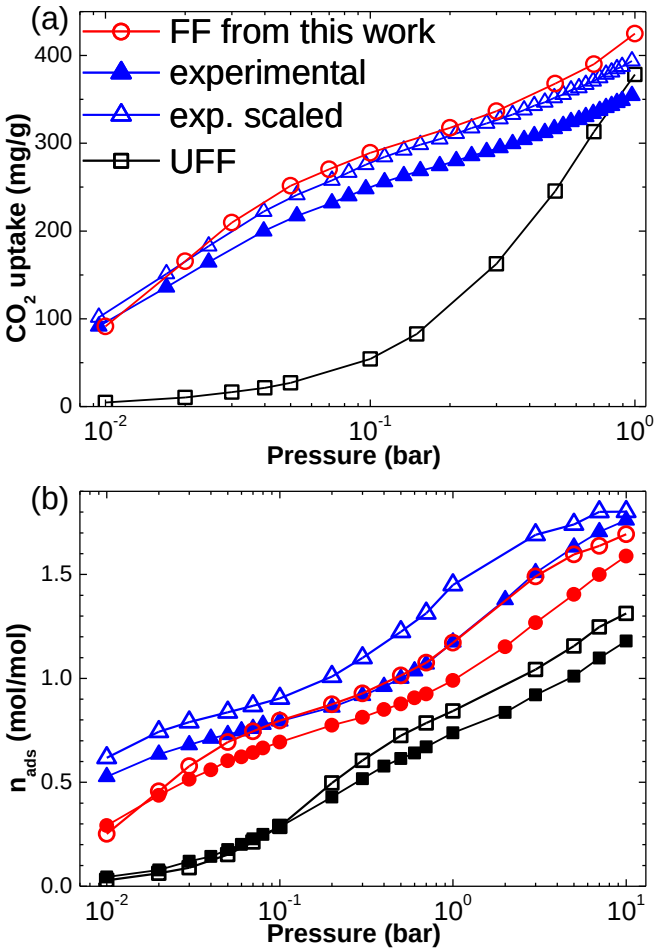

Figure 4.13. CO_2 adsorption isotherms for CPO-27-Mg. (a) Adsorption isotherms at 298 K. The scaled experimental isotherm was obtained by multiplying the corresponding experimental results by 1.1, the ratio between simulated and experimental surface areas. (b) Comparison between experimental (closed symbol; un-scaled) and simulated (open symbol) adsorption isotherms – CO_2 uptake is expressed per unit cell as (number of molecules adsorbed) / (number of Mg atoms) – at 278 (blue triangle), 298 (red circle), and 343 K (black square). Note that the isotherms are represented on a logarithmic pressure axis to better show the adsorption behaviour at low pressure. Experimental data were taken from the work of Dietzel et al (2009).

The force field (Table 4.5) is able to predict quantitatively the uptake of CO_2 not only for 298 K but also for 278 and 343 K as illustrated in Figure 4.13 (b). The simulations not only reproduce the general trends of the experimental adsorption isotherms but also the inflection in the isotherm (Dietzel et al., 2009), which occurs when one CO_2 molecule is adsorbed per magnesium(II) site. In line with this good prediction of the adsorption isotherms, the calculated initial (at ca. 8% gravimetric CO_2 uptake) isosteric heat of

adsorption (Q_{st}; Equation 4.11) of 9.5 kcal mol^{-1} at 298 K is also in good agreement with experimental values in the literature: 9.3 kcal mol^{-1} (Britt et al., 2009), 10.0 kcal mol^{-1} (Dietzel et al., 2009), and 11.2 kcal mol^{-1} (Caskey et al., 2008). Moreover, in the simulation the first CO_2 molecules are exclusively adsorbed at the unsaturated magnesium(II) sites in an end-on fashion at low loadings, which is also in line with the experimental findings (Wu et al., 2010; Queen et al., 2011). At a loading of ca. 0.75 adsorbed CO_2 per magnesium(II) site at 298 K, the simulated distance between the Mg atom and the nearby oxygen of the adsorbed CO_2 molecule varies between 2.3 and 2.8 Å, with the angle of Mg–O(CO_2)–C(CO_2) varying between 120 and 150 °. These values are in good agreement with the neutron diffraction experiments performed at 20 K, where the corresponding distance and angle were found to be 2.3 Å and 129 °, respectively, for the same loading (Queen et al., 2011). This further confirms that the proposed force field provides a correct description of the adsorption mechanism on the molecular level.

4.7 Conclusions

In order to improve the description of the interaction between gas molecules and MOFs with coordinatively unsaturated metal sites, two systems were studied – namely CO_2 adsorption in CPO-27-Mg and CH_4 adsorption in CuBTC. Several model potentials were carefully compared and the MMSV and Buck-CK potentials were chosen for describing the fluid–framework interactions. On the basis of the accurate *ab initio* reference data, the force fields were parameterized using a multi-objective genetic algorithm and were subsequently validated through extensive comparisons between the

force-field-based simulation results and experimental data available in the literature. In both cases, the adsorption isotherms are in very good agreement with experiments, and more importantly, the interactions at the cus's as well as the overall adsorption mechanisms in the frameworks are captured correctly. Using the force-field parameters developed for the CuBTC–CH_4 system, CH_4 adsorption in another Cu-MOF with cus's, PCN-14, can be predicted quantitatively for four different temperatures. These results are promising in terms of developing force-field parameters that are transferable to other MOFs. However, more high quality adsorption data, ideally measured at low temperatures to capture the adsorption mechanism in more detail in MOFs with Cu and Mg cus's, are necessary to judge how widely transferable these parameters are.

Furthermore, the proposed bottom-up methodology of combining the advantages of both *ab initio* methods and GCMC simulation holds promise for correctly describing the enhanced interactions at cus's in molecular simulation of adsorption. A straightforward application of this protocol is to extend it to the isostructural analogues of CPO-27-Mg, i.e., CPO-27-M (M = Co, Ni, Fe, etc.). This series of MOFs have been identified as promising candidates in various applications, and GCMC simulations based on generic force fields cannot correctly describe the interactions with the cus's (Yazaydın et al., 2009). In the development of an *ab initio* force field for another CPO-27 MOF, it may be expected that the parameters for the linker to remain the same as, or related to, those from the herein proposed CO_2 – CPO-27-Mg force field. More *ab initio* calculations are, of course, required to parameterize the metals and their immediate environment. This idea of applying the proposed methodology to improving the prediction of CO_2 adsorption in another CPO-27 MOF, CPO-27-Co, is demonstrated in the next

Chapter. Last but not least, this Chapter highlights that the choice of model potentials, or potential functional forms to be specific, has a critical influence on the accuracy of the predictions of adsorption in MOFs with cus's. Potentials like the LJ and Morse potentials are simple and widely adopted in majority of the existing force fields and they will undoubtedly continue to play an important role in molecular simulation. Nevertheless, the correct description of adsorption at coordinatively unsaturated metal sites requires more complicated potentials and this work is only a first step for deriving reliable and hopefully transferable force fields for this purpose.

Chapter 5 Towards a Systematic Development of *ab initio* Force Fields for CO_2 Adsorption in MOFs with Cus's

5.1 Introduction

Chapter 4 introduces a systematic, robust protocol for parameterizing some well-established semiempirical model potentials from accurate *ab initio* reference data. Here, following the same procedure – i.e., model cluster construction, *ab initio* calculation, and force-field fitting – an *ab initio* parameterized force field is proposed for CO_2 adsorption in CPO-27-Co (Dietzel et al., 2005). Taking advantage of the CO_2 – CPO-27-Mg force field, considerably fewer *ab initio* calculations are needed for the CO_2 – CPO-27-Co system. Thus, the force-field development is markedly less computationally expensive, demonstrating the possibility of readily and rapidly applying this multi-scale simulation strategy to other CPO-27 analogues with different unsaturated metal centres.

To further explore the ease with which the proposed bottom-up strategy of combining GCMC simulation with *ab initio* calculation can be adopted to improve predictions of gas adsorption in MOFs with cus's, CO_2 adsorption in MOFs consisting of the $Cu_2(O_2CR)_4$ paddle-wheel copper dimer is studied. Two cus-containing Cu-MOFs – namely, CuBTC (Chui et al., 1999), and NOTT-140a (Tan et al., 2011) – are chosen for two reasons.

First, the $Cu_2(O_2CR)_4$ paddle-wheel building block has been extensively used to combine with a wide variety of organic linkers to afford an even larger

number of framework topologies. Because of the incorporation of unsaturated copper sites in these MOFs, GCMC simulations based on generic force fields have been reported to exhibit pronounced underestimations of uptake of certain sorbate species such as CO_2 (Yazaydın et al., 2009), H_2O (Zang et al., 2013), H_2 (Fischer et al., 2010), and alkenes (Fischer et al., 2012). For the latter three cases – i.e., the adsorption of H_2O, H_2, or alkenes in the Cu-MOFs – *ab initio* calculations were used to yield accurate adsorbate–cus interactions, which in turn enabled the GCMC simulations based upon them to correctly predict the adsorption isotherms. Therefore, this work presents an *ab initio* parameterized force field that allows for accurate predictions of CO_2 adsorption in the CuBTC MOF, while the predicted CO_2 adsorption in NOTT-140a is used to examine the transferability of the proposed force-field parameters.

Second, and perhaps more instructively, this work seeks to ascertain the underlying (but still largely tentative in the case of MOFs with cus's) possibility of developing fluid–MOF force fields on a building-block basis rather than for any particular frameworks, stemming from the very essence of the modular building-block synthesis of MOFs. That is, since MOFs are constructed from modular molecular building blocks, force-field parameters that correctly describe the CO_2 interaction with the $Cu_2(O_2CR)_4$ in (for example) CuBTC should be able to correctly describe such interaction in (for example) NOTT-140a, or any other MOF with this building block. Indeed, Han et al. (2012) showed that their *ab initio* force fields simulated CO_2 adsorption in several MOFs and ZIFs in very good agreement with experiment, although the force-field parameters were derived based on the organic compounds, such as benzene and its derivatives, and were not specifically fitted to the frameworks. Note, however, that the authors did not

specify how the parameters for the CO_2–Zn interaction were derived (Han et al., 2012). Similarly, Yu et al. (2012) were able to study the adsorption of ammonia in four MOFs modified with different functional groups using a combined force field approach in the GCMC simulations. The NH_3 interaction with the functional groups was described by therein *ab initio* parameterized Morse potential, while the NH_3 interaction with the rest of the MOF atoms was described by the LJ potential using generic force fields.

In the context of MOFs with cus's, ideally, only a new set of force-field parameters for the adsorbate–cus interaction needs deriving from high-level *ab initio* calculations on a finite-size model cluster. The adsorbate–linker interaction should be satisfactorily modelled with some generic force fields, such as UFF and DREIDING, or with some more specialized force fields for organic molecules, such as OPLS-AA and AMBER (Cornell et al., 1995). Compared to a whole repetition of the procedure outlined in Chapter 4 for every new fluid–MOF system, a modelling procedure of this type is not only computationally more efficient but can also (almost certainly) effectively augment the applicability of generally transferable generic force fields to studying gas adsorption in MOFs with cus's.

In this Chapter, the CO_2 – CPO-27-Mg force field (presented in Chapter 4) is first revisited with the purpose of unifying the use of model potentials; the MMSV potential is used for all interatomic interactions involved in the CO_2 – CPO-27-Mg system (i.e., the Buck-CK potential is no longer needed). Thereafter, force-field parameterizations for the CO_2 – CPO-27-Co and CO_2 – Cu-MOFs systems are presented.

5.2 Revisiting the *ab initio* Force Field for CO_2 – CPO-27-Mg

The primary reason for re-parameterizing the CO_2 – CPO-27-Mg force field – on the basis of the same *ab initio* reference data (detailed in Section 4.6.2) – is that using a single model potential (as the MMSV potential chosen here) gives a more concise format, making future force-field extension more easily and systematically. Moreover, a uniform potential energy expression can markedly simplify the implementation of such force field in GCMC simulations. Most importantly, by relating the parameterization of the MMSV potential function to the B2PLYP-D2 functional used in calculation of the *ab initio* reference data, the force-field parameters thereby obtained can be considered as having a better physical justification. In addition, the robustness of the fitting procedure and hence the quality of the parameters fitted can be enhanced, as fewer variables are adjusted independently in the fitting process. It is worth pointing out that, from a physical point of view, using the MMSV potential for all of the interatomic interactions involved in the CH_4 – CuBTC system does not offer any obvious advantages over the combination of the MMSV and Buck-CK potentials, as the *ab initio* reference data for the system were calculated at the DFT/CC level.

5.2.1 B2PLYP-D2 functional and MMSV potential

The *ab initio* reference data for the CO_2···Model I (of CPO-27-Mg) complex were calculated using the B2PLYP-D2 functional, as described in Chapter 4. The B2PLYP functional is one of Grimme's double-hybrid functionals, which adds an "exact" Hartree–Fock (HF) exchange to semi-local GGA type exchange (X) and adds a second-order perturbation correlation term (PT2) to

a semi-local GGA type correlation (C) (Grimme, 2006). The total exchange–correlation (XC) energy is given by

$$E_{\mathrm{XC}} = (1-\alpha_{\mathrm{X}})E_{\mathrm{X}} + \alpha_{\mathrm{X}}E_{\mathrm{HF}} + (1-\alpha_{\mathrm{C}})E_{\mathrm{C}} + \alpha_{\mathrm{C}}E_{\mathrm{PT2}} \tag{5.1}$$

where α_X and α_C are mixing parameters; for the B2PLYP functional, $\alpha_X = 0.53$ and $\alpha_C = 0.27$ (Grimme, 2006).

Within Grimme's DFT-D2 dispersion correction scheme, the standard self-consistent Kohn-Sham energy as obtained from the chosen DFT functional, $E_{\mathrm{KS\text{-}DFT}}$, is augmented by a semiempirical dispersion potential, E_{disp}; the total energy for any DFT functional is given by

$$E_{\mathrm{DFT-D2}} = E_{\mathrm{KS-DFT}} + E_{\mathrm{disp}} \tag{5.2}$$

where the dispersion correction E_{disp} is given by

$$E_{\mathrm{disp}} = -s_6 \sum_{i=1}^{N_{\mathrm{at}}-1} \sum_{j=i+1}^{N_{\mathrm{at}}} \frac{C_6^{ij}}{r_{ij}^6} f_{\mathrm{dmp}}(r_{ij}). \tag{5.3}$$

Here, r_{ij} is the interatomic distance; N_{at} is the number of atoms in the system; C_6^{ij} denotes the dispersion coefficient for atom pair ij; and s_6 is a global scaling factor that only depends on the DFT functional used, and $s_6 = 0.55$ for B2PLYP-D2. The value of s_6 adopted in conjunction with the B2PLYP functional is quite small, as compared to $s_6 = 0.75$ for PBE and $1.00 \leq s_6 \leq 1.25$ for most other GGA functionals. This is not surprising, considering that parts of the dispersion effects are accounted for by the perturbation component (E_{PT2}) of the total energy (Equation 5.1). $f_{\mathrm{dmp}}(r_{ij})$ is a damping function that

must be used to avoid near-singularities for small r_{ij} (Grimme, 2006). The atomic C_6 coefficients for the elements from H to Xe are available from the original DFT-D2 work (Grimme, 2006), in which the cross-term dispersion coefficient for an atom pair is given by a geometric mean of the form: $C_6^{ij} = \sqrt{C_6^i C_6^j}$.

In terms of fitting the MMSV potential to the B2PLYP-D2 energy (together with the Coulomb potential modelling the electrostatic contribution), it is immediately obvious that the C_6 parameter in the MMSV potential need not be determined independently, but rather should take some form that adheres to the DFT-D2 definition. In this respect, the MMSV potential can be re-written as

$$E_{\mathrm{vdW}}^{\mathrm{MMSV}}(r_{ij}) = \begin{cases} D_{eq}\left\{\exp\left[\alpha_1\left(1-\dfrac{r_{ij}}{R_{eq}}\right)\right]-2\exp\left[\dfrac{\alpha_1}{2}\left(1-\dfrac{r_{ij}}{R_{eq}}\right)\right]\right\} \\ \qquad\qquad \text{for } 0 \le r_{ij} \le R_{eq} \\ D_{eq}\left\{\exp\left[\alpha_2\left(1-\dfrac{r_{ij}}{R_{eq}}\right)\right]-2\exp\left[\dfrac{\alpha_2}{2}\left(1-\dfrac{r_{ij}}{R_{eq}}\right)\right]\right\} \\ \qquad\qquad \text{for } R_{eq} \le r_{ij} \le R_1 \\ b_1 + (r_{ij}-R_1)\{b_2 + (r_{ij}-R_2)[b_3 + (r_{ij}-R_1)b_4]\} \\ \qquad\qquad \text{for } R_1 \le r_{ij} \le R_2 \\ -s_6^{\mathrm{FF}} C_6^{ij} r_{ij}^{-6} \\ \qquad\qquad \text{for } R_2 \le r_{ij} < \infty \end{cases} \tag{5.4}$$

where s_6^{FF} is a global scaling parameter for the DFT-D2 dispersion coefficients, C_6^{ij}, to be used in the force field, and it can be expected to be greater than the s_6 value of 0.55 in the B2PLYP-D2 method. The reason is that

at large interatomic distances the B2PLYP-D2 energy comprises both E_{disp} and E_{PT2} terms. In addition, no damping function is needed in Equation 5.4, since at small separation distances the MMSV potential does not take the form of ~$(1/r_{ij})^6$, a function that diverges as r_{ij} approaches zero. Comparing Equation 5.4 with Equation 4.8 (Chapter 4), it is clear that the only difference lies in the two last terms: $-s_6^{\mathrm{FF}} C_6^{ij} r_{ij}^{-6}$ in Equation 5.4 and $-C_6 r_{ij}^{-6}$ in Equation 4.8. In terms of force-field parameterization, the C_6 value (in Equation 4.8) was fitted for each of the defined atom pairs while all of the C_6^{ij} values (in Equation 5.4) were taken directly from the original DFT-D2 method (not fitted). Instead, with Equation 5.4 the s_6^{FF} parameter, a global factor having the same value for all of the atom pairs, was determined in the force-field fitting.

Another aspect of aligning the parameterization of the MMSV potential with the B2PLYP-D2 method concerns the CO_2 interaction with model-cluster atoms that are not involved in the GCMC simulations of the MOF, i.e., the lithium atoms used to cap Model I for the CPO-27-Mg framework. In Chapter 4, the CO_2–Li vdW interactions are described by the LJ potential with D_{eq} values determined in the force-field fitting and R_{eq} fixed at the values given by the generic force fields. Here, the CO_2–Li vdW interactions are calculated according to the expression proposed by Sholl and co-workers (Fang et al., 2012; Zang et al., 2013), which is also motivated by the DFT-D2 method and is given by

$$E_{\mathrm{vdW}}^{\mathrm{Sholl}} = s_{12}^{\mathrm{FF}} \frac{C_{12}^{ij}}{r_{ij}^{12}} - s_6^{\mathrm{FF}} \frac{C_6^{ij}}{r_{ij}^{6}} \tag{5.5}$$

where s_{12}^{FF} and s_6^{FF} are global scaling factors that only depend on the chosen first-principles method used in calculation of the reference data for force-field fitting; and C_6^{ij} is, again, the DFT-D2 pairwise dispersion coefficient. The repulsive coefficient C_{12}^{ij} is defined by

$$\frac{C_{12}^{ij}}{C_6^{ij}} = \frac{\left(R_{\mathrm{vdW}}^{i} + R_{\mathrm{vdW}}^{j}\right)^6}{2} \tag{5.6}$$

where R_{vdW}^{i} and R_{vdW}^{j} are the vdW radii of atoms *i* and *j*, respectively. Like the C_6 coefficients, R_{vdW} for the elements from H to Xe are available from the original DFT-D2 work (Grimme, 2006). The justification of Equation 5.6 for determining C_{12} is given in the work by Fang et al (2012).

5.2.2 Force-field fitting for CO_2···Model I of CPO-27-Mg

All of the interatomic interactions involved in the CO_2···Model I complex are calculated, in the force field, by the sum of electrostatic interaction calculated by the Coulomb potential and vdW interaction represented by the MMSV potential. As discussed above, for fitting the MMSV model potential to the B2PLYP-D2 reference data, the $-C_6 r_{ij}^{-6}$ term in the original function (of MMSV) can be modified to adopt the form of $-s_6^{FF} C_6^{ij} r_{ij}^{-6}$; this allows for the use of the DFT-D2 dispersion coefficients directly in the force field. This treatment, to a certain extent, enhances the robustness of the force field, and significantly reduces the number of adjustable parameters if the MMSV potential is to be used for all atom pairs. Guided by the fact that the DFT-D2 dispersion coefficients are element-wise (i.e., a single value for each element

and the chemical environment of an atom is not considered), the stiffness parameters, α_1 and α_2, in the MMSV potential can also be fitted in an element-pairwise manner. That is, for example, α_1 has the same value for O(CO_2)–C(MOF) and C(CO_2)–O(MOF). Together with Equation 5.5 describing the CO_2–Li interactions in the CO_2···Model I complex, Table 5.1 lists all of the force-field parameters for the CO_2 – CPO-27-Mg system, 44 of which were determined in the force-field fitting. In comparison, using the MMSV potential for all interatomic interactions involved in the CO_2···Model I complex without imposing the above rules would result in a total of 72 independent parameters to be fitted; 72 = 14 (atom pairs) × 5 (variables in one MMSV potential) + 2 (s_6^{FF}, s_{12}^{FF}).

Table 5.1. Force field for CO_2 – CPO-27-Mg using the MMSV potential.[a]

force-field type	Mg	O1	O2	C1	C2	C3	H
				$O(CO_2)$ [b]			
D_{eq} (kcal mol^{-1})	1.380	0.151	0.120	0.122	0.121	0.118	0.074
R_{eq} (Å)	2.671	3.460	3.494	3.448	3.923	3.761	2.965
α_1	7.887	12.381	12.381	11.006	11.006	11.006	12.016
α_2	16.621	13.301	13.301	13.115	13.115	13.115	12.016
C_6^{ij} [c] (kcal mol^{-1} Å^6)	454.646	167.304	167.304	264.531	264.531	264.531	74.821
				$C(CO_2)$ [b]			
D_{eq} (kcal mol^{-1})	0.161	0.099	0.085	0.078	0.078	0.081	0.040
R_{eq} (Å)	3.289	3.549	3.407	3.600	3.498	3.489	3.203
α_1	10.158	11.006	11.006	12.954	12.954	12.954	10.403
α_2	10.723	13.115	13.115	11.866	11.866	11.866	10.403
C_6^{ij} [c] (kcal mol^{-1} Å^6)	533.577	264.531	264.531	418.260	418.260	418.260	118.302

	$O(CO_2)$–Li [d]	$C(CO_2)$–Li [d]
C_6^{ij} [c] (kcal mol^{-1} Å^6)	253.729	401.181
C_{12}^{ij} [e] (kcal mol^{-1} Å^{12})	13136.926	27956.865

[a] The MMSV potential for this CO_2 – CPO-27-Mg force field is in the form of Equation 5.4, and s_6^{FF} was found in the fitting to be 0.825, which is, as expected, greater than the value of 0.550 for s_6 in the B2PLYP-D2 method. For all atom pairs, R_2 was fixed at $1.6 \cdot R_{eq}$. [b] The MMSV cross-terms for $O(CO_2)$–MOF interactions, followed by the cross-terms for $C(CO_2)$–MOF interactions. [c] The pairwise dispersion coefficients, C_6^{ij}, were taken from the DFT-D2 correction (Grimme, 2006), except that the $C_6^{O(CO_2)-Mg}$ and $C_6^{C(CO_2)-Mg}$ were fitted independently. [d] The CO_2–Li interactions were described by Equation 5.5, and s_{12}^{FF} was fitted to a value of 6.500. [e] The C_{12}^{ij} values were calculated according to Equation 5.6 using 0.825, 1.452, and 1.342 Å for the vdW radii of Li, C, and O, respectively (Grimme, 2006).

5.2.3 Force-field validation and GCMC simulations

For clarity and ease of comparison, the *ab initio* parameterized force field presented in Table 4.5 (Chapter 4), which adopts the combination of MMSV and Buck-CK potentials, is referred to as AIFF-G1 (which stands for *ab initio* force field-1st generation) hereafter. Likewise, the force field given in Table 5.1, which uses the MMSV potential for all CO_2–MOF interactions, is referred to as AIFF-G2.

AIFF-G2 is first subject to examination of how well it reproduces the potential energy surface of CO_2···Model I, as described at the B2PLYP-D2/Def2-TZVPP level of theory. The force field results in a slightly better fit to the *ab initio* reference data, compared to that obtained for AIFF-G1. For the same 1065 interaction energies, the RMSD between AIFF-G2 and the *ab initio* data is 0.31 and 0.25 kcal mol^{-1} for the whole range and the range up to +1 kcal mol^{-1}, respectively (compared to 0.33 and 0.26 kcal mol^{-1} for AIFF-G1). Furthermore, it can be clearly seen from Figure 5.1 that both AIFF-G1 and -G2 reproduce the *ab initio* data with an impressive accuracy. For the "end-on" approach route (Figure 5 (a)) to the Mg cus, both force fields perform equally well, predicting CO_2···Model I interaction energies in excellent agreement with the B2PLYP-D2 method. This was expected, since both force fields use the MMSV potential to describe the O(CO_2)–Mg interaction. The most marked improvement of AIFF-G2 from AIFF-G1 is seen for the approach routes (Figure 5.1 (b), (c), and (d)) where the CO_2···Model I interaction energy has major contributions from the interatomic interactions other than the O(CO_2)–Mg one. This comparison affirms the aforementioned understanding that the MMSV potential is a good choice for accurately reproducing the potential energy curve. This is rather conceivable than surprising, because

the piecewise format offers desirable flexibility in fitting while each piece, represented by a model potential, may also be physically motivated and/or justified separately, the benefit of which can be clearly seen in the fitting of AIFF-G2.

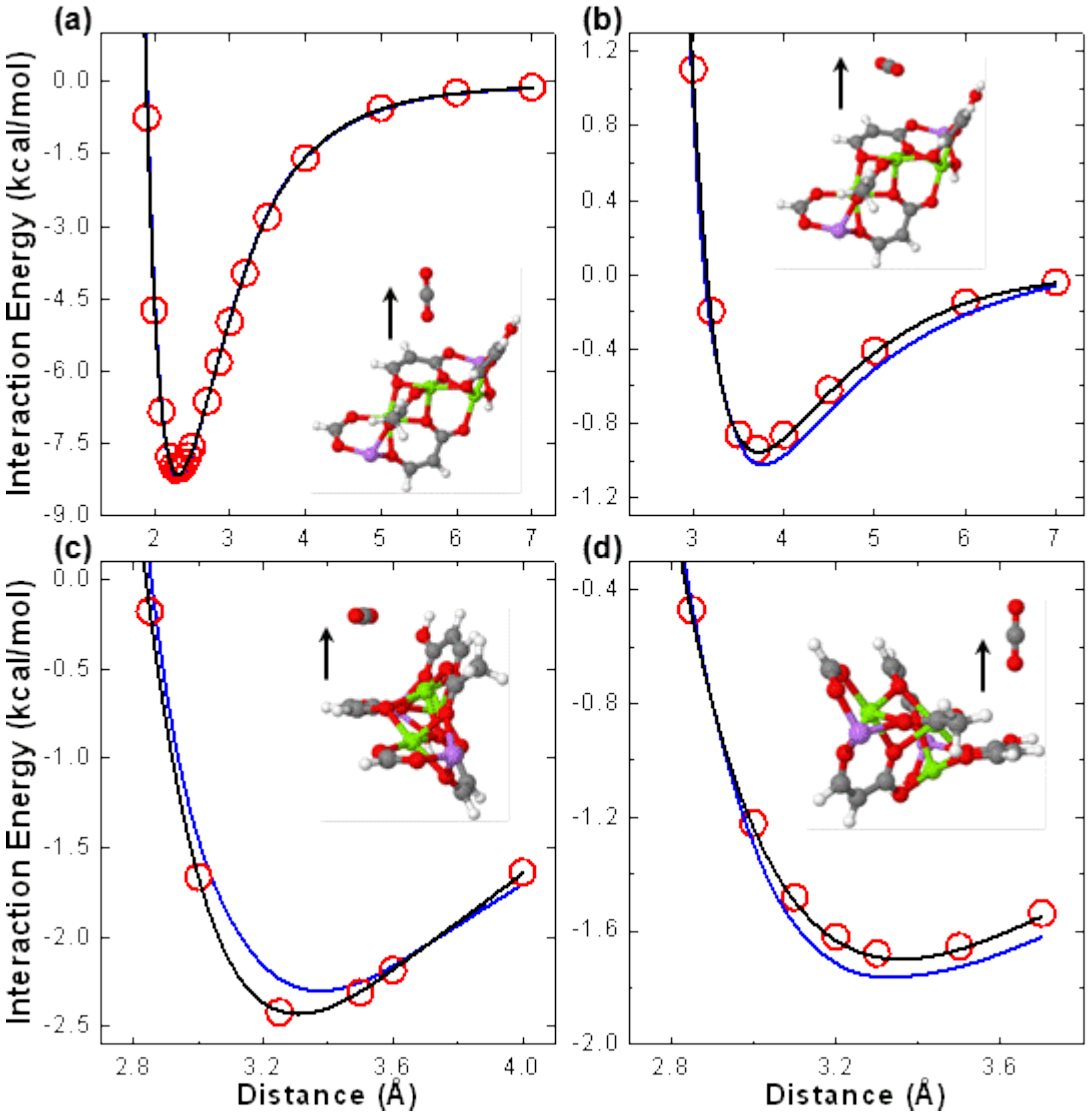

Figure 5.1. Comparison of CO_2···Model I interaction energies calculated with the B2PLYP-D2/Def2-TZVPP method (red circle) and the AIFF-G1 (blue line) and -G2 (black line) force fields for the different relative configurations shown in the insets. The arrow indicates the direction of the CO_2 molecule moving away from Model I.

Using AIFF-G1 and -G2, CO_2 adsorption in CPO-27-Mg was studied at 303 K, in order to compare force-field predictions with a recent experimental work (Remy et al., 2013), where CO_2 uptake in this MOF was recorded at low pressures down to 10^{-4} bar (Figure 5.2).

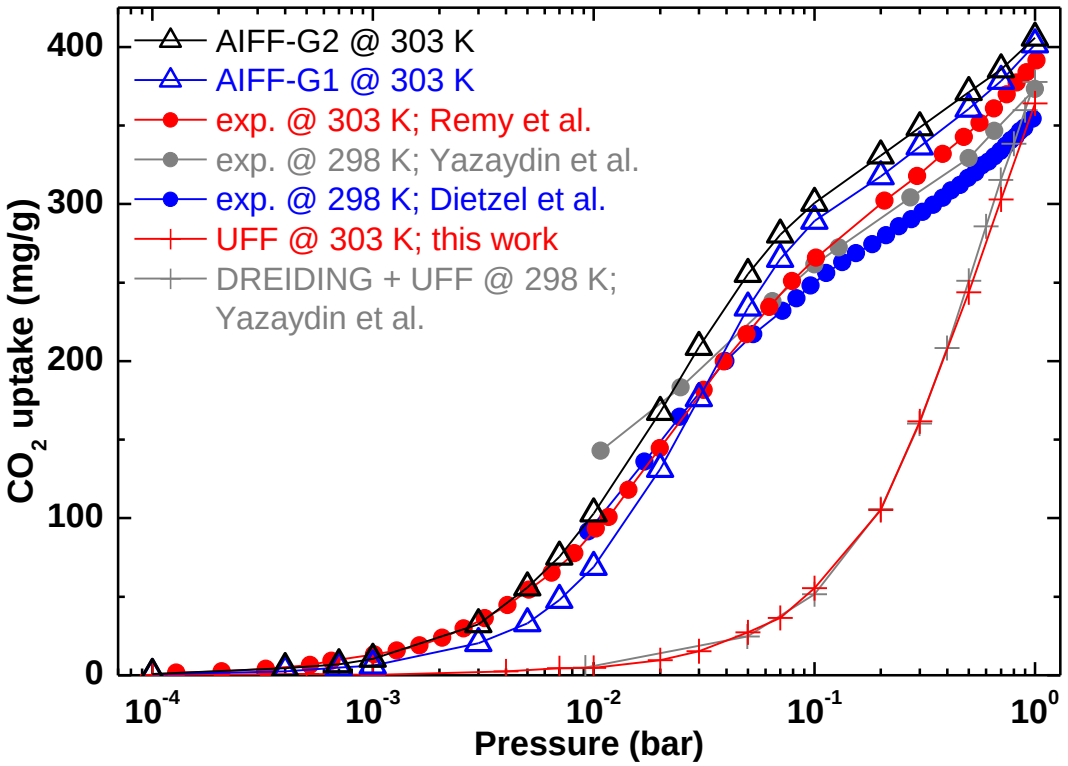

Figure 5.2. Comparison of CO_2 adsorption isotherms at 298 and 303 K in the CPO-27-Mg MOF between simulation and experiment (Dietzel et al., 2009; Yazaydın et al., 2009; Remy et al., 2013). Note that the isotherms are represented on a logarithmic pressure axis to better show the adsorption behaviour at low pressure and the lines were added to guide the eye.

Two points are particularly worth commenting. First, the UFF-based GCMC simulation results in this work agree very well with the modelling predictions of Yazaydın et al. (Yazaydın et al., 2009), also obtained using generic force fields (DREIDING + UFF). Figure 5.2 reiterates the by-now known difficulties with using generic force fields to predict correctly gas adsorption in MOFs with cus's, at least at low pressures (sometimes up to moderate pressures). Moreover, although the two GCMC simulations based

on the generic force fields predict CO_2 uptakes in quantitative agreement with each other, the partial atomic charges used for the CPO-27-Mg framework are quite different. That is, the charges used by Yazaydın et al. (2009) are, on average, ca. 10% (in absolute value) smaller than the ones in this work (e.g., 1.458 vs. 1.6311 for Mg). The discrepancies are mainly a result of the different DFT methods – B3LYP/Def2-TZVPP here and B3LYP/6-31+G* in the work of Yazaydın et al. – chosen for calculation of charges, and are also (but to a lesser degree) due to the different derivation schemes used: i.e., MK vs. CHelpG. This result, in a way, places an "unexpected" emphasis on the necessity for a bespoke force field for CO_2 – CPO-27-Mg, because it appears to be unlikely to enhance simulated uptake in this MOF by simply enlarging the partial charges of the framework – a measure that has been shown to be "effective" for H_2O in CuBTC (Castillo et al., 2008), for example. Nevertheless, it should be emphasized that despite the differences between the two sets of DFT derived charges, they can be considered "faithful" to the electrostatic potential of the system as described by the chosen DFT method. This is fundamentally different from the above-mentioned "effective" approach that enlarges the partial charges by multiplying them by a factor greater than one, which in effect increases the electrostatic potential of the system and hence enhances the uptake.

Second, both AIFF-G1 and -G2 yield very good predictions of CO_2 adsorption in CPO-27-Mg, compared to the experimental isotherms (Dietzel et al., 2009; Yazaydın et al., 2009; Remy et al., 2013). In particular, the simulated isotherms based on either AIFF-G1 or -G2 accurately reproduce the shape of the experimental isotherm at 303 K for the whole pressure range 10^{-4}–1 bar. In the very low pressure range ($\leq 10^{-2}$ bar), the AIFF-G2-based predictions are in better agreement with the experimental results, in

comparison to those from the simulation using AIFF-G1. Accordingly, for the uptake of first CO_2 per unit cell (corresponding to ca. 0.06 CO_2/Mg), the isosteric heats of adsorption were calculated to be 9.7 and 10.3 kcal mol^{-1} from the GCMC simulations based on AIFF-G1 and -G2, respectively. As the CO_2 uptake approaches the coverage of one per Mg atom, the primary adsorption sites (cus's) have been occupied and following CO_2 adsorption occurs as a result of interactions with secondary sites and filling of the pores. At the uptake of 1 CO_2/Mg, the isosteric heats of adsorption, respectively, decrease to 7.3 and 7.5 kcal mol^{-1} with AIFF-G1 and -G2. For both uptakes (i.e., 0.06 and 1 CO_2/Mg), these simulated results are in very good agreement with experiment (Dietzel et al., 2009; Remy et al., 2013), where ca. 10 and ca. 7 kcal mol^{-1} were determined as the isosteric enthalpies for the uptakes.

The enhanced CO_2 uptakes simulated by AIFF-G2 at the very low pressures primarily result from the larger D_{eq} value for the O(CO_2)–Mg pair in AIFF-G2 than that in AIFF-G1 (Figure 5.3 (a)). Nonetheless, the AIFF-G2-based predictions of CO_2 adsorption at higher pressures are not (markedly) compromised; that is, they are (almost) in as good agreement with experiment as the AIFF-G1 ones. The reason for this is that the O(CO_2)–Mg attraction decreases rapidly beyond the equilibration distance; it converges to a dispersion-dominant behaviour within a separation less than 2 Å away from the equilibrium distance and converges to the AIFF-G1 potential curve within 1 Å. As a result, in most cases the non-nearby O(CO_2) does not "feel" the strong attraction from the Mg cus – as the distance between O(CO_2) and O'(CO_2) is 2.322 Å – but rather interacts with it in a "normal" manner, i.e., dispersion. Figure 5.3 (b) provides a further demonstration for how a "soft" repulsion can be guaranteed without a large, undesirable "tail" by the MMSV potential, which is especially important for describing the adsorbate–

cus interaction but cannot be achieved by either the LJ potential or the Morse potential.

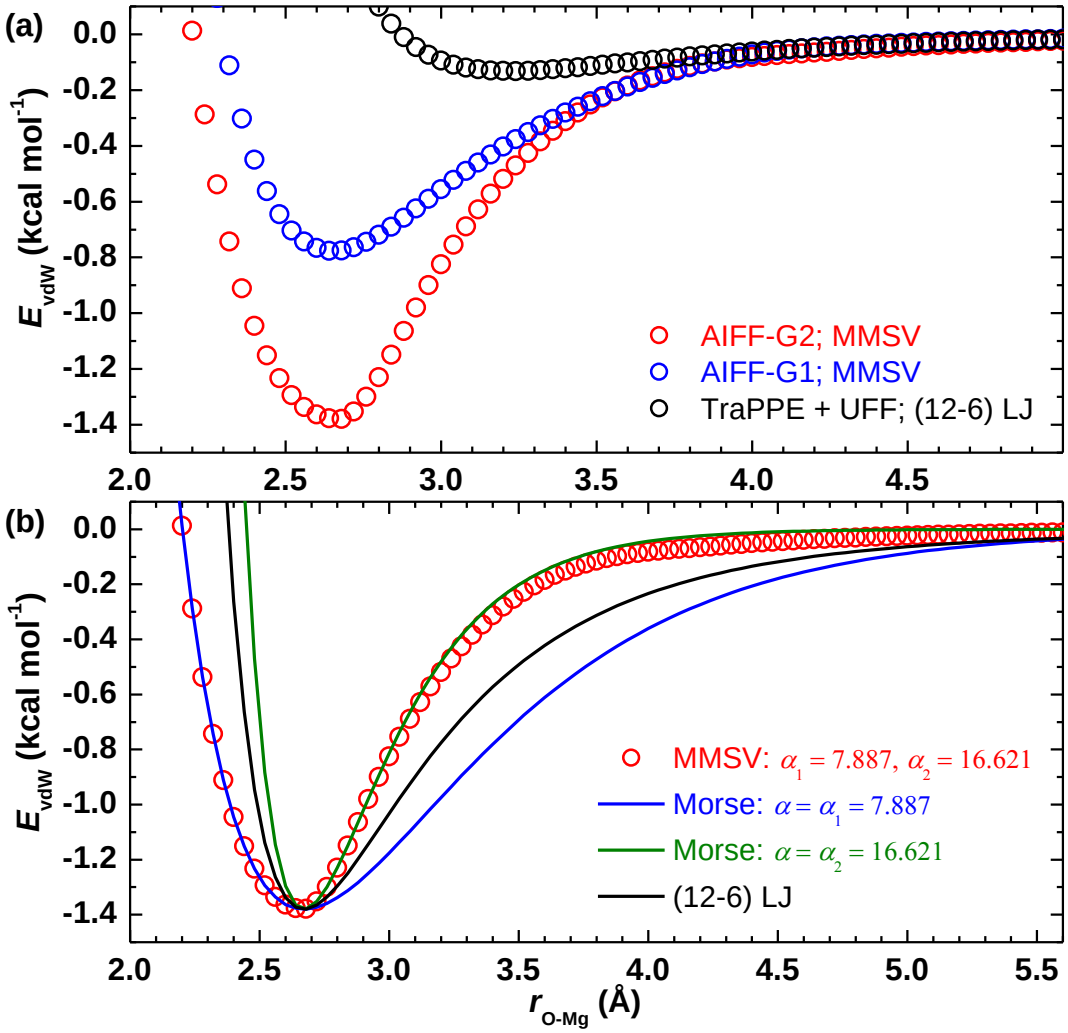

Figure 5.3. (a) O(CO_2)–Mg vdW potential energy curves from the different force fields as a function of the interatomic separation. The generic force fields based potential curve was included for comparison, where the O(CO_2) and Mg atoms were described by the TraPPE and UFF force fields, respectively. (b) Potential energy curves are characterized with the same values for D_{eq} and R_{eq} (from AIFF-G2) but with the different functional forms.

In summary, both AIFF-G1 and -G2 are a good fit to the *ab initio* reference data and consequently yield very good description of all of the interatomic interactions involved in the CO_2 – CPO-27-Mg system, including those between CO_2 and the Mg cus's. The AIFF-G1(2)-based GCMC simulations

predict CO_2 adsorption in very good agreement with experiment for this MOF, whereas AIFF-G2 outperforms its counterpart at very low pressures (≤ 0.01 bar). The unified use of the MMSV potential, together with the physically motivated force-field fitting of the dispersion component, offers a promising perspective for AIFF-G2 to be extended readily and relatively easily to include force-field parameters for other MOFs, at least for CPO-27 analogues. This is indeed evident from the case of CO_2 adsorption in CPO-27-Co, which is discussed in the following Section.

5.3 Force Field for CO_2 – CPO-27-Co

5.3.1 *Ab initio* reference data

The framework topology of CPO-27-Co (Figure 5.4 (a)) is identical to the one previously described for CPO-27-Mg (Section 4.6). Both CPO-27 materials crystalize in a trigonal setting, space group $R\bar{3}$ (no. 148), with a unit-cell volume of 3949.0 or 3993.5 Å^3 for the Co or Mg version, respectively (Dietzel et al., 2005; Dietzel et al., 2009).

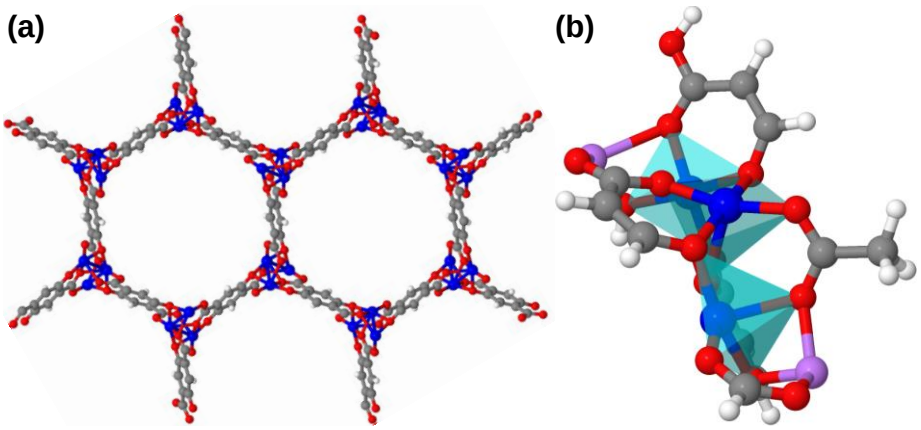

Figure 5.4. (a) CPO-27-Co framework. (b) Model I(Co) on which the *ab initio* calculations of reference data for force-field parameterization were performed. Colour code: white, hydrogen; grey, carbon; red, oxygen; purple, lithium; and blue, cobalt.

The generation of *ab initio* reference data for parameterization of the CO_2 – CPO-27-Co force field closely followed the computational procedure described in Section 4.6; that is, adopting the same calculation setups, unless explicitly stated otherwise. The chosen model cluster (Figure 5.4 (b)) for the CPO-27-Co framework is of the same size as the one (Model I) used for CPO-27-Mg, hence denoted as Model I(Co) hereafter. To construct the cluster, the experimental crystal structure of CPO-27-Co (Dietzel et al., 2005) was first subject to geometry optimization using periodic DFT at the GGA-PBE level with the CASTEP (version 5.501) simulation package (Clark et al., 2005). The minimum energy was obtained for a hexagonal unit cell with lattice parameters $a = b = 25.401$ Å, and $c = 6.580$ Å, which are in good agreement with the experimental unit cell: $a = b = 25.885$ Å, and $c = 6.806$ Å (Dietzel et al., 2005). The optimized Co–O bond distances (with differences between simulation and experiment given in parentheses) in one 5-coordinated, square-pyramidal cus are 1.861 (-6.4%), 2.000 (-3.3%), 1.922 (-3.8%), 1.961 (-3.0%), and 2.185 (+5.1%) Å, in fairly good agreement with the corresponding experimental values of 1.989, 2.068, 1.997, 2.022, and 2.079 Å in the dehydrated CPO-27-Co crystal (Dietzel et al., 2005). Model I(Co) was thereafter carved out from the PBE-optimized structure thus obtained, with all dangling bonds saturated by hydrogen or lithium atoms, following the same treatment as used for Model I of CPO-27-Mg. The structure of Model I(Co) was further relaxed using the B3LYP/Def2-TZVPP method, with all of the Co and O atoms belonging to the cus's fixed at the PBE-optimized positions.

All gas-phase calculations – namely, geometry optimization, single-point energy, and wavefunction-stability test (via the Stable job) – on Model I(Co) were carried out with Gaussian 09 programme (Frisch et al., 2009). Spin-

polarized (unrestricted) DFT methods (i.e., UB3LPY and UB2PLYP-D2) were used, together with a convergence of the SCF procedure to a broken-symmetry wavefunction (via keyword Guess=Mix). Tight convergence criteria were imposed on all geometry-optimization calculations (Opt=Tight), and an ultra-fine grid was used for numerical integrations in all calculations throughout, via Integral(Grid=UltraFineGrid). In addition, to ensure quality of the SCF solution, the control of the functioning of the SCF procedure adopted here (and for the Cu cluster discussed below) closely followed a DFT study of 3*d* transition metal hydrides by Goel and Masunov (2008). That is, the keywords SCF=Fermi and IOp(5/22=5) were used to request the "FON" version of Fermi temperature broadening during early SCF iterations (Rabuck and Scuseria, 1999). When necessary, the stability of the thus-obtained unrestricted DFT wavefunction was tested by "Stable" calculations, and the wavefunction was re-optimized (Stable=Opt) if any instability was found.

The choice of spin multiplicity for Model I(Co) in gas-phase DFT calculations needs to be carefully justified, as the number of unpaired electrons for one Co(II) ion can be either 1 (low-spin) or 3 (high-spin), resulting in, respectively, a multiplicity of 4 or 10 for Model I(Co) (containing three Co atoms). With either of the two feasible multiplicities (4 and 10), the structure of Model I(Co) was first optimized using the UB3LYP/Def2-TZVPP method, followed by a single-point energy calculation on the final, geometry-optimized Model I(Co) at the UB2PLYP-D2/Def2-TZVPP level of theory (using the same multiplicity as in the corresponding geometry optimization). The stability tests of the two UB2PLYP-D2 wavefunctions (with a multiplicity of either 4 or 10) confirmed that no internal instability existed in either of the SCF solutions.

However, the high-spin state of Model I(Co) was chosen over the low-spin state for *ab initio* reference calculations for the following two reasons. First, the low-spin state (multiplicity = 4) was found to have a higher internal energy than its high-spin (multiplicity = 10) counterpart by 46 kcal mol^{-1}. Second, the spin contamination in the low-spin UB2PLYP-D2 wavefunction is serious. The presence of significant spin contamination in the low-spin wavefunction was established by comparing the total spin, $\langle S^2 \rangle$, of the converged SCF solution to the value of $S(S+1)$ where S = ½ × (number of unpaired electrons) – no spin contamination is present if $\langle S^2 \rangle = S(S+1)$. The low-spin wavefunction was, however, found to have a $\langle S^2 \rangle$ of 4.65 (after annihilation), which is markedly larger than 3.75 (= $S(S+1)$, where S = 3/2). Since spin contamination often leads to arbitrary changes in the computed total energies (an artefact of incorrect wavefunctions as discussed by Perdew et al. (2009) and Tafipolsky et al. (2010), for example), the resulting ambiguous differences in energy between calculations would adversely affect the use of these energy data as a reference for force-field parameterization. In contrast to the low-spin state, a negligible spin contamination was found in the high-spin UB2PLYP-D2 wavefunction (multiplicity = 10), as the final $\langle S^2 \rangle$ = 24.7501 (24.77 before annihilation), which almost equals $S(S+1)$ = 24.75 (S = 9/2). This observation of Co(II) adopting a high-spin state in Model I(Co) is in line with the finding made by Zhou et al. (2008), where S = 3/2 (high-spin) was confirmed to be the only possible spin state for each Co(II) ion in the CPO-27-Co framework. Therefore, from this point onwards, all DFT calculations on Model I(Co) (and on Model I(Co) with CO_2) were done with a multiplicity of 10 (S = 9/2) – the cluster consists of three Co(II) ions, each containing three unpaired electrons (S = 3/2).

Ab initio potential energies of different relative configurations between a CO_2 molecule and Model I(Co) were calculated by the UB2PLYP-D2/Def2-TZVPP method, using the thus-far described combination of SCF=Fermi, IOp(5/22=5), Guess=Mix, and Integral(Grid=UltraFineGrid); the multiplicity of the CO_2···Model I(Co) complex is 10. For all gas-phase calculations on this complex, one more measure was used to ensure consistency of SCF solution for all geometries. As pointed out by Goel and Masunov (2008), for systems with nearly degenerate energy levels (which is often true for compounds containing transition metals), there is a danger of obtaining distinctly different SCF solutions at different interatomic distances. That is, when moving a CO_2 molecule away from Model I(Co), different SCF solutions could be obtained for different separations between the two monomers, thus making the energy differences no longer reflect the interaction energy between the two as a function of the intermolecular distance. In order to build potential energy curves (PECs) in a self-consistent manner, the procedure depicted in Figure 5.5 was repeated for each of the sampling "approach routes", where a CO_2 molecule was moved toward and away from the Co(II) cus with a particular orientation.

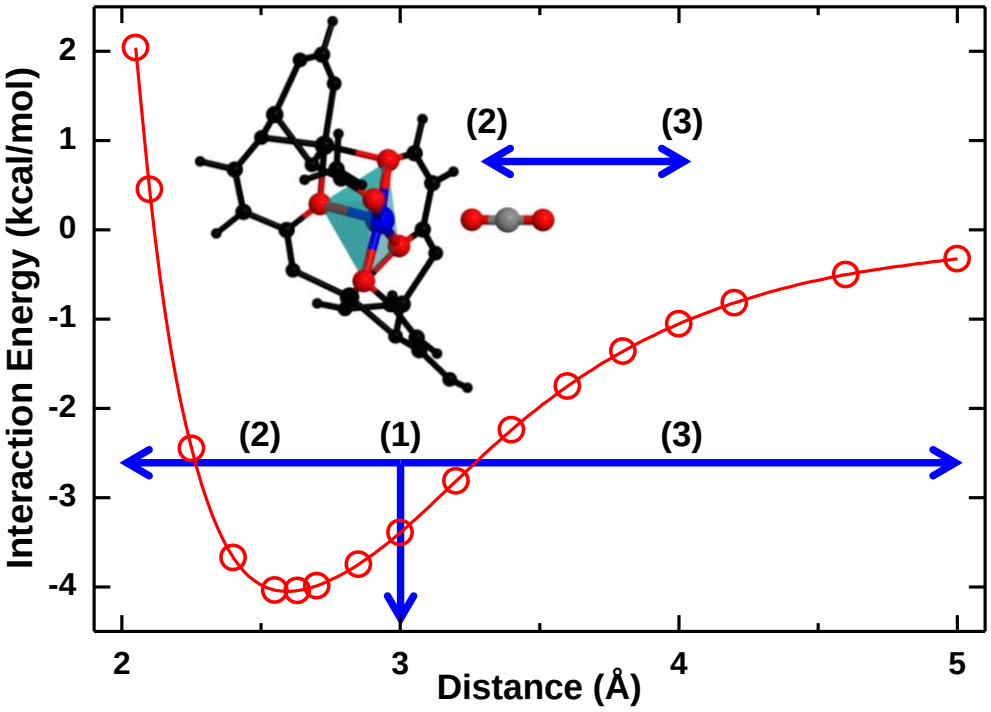

Figure 5.5. Procedure used to construct the potential energy curve (PEC) for the relative configuration of CO_2···Model I(Co) shown in the inset, with the arrows indicating the varying separations between the two monomers. Step (1): single-point energy evaluation, followed by a stability test. Steps (2) and (3): scan along the PEC with, respectively, decreasing and increasing interatomic distance between the Co(II) cus and the nearby O(CO_2). The line was added to guide the eye.

Take the "end-on" configuration in Figure 5.5 as an example. A single-point energy calculation (step 1) is first performed on the CO_2···Model I(Co) complex where the distance between the nearby O(CO_2) and the Co is 3.0 Å, a choice guided by the sum of the vdW radii of Co and O being ca. 3.0 Å. The "starting" separation distance (i.e., 3 Å in this case) is not expected to affect the final, computed PEC, but rather is chosen for the sake of consistency for all "approach routes" of CO_2···Model I(Co). The wavefunction obtained in the single-point calculation (i.e., O(CO_2)–Co distance: 3.0 Å) is then checked and re-optimized if found unstable (step 1). Using the SCF solution thus confirmed stable as an initial guess, the PEC is constructed by two "Scan" calculations (steps 2 and 3), each of which comprises a number of single-point energy evaluations over a stepped increase (step 3) or decrease (step 2)

in the O(CO_2)–Co distance. In other words, during the PEC scans, each single-point energy calculation takes the SCF solution from the proceeding one as the initial guess. It is clear from Figure 5.5 that the PEC constructed in this approach does not exhibit any observable discontinuities. PECs for the different "approach routes" of a CO_2 molecule to Model I(Co) were checked and confirmed to be smooth.

A set of 130 relative configurations of CO_2···Model I(Co) were explicitly evaluated by *ab initio* calculations to sample the potential energy surface in the vicinity of the "central" cus, following the procedure detailed in Section 4.6.2. Primarily sampled are "approach routes" where either O(CO_2) or C(CO_2) is in close contact with the Co(II) cus, as these configurations are important for force-field parameterization described below. As for the CO_2···Model I complex, the CO_2···Model I(Co) interaction energy may be calculated by Equation 4.12, adopting frozen-monomer approximation. Here, however, it is given alternatively by

$$E_{\text{int}} = E\left(\text{CO}_2 \cdots \text{Model I(Co)}\right) - E\left(\text{CO}_2 \cdots \text{Model I(Co)}\right)_{R=\infty} \tag{5.7}$$

where E and $E_{R=\infty}$ are the total energies of the CO_2···Model I(Co) complex at a given intermolecular distance, R, and in "infinite" separation (R = 1000.0 Å), respectively. It is worth noting that $E\left(\text{CO}_2 \cdots \text{Model I(Co)}\right)_{R=\infty}$ at a large enough separation (like the 1000.0-Å distance chosen here) is almost identical to the value of $E\left(\text{CO}_2\right) + E\left(\text{Model I(Co)}\right)$; that is, Equations 4.12 and 5.7 can be considered equivalent in calculating interaction energies. Indeed, it was found that the biggest discrepancy between the calculated energies using the two equations was 1.3% among all of the 130 configurations. Equation 5.7 was chosen here, again, aiming at making sure that SCF solution is consistent

for all points in the PEC. The energy of CO_2···Model I(Co) at "infinite" separation – rather than the sum of the energies of two frozen monomers – is the reference state for building the PEC and the energy of this state is also calculated using the same initial guess of wavefunction as any other points in the PEC.

5.3.2 Force-field fitting

The force field proposed here describes all interatomic interactions involved in the CO_2···Model I(Co) complex using the sum of electrostatic interaction calculated by the Coulomb potential and vdW interaction represented by the MMSV potential, except that the CO_2–Li interaction is determined according to the $E_{\mathrm{vdW}}^{\mathrm{Sholl}}$ expression (Equation 5.5). The force field is denoted as AIFF-G2(Co), since its potential expressions, as well as its atom-type definitions, are all in analogy to the AIFF-G2 force field for CO_2 – CPO-27-Mg. Moreover, the AIFF-G2 parameters for interactions between CO_2 and non-cus atoms (i.e., H, C, O, and Li) are directly transferred to AIFF-G2(Co). These parameters are used for CO_2···Model I(Co) (and for CO_2 – CPO-27-Co in GCMC simulations) by scaling the corresponding interatomic energies of AIFF-G2 with a global scaling factor s_{ener}, which was found by the force-field fitting. For example, the interaction potential of the O(CO_2)–H(Model I(Co)) pair is given by $E_{\mathrm{vdW}}^{\mathrm{AIFF-G2(Co)}} = s_{\mathrm{ener}} E_{\mathrm{vdW}}^{\mathrm{AIFF-G2}}$. The MMSV parameters for the O(CO_2)–Co and C(CO_2)–Co interactions were all fitted independently. Table 5.2 lists all AIFF-G2(Co) parameters, only 11 of which were determined in the force-field fitting with the others taken from either AIFF-G2 or the DFT-D2 method (Grimme, 2006).

Table 5.2. AIFF-G2(Co) for CO_2 – CPO-27-Co.[a]

force-field type	Co	O1	O2	C1	C2	C3	H
				O(CO_2) [b]			
D_{eq} [c] (kcal mol^{-1})	0.957	0.146	0.117	0.118	0.118	0.114	0.072
R_{eq} [d] (Å)	2.845	3.460	3.494	3.448	3.923	3.761	2.965
α_1 [d]	8.514	12.381	12.381	11.006	11.006	11.006	12.016
α_2 [d]	13.890	13.301	13.301	13.115	13.115	13.115	12.016
C_6^{ij} [e] (kcal mol^{-1} Å^6)	430.413	167.304	167.304	264.531	264.531	264.531	74.821
				C(CO_2) [b]			
D_{eq} [c] (kcal mol^{-1})	0.189	0.096	0.083	0.075	0.076	0.079	0.038
R_{eq} [d] (Å)	3.475	3.549	3.407	3.600	3.498	3.489	3.203
α_1 [d]	10.314	11.006	11.006	12.954	12.954	12.954	10.403
α_2 [d]	12.306	13.115	13.115	11.866	11.866	11.866	10.403
C_6^{ij} [e] (kcal mol^{-1} Å^6)	576.412	264.531	264.531	418.260	418.260	418.260	118.302

[a] The MMSV potential in AIFF-G2(Co) is in the form of Equation 5.4. The value of s_{ener} was found to be 0.970, resulting in a value of 0.800 for s_6^{FF} given by $s_{\text{ener}} \times 0.825$ (the s_6^{FF} value in AIFF-G2). R_2 was fixed at $1.6 \cdot R_{eq}$ in all MMSV calculations. [b] The MMSV cross-terms for O(CO_2)–MOF interactions, followed by the cross-terms for C(CO_2)–MOF interactions. [c] Except for $D_{eq}^{\text{O}(\text{CO}_2)-\text{Co}}$ and $D_{eq}^{\text{C}(\text{CO}_2)-\text{Co}}$ that were fitted, each of the values listed was obtained by multiplying the corresponding one in AIFF-G2 by s_{ener} (= 0.970). [d] Except for the fitted Co-related values, the parameters are the same as the corresponding ones in AIFF-G2. [e] The pairwise dispersion coefficients, C_6^{ij}, were taken from the DFT-D2 correction (Grimme, 2006), except that the $C_6^{\text{O}(\text{CO}_2)-\text{Co}}$ and $C_6^{\text{C}(\text{CO}_2)-\text{Co}}$ were fitted independently. The CO_2–Li interactions – involved in CO_2 interacting with Model I(Co) but not in CO_2 with the CPO-27-Co framework – were described by Equation 5.5 in the force-field fitting and s_{12}^{FF} used was 6.500 (the value from AIFF-G2). The CO_2–Li parameters are given in Table 5.1 and were omitted here for clarity.

5.3.3 Force-field validation and GCMC simulations

The AIFF-G2(Co) parameters in Table 5.2 yield a very good reproduction of the whole range of *ab initio* data (Figure 5.6). The RMSD value between force-

field predictions and *ab initio* reference is only 0.15 kcal mol^{-1} for the whole set of 130 configurations.

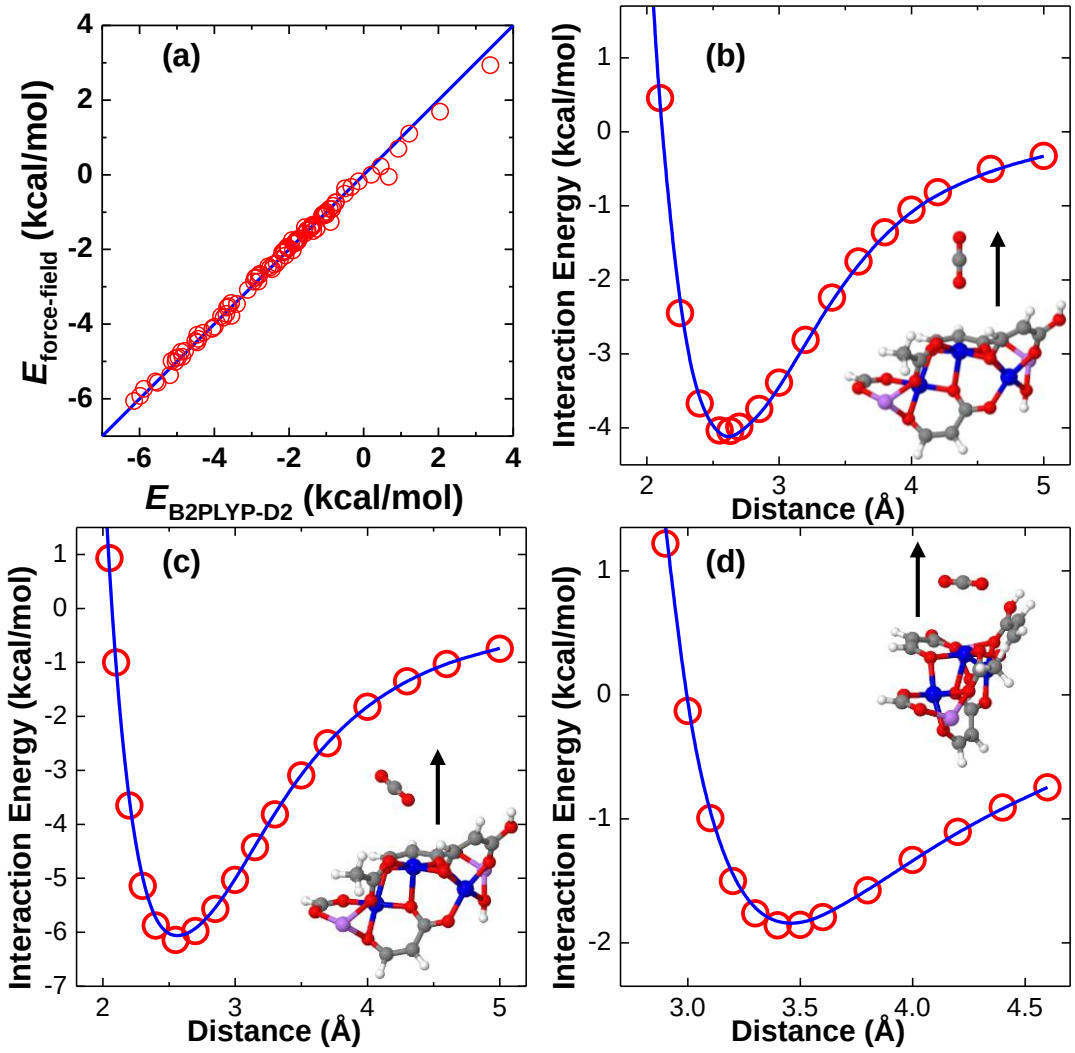

Figure 5.6. Comparison of CO_2···Model I(Co) interaction energies obtained by the UB2PLYP-D2/Def2-TZVPP method and the force field (Table 5.2). (a) 130 configurations in the training set for the force-field parameterization. (b, c, d) For the different relative configurations shown in the insets, force-field predictions (blue line) and *ab initio* reference data (red circle) were plotted as a function of the separation distance, with the arrow indicating the direction of the CO_2 molecule moving away from Model I(Co).

The *ab initio* interaction energies generated for the three "approach routes" shown in Figure 5.6 (b, c, d) are all reproduced very well by AIFF-G2(Co). Furthermore, it is worth noting that all of the three *ab initio* PECs are smooth; a "trough" or a "peak" would indicate a switch from one SCF solution to

another (which is not observed here), leading to physically meaningless energy differences (Goel and Masunov, 2008). This confirms the robustness of the computational setup and procedure adopted, hence indicating a good quality of these energy data as a reference for force-field parameterization.

To obtain partial atomic charges for the CPO-27-Co framework, the same cluster models as those for CPO-27-Mg (Figure 4.12) were used for calculations, performed at the B3LYP/Def2-TZVPP level of theory. The MK scheme was used to derive partial charges, in conjunction with IOp(6/41=15,6/42=27,6/43=15) to ensure a sampling grid of ca. 2000 points per atom. The partial atomic charges for CPO-27-Co are reported in Table 5.3.

Table 5.3. Partial atomic charges[a] and force-field atom types[b] for CPO-27-Co.

atom	Co	Oa	Ob	Oc	Ca	Cb	Cc	Cd	H
q (e)	1.3791	-0.8042	-0.7591	-0.7856	0.9266	-0.3358	0.3851	-0.1768	0.1707
type	Co	O1	O1	O2	C1	C2	C3	C2	H

[a] The vdW exclusion radii for the Co, O, C, and H atoms are 1.562, 1.342, 1.452, and 1.001 Å, respectively. [b] Force-field atom types as defined in Table 5.2.

With the partial atomic charges thus obtained and the force-field parameters listed in Table 5.2, CO_2 adsorption in the CPO-27-Co framework was studied by GCMC simulations, performed at 298 K (Figure 5.7). For comparison, a combination of UFF (with TraPPE describing CO_2) and the charges in Table 5.3 was also used to simulate CO_2 adsorption in this MOF at 298 K.

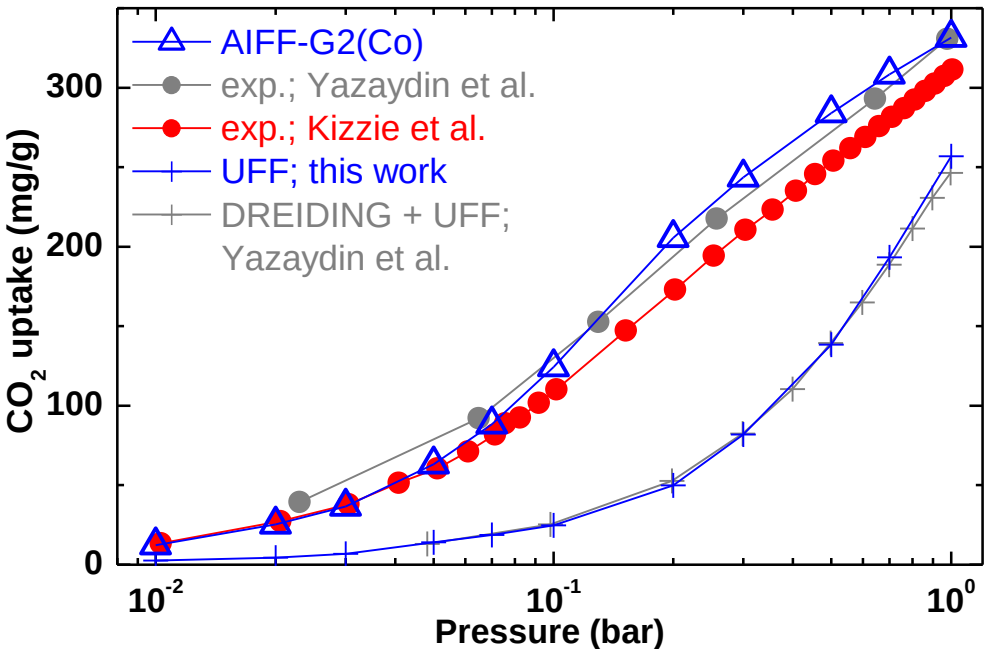

Figure 5.7. Comparison of CO_2 adsorption isotherms at 298 K in the CPO-27-Co MOF between simulation and experiment (Yazaydın et al., 2009; Kizzie et al., 2011). Note that the isotherms are represented on a logarithmic pressure axis to better show the adsorption behaviour at low pressure and the lines were added to guide the eye.

The situation here clearly resembles that previously described for CO_2 adsorption in CPO-27-Mg (Figure 5.2). Because of the presence and the high density of the Co(II) cus's, the generic force fields (DREIDING and UFF) were, again, found to substantially underestimate the amounts adsorbed up to atmospheric pressure at 298 K. This is also true for the Ni and Zn versions of the CPO-27 family, as reported by Yazaydın et al (2009). In contrast, the AIFF-G2(Co)-based simulation results are in very good agreement with the experimental measurements (Yazaydın et al., 2009; Kizzie et al., 2011) for the whole pressure range from 0.01–1 bar. At much higher pressures (not shown in Figure 5.7), AIFF-G2(Co) and the generic force fields perform equally well in terms of predicting CO_2 uptakes in CPO-27-Co, since pore-filling effect plays an increasingly important role as the CO_2 partial pressure rises. The isosteric heat of adsorption that corresponds to 1 CO_2/Co, calculated from the GCMC simulation based on AIFF-G2(Co), is 7.7 kcal mol^{-1}, which is

comparable to experimental values – for example, Caskey et al. (2008) reported a value of 8.3 kcal mol^{-1} for CO_2 adsorption in this MOF. It is noteworthy that the lower CO_2 uptakes (in both gravimetric and CO_2 per unit cell terms) in CPO-27-Co, compared to its Mg counterpart (Figures 5.2 and 5.7), are in line with the understanding that the affinity of the Co(II) cus towards CO_2 is weaker than that of Mg(II), which has been shown in the literature both experimentally (Caskey et al., 2008) and theoretically (Park et al., 2012).

In summary, the significantly improved predictions of CO_2 adsorption in both CPO-27 MOFs, compared to those based on the generic force fields, are encouraging. In particular, the AIFF-G2 parameters (derived for CO_2 – CPO-27-Mg), augmented by only one global scaling factor (s_{ener}), yield a very accurate description of the interactions between CO_2 and non-metal atoms in CPO-27-Co. Put precisely, AIFF-G2(Co), with majority of the parameters directly taken from AIFF-G2 and parameters specifically derived for CO_2–Co, is able not only to reproduce the *ab initio* CO_2···Model I(Co) data but also to predict CO_2 adsorption in the CPO-27-Co framework in quantitative agreement with experiment. This demonstrates that the force-field parameters exhibit a marked degree of transferability. It is hereby expected that force-field extension to another CO_2 – CPO-27-M (e.g., M = Ni) system should be straightforward and fast, as only ca. 100 *ab initio* calculations on a representative model are needed to derive new force-field parameters for CO_2–metal interaction and s_{ener}. Furthermore, the computational setups and procedures presented – especially concerning treatment of transition metals in DFT calculations and construction of self-consistent PECs – can be considered to be generally applicable to force-field parameterization, which is demonstrated further below.

5.4 Force Field for CO_2 – MOFs with $Cu_2(O_2CR)_4$

As discussed in the Introduction to this Chapter, parameterizing a force field using *ab initio* data based on the building-block approach can be computationally advantageous over developing force fields for specific MOFs separately. More likely than not, force-field parameters derived for a particular adsorbate–building block complex can be readily applied to MOFs built of that same building block. To be precise, the underestimation of sorbate uptakes in MOFs with cus's by GCMC simulations based on generic force fields may be (partly) resolved by only deriving new force-field parameters for the adsorbate–cus interaction. To realize this, the cus-containing building block can be "isolated" from the framework and *ab initio* calculations of the adsorbate interacting with a model cluster representing the cus can then be performed. This idea is demonstrated here by means of improving predictions of CO_2 adsorption in the CuBTC MOF through a combined force field approach. That is, in the GCMC simulation of CO_2 adsorption in CuBTC, the CO_2–$Cu_2(O_2CR)_4$ interaction is described by an *ab initio* parameterized MMSV potential, and the CO_2 interactions with other framework atoms are determined by literature force fields.

5.4.1 Model cluster and *ab initio* reference data

A number of dimeric copper(II) tetracarboxylates of different size have been used in *ab initio* calculations to represent the copper paddle-wheel $Cu_2(O_2CR)_4$ building block in the CuBTC framework. For instance, the basic dicopper tetraformate (R = H) was used by Tafipolsky et al. (2010) in the parameterization of a flexible molecular-mechanics force field for MOFs with copper paddle-wheel units. Similarly, the formate cluster was adopted by

Grajciar et al. (2010) in their high-level CCSD(T) calculations to understand water adsorption on the cus's of CuBTC. Larger dicopper clusters, such as the benzoate (R = C_6H_5) and 1,3,5-benzene-tricaboxylate (R = $C_6H_3(CO_2H)_2$) models, have been used to derive force-field parameters for adsorbate–Cu(II) interactions (Fischer et al., 2010; Fischer et al., 2012). In both cases, pure DFT calculations at the PBE level were used to determine the interaction energies between the adsorbate (dihydrogen or ethylene) and the Cu(II) cus, despite that the intermolecular interactions were of concern – which normally requires a higher level of theory than pure DFT. The level of theory – PBE/DNP (DNP: a double-ζ plus polarization quality basis set) – chosen in those two studies allowed for calculations on systems of such large sizes. The B2PLYP-D2/Def2-TZVPP method to be utilized here, however, necessitates the use of a relatively small model cluster. It should be noted that properly accounting for the dispersive interaction between a CO_2 molecule and a chosen model cluster is of crucial importance to the force-field parameterization proposed in this work, while such interaction was not the primary aim for DFT calculations in the work of Fischer et al (2012).

Tafipolsky et al. (2010) carefully investigated the effect of cluster size on the quality of DFT-optimized structure, and concluded that even the formate model, $Cu_2(O_2CH)_4$, could be used as a reference for their force-field parameterization. Taking account of their findings, the dicopper tetraacetate cluster, $Cu_2(O_2CCH_3)_4$, was chosen for *ab initio* calculations of reference data. The acetate model was found to be a good compromise between size of the reference structure and tractable computation at the desired level of theory. A comparative UB2PLYP-D2/Def2-TZVPP calculation on the benzoate $Cu_2(O_2CC_6H_5)_4$ model confirmed that it would be unmanageable to perform 100s of such calculations given the computing power available. Furthermore,

in parameterization of *ab initio* $CO_2\cdots Cu_2(O_2CC_6H_5)_4$ interaction energy, force-field parameters, such as $O(CO_2)$–C(benzoate), would need to be definined and fitted. This is not intended here, because this Section investigates the feasibility of combining *ab initio* derived CO_2–cus parameters with literature force fields to improve predictions of CO_2 adsorption in MOFs with Cu(II) cus's. It is worth noting that the *ab initio* calculations carried out here were primarily used to provide energy data for the CO_2–model cluster interactions. That is, compared to computing forces and vibrational frequencies, energy calculations are theoretically less "demanding" and hence are less likely to be prone to systematic errors induced by the simplified cluster representation.

The geometry of the acetate $Cu_2(O_2CCH_3)_4$ cluster, denoted as Model(Cu) hereafter, was fully relaxed at the UB3LYP/Def2-TZVPP level of theory, using the same protocol for SCF solution as described for Model I(Co) in Section 5.3.1. In brief, SCF=Fermi, IOp(5/22=5), Guess=Mix, and Integral(Grid=UltraFineGrid). Model(Cu) was in a triplet electronic state in all *ab initio* calculations, in accordance with the common treatment adopted for dicopper paddle-wheel clusters, for example, by Grajciar et al. (2010) and Tafipolsky et al (2010). The minimum energy was found for Model(Cu) in a geometry with selected bond distances and angle shown in Figure 5.8 (a). The UB3LYP/Def2-TZVPP-optimized Cu–Cu distance of 2.503 Å is in good agreement with the one (2.495 Å at 100 K) found in a fully desolvated CuBTC framework reported by Wu et al (2008). For comparison, the experimentally determined Cu–O and O–C1 distances, and O–C1–O angle are 1.933 and 1.263 Å, and 125.47 °, respectively (Wu et al., 2008). On the basis of the good agreement between optimized and experimental geometries, Model(Cu) is thus considered as a good representation of the dicopper paddle-wheel building block in the CuBTC framework.

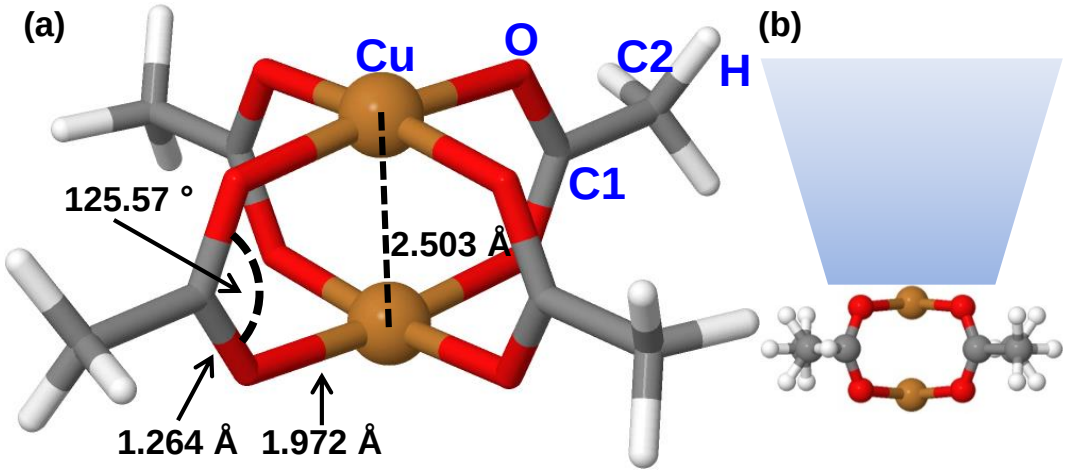

Figure 5.8. (a) Model(Cu) in C_{4h}-symmetry, with selected bond distances and angle from the UB3LYP/Def2-TZVPP-optimized geometry (Opt=Tight). Also shown are definitions of atom types that are used in the force-field parameterization. The partial atomic charges of Cu, O, C1, C2, and H, respectively, are 1.1852 (1.562), -0.6958 (1.342), 0.8752 (1.452), -0.5178 (1.452), and 0.1472 (1.001). The corresponding vdW exclusion radii in Å are given in the parentheses, which were taken as those of Grimme's (2006). (b) Illustration of the region (in light blue) where the CO_2···Model(Cu) potential energy surface was primarily sampled.

The atomic charge (1.1852) of Cu in Model(Cu) – derived by the MK method from fitting to the UB2PLYP-D2/Def2-TZVPP electrostatic potential on the UB3LYP/Def2-TZVPP-optimized structure – is comparable to that (1.16) of Cu in the formate cluster used by Tafipolsky et al (2010). The discrepancy can be attributed to the different choices made for cluster size, level of theory, and atomic vdW radii. The fair agreement between the charges of Cu in the two clusters provides further evidence that Model(Cu) is a valid model for force-field parameterization.

The *ab initio* CO_2···Model(Cu) interaction energies, reference data for force-field parameterization, were calculated at the UB2PLYP-D2/Def2-TZVPP level of theory for different CO_2···Model(Cu) configurations generated in accord with the scheme detailed in Section 4.6.2 (Figure 4.8). Here, fewer *ab initio* calculations were needed to properly sample the PES in the vicinity of the Cu(II) cus because of the higher symmetry of Model(Cu). Moreover, the

sampled relative configurations mostly concentrate on a CO_2 molecule "exploring" the PES of CO_2···Model(Cu) with respect to the square-planar CuO_4 coordination (Figure 5.8 (b)). In other words, CO_2···Model(Cu) configurations, in which the CO_2 is only in close contact with the methyl group(s) and is away from the cus, were not considered. The main reason is that there is no need to derive new force-field parameters for these atom pairs, e.g., O(CO_2)–H(methyl), as they are not involved in GCMC simulations of CO_2 adsorption in CuBTC. The treatment of these atom pairs in the force-field fitting is discussed below.

For each of the "approach routes" sampled, the CO_2···Model(Cu) PEC was constructed following the procedure described in Section 5.3.1 (Figure 5.5), carefully ensuring consistency of the SCF solutions as the PEC was scanned. In brief, the stability of the wavefunction obtained in the first single-point calculation was checked and re-optimized if found unstable. The CO_2 molecule was then moved away or towards the cus; each of the following energy evaluations was done using the proceeding SCF solution as the initial guess. The energy of CO_2···Model(Cu) in an intermolecular separation of 1000.0 Å was taken as reference – which was calculated for each particular "approach route" – in constructing the PEC (Equation 5.7). A total of 19 routes were sampled for the CO_2···Model(Cu) complex, amounting to 290 *ab initio* data points for force-field parameterization.

5.4.2 Force-field fitting and validation

The *ab initio* CO_2···Model(Cu) interaction energies thus obtained are approximated by herein proposed force field using pairwise additive sum of electrostatic and vdW potentials for all interatomic interactions between a

CO_2 molecule and Model(Cu). Considering (primarily) the force-field parameters required for GCMC simulations of CO_2 in CuBTC and the configurations sampled *ab initio*, the interatomic interactions involved in CO_2···Model(Cu) are calculated differently.

Firstly, the C(CO_2)–Cu, O(CO_2)–Cu, C(CO_2)–O, and O(CO_2)–O vdW interactions are modelled by the MMSV potential in the form of Equation 5.4 (atom definitions in Figure 5.8 (a)). Secondly, in fitting of MMSV potentials for the C(CO_2)–C1 and O(CO_2)–C1 atom pairs, the following two constraints were imposed: (1) $\alpha_1 = \alpha_2$; and (2) $R_{eq}^{C(CO_2)-C1} = 3.55$ Å and $R_{eq}^{O(CO_2)-C1} = 3.70$ Å. The chosen values in the second constraint were guided by the corresponding values determined by commonly used generic force fields. That is, the TraPPE CO_2, together with DREIDING, UFF, or OPLS-AA representing C1, (respectively) gives an equilibrium distance (R_{eq}) of 3.52 (3.66), 3.50 (3.64), or 3.68 (3.82) Å for the C(CO_2)–C1 (O(CO_2)–C1) atom pair. The reason for imposing these two constraints in the force-field fitting is that the C1 atoms, carboxylate carbon atoms in Model(Cu), are "buried" inside the cluster and the sampled region (Figure 5.8 (b)) does not encompass areas where a CO_2 molecule can be in close enough contact with a C1 atom to "feel" the inner repulsion-wall between the two. As a result, a varying $R_{eq}^{C(CO_2)-C1}$ or $R_{eq}^{O(CO_2)-C1}$ in the fitting would be determined ambiguously – neither would α_1, stiffness parameter of the MMSV potential in the repulsive region, be fitted properly. Indeed, fixing both parameters at the given values was found not only to yield a good fit to the *ab initio* reference data but also to ensure sensible values for (the other) parameters that needed fitting.

Finally, the probe CO_2 molecule was located, in most cases, even farther away from the methyl groups than from the C1 atoms in the sampled region (Figure 5.8 (b)). Thus, the C(CO_2)–C2, O(CO_2)–C2, C(CO_2)–H, and O(CO_2)–H vdW interactions were calculated by the $E_{\mathrm{vdW}}^{\mathrm{Sholl}}$ expression (Equation 5.5) in the force-field parameterization. The atom-pairwise C_6^{ij} coefficients were taken directly from the DFT-D2 scheme (Grimme, 2006) and the corresponding C_{12}^{ij} values were given by Equation 5.6. Thus, only the value of s_{12}^{FF} needed to be fitted when using $E_{\mathrm{vdW}}^{\mathrm{Sholl}}$ to describe the CO_2–C2 and CO_2–H vdW interactions. In summary, this combination of model potentials – MMSV for CO_2 interactions with Cu, O, and C1 (with constraints) and $E_{\mathrm{vdW}}^{\mathrm{Sholl}}$ for CO_2 interactions with C2 and H – results in a total of 24 force-field parameters to be fitted independently on the basis of 290 *ab initio* reference data points.

The force-field parameters (Table 5.4) thus determined reproduce the *ab initio* CO_2···Model(Cu) interactions with a high accuracy, giving an RMSD value of 0.15 kcal mol^{-1} between the two for the whole set of configurations. A more detailed picture of the good performance of the force field can be gained from Figure 5.9. It is clearly demonstrated in Figure 5.9 (c, d) that the force-field parameters can accurately reproduce the *ab initio* reference data for both the enhanced attraction between O(CO_2) and Cu(II) cus and the strong repulsion between C(CO_2) and Cu(II) cus.

Table 5.4. Force-field parameters for CO_2 – $Cu_2(O_2CR)_4$.[a]

force-field type	Cu	O	C1	
		$O(CO_2)$ [b]		
D_{eq} (kcal mol^{-1})	1.490	0.103	0.107	
R_{eq} (Å)	2.861	3.593	3.700	
α_1	7.870	11.933	12.501	
α_2	15.037	13.078	12.501	
C_6^{ij} [c] (kcal mol^{-1} Å^6)	569.313	167.304	264.531	
		$C(CO_2)$ [b]		
D_{eq} (kcal mol^{-1})	0.123	0.065	0.063	
R_{eq} (Å)	3.800	3.647	3.550	
α_1	10.004	10.613	10.227	
α_2	11.330	12.588	10.227	
C_6^{ij} [c] (kcal mol^{-1} Å^6)	620.388	264.531	418.260	
	$O(CO_2)$–C2 [d]	$C(CO_2)$–C2 [d]	$O(CO_2)$–H [d]	$C(CO_2)$–H [d]
C_6^{ij} [c] (kcal mol^{-1} Å^6)	264.531	418.260	74.821	118.302
C_{12}^{ij} [c] (kcal mol^{-1} Å^{12})	62922.328	125428.448	6189.066	12886.847

[a] The MMSV potential for this force field is in the form of Equation 5.4, and the value of s_6^{FF} was found to be 0.821. R_2 was fixed at $1.6 \cdot R_{eq}$ for all atom pairs. [b] The MMSV cross-terms for $O(CO_2)$ – $Cu_2(O_2CR)_4$ interactions, followed by the cross-terms for $C(CO_2)$ – $Cu_2(O_2CR)_4$ interactions. [c] The pairwise dispersion coefficients, C_6^{ij}, were taken from the DFT-D2 correction (Grimme, 2006), except that the $C_6^{O(CO_2)-Cu}$ and $C_6^{C(CO_2)-Cu}$ were fitted independently. The C_{12}^{ij} values were calculated by Equation 5.6 using 1.452 and 1.342 Å for the vdW radii of C and O, respectively (Grimme, 2006). [d] These interactions were described by Equation 5.5, and s_{12}^{FF} was fitted to a value of 2.300.

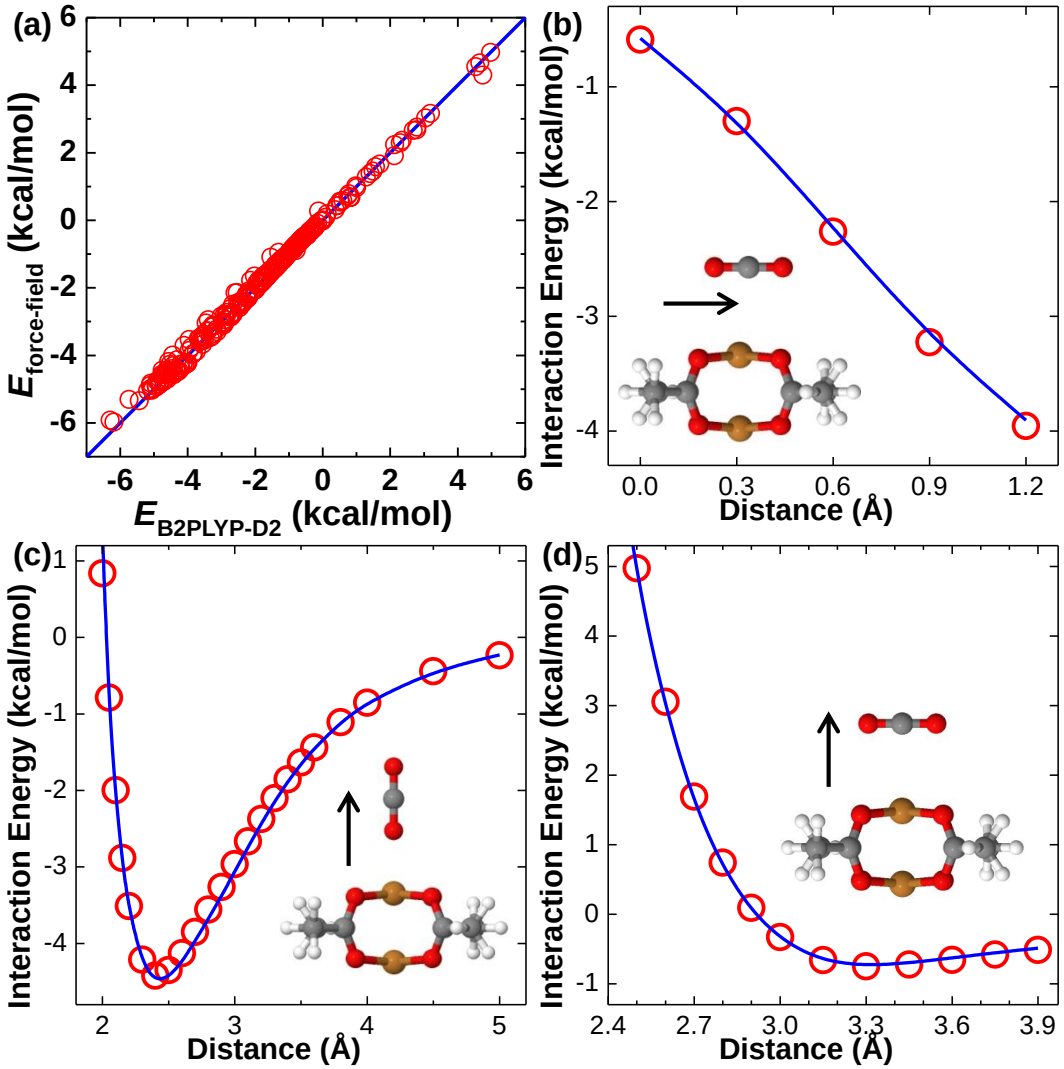

Figure 5.9. Comparison of CO_2···Model(Cu) interaction energies obtained by the UB2PLYP-D2/Def2-TZVPP method and the force field (Table 5.4). (a) 290 configurations used for fitting of 24 force-field parameters. (b, c, d) For the different relative configurations shown in the insets, force-field predictions (blue line) and *ab initio* reference data (red circle) were plotted as a function of the separation distance, with the arrow indicating the direction of the CO_2 molecule moving away from Model(Cu).

The D_{eq} value fitted for O(CO_2)–Cu is almost 50 times that of the same atom pair given by the combination of TraPPE and UFF force fields – 1.49 vs. 0.03 kcal mol^{-1}. This is not surprising, considering that the largely enhanced guest-molecule interaction with cus is not of a dispersion-dominant origin as discussed above. The PEC of the O(CO_2)–Cu pair was found to be similar to the one of O(CO_2)–Mg (Figure 5.3). That is, the attractive interaction between

the two atoms decreases very fast beyond the equilibrium distance, in line with the short-range nature of the CO_2 interaction with cus's. It is worth noting that Fischer et al. (2012) demonstrated an alternative approach to reproducing such enhanced, localized interactions associated with cus's. In order to compensate the lack of representation of commonly used generic force fields for describing the interactions between alkenes and the Cu(II) cus's in CuBTC, Fischer et al. (2012) added a DFT derived, specific attractive Cu–π interaction to augment the Cu–alkene interaction that was given by the generic classical force fields. These Cu–π interactions were switched off beyond a separation distance of 5.0 Å. Both approaches – using a piecewise potential or adding an extra term – have been demonstrated to be effective in terms of using classical model potentials to capture the deep-potential-well, short-range feature of adsorbate–cus interactions.

5.4.3 GCMC simulations

GCMC simulations using generic force fields. The primary objective, as set out at the beginning of the development of this CO_2 – $Cu_2(O_2CR)_4$ force field, is to assess the idea of combining *ab initio* parameterized force fields based on the building-block approach with literature ones (being either generic or *ab initio* derived) in GCMC simulations of CO_2 adsorption in MOFs with cus's. Before demonstrating the performance of this combined force field approach, it is important to establish first the performance of commonly used generic classical force fields, in order to place improved predictions from the proposed approach into perspective. To realize this in the context of MOFs with the copper paddle-wheel building block, CO_2 adsorption in the CuBTC framework was studied by GCMC simulations using three generic force fields, namely, DREIDING, OPLS-AA, and UFF. Note that force-field

parameters for the element Cu are only available in the UFF and hence were used in all three GCMC simulations to describe the interactions between Cu atoms and CO_2 molecules (represented by TraPPE). For ease of discussion, the potential-well depths for the CO_2–MOF interactions according to the different generic force fields are summarized in Table 5.5.

Table 5.5. Atom-pairwise D_{eq} values (in kcal mol^{-1}) determined by the generic force fields.[a]

	$O(CO_2)$			$C(CO_2)$		
MOF atom	DREIDING	UFF	OPLS-AA	DREIDING	UFF	OPLS-AA
H	0.049	0.083	0.069 (C_6H_6)	0.029	0.049	0.040 (C_6H_6)
C	0.122	0.128	0.128 (O_2CR) 0.102 (O_2CCR) 0.105 (C_6H_6)	0.071	0.075	0.075 (O_2CR) 0.060 (O_2CCR) 0.061 (C_6H_6)
O	0.123	0.097	0.182 (O_2CR)	0.072	0.057	0.106 (O_2CR)
Cu	n/a	0.028	n/a	n/a	0.016	n/a

[a] The LJ cross-terms of D_{eq} for $O(CO_2)$–MOF (left) and $C(CO_2)$–MOF (right) interactions, calculated by a geometric mean. The OPLS-AA force field defines atoms taking into account their hybridizations and/or coordination numbers; hence the OPLS-AA values listed here are followed by their atom types (given in parentheses) as defined in the force field.

Partial atomic charges of the CuBTC framework were determined on a representative cluster shown in Figure 5.10. The cluster was carved out from the experimental structure (Chui et al., 1999), with all dangling bonds saturated by hydrogen atoms. These added hydrogen atoms were geometry-optimized (B3LYP/TZVP) with respect to the fixed positions of the atoms from the experimental framework. The final single-point calculation was performed at the B3LYP/Def2-TZVPP level of theory, followed by the MK method fitting atomic charges to the first-principles electrostatic potential on a grid having a density of ca. 2000 points per atom. The resulting charges are reported in Table 5.6.

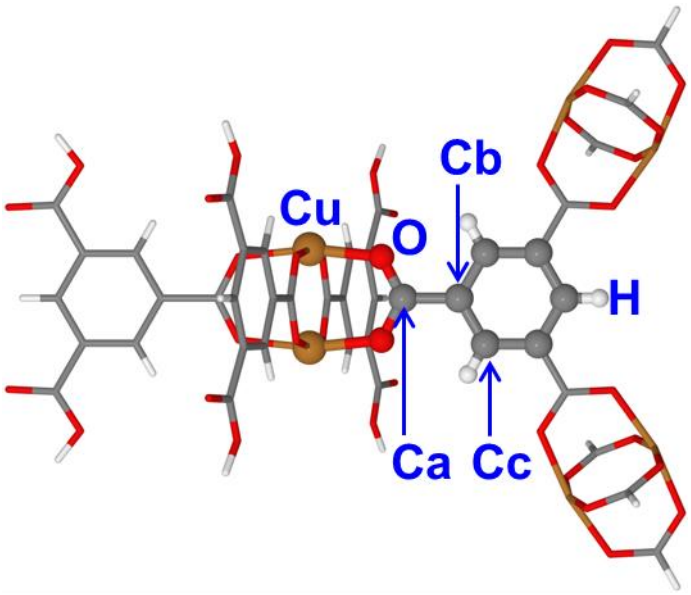

Figure 5.10. Cluster for calculation of partial charges for the CuBTC framework.

Table 5.6. Partial atomic charges for CuBTC.[a]

atom	Cu	O	Ca	Cb	Cc	H
q (e)	1.1334	-0.6464	0.7304	-0.0529	-0.1047	0.1533

[a] The vdW exclusion radii of the Cu, O, C, and H atoms are 1.562, 1.342, 1.452, and 1.001 Å, respectively.

Using the partial charges thus obtained, together with the generic force fields describing the interatomic vdW interactions, CO_2 adsorption isotherms were calculated for CuBTC at 295 K over the pressure range 0.01–1 bar and are compared with experiment in Figure 5.11. The CuBTC material is one of the most extensively characterized MOFs by experiment; available CO_2 adsorption isotherms are therefore in abundance in the literature. The variations in the experimental data are, however, quite substantial. This is likely to be a result of, for example, sample preparation and/or activation as investigated and reported by Liu et al (2007). Following the practice of Yazaydın et al. (2009), two experimentally measured adsorption isotherms

that show some of the highest CO_2 uptakes at room temperature and up to atmospheric pressure were chosen for benchmarking the simulation results.

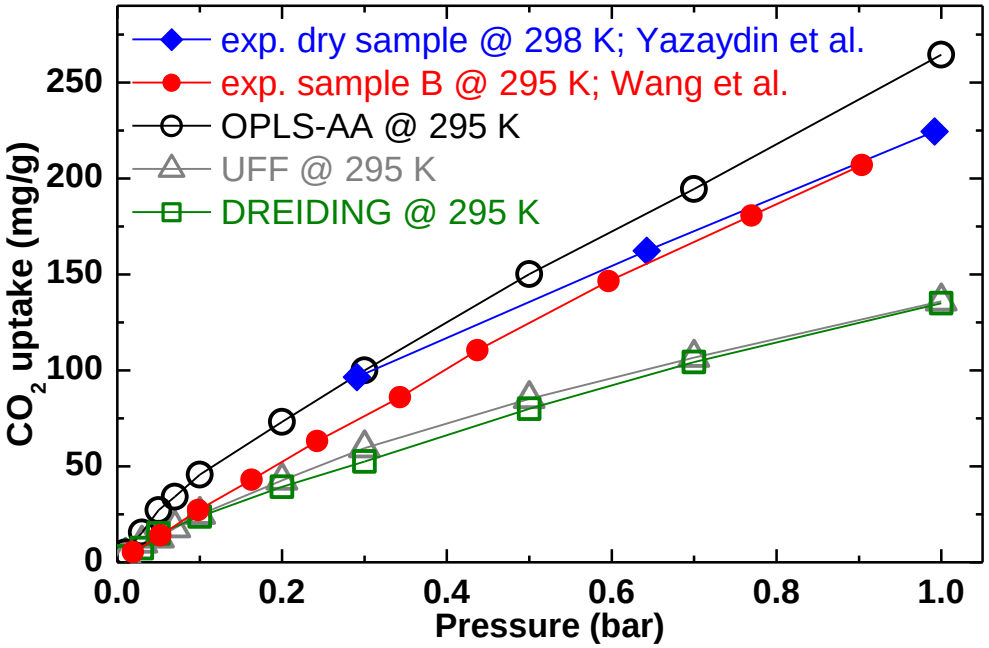

Figure 5.11. Comparison of CO_2 adsorption isotherms in CuBTC calculated by simulations based on the generic force fields with experiment (Wang et al., 2002; Yazaydın et al., 2009). The lines were added to guide the eye.

Figure 5.11 re-affirms that GCMC simulations based solely on UFF or DREIDING pronouncedly underestimate CO_2 uptakes in CuBTC at low pressures, a finding that was also made by Yazaydın et al (2009), for example. In terms of the amounts of CO_2 adsorbed, the OPLS-AA force field yields qualitative agreement with the experimental results. These "improved" predictions delivered by OPLS-AA, however, cannot be ascribed to the simulation based upon it capturing correctly the enhanced uptakes of CO_2 at the cus's in CuBTC, an experimental observation gained in a neutron diffraction study of the system by Wu et al (2010). The reason is that the Cu atoms in all of the three GCMC simulations were described by UFF, which gives a very small Cu interaction with CO_2 (Table 5.5). In fact, the enhanced

uptakes from the OPLS-AA-based GCMC simulation are a direct result of the stronger interactions (compared to the ones determined by DREIDING and UFF) between CO_2 and the carboxylate oxygen and carbon atoms of CuBTC as given by the force field (Table 5.5).

The molecular-level adsorption mechanism resulting from the OPLS-AA-based GCMC simulation indicates that there is no adsorption on the cus's (site C in Figure 5.12 (a)) up to a loading of 1 CO_2/Cu (or 48 CO_2 per unit cell (uc)). This loading corresponds to a gravimetric uptake of 218.3 mg g^{-1}, a capacity measured in the experiments at ca. 1 bar (Figure 5.11). While adsorption of CO_2 on the cus's is completely absent from the OPLS-AA-based predictions, Figure 5.12 (b) explains the adsorption mechanism that corresponds to this uptake (1 CO_2/Cu). At this loading, CO_2 molecules are mostly located at the centre and the four windows (i.e., triangular-shaped openings or site A) of each of the small octahedral cage. One unit cell of the CuBTC framework consists of eight such small cages, amounting to 40 primary adsorption sites for CO_2 as identified by the OPLS-AA-based simulations, 37 of which are occupied in the snapshot taken for analysing the sitings. The other 11 adsorbed CO_2 molecules are positioned at the corners of the large cuboctahedral pores (site B), where the CO_2 molecules interact strongly with the non-black atoms of the CuBTC framework as illustrated in Figure 5.12 (c). The GCMC simulations based on either DREIDING or UFF predict similar adsorption mechanisms; that is, the uptakes occur at the small-cage-centre, small-cage-window, and large-pore-corner sites and not at the cus's.

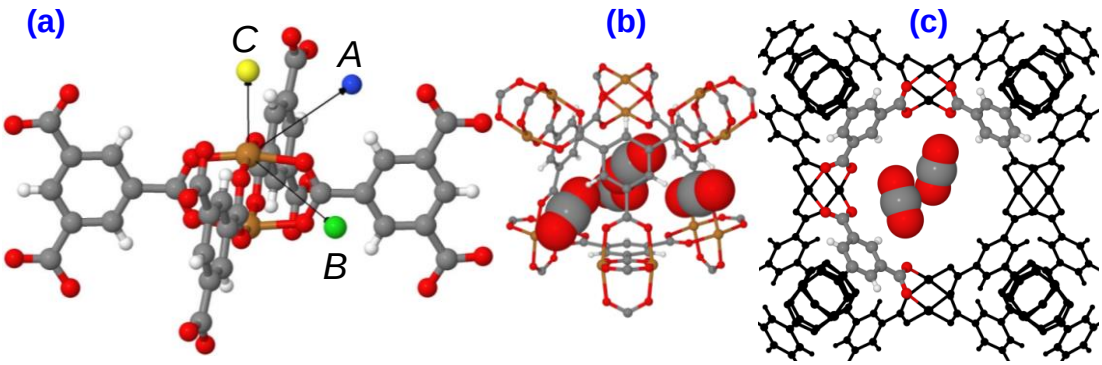

Figure 5.12. (a) One dicopper paddle-wheel of the CuBTC framework, where two adjacent copper(II) cus's are connected by four BTC ligands. A, B, and C are the small-cage-window, large-pore-corner, and cus sites, respectively. (b, c) Locations of the adsorbed CO_2 molecules in (b) the small cage and (c) one of the two large pores (with a dimension of ~10 or ~11 Å), as predicted by the GCMC simulations based on OPLS-AA at 295 K.

These simulation results based solely on the generic force fields are, however, in contradiction with the experimental findings made by Wu et al (2010). In their neutron diffraction experiment (at 20 K) on CuBTC with a loading of 1.07 CO_2/Cu (or 51 CO_2/uc), two primary adsorption sites were clearly identified to be the Cu(II) cus's (site C) and the small-cage windows (site A). The former was found to be first populated by CO_2 molecules and then was the latter, with site occupancies of 0.962 and 0.164, respectively. Put precisely, 46 of the 51 adsorbed CO_2 molecules went to the cus's (48 cus's/uc) with the rest located at the small-cage windows. The adsorption of CO_2 at two secondary adsorption sites (i.e., small-cage-centre and large-pore-corner sites) could only be observed at a higher loading of 1.47 CO_2/Cu. Out of the 71 adsorbed CO_2 molecules, 47, 21, 2, and 1 molecules were found at the cus, small-cage-window, small-cage-centre, and large-pore-corner sites, respectively (Wu et al., 2010).

To summarize these findings made for the predictions of CO_2 adsorption in CuBTC based on the generic force fields, it becomes clear that simulated adsorption isotherms on their own are not adequate to allow for assessing

accuracy of force fields and that quantitatively comparable isotherms can result from very different underlying adsorption mechanisms. The observed discrepancies, especially the completely different adsorption mechanisms, between experiment and simulation (based on the generic force fields) re-emphasize the need for a new set of force-field parameters to correctly describe the CO_2 interactions with CuBTC, cus's in particular. Only by achieving this can the GCMC simulations based upon these force-field parameters be expected to yield an accurate prediction of the adsorption isotherm as well as a correct description of the adsorption mechanism at play.

GCMC simulations using combined force fields. Having demonstrated that generic force fields fail to describe correctly CO_2 adsorption in CuBTC, the above-described combined force field approach can be examined and discussed. The *ab initio* derived force-field parameters (Table 5.4; denoted as AIFF-G2(Cu) hereafter) for the $CO_2\cdots Cu_2(O_2CR)_4$ complex were used in GCMC simulations to describe the CO_2 interactions with the paddle-wheel units of the CuBTC framework: i.e., the Cu, $O(O_2CR)$, and $C(O_2CR)$ atoms. The interactions between a CO_2 molecule and the other MOF atoms (i.e., Cb, Cc, and H in Figure 5.10) were calculated using one of the three generic force fields investigated above. The resulting CO_2 adsorption isotherms are presented in Figure 5.13 and are compared with the same experimental data as the ones in Figure 5.11.

The results are quite interesting. The enhancement of predicted uptakes is most significant in the case of the AIFF-G2(Cu)+UFF combination, followed by AIFF-G2(Cu)+DREIDING. The enhanced uptakes come from the fact that the AIFF-G2(Cu) parameters give rise to CO_2 being adsorbed at the cus's sites, which is completely absent from the simulations solely based on the generic

force fields (UFF for Cu). The two combinations yield a larger difference (Figure 5.13) in the predicted adsorption amounts (for example) at 1 bar CO_2 pressure than the difference between the UFF- and DREIDNG-based predictions in Figure 5.11. The reason is that C and H atoms have larger potential-well depths in UFF than in DREIDING (Table 5.5), making AIFF-G2(Cu)+UFF characterize a stronger CO_2–MOF interaction when compared to the other combination. On the molecular level, both force-field combinations result in similar adsorption mechanisms. Not only are the cus's occupied by CO_2 molecules, but the other primary (small-cage-window) and the two secondary (small-cage-centre and large-pore-corner) adsorption sites also take up considerable amounts of CO_2, especially when using the UFF parameters.

The AIFF-G2(Cu)+OPLS-AA combination yields the best agreement with experiment among the three combinations with the generic force fields (Figure 5.13). This, again, can be rationalized by the differences in the interaction strengths summarized in Table 5.5. Among the three generic force fields, OPLS-AA gives the smallest D_{eq} values for the CO_2–linker interaction and hence predicts the lowest uptakes at the adsorption sites where the CO_2–linker interactions are dominant. This is evident from the sitings of the CO_2 adsorbed at 1 bar. The occupancy ratio of cus/non-cus is 44/15, 45/21, or 45/31 for AIFF-G2(Cu) combined with OPLS-AA, DREIDING, or UFF, respectively. Note that this ratio as determined experimentally by Wu et al. (2010) is 46/5 at a loading of 1.07 CO_2/Cu, which corresponds to the experimental uptake at 1 bar. In other words, all of the three combinations result in very good predictions of the CO_2 uptake at the cus's, but accompanied by pronounced overestimations for the other adsorption sites.

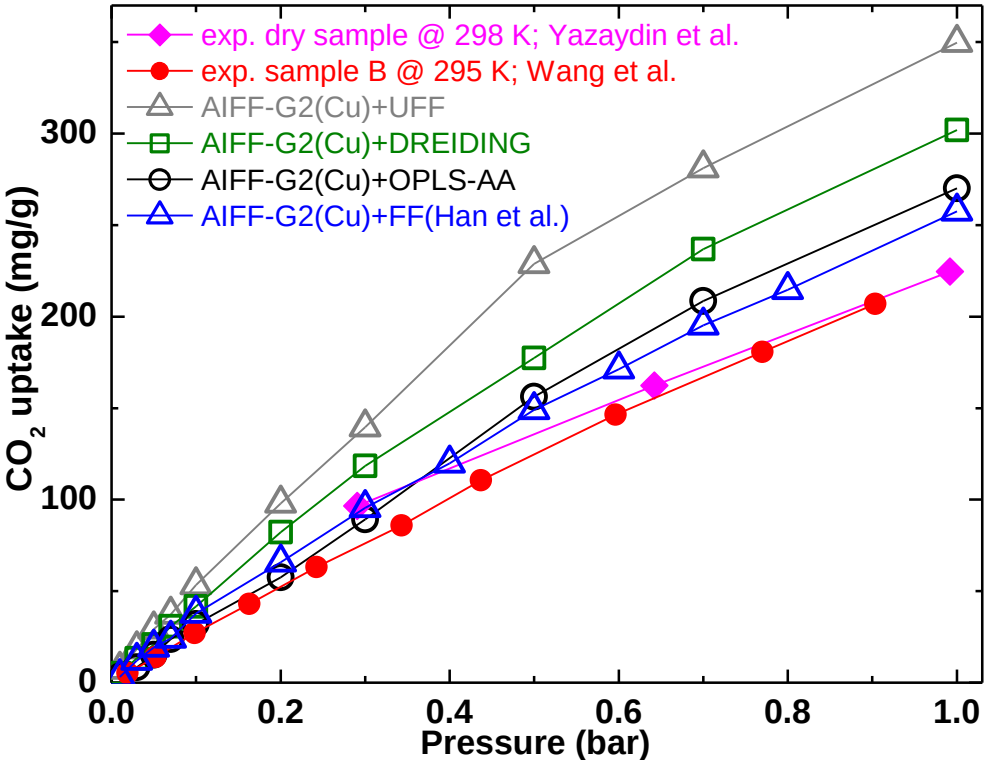

Figure 5.13. Comparison of CO_2 adsorption isotherms in CuBTC between simulation and experiment (Wang et al., 2002; Yazaydın et al., 2009). The simulations were performed at 295 K, using the different force-field combinations indicated in the legends. The AIFF-G2(Cu) parameters are given in Table 5.4. FF(Han et al.) denotes the *ab initio* derived force field from Han et al (2012). The lines were added to guide the eye.

The AIFF-G2(Cu) parameters, representing the CO_2–$Cu_2(O_2CR)_4$ interaction, were further combined with an *ab initio* parameterized force field from Han et al (2012) (denoted as FF(Han et al.)), which describes the CO_2 interactions with the other MOF atoms. FF(Han et al.) was developed explicitly for simulations of CO_2 adsorption in MOFs and ZIFs (zeolitic imidazolate frameworks) using the MP2 method, together with a quadruple-ζ quality basis set. Moreover, the force field was parameterized on a building-block basis; that is, it was not fitted to any particular framework topologies. The agreement between simulation and experiment was therein found to be very good for CO_2 adsorption in several MOFs and ZIFs. FF(Han et al.) uses the Morse potential to model the vdW contribution to the total interatomic

energy, with the electrostatic contribution calculated by the Coulomb potential.

The combined AIFF-G2(Cu)+FF(Han et al.) force field simulates CO_2 adsorption in CuBTC in even better agreement with the experiments than the simulation based on AIFF-G2(Cu)+OPLS-AA (Figure 5.13). More importantly, it captures the molecular-level adsorption mechanism to a high accuracy, when compared to the neutron diffraction experiment (Wu et al., 2010). At 1 bar CO_2 pressure, AIFF-G2(Cu)+FF(Han et al.) gives an uptake of 46 (corresponding experimental value: 46), 7 (5), or 2 (0) CO_2 molecules at the cus, small-cage-window, or small-cage-centre sites, respectively. Moreover, no apparent adsorption at the large-pore corners was observed over a number of snapshots taken during the GCMC simulation at this loading – which agrees well with experiment.

The AIFF-G2(Cu)+FF(Han et al.)-simulated CO_2 adsorption complexes on the CuBTC framework agree remarkably well with the experimentally refined locations of CO_2 inside the pores (Wu et al., 2010). Experimentally, each Cu(II) cus can accommodate one CO_2 molecule with one O(CO_2) affixed to the Cu atom. The CO_2 molecule can orient in four possible directions to "align" with one of the four Cu–O(O_2CR) bond of the square-planar coordination of the cus. At the other primary adsorption site, small-cage window, one CO_2 molecule "sits" at the centre of and is almost perpendicular to the opening of the small tetrahedral cage. These observations are reproduced very well by the AIFF-G2(Cu)+FF(Han et al.)-based simulations. Figure 5.14 (a) shows a typical geometry of the most frequently predicted conformation between the adsorbed CO_2 molecules and the framework. Most of the cus's are occupied by a CO_2 molecule with one O(CO_2) affixed to the Cu atom, while a small

amount of CO_2 molecules "sit" at the centres of the triangular-shaped openings into the small cage, with one O(CO_2) pointing toward the cage centre. Moreover, the CO_2 molecule, of which one O(CO_2) is affixed to a cus, orients itself to favour a configuration where it "lies" on the "edge" of a BTC linker, allowing the other O(CO_2) to interact strongly with the hydrogen atom of the linker and with the nearby Cu atom of a neighbouring paddle-wheel (Figure 5.14 (b)). The geometry shown in Figure 5.14 (b), for example, exhibits interatomic distances of 2.7, 4.1, and 3.3 Å for O(CO_2)–Cu, O'(CO_2)–Cu', and O'(CO_2)–H, respectively; the Cu–O(CO_2)–C(CO_2) angle is 131.0 °.

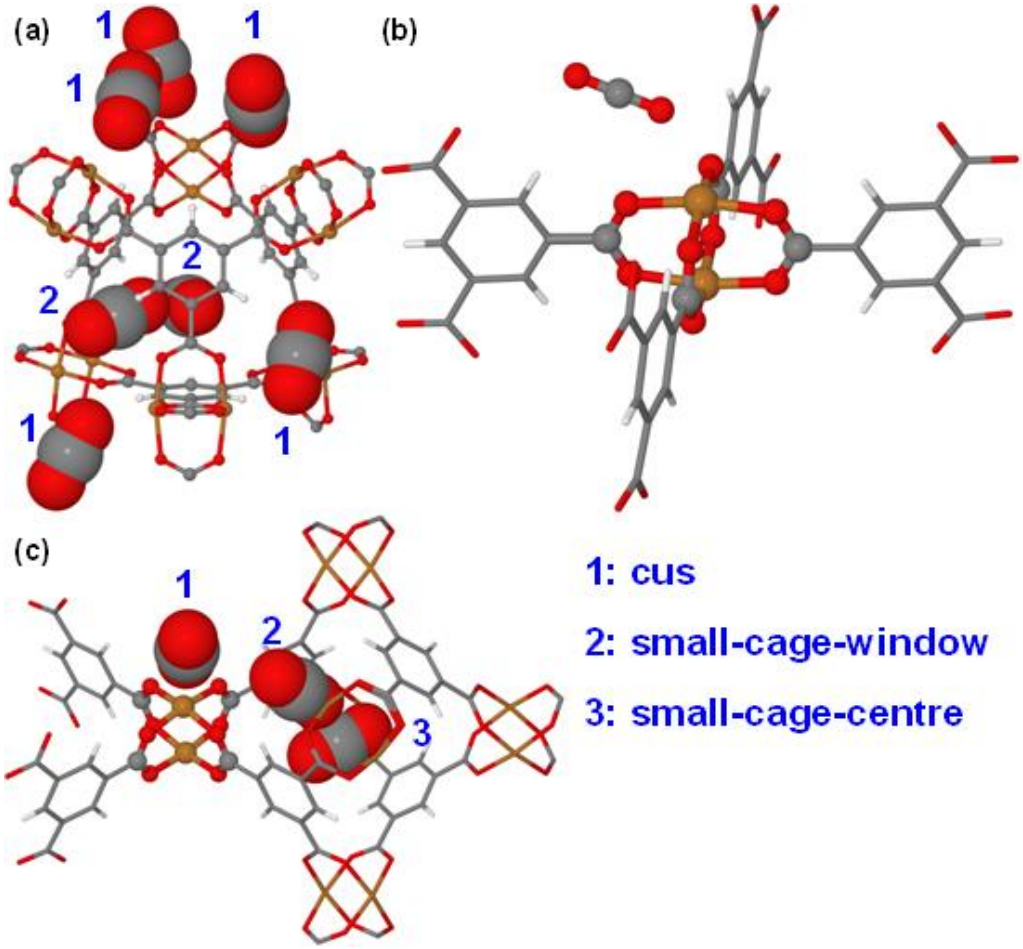

Figure 5.14. Structures of the CO_2 adsorption complexes on the CuBTC framework observed in the GCMC simulations using the combined AIFF-G2(Cu)+FF(Han et al.) force field. (a, b) Most frequently seen arrangements (a) of CO_2 molecules in or around one small cage, with a zoom-in view (b) of the CO_2 configuration with respect to a cus. (c) A typical geometry of the less frequently seen CO_2 arrangement. Note that some CO_2 molecules on nearby cus's or in adjacent cavities have been omitted from (a, c) for clarity.

A secondary CO_2 adsorption complex is also present (but less frequently observed) in the GCMC simulations based on AIFF-G2(Cu)+FF(Han et al.). Figure 5.14 (c) shows that in this configuration the cus, small-cage-window, and small-cage-centre sites are each occupied by a CO_2 molecule. The CO_2 molecule at cus is now in an "end-on" conformation with the Cu(II) ion ($\angle C(CO_2)-O(CO_2)-Cu = 157.0°$), pointing toward a large pore. The "freed-up" C atom of this CO_2 interacts strongly with the nearby O atom of the CO_2 at small-cage-window site with $r\left(C(CO_2^{cus})-O(CO_2^{window})\right)$ being 3.7 Å. This small-cage-window CO_2 in turn helps to stabilize a CO_2 molecule to stay inside the small cage; $r\left(O(CO_2^{window})-C(CO_2^{centre})\right)$ = 2.9 Å. In other words, the strong CO_2–CO_2 interactions play an important role in maintaining this secondary adsorption complex on the CuBTC framework. These detailed observations (Figure 5.14) gained in the GCMC simulations are supported by the findings made in a periodic DFT/CC study of the system (Grajciar et al., 2011), indicating that the combined AIFF-G2(Cu)+FF(Han et al.) force field is able to capture the CO_2 adsorption mechanism in CuBTC under the conditions studied here.

It is worth noting that the CO_2–linker interaction is markedly weaker when represented by FF(Han et al.), as compared to the ones of UFF, DREIDING, or OPLS-AA (but to a lesser extent in the last case). This is demonstrated by Figure 5.15, where one more simulated CO_2 adsorption isotherm was added to comparison. The simulation was performed using UFF representing the Cu atoms in CuBTC, while all other interactions between a CO_2 molecule and the framework were described by FF(Han et al.) – the force field does not have parameters for Cu.

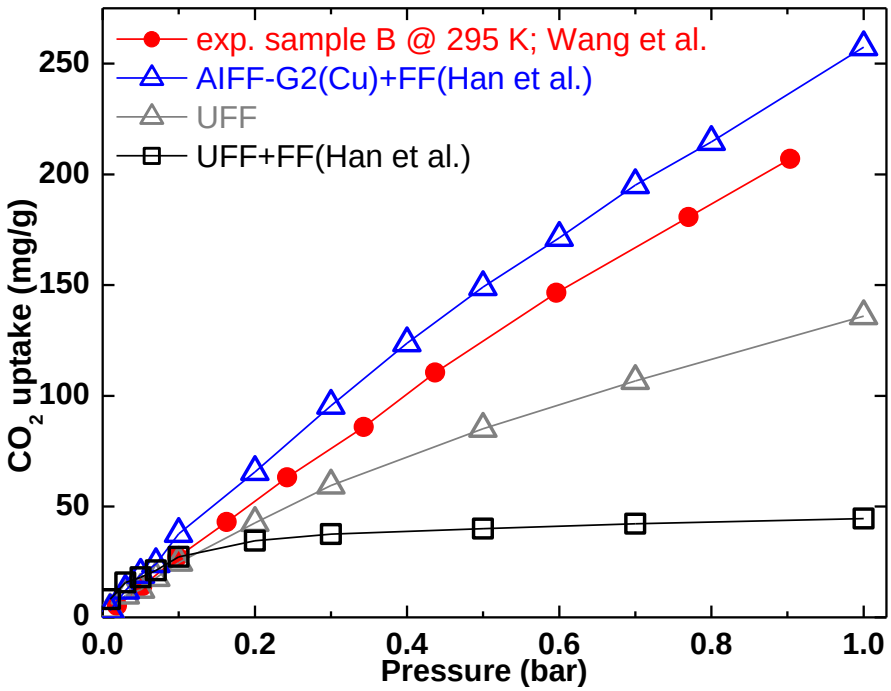

Figure 5.15. Comparison of adsorption isotherms for CO_2 in CuBTC between simulation (295 K) and experiment (Wang et al., 2002). The lines were added to guide the eye.

The UFF+FF(Han et al.) combination simulates an uptake of 9 CO_2/uc at 1 bar, with 8 of which occupying the small-cage-centre sites (occupancy = 1) and the remaining one "sitting" at a small-cage window. Taking into account the observation made in the AIFF-G2(Cu)+FF(Han et al.)-based simulation (where 7 and 2 CO_2 molecules were found at the small-cage-window and small-cage-centre sites, respectively), it becomes clear that the CO_2 interaction at the small-cage-window site is enhanced by the adjacent cus's and, in some cases, by strong CO_2–CO_2 interactions (Figure 5.14 (c)). In contrast, despite not adsorbing any CO_2 at the cus's, simulations of CO_2 adsorption in CuBTC described by the generic force fields show considerable uptakes of CO_2 in not only the small cages but also the large pores (primarily at the corners), an artefact (compared to experiment) that has been seen for both "purely" generic and combined force field approaches. In summary, all of these observations combined together, again, place an emphasis on the

importance of carefully parameterized force fields – e.g., AIFF-G2(Cu) and FF(Han et al.) – for capturing correctly the adsorption mechanism, which is certainly more difficult than reproducing the adsorption isotherm. The latter, in the case studied here, even can be achieved by scaling down the interaction strengths (potential-well depths) of the generic force fields, a practice that has been seen repeatedly in the literature. Good and detailed experimental data are, of course, necessary for validating the parameterized force fields and the simulations based upon them.

To investigate the performance of AIFF-G2(Cu) in describing CO_2 adsorption in another MOF with Cu(II) cus's, the combined AIFF-G2(Cu)+FF(Han et al.) force field was further used to simulate CO_2 adsorption in the MOF NOTT-140a (Tan et al., 2011). The NOTT-140a framework is built of $Cu_2(O_2CR)_4$ paddle-wheels bridged by tetrahedrally-branched octacarboxylate linkers; one unit cell of the structure is depicted in the inset of Figure 5.16. Experimental CO_2 adsorption measurements at 283 K were reported for NOTT-140a by Tan et al (2011).

The fluid–framework and fluid–fluid electrostatic interactions were modelled by the Coulomb potential, while the partial atomic charges derived and used for the NOT-140a framework are provided in Appendix A2. GCMC simulations – using either AIFF-G2(Cu)+FF(Han et al.) or UFF (included for comparison) – were performed on the experimentally determined NOTT-140a framework at 283 K. It is clear from Figure 5.16 that the simulation based on AIFF-G2(Cu)+FF(Han et al.) predicts CO_2 uptakes in very good agreement with experiment, providing further evidence for the accuracy of this combined force field. It is worth emphasising that the combination yields very good predictions of CO_2 adsorption in two copper-paddle-wheel-

containing MOFs, CuBTC and NOTT-140a, despite that both the AIFF-G2(Cu) and the FF(Han et al.) force fields were parameterized based on model clusters and were not fitted to either of the two frameworks.

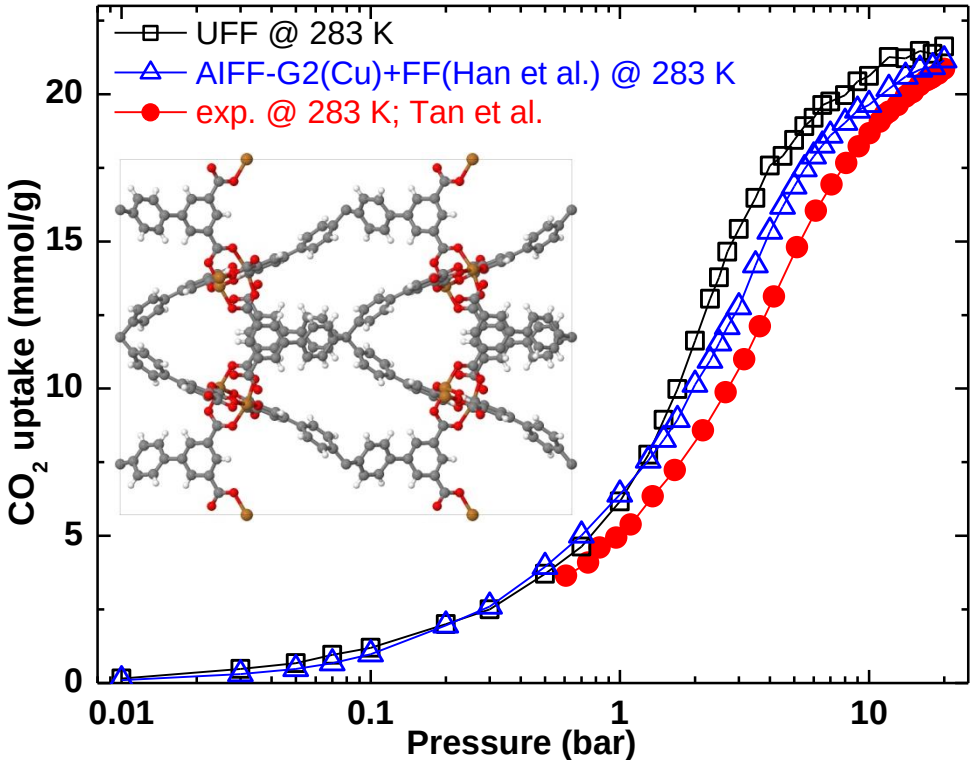

Figure 5.16. Comparison of simulated CO_2 adsorption isotherms in NOTT-140a with experiment (Tan et al., 2011). The framework topology of NOTT-140a is shown in the inset. The lines were added to guide the eye.

On the other hand, the UFF-based simulation results are also in good agreement with experiment (Figure 5.16). However, different adsorption mechanisms are predicted by the two simulations, resembling the situation of CO_2 adsorption in CuBTC. The cus's in NOTT-140a are at first and rapidly occupied by CO_2 molecules in the simulation with AIFF-G2(Cu)+FF(Han et al.). In contrast, the UFF-based simulation predicts that CO_2 molecules first go to the corners of the tetrahedrally-branched linkers, where vdW interactions between a CO_2 molecule and the framework are significant. It may be intuitive to assume that the combined AIFF-G2(Cu)+FF(Han et al.)

force field captures correctly the adsorption mechanism, given the general understanding of CO_2 adsorption in MOFs with cus's, such as the case of CuBTC discussed above. However, *in situ* data (e.g., neutron diffraction) that can reveal localization of the adsorbates inside the framework would be necessary to judge the accuracy of both simulation predictions.

5.5 Conclusions

First, the unification of force-field expression and the alignment of force-field fitting with the *ab initio* method used to provide reference data have seen AIFF-G2, a force field derived for CO_2 – CPO-27-Mg, be relatively easily extended to include force-field parameters for the CO_2 – CPO-27-Co system. The procedure is computationally efficient and the MMSV potential has been shown to be a good choice for fitting of potential energy curves, especially in the case of adsorbate–cus interactions. This suggests a possible scope of using the MMSV potential – or a combination of MMSV and MSV to reduce the number of parameters – to "mass-produce" force-field parameters for adsorption simulations in MOFs with cus's. Comparing the MMSV potential with the Morse potential, the former surely offers a larger degree of flexibility in fitting, at the expense of introducing more fitting variables. Moreover, the correct asymptotic r_{ij}^{-6} behaviour of the MMSV function has been found to be important not only in terms of the physical meaning but also for enhancing the robustness of the fitting. It is noteworthy that, however, some have argued that an asymptotic correctness may be of less importance within the distances that are relevant to the common pore sizes of MOFs (Han et al., 2012). Nevertheless, the extra variables introduced by

MMSV may not be too much a "burden" for force-field parameterization. This is because, for example, the number of parameters that needed fitting was significantly reduced when values readily available from the DFT-D2 method were used in the force field.

Second, on the basis of the different force fields investigated here, force fields tailor-made for MOFs can (almost) certainly outperform generic ones, especially for MOFs with cus's. This is hardly inconceivable, considering bespoke force fields acquire high accuracy (usually) at the expense of transferability. For example, *ab initio* derived force fields for GCMC simulations, more often than not, define cross-terms for adsorbate–MOF interactions rather than give parameters explicitly for individual framework atoms. This can be a serious disadvantage of such force fields compared to generic ones. The latter, although generally generic, need to be used for particular systems after careful justification, especially in the cases of MOFs with cus's. As evidenced by CO_2 adsorption in CuBTC at pressures up to 1 bar, the OPLS-AA force field (with UFF for Cu), for example, yields fairly good agreement with experiment in terms of CO_2 uptakes; however, a completely different adsorption mechanism is predicted by the simulation when compared to experiment. On the other hand, OPLS-AA has also been found to be the best option among the three generic force fields to be coupled with the *ab initio* derived AIFF-G2(Cu) force field for studying CO_2 adsorption in CuBTC. Put together, a thorough investigation – comparing a larger number of MOFs with $Cu_2(O_2CR)_4$ – may be worth conducting to provide conclusive evidence to ascertain the observations made here. More generally speaking, the combined force field approach certainly holds promise, as it can effectively and efficiently augment the performance of available (and often well-tested) literature force fields in describing specific,

"difficult" situations such as gas adsorption in MOFs with cu's. The building-block-based force-field parameterization may be further made objective-oriented by only deriving new parameters when necessary. As such, the required *ab initio* reference calculations may be achieved in a time frame of days, given a moderate computing resource.

Chapter 6 *Ab initio* Molecular Dynamics Studies of the Breathing of the Flexible MOF MIL-53(Sc)

6.1 Introduction

Breathing metal–organic frameworks combine "regularity" with "softness" by exhibiting large, reversible structural deformations (softness) upon the action of various external physical (e.g., temperature or mechanical pressure) or chemical (e.g., guest-molecule inclusion) stimuli without loss of crystallinity or bond breaking (regularity) (Férey and Serre, 2009; Horike et al., 2009). This phenomenon is characterized by pronounced reversible structural transitions between two (or more) states resulting from the expansion or contraction of the three-dimensional porous framework. The associated large variations in unit-cell volume, sometimes as much as 40% to 270% (Serre et al., 2002; Serre et al., 2007), give rise to promising applications of these breathing MOFs in numerous fields ranging from gas storage and separation to drug encapsulation and delivery (Férey et al., 2011; Horcajada et al., 2012).

Among these soft porous solids, the trivalent metal (M^{3+}; M = Cr, Al, Fe, Sc, etc.) terephthalate MIL-53 ("MIL" stands for Materials of Institute Lavoisier) is one of the most widely studied of all MOFs, because of its ability to change crystal structure markedly in response to changes in temperature and guest-molecule adsorption (Figure 6.1) (Serre et al., 2002; Loiseau et al., 2004; Whitfield et al., 2005; Mowat et al., 2011). The compounds belonging to the MIL-53 family are built up from chains of μ_2-OH corner-sharing $MO_4(OH)_2$ octahedra linked via terephthalate linkers to define a three-dimensional

ordered network with one-dimensional diamond-shaped channels. One intriguing feature of the MIL-53 family is the dramatically different breathing behaviours observed for different M^{3+} centres. The MIL-53(Cr) solid (Serre et al., 2002), for example, exhibits either an orthorhombic *large-pore* (*lp*) form (Figure 6.1 (e)) – that is favoured by dehydration, higher temperatures and larger adsorbate uptakes – or a monoclinic *narrow-pore* (*np*) form (Figure 6.1 (d)) that is found at lower temperatures and lower uptakes. The iron analogue, MIL-53(Fe), shows a more complex breathing behaviour (Millange et al., 2008; Devic et al., 2012), with the dehydrated material adopting a *very-narrow-pore* (*vnp*) form (*C* 2/*c* symmetry, Figure 6.1 (b)) that takes up CO_2 to give an *intermediate* (*int*) form (Figure 6.1 (c)) before opening sequentially to give the *np* (Figure 6.1 (d)) and *lp* (Figure 6.1 (e)) forms.

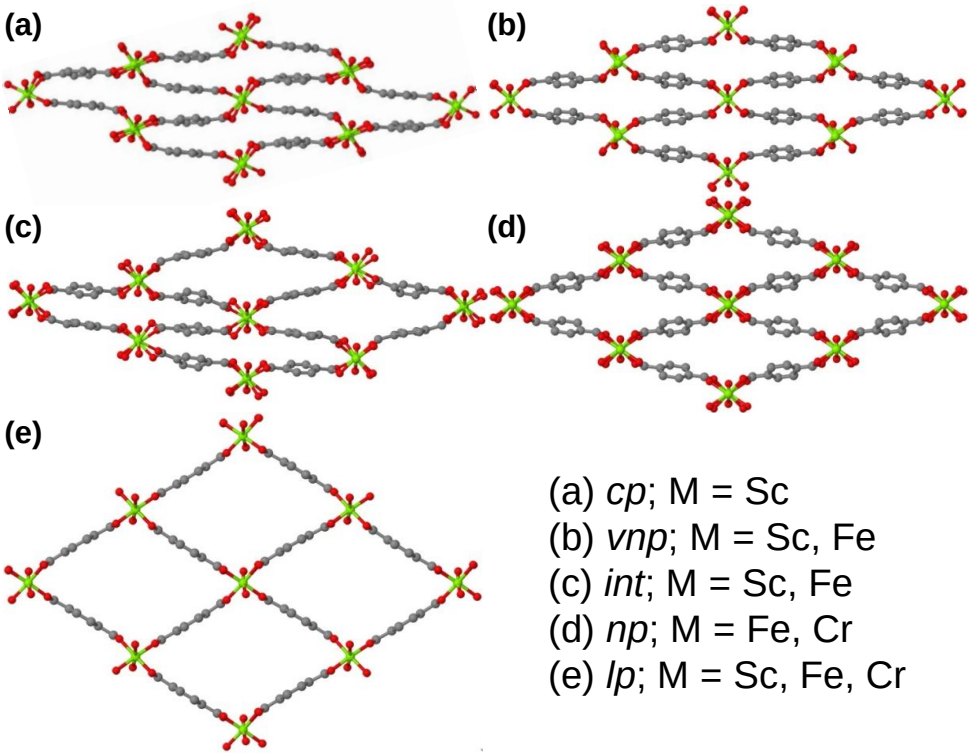

Figure 6.1. Schematic representation, together with examples, of the different structural forms of MIL-53 observed for different metals. Colour code: grey, carbon; red, oxygen; and green, metal. Note that hydrogen atoms were omitted for clarity.

The scandium analogue, MIL-53(Sc), has been shown to exhibit a similarly complex, but crystallographically distinct, breathing behaviour in response to solvent removal, temperature variation, and adsorption of H_2O and CO_2 (Mowat et al., 2011; Mowat et al., 2012). Upon removal of occluded dimethylformamide (DMF) solvent from the as-prepared form, MIL-53(Sc) does not open but instead contracts to give a *closed-pore* (*cp*) form with *P* $2_1/c$ symmetry (Figure 6.1 (a)) that is distinct from the *vnp* form (Figure 6.1 (b)) and without accessible porosity to N_2 or CO_2. The MIL-53(Sc) solid is observed to be in the *cp* form from 100–573 K with a gradual expansion in the unit-cell volume in response to increasing temperature; by 623 K it has undergone a transition to a *vnp* form with *C* 2/*c* symmetry that is isostructural to MIL-53(Fe)-*vnp* (Devic et al., 2012). The transition complexity of MIL-53(Sc) goes beyond this sensitive response to temperature variation. Hydration of MIL-53(Sc)-*cp* at room temperature, for example, leads to MIL-53(Sc)-H_2O in an *intermediate* (*int*) phase having triclinic symmetry (Figure 6.1 (c)) in which half of the channels are partially open as a result of the uptake of H_2O molecules while the others are empty and closed (Mowat et al., 2011). The CO_2 adsorption isotherm of MIL-53(Sc) (Mowat et al., 2011; Mowat et al., 2012) is different from the ones reported for MIL-53(Cr) and MIL-53(Fe): an initial region of zero uptake is followed by two steps – the first at 2–3 mmol g^{-1} and the second at 13 mmol g^{-1}. The latter is attributed to full opening to the *lp* form (Figure 6.1 (e)), as observed for various solids of the MIL-53 structure type upon uptake of large amounts of adsorbates (Serre et al., 2002; Loiseau et al., 2004; Millange et al., 2008; Llewellyn et al., 2009). Indeed, *in situ* diffraction experiments (Chen et al., 2013) were reported recently to confirm the presence of the *lp* form and to establish the structure responsible for uptakes of 2–3 mmol g^{-1}, which are discussed in detail below.

A considerable number of multidisciplinary studies have been devoted to understanding the structural transformations observed for breathing MOFs of the MIL-53 type and others (Hamon et al., 2009; Llewellyn et al., 2009; Rabone et al., 2010; Salles et al., 2010; Hoffmann et al., 2011; Yang et al., 2011). In particular, MIL-53(Cr), a textbook example of a bi-stable (i.e., *lp* ⇄ *np* transition) breathing MOF, has been extensively explored. Some well-established experimental methods that have routinely been deployed include (1) manometric/gravimetric and microcalorimetric measurements for studying a variety of adsorbate molecules; (2) *in situ* techniques (e.g., X-ray diffraction, infrared or Raman spectroscopy) used, for example, to locate adsorbates in the pores or probe the nature of adsorption sites; and (3) quasi-elastic neutron scattering experiments to help with understanding the dynamics of a probe molecule in a host MOF (Férey et al., 2011; Férey, 2012). Hand-in-hand with the experimental efforts, theoretical investigations of breathing MOFs on different length and/or time scales have also been carried out (Coudert et al., 2009; Dubbeldam et al., 2009; Ghoufi et al., 2010; Ghoufi et al., 2012; Triguero et al., 2012). The richness of the insights provided by computational methodologies spans from mechanistic details realized through a quantum-mechanical (QM) description of the electronic structure of the system (Coombes et al., 2008; Devic et al., 2012) – primarily relying on static density functional theory (DFT) calculations – to macroscopic thermodynamic information on the sample level, which can provide insight into, for instance, the interplay between the adsorbent elasticity and guest molecule adsorption (Triguero et al., 2011; Triguero et al., 2012). In particular, force-field-based molecular simulation studies, including Monte Carlo (MC) and molecular dynamics (MD) methods (Frenkel and Smit, 2002), have made substantial contributions toward elucidating the microscopic mechanisms

that govern the structural deformations (Serre et al., 2007; Salles et al., 2008; Hamon et al., 2009; Bourrelly et al., 2010; Ghoufi et al., 2010; Rabone et al., 2010; Hamon et al., 2011; Salles et al., 2011; Ghoufi et al., 2012; Zhang et al., 2013).

MD simulations are particularly suited to coupling with experiment to study MOF breathing phenomena because they offer a detailed description of the system of interest on the atomistic/molecular level. As an MD simulation reveals points in phase space that are connected in time, it can provide an evolving picture of the breathing behaviour that readily conveys valuable details on, for instance, how cooperative movements of the framework ligands, together with the interactions between the inorganic and organic moieties, facilitate the major structural changes of the MIL-53 solids (Serre et al., 2007; Férey and Serre, 2009). Moreover, information concerning the kinetics and energetics of the breathing motion can be extracted from MD simulations to help reveal collective effects of the guest–guest, guest–host and sometimes host–host interactions. To date, most of the reported MD studies aimed at capturing the breathing phenomena of MOFs have made use of flexible force fields tailor-made for the frameworks. Such force fields are usually obtained either by employing accurate QM calculations (Vanduyfhuys et al., 2012; Bureekaew et al., 2013) or via a combination of chemical intuition, existing force fields, and an iterative process to tune the parameters to reproduce the experimental data (Ghoufi et al., 2012).

Despite being very successful in reproducing and helping to interpret many structural and dynamical properties of the breathing motions of MOFs, force-field-based MD simulations have been applied to only a handful of selected structures. From a simulation point of view, the lack of suitable force fields

and the effort involved in developing new ones are to blame for this. These problems may be avoided by using DFT-based *ab initio* molecular dynamics (AIMD) simulation techniques (also called DFT-MD or first-principles MD) (Car and Parrinello, 1985; Mark, 2002; Kirchner et al., 2012). Since the finite-temperature dynamics is developed with forces obtained directly from first-principles electronic-structure calculations made "on the fly", AIMD simulations in principle allow an accurate and unbiased investigation of the chemical processes of interest. In addition, they can be more predictive compared to the force-field approach, mainly because predefined force fields can be expected only to reproduce the chemical events against which they were parameterized prior to the simulations.

AIMD simulations have been used successfully in multiple fields of chemistry. A few examples include: Poater et al. (2009) explored the reactivity induced by coordination of a CO molecule trans to the Ru−ylidene bond of a prototypical Ru−olefin metathesis catalyst; Schmidt et al. (2009) studied the structure and density of water at near-ambient conditions; Mallik and Siepmann (2010) investigated the thermodynamic, structural and transport properties of an ionic liquid, tetramethyl ammonium fluoride; Kimmel et al. (2012) looked at the system of thin water films adsorbed on TiO_2(110) surfaces; and Sieffert et al. (2012) compared several AIMD simulation protocols for the description of liquid methanol. However, the application of AIMD simulations to the field of MOFs is still rare. Using AIMD simulations, Hoffmann et al. (2011) predicted a "closed-pore" structure for the empty DUT-8 MOF, which agrees well with their xenon adsorption measurements that showed no uptake up to a certain pressure; however, the simulated structure was not further validated by, for example, X-ray diffraction data therein. Haldoupis et al. (2012) and Kanoo et al. (2012)

studied different adsorbate–MOF systems with AIMD simulations; both studies are (primarily) focused on the effects of the rotation of linker rings on the diffusion/adsorption of guest molecules. AIMD simulations were also used by Schröder et al. (2013) to complement their experiments in understanding the polymorphism of certain zinc-imidazolate framework topologies.

In this Chapter, AIMD simulations are used to predict structural changes of MIL-53(Sc) in response to changes in temperature over the range 100–623 K and adsorption of CO_2 at 0–0.9 bar at 196 K. As stated above, the complex stimuli-responsive phase transitions of MIL-53(Sc), which are different from those of the Cr and Fe forms, have yet to be fully understood. In particular, one structural phase that was observed by experimental X-ray diffraction during the adsorption of CO_2 could not be resolved via conventional methods because of diffraction peak broadening (Chen et al., 2013). The MIL-53(Sc) material is therefore an ideal test case to assess AIMD simulations as a tool to assist with experimental structure determination and to provide fundamental insight into the breathing mechanism. The experimental data used to validate the simulation results in this Chapter come from the two reports of Mowat et al. (2011) and (2012). Additionally, experimental data are available for the adsorption of CO_2 on dehydrated MIL-53(Sc) at 196 K, followed by *in situ* synchrotron X-ray powder diffraction (XRPD) experiments, which was studied by Professor Paul A. Wright and co-workers at University of St. Andrews (Chen et al., 2013).

6.2 Computational Setup for DFT Calculations and AIMD Simulations

The use and further development of AIMD methodology was initiated by Car and Parrinello (1985), although the foundation of the technique was laid down much earlier by Ehrenfest (1927) and Dirac (1930). The methodological details about AIMD simulations can be found in, for example, the article by Kirchner et al. (2012). Here, only the calculation settings and simulation parameters that have been used in this work are detailed and discussed.

All of the AIMD simulations, geometry-optimization calculations, and single-point energy evaluations were performed employing DFT (with periodic boundary conditions and *P* 1 symmetry) as implemented in the QUICKSTEP (VandeVondele et al., 2005) module of the CP2K simulation package (http://www.cp2k.org/). Energies and forces were calculated with the Gaussian plane-wave scheme (Lippert et al., 1997; VandeVondele et al., 2005), which uses a dual basis set method wherein a linear combination of Gaussian-type orbitals is used to describe the Kohn–Sham molecular orbitals while the electron density is described by an auxiliary plane-wave basis set. A double-ζ valence plus polarization basis set (DZVP), in conjunction with the relativistic, norm-conserving Goedecker–Teter–Hutter pseudopotentials, was used for all elements other than Sc, which was described by the MOLOPT basis set (Goedecker et al., 1996; Hartwigsen et al., 1998; Krack, 2005; VandeVondele and Hutter, 2007). The auxiliary plane-wave basis set was defined by an energy cutoff of 350 Ry, accompanied by a relative cutoff of 50 Ry for the Gaussian basis set collocation. All of the calculations were done using the Becke–Lee–Yang–Parr (BLYP) (Becke, 1988; Lee et al., 1988) exchange–correlation functional with semiempirical dispersion corrections to

the energies and gradients from the DFT-D3 method (Grimme et al., 2010), unless explicitly stated otherwise. A cutoff radius of 25 Å was used for all DFT-D3 dispersion calculations and the three-body contribution to dispersion was explicitly evaluated. During each SCF cycle, the electronic structure was explicitly minimized to a tolerance of 10^{-7} Hartree. Structures were considered to be geometry-optimized when the maximum geometry change, root-mean-square geometry change, maximum force, and root-mean-square force converged to the values of 3.0×10^{-3} Bohr, 1.5×10^{-3} Bohr, 4.5×10^{-4} Hartree Bohr^{-1}, and 3.0×10^{-4} Hartree Bohr^{-1}, respectively.

Born–Oppenheimer MD simulations were carried out in the isobaric–isothermal (*NPT*) ensemble (i.e., constant number of particles, pressure, and temperature). In all of the AIMD simulations carried out in this work, both the shape and dimensions of the simulation box could vary, and no constraints were applied to any degree of freedom of the system. The equations of motion were integrated using a time step of 0.5 fs. The temperature was controlled by a chain of Nosé–Hoover thermostats (Martyna et al., 1992) coupled to every degree of freedom (the so-called massive thermostat) with a frequency of 4000 cm^{-1}. This frequency allowed the AIMD simulations to sample properly the O–H bond of the hydroxyl groups in MIL-53(Sc), as it is higher than the experimental values that were reported for the MIL-53 solids (Serre et al., 2002; Vimont et al., 2007). The barostat was set up with a coupling time constant of 300 fs and an external pressure of 1 bar.

Considering that the QUICKSTEP module employs Γ-point only calculations, relatively large simulation boxes were used in the AIMD simulations, ensuring the shortest dimension being larger than 14 Å (i.e., a 1 × 2 × 2 unit-

cell representation). Alongside this supercell representation, a reference cell of constant volume was used to fix the number of grid points used to compute the Coulomb and exchange–correlation energies. The reference cell was used to mitigate the effect of varying grid points due to fluctuating volume of the simulation box resulting from the large breathing motions of MIL-53(Sc). It was shown previously (McGrath et al., 2005; Schmidt et al., 2009), and has also been seen in this work, that a reference cell was needed to avoid large jumps and/or discontinuities in the potential energy profile when the simulation box was not kept fixed. In this work, the use of the reference cell significantly improved the accuracy of the simulation and yielded a good conservation of energy with a drift in energy of less than 3×10^{-5} Hartree $atom^{-1}$ $step^{-1}$ recorded. Technical details about the reference-cell treatment in the context of *NPT* simulations within the CP2K package are discussed elsewhere (McGrath et al., 2005; Schmidt et al., 2009), while the influence of this treatment on the AIMD simulations of MIL-53(Sc) is described below. Note, for clarity and ease of discussion, the validations of specific simulation parameters chosen are provided where appropriate, mostly alongside presenting the corresponding simulation results.

It needs to be noted that the use of a reference cell in an isobaric MD (or MC) simulation means that the number of exchange–correlation grid points is always kept constant. Consequently, as the volume of the simulation box changes (i.e., responding to the breathing motion of MIL-53(Sc)), the density of grid points is varied, ultimately resulting in a different plane-wave cutoff being used at each step. Changing the cutoff in turn modifies the computed total energy numerically, so that the energy differences thus obtained for the various phases of MIL-53(Sc) of different volume would belie the true relative stabilities of them. Therefore, the same grid (constant grid density)

was used for all of the static DFT calculations that were intended for comparing energies. In other words, all energy values reported below – for the purpose of comparing the relative stabilities of the different structural forms of MIL-53(Sc) – were not taken from AIMD simulations, but instead were determined by single-point DFT calculations, where the same exchange–correlation grid (constant density of grid points) was used.

6.3 Structural Response to Temperature Variations at Zero Guest-Molecule Loading

6.3.1 Generating MIL-53(Sc)-*cp* and -*vnp* structures *in silico*

Previously, Mowat et al. (2012) reported the novel *cp* structural form of MIL-53(Sc) upon removal of the guest molecules. Interestingly, the evacuated structure exhibited unusual thermal behaviour. The framework underwent a gradual expansion of the unit cell in response to increasing temperature until it changed symmetry from $P\,2_1/C$ to $C\,2/c$ at 623 K. The structures obtained at the different temperatures were successfully refined against the XRPD patterns in the same work. Because of the availability and, more importantly, the subtlety of the structural changes caused simply by varying the temperature, these experimental structures provide an ideal test case for critically assessing the validity of the AIMD-simulation-based computational approach in studying the breathing motions of MIL-53(Sc).

To mimic the experiments *in silico*, the as-prepared MIL-53(Sc) containing DMF solvent molecules (Mowat et al., 2011) was used as the starting configuration for the framework. The DMF molecules were removed from

the framework prior to the simulations, analogous to the activation in the experiment. The structure, denoted as MIL-53(Sc)-*DMF(removed)*, was then used as a starting structure for AIMD simulations performed at three temperatures, namely, 100, 293, and 623 K, which were among the ones investigated experimentally (Mowat et al., 2012). For all three AIMD simulations, the starting configuration of the simulation box consisted of a 1 × 2 × 2 supercell representation of the MIL-53(Sc)-*DMF(removed)* structure, corresponding to 16 $ScO_4(OH)_2$ units per simulation box. At 100 and 293 K, the structure was equilibrated for at least 5 ps, whereas the equilibration was extended to 7 ps at 623 K. Following the equilibration, the simulation was continued for at least 5 ps for production of results at 100 and 293 K. The production run was ca. 13 ps at 623 K. The structures were considered converged to a satisfactory level when all cell parameters (i.e., a, b, c, α, β, γ, and V) fluctuated around some mean values. Figure 6.2, for example, illustrates the structural fluctuations of MIL-53(Sc) observed in the AIMD simulations performed at 100 and 623 K – both structures can be considered equilibrated as the cell parameters fluctuate around the mean values. The final, static AIMD-simulated structures, which represent the MIL-53(Sc)-*cp* and -*vnp* forms hereafter, were generated by averaging the corresponding AIMD trajectories after equilibration, followed by an energy minimization at 0 K in conjunction with the time-averaged unit-cell parameters.

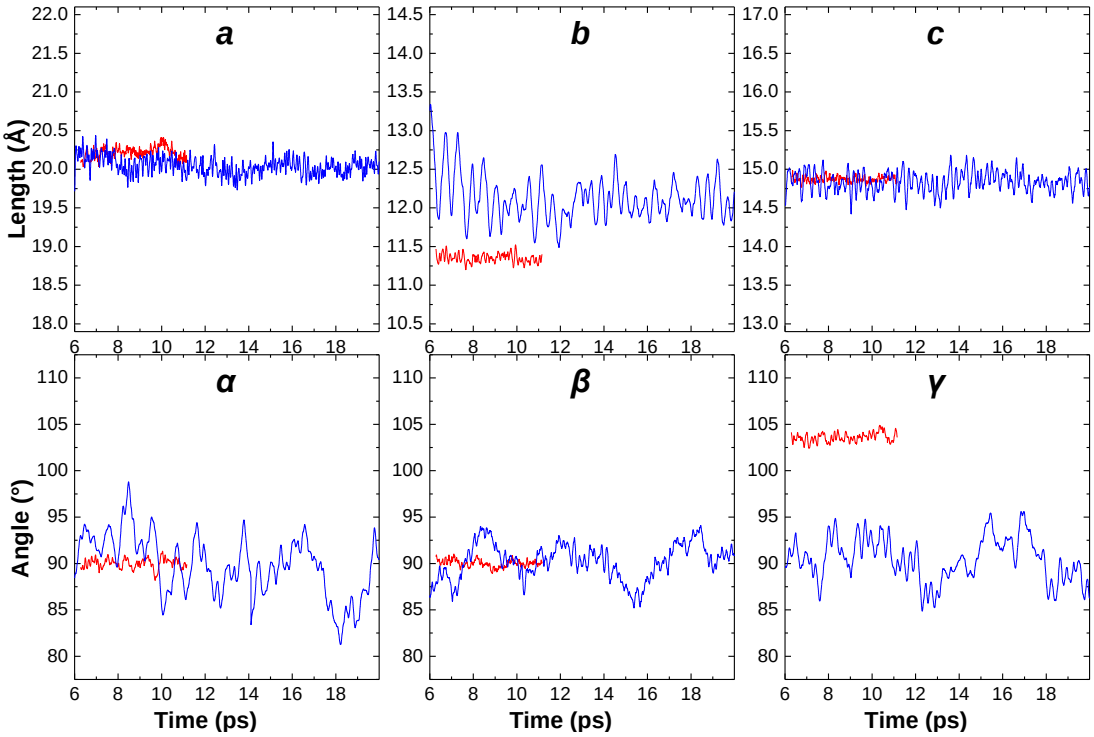

Figure 6.2. Time evolution of the cell parameters during the courses of the AIMD simulations performed at 100 (red) and 623 (blue) K.

6.3.2 AIMD-simulated *cp* and *vnp* forms

The simulated cell parameters and their standard deviations are given in Table 6.1, together with the corresponding values from the experiments (in *italic*) (Mowat et al., 2012). For comparison, the cell parameters for the starting configuration, MIL-53(Sc)-*DMF(removed)*, in these AIMD simulations are also included in Table 6.1 to illustrate the significant structural changes observed between the start and finish of the AIMD simulations. Table 6.1 shows that the agreement between the simulated and experimental unit cells is very good for all three temperatures investigated. The discrepancies are very small and in most cases within the limits of statistical error.

Table 6.1. Comparison of AIMD-simulated and experimental (in *italic*)[a] unit-cell parameters for the *cp* (100 and 293 K) and *vnp* (623 K) forms of MIL-53(Sc).

T (K)	100		293		623		starting[b]
	sim.	*exp.*	sim.	*exp.*	sim.	*exp.*	*exp.*
a (Å)	20.22 ± 0.08	*20.30*	20.33 ± 0.14	*20.33*	20.04 ± 0.13	*19.71*	*19.34*
b (Å)	7.44 ± 0.04	*7.33*	7.44 ± 0.08	*7.33*	7.42 ± 0.20	*7.27*	*7.30*
c (Å)	11.35 ± 0.06	*11.69*	11.48 ± 0.13	*11.84*	13.12 ± 0.15	*13.26*	*18.36*
α (°)	90.00 ± 0.55	*90.00*	90.00 ± 1.15	*90.00*	89.58 ± 3.25	*90.00*	*90.00*
β (°)	103.60 ± 0.52	*104.96*	104.07 ± 1.09	*105.21*	90.25 ± 2.17	*90.00*	*90.00*
γ (°)	90.00 ± 0.40	*90.00*	90.00 ± 0.83	*90.00*	90.36 ± 2.39	*90.00*	*90.00*
V (Å^3)	1658.18 ± 7.82	*1680.75*	1684.89 ± 16.98	*1701.36*	1950.77 ± 43.39	*1901.65*	*2593.16*

[a] Experimental data were taken from the work of Mowat et al (2012). [b] The experimental MIL-53(Sc)-*DMF(removed)* structure (Mowat et al., 2011) was used as the starting configuration for the AIMD simulations at the three temperatures. In order to allow for a direct comparison with the experimental results reported in the literature, the simulated cells (the original simulation cell axes can be seen in Figure 6.2) were aligned with the corresponding experimental ones when reporting the simulation results here.

In addition, a comparison of selected bond distances and angles from the simulations and the experiments (Mowat et al., 2012) is given in Table 6.2. It is clearly demonstrated that the simulated geometries of the Sc hydroxide chains of the framework are in quantitative agreement with the experimental structures at all three temperatures. The differences between simulated and experimental bond distances for Sc–O(μ_2-OH) and Sc–O(RCOO) are, respectively, smaller than 1.5% and 2.4%, while the differences between simulated and experimental Sc–(μ_2-O)–Sc angles are smaller than 2.8% for all three temperatures. These small discrepancies between simulation and

experiment demonstrate the very good performance of the chosen computational setup in describing the chemistry involved in the MIL-53(Sc) solid responding to temperature variations. In particular, the very well reproduced Sc-hydroxide geometry confirms that the BLYP-D3 functional treats the metal–oxygen interactions with a high level of accuracy. The atomic coordinates for the AIMD-simulated MIL-53(Sc)-*cp* and -*vnp* structures can be found in the article by Chen et al (2013).

Table 6.2. Comparison of selected bond distances (Å) and angles (°) for the *cp* (100 and 293 K) and *vnp* (623 K) forms between simulation and experiment (Mowat et al., 2012).[a]

	$d_{Sc–O(\mu_2\text{-}OH)}$		$d_{Sc–O(RCOO)}$		$\angle$ Sc–(μ_2-O)–Sc	
structure	sim.	*exp.*	sim.	*exp.*	sim.	*exp.*
MIL-53(Sc)-*cp*(100 K)	2.105 ± 0.006	*2.090*	2.134 ± 0.009	*2.093*	124.4 ± 0.1	*122.8*
MIL-53(Sc)-*cp*(293 K)	2.108 ± 0.007	*2.109*	2.142 ±0.009	*2.105*	124.2 ± 0.4	*120.8*
MIL-53(Sc)-*vnp*(623 K)	2.099 ± 0.005	*2.068*	2.125 ±0.006	*2.075*	123.5 ± 0.3	*123.2*

[a] Simulation results are reported together with corresponding error bars, which were determined as a 95 % confidence interval while assuming a normal distribution.

In both the experiments and the simulations, remarkable cell-volume reductions were observed upon removal of the DMF molecules from the as-prepared framework; for instance, the structure shrank by as much as 35% at 100 K. Moreover, the AIMD trajectories show that the structural contractions at all three temperatures occurred almost immediately after the simulations started, implying that the as-prepared structure with DMF removed is thermodynamically unfavourable. It is also clear from the standard deviations in Table 6.1 that considerably larger fluctuations in the simulated

cell parameters are associated with the structure at 623 K and that, on the whole, higher temperatures produce larger-amplitude fluctuations (also see Figure 6.2). This observation is, of course, in accordance with thermodynamic principles.

Besides the gradual expansion of the structure, rotation of the chains of $ScO_4(OH)_2$ octahedra around their long axes in response to increasing temperature was observed both experimentally and computationally for MIL-53(Sc). The extent of rotation can be quantified using the angle formed between the two planes defined by the two Sc–(μ_2-O)–Sc groups (shown as dashed lines in Figure 6.3). This angle is 0 ° in the as-prepared framework structure, MIL-53(Sc)-*DMF(removed)*, the starting configuration for all three simulations. Experimentally, the angles were found to be 36 and 0 ° for the structures at 100 and 623 K, respectively (Figure 6.3). As clearly shown in Figure 6.3, the AIMD simulations are able to capture almost quantitatively the rotations of the Sc hydroxide chains observed experimentally at the different temperatures, in addition to the accurate reproduction of the cell expansions seen in Table 6.1. As suggested by these correct predictions of the various MIL-53(Sc) structures, this AIMD-simulation-based modelling approach might serve as a means to predict the response of other forms of MIL-53(Sc) and other MOF structures to temperature. However, as with all simulation methods, care must be taken to ensure that the computational procedure is robust.

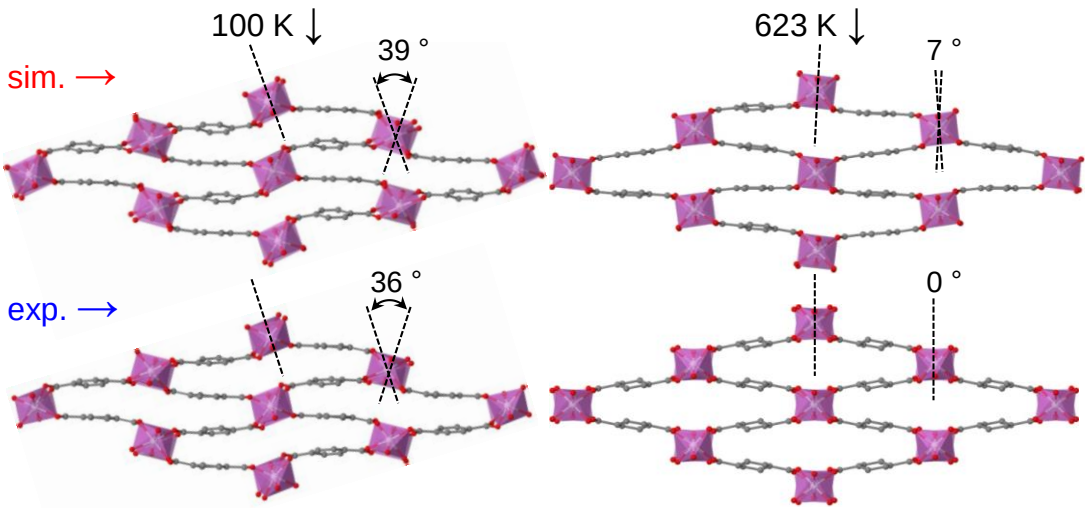

Figure 6.3. Comparison of the rotation of the Sc hydroxide chains in the (top) AIMD-simulated and (bottom) experimental structures at (left) 100 and (right) 623 K. Dashed lines represent the planes of the infinite Sc–(μ_2-O)–Sc chains. Hydrogen atoms were omitted for clarity.

It is also worth noting that the AIMD simulations yielded the correct MIL-53(Sc) structures at the various temperatures without any input based on prior knowledge of the target structures. This level of predictive ability cannot be easily achieved by computational approaches based on energy minimization at 0 K. Therefore, these results show that the entropic effects resulting from molecular motion are successfully included in the AIMD approach. Furthermore, the AIMD simulations provided a dynamic picture on the molecular level that can help in interpreting the unit-cell evolution with increasing temperature. In the AIMD simulations performed at the different temperatures, significantly larger rotational and vibrational movements of the phenyl rings of the terephthalate ligands of the framework were observed at 623 K. The length of the ligand is almost invariant upon cell deformation. Thus, in order to accommodate these large movements of the phenyl rings, the two Sc hydroxide chains corresponding to the short diagonal of the rhombic cross section of the channel have to move away from each other. At the same time, they continue to rotate until they become

parallel to each other, ultimately resulting in unit-cell expansion and the higher symmetry adopted by the solid at 623 K. Interestingly, despite the large movements of the phenyl rings observed in the simulation at 623 K, no complete "flipping" of the rings was found in the ca. 20-ps trajectory (nor was it observed at the lower temperatures). Although the time frame may be too short to establish conclusive evidence, these AIMD simulations suggest that "flipping" may be prevented (probably by sterics) in the less-open forms of MIL-53(Sc), which agrees well with the recent ^{2}H NMR data for the solid measured at 400 K (Wright and Mowat, unpublished data).

6.3.3 Energetics of MIL-53(Sc)-*cp* and -*vnp*

As a further step to elucidate the structural response of MIL-53(Sc) to temperature variations, energetic information was extracted from the simulations. For each of the three MIL-53(Sc) frameworks simulated, the potential energy was determined on the corresponding energy-minimized, time-averaged AIMD structure and is given in Table 6.3. The potential energy of MIL-53(Sc)-*DMF(removed)* was calculated using the energy-minimized, experimental structure. The potential energy values in Table 6.3 unambiguously confirm that the *cp* structure is indeed energetically favoured, corroborating the experimental observation that the solid contracts to adopt the *cp* form upon removal of the guest molecules (water or DMF) from the framework (Mowat et al., 2011; Mowat et al., 2012). The data in Table 6.3 also show that there is a correlation between the potential energy and the volume of the framework, indicating that the structure becomes increasingly energetically unfavourable as it expands.

Table 6.3. Calculated potential energies and volumes for various MIL-53(Sc) framework structures.[a]

structure	ΔE (kJ mol^{-1})	ΔV (Å^3)
MIL-53(Sc)-*cp*(100 K)	0.0	0.0
MIL-53(Sc)-*cp*(293 K)	3.4	26.7
MIL-53(Sc)-*vnp*(623 K)	194.6	292.6
MIL-53(Sc)-*DMF(removed)*	359.6	935.0

[a] Potential energies (ΔE) and volumes (ΔV) were calculated using MIL-53(Sc) frameworks consisting of eisht $ScO_4(OH)_2$ units. For each framework, the two values are reported with respect to those for the MIL-53(Sc)-*cp* structure simulated at 100 K. The potential energies were determined by single-point calculations in which the same exchange–correlation grid (constant density of grid points) was used.

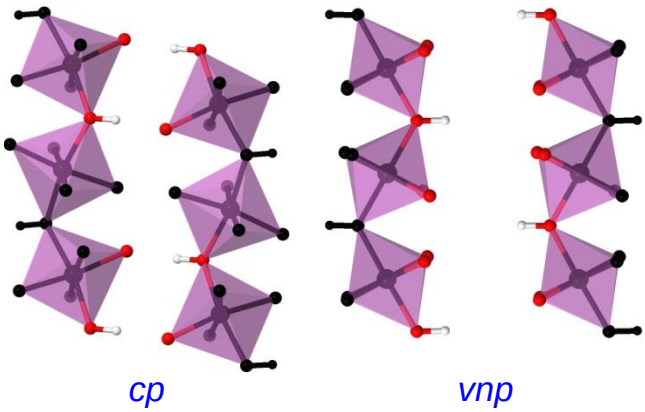

Figure 6.4. Illustration of the different conformations of the two opposite Sc hydroxide chains in the *cp* and *vnp* forms of MIL-53(Sc). The hydroxyl groups in the central channel and their nearest oxygen atoms of the carboxylate groups belonging to the opposite chain are colour coded: white, hydrogen; red, oxygen.

Figure 6.4 provides a structural basis for understanding the relative stabilities of the *cp* and *vnp* structures. In the *cp* structure (at both 100 and 293 K), the two opposite Sc hydroxide chains corresponding to the short diagonal of the rhombic cross section of the channel are present in an energetically favourable conformation. That is, the hydrogen atom of every hydroxyl group interacts strongly with the nearest oxygen atom of the carboxylate group belonging to the opposite chain. The interatomic distances are 2.05 and 2.15 Å at 100 and 293 K, respectively. In contrast, the formation of such

strong and directional hydrogen bonds does not occur in the *vnp* structure (the distance between the pair is 3.8 Å) because of the different alignment of the chains at 623 K compared with the configuration in the *cp* structure (Figure 6.4). Therefore, the predominant hydrogen bonds formed between the two opposite inorganic chains give rise to large intra-framework interactions that in turn cause the *cp* structure to be more stable than the *vnp* structure (Table 6.3). This energetic information complements the dynamic picture of the structural transformation with changing temperature obtained from the AIMD trajectories in explaining why the *vnp* structure can be realized only at much higher temperatures. The larger variations and rotations within the framework (larger kinetic energies) resulting from the higher temperature help to overcome the strong intra-framework interactions present in the *cp* form and eventually stabilize the structure in a relatively high potential energy configuration (i.e., *vnp*).

While an increase in entropy with increasing volume of the framework is likely to be driving the changes in structure observed for MIL-53(Sc), attempts to formally quantify any entropic changes for these systems proved unsuccessful. To quantify entropy for an AIMD simulation would require the calculation of a power spectrum, obtained by Fourier transforming the velocity autocorrelation spectrum, to obtain the phonon modes of vibration, from which an estimate of system entropy can be obtained using statistical thermodynamics partition functions. This analysis was performed for all three AIMD trajectories generated at the different temperatures, but it was found that the low-energy phonons (which make the biggest contribution to the entropy term) were under-expressed in the courses of the ca. 10–20-ps simulation runs. Consequently, the discussions are primarily placed on

energetic grounds (potential and kinetic energies), while referencing to the effects of entropy where appropriate.

The influence of dispersion (or van der Waals) interactions on the MIL-53(Sc) structure needs to be emphasized. A complementary AIMD simulation starting with the *cp* structure (obtained at 100 K with dispersion-corrected DFT *a priori*) was performed at 100 K employing only DFT, which is known to account poorly for dispersion interactions (Kristyán and Pulay, 1994; Cohen et al., 2011; Klimeš and Michaelides, 2012). It was found that the initial *cp* framework gradually opened and the unit-cell volume increased by 30% within 3 ps in the AIMD simulation (Figure 6.5), clearly demonstrating that the dispersion interactions play a pivotal role in maintaining the *cp* structure. The importance of dispersion interactions in determining the MIL-53(Sc) structure is in good agreement with the findings for other flexible MOFs; for example, see Hoffmann et al. (2011), Stavitski et al. (2011), Ghoufi et al. (2012), and Zhang et al (2013).

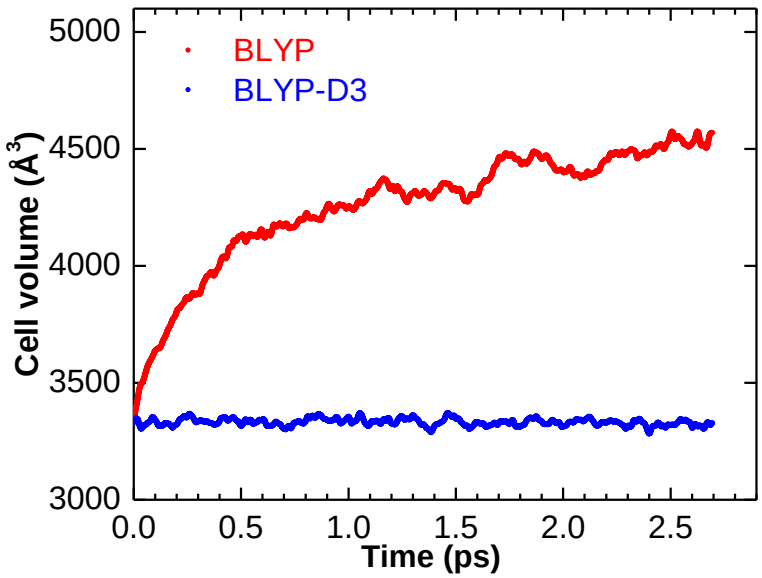

Figure 6.5. Time evolution of the framework volume (corresponding to sixteen $ScO_4(OH)_2$ units) during the AIMD simulations at 100 K. Using the same MIL-53(Sc)-*cp* structure as a starting configuration, the two AIMD simulations were performed employing either the

BLYP functional (i.e., no dispersion corrections) or the dispersion-corrected BLYP-D3 method.

As the long-rang part of the interaction between three ground-state atoms is not exactly equal to the interaction energies taken in pairs, the DFT-D3 method of Grimme et al. (2010) takes into account this three-body effect by including the leading non-additive dispersion term (known as the Axilrod–Teller–Muto or triple dipole term) as derived from the third-order perturbation theory. In the original DFT-D3 paper, Grimme et al. pointed out that inclusion of dispersion non-additivity by the three-body term was not recommended as a default, not least because (at the time) little was known about how their way of calculating the three-body dispersion was treated by standard density functionals in overlapping density regions. Moreover, calculation of three-body energy increases the formal scaling behaviour of the computational cost with system size from $\boldsymbol{O}(N_{\text{atoms}}^2)$ to $\boldsymbol{O}(N_{\text{atoms}}^3)$; nevertheless, its computation cost is still (at least) two to three orders of magnitude smaller than the KS-DFT part of a standard density functional.

For the MIL-53(Sc) MOF studied in this work, it is, however, worth noting that the importance of explicitly taking account of three-body dispersion effects has been found to be nontrivial, even though the magnitude of the three-body contribution to the total DFT-D3 dispersion energy was typically only ca. +7 % (i.e., reduced by 7 %) in the cases of the *cp* and *vnp* structures. Put precisely, a test AIMD simulation employing BLYP-D3 without inclusion of the three-body dispersion resulted in a markedly denser MIL-53(Sc) framework at 100 K, as compared to the experimentally determined *cp* structure at the same temperature. This observation is in line with the generally known phenomena that many-body dispersion energies can have a

significant influence on structural properties of systems such as condensed matters and macromolecules; for example, see Lilienfeld and Tkatchenko (2010). Therefore, it was decided that inclusion of the three-body dispersion energy was necessary to improve the accuracy of the BLYP-D3 description of the MIL-53(Sc) systems; the three-body term was evaluated in all of the DFT-D3 calculations performed in this work.

There is an argument that the empty MIL-53 material should be observed in the *lp* form at high enough temperatures regardless of the nature of the metal and that being able to "reproduce" this *lp* form would be a perfect test case to prove that a chosen combination of exchange–correlation functional and dispersion correction really describes the balance between metal–oxygen and inter-aromatic-ring interactions. To address this argument, two points need to be emphasised with respect to the temperature-responsive breathing phenomena of MIL-53(Sc) studied here. First and foremost, in the experiment MIL-53(Sc) was heated up to 673 K, just 50 K higher than the highest temperature at which the XRD measurements were made. At this temperature the sample began to lose crystallinity and the *lp* form was not observed (Wright and Mowat, personal communication). It is true that one could simulate MIL-53(Sc) at very high temperatures, but in that case any predicted structural changes could not be confirmed experimentally. Second, as demonstrated above, the AIMD-simulated *cp* and *vnp* structures are in very good agreement with experiment from 100 to 623 K. To be specific, Table 6.2 shows the geometry of the Sc hydroxide chains was reproduced very well, indicating the exchange–correlation functional (BLYP) is accurate in describing the metal–oxygen interactions. Furthermore, Figure 6.5 shows that removing the DFT-D3 dispersion correction to the BLYP functional re-opened the initially-closed structure, meaning that dispersion correction is

mandatory and the DFT-D3 method is adequate for accounting properly for the dispersion in the MIL-53(Sc) solid. On the basis of these observations, the BLPY-D3 method, together with the simulation settings used, can be considered a good choice for simulating the breathing behaviours of MIL-53(Sc).

6.4 Structural Response to CO_2 Adsorption at 196 K

6.4.1 Adsorption isotherm and *in situ* XRPD patterns

All of the experimental results in this Section were provided by Professor Paul A. Wright and co-workers, and they are described here for ease of comparison with simulation. Experimental details about the material synthesis, CO_2 adsorption, and *in situ* XRPD measurements can be found in the report by Chen et al (2013).

The CO_2 adsorption behaviour of dehydrated MIL-53(Sc) at 196 K (Mowat et al., 2011) is shown in Figure 6.6 (a). In the adsorption branch of the isotherm, negligible amounts of CO_2 are adsorbed up to 0.05 bar. After that, a first step with adsorption of around 2–3 mmol g^{-1} is observed, followed by a second step (starting at ca. 0.75 bar) to an uptake of ca. 13 mmol g^{-1}. The *in situ* XRPD patterns collected on the MIL-53(Sc) sample during CO_2 adsorption at 196 K (Figure 6.6 (b)) show a remarkable phase evolution of the structure as a function of the CO_2 pressure.

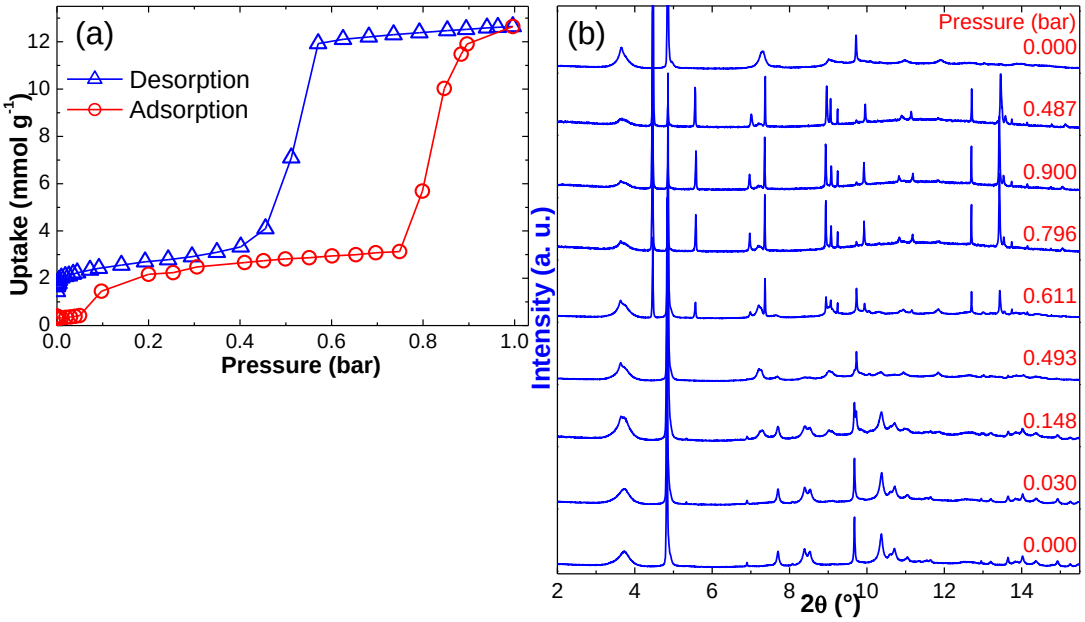

Figure 6.6. Experimental adsorption of CO_2 on dehydrated MIL-53(Sc) at 196 K as followed by XRPD: (a) adsorption and desorption isotherms of CO_2, taken from the report by Mowat et al. (2011); (b) variation of the XRPD patterns with the CO_2 pressure, as reported by Chen et al (2013).

The initial structure after outgassing is the *cp* form, which has no apparent porosity to accommodate any measurable amount of CO_2. This is evident from both the adsorption isotherm and the pattern collected at 0.03 bar, which is largely identical to the one for the starting, evacuated solid. As the partial pressure of CO_2 is increased, characteristic XRPD peaks appear at the same pressure regions where the steps in the adsorption isotherm can be observed, displaying a clear correlation between the structural transformations and the amounts of CO_2 adsorbed. At 0.148 bar, corresponding to the beginning of the first plateau in the adsorption branch, a new XRPD signature can be observed, and it continues to be distinguishable up to higher pressures. The uptake of 2–3 mmol g^{-1} might be accommodated by either an *int* form where half of the channels are partially open and the others are closed (Figure 6.1 (c)) or by a *np* form where all of the channels are partially open (Figure 6.1 (d)). It should be noted that both

forms are observed for MIL-53(Fe) with CO_2 adsorbed (Devic et al., 2012). Further investigations were conducted to determine the structural form and are discussed in detail below. After this initial period of low uptake (2–3 mmol g^{-1}), the second step happens in a much narrower pressure region, and the complete filling of the pores results in a new structural phase, as suggested by the XRPD patterns at the high pressures. However, the existence of the high-pressure form is notably as a mixture with the other forms observed at the lower pressures. The coexistence of multiple crystallites is similar to the previously reported structures of MIL-53(Fe) upon adsorption of (C_2–C_4) alkanes (Llewellyn et al., 2009). Interestingly, although the XRPD patterns show reversible phase transitions upon desorption, the structure observed at the first plateau of the adsorption isotherm rather than the *cp* form was retained in the final, outgassed solid. This somewhat surprising result suggests that a longer evacuation time (and possibly a more aggressive procedure) may be needed to reactivate the solid fully.

6.4.2 MIL-53(Sc) structure at low CO_2 loadings

Motivation for AIMD simulations. According to Professor Paul A. Wright and co-workers, unambiguous indexing of the XRPD pattern at 0.493 bar was unsuccessful because of significant diffraction peak broadening in the experimental pattern (Figure 6.6 (b)). Since the patterns at higher loadings show clear evidence for the high-pressure form as a highly crystalline phase, there is no indication that the broadening was a result of beam damage or other degradation in the synchrotron experiments. Thus, it is more likely to be a structural feature associated with a lowering of crystallographic symmetry. Professor Paul A. Wright and co-workers also noted that Rietveld

refinement using other published MIL-53 structures, including those of MIL-53(Sc), as starting models could not be performed. The reason is that the ambiguity in the unit-cell parameters and the broadened features of the experimental pattern resulted in that a suitable model for refinement could not be found. On the other hand, conventional computational approaches based on energy minimization could not be used to assist the structure determination, because they rely on prior knowledge of both unit-cell parameters and a starting configuration for the target structure. A few examples of the application of such energy-minimization-based approach include the reports by Surble et al. (2006), Devic et al. (2009), and Devic et al (2012). Here, to circumvent these restrictions, the AIMD-simulation-based modelling approach, whose ability to predict structural changes in MIL-53(Sc) in response to temperature variations have already been demonstrated, was used to resolve the structural phase observed at 0.493 bar CO_2 pressure.

Generating MIL-53(Sc)-int and -np structures for a CO_2 loading of 2.2 mmol g^{-1} (eight CO_2 molecules per simulation box). As MIL-53(Sc) exhibits the *cp* form after activation, from a simulation standpoint two scenarios regarding the pore-opening mechanism exist. That is, CO_2 adsorption occurs in either half or all of the channels, leading to the *int* or *np* topology (Figure 6.1 (c, d)), respectively. No conclusive evidence could be established at this stage to verify these structural assignments. Therefore, both hypotheses were tested computationally in parallel. To realize this, the MIL-53(Sc)-*DMF(removed)* structure – in a 1 × 2 × 2 unit-cell representation – was again used as the starting configuration for the framework, while the initial positions of the CO_2 molecules were generated by GCMC simulations of CO_2 adsorption in MIL-53(Sc)-*DMF(removed)* at 196 K. GCMC simulation details, generic force-field parameters for MIL-53(Sc) and CO_2 atoms, and partial atomic charges

for the MIL-53(Sc) framework can be found in Appendix A3. In the simulation box aiming at generating the *int* topology where half of the channels are open while the others are closed, a total of 16 CO_2 molecules were initially placed into the pores by the GCMC simulation; 8 of the 16 CO_2 molecules were then removed from the simulation box manually, leaving half of the channels empty. A schematic diagram demonstrating how the *int* and *np* topologies of MIL-53(Sc) were realized is given in Figure 6.7.

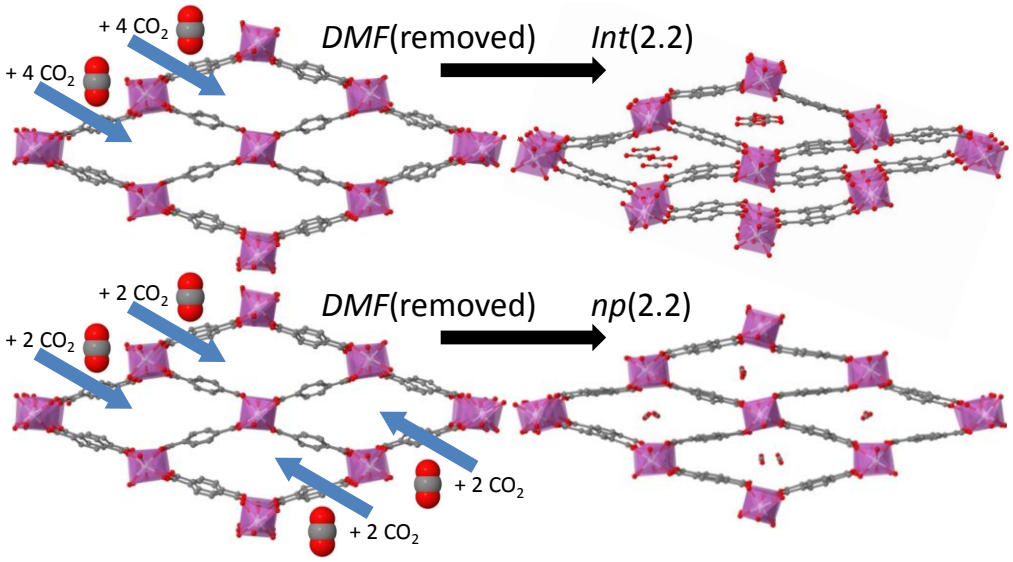

Figure 6.7. Setup of simulations to investigate the structural forms of MIL-53(Sc) for a CO_2 loading of 2.2 mmol g^{-1} (8 CO_2 per simulation box). Hydrogen atoms are omitted for clarity.

With the starting configurations thus obtained, the AIMD simulation for the *int* form was run for 10 ps as equilibration and for further 10 ps as production, while for the *np* counterpart 5 and 5 ps were used. The reason why the AIMD simulation for the *np* topology was not continued after the 10-ps run is twofold. First, the resulting *np* structure was considered equilibrated satisfactorily – no significant variations in the unit-cell parameters were observed during the last 5-ps production run. Second, and more importantly, the presence of the *np* structure in the MIL-53(Sc) solid

could not be established when comparing its simulated pattern with the experimental XRPD patterns (detailed discussion is given below). Comparing the two AIMD simulations for the *int* and *np* topologies, Figure 6.8 clearly shows that the *int* structure is energetically favoured as it stays lower in energy than the *np* structure. This provides the first evidence for MIL-53(Sc) adopting the *int* phase at the first plateau of the CO_2 adsorption isotherm (2–3 mmol g^{-1}).

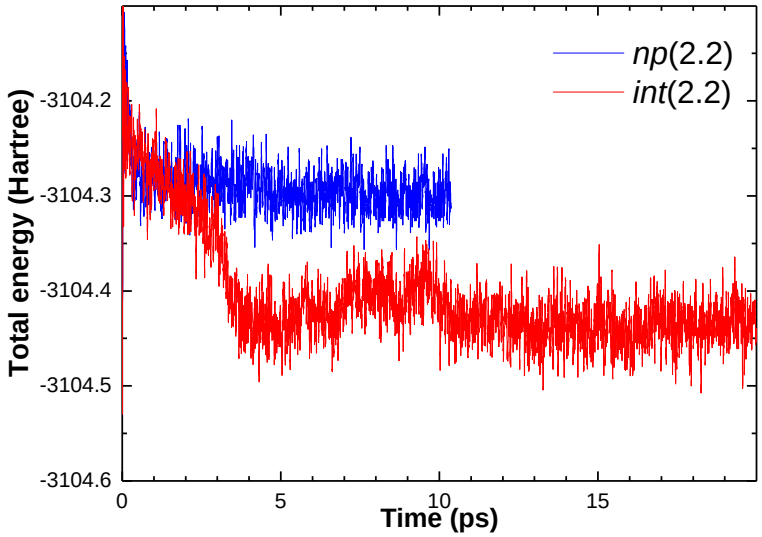

Figure 6.8. Time evolution of the total (= kinetic + potential) energy during the courses of the AIMD simulations for the MIL-53(Sc)-*int* (red) and -*np* (blue) structures at a CO_2 loading of 2.2 mmol g^{-1}.

AIMD-simulated MIL-53(Sc)-int and -np structures. The final representative geometry for either the *int* or the *np* form of MIL-53(Sc) was obtained by averaging the corresponding production-run trajectory, followed by energy-minimizing the time-averaged structure (at 0 K) with respect to the time-averaged cell parameters. The two resulting structures, depicted in Figure 6.9 (a, b), are remarkably different. The uniform distribution of adsorbate CO_2 molecules among all of the channels in the starting MIL-53(Sc)-*DMF(removed)* structure unsurprisingly resulted in the *np* topology where all channels are

partially open (Figure 6.9 (b)). The *np* form has been observed for some MIL-53 solids (Serre et al., 2002; Loiseau et al., 2004; Whitfield et al., 2005). In contrast, the "half-filled" MIL-53(Sc)-*DMF(removed)* structure evolved to the so-called *int* topology, characterized by two sets of diamond-shaped channels with different pore sizes (open and closed), doubling the number of atoms in the unit cell of the as-prepared structure (Figure 6.9 (a)).

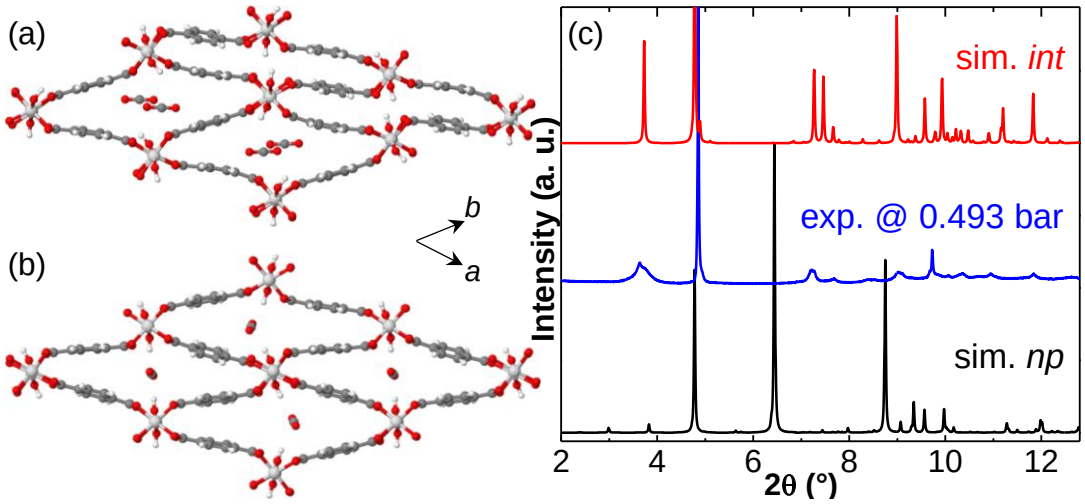

Figure 6.9. Two possible structural forms for MIL-53(Sc) at a CO_2 loading of 2.2 mmol g^{-1} as generated by AIMD simulations: (a) MIL-53(Sc)-*int* and (b) MIL-53(Sc)-*np*. (c) Comparison of the calculated XRPD patterns based on the *int* and *np* structures with the experimental one corresponding to the CO_2 uptake of ca. 2 mmol g^{-1}.

The final energy-minimized, time-averaged AIMD structure for the MIL-53(Sc)-*int* form has a triclinic setting (space group *P* 1) with simulated lattice parameters a = 20.658 ± 0.152 Å, b = 21.211 ± 0.170 Å, c = 7.413 ± 0.093 Å, α = 92.055 ± 0.830 °, β = 88.335 ± 0.547 °, and γ = 38.051 ± 0.445 °. This *int* form induced by the presence of CO_2 in only half of the channels is similar to the hydrated MIL-53(Sc) and the MIL-53(Fe)-*int* structures, although it differs in crystallographic detail. The AIMD-simulated closure of the empty channels observed for the MIL-53(Sc)-*int* structure agrees with the above-described MIL-53(Sc)-*cp* structures simulated at 100 and 293 K – when empty, the

channels of the as-prepared MIL-53(Sc) contracts rather than expands. The atomic positions for the simulated MIL-53(Sc)-*int* and -*np* forms can be found in the report by Chen et al (2013).

It is clear from Figure 6.9 (c) that the experimental XRPD pattern corresponding to the first plateau of the CO_2 adsorption isotherm compares well to the simulated pattern based on the *int* structure, thus confirming that MIL-53(Sc) adopts this form rather than the *np* form. This establishment of MIL-53(Sc)-*int* being responsible for accommodating the CO_2 uptake is in accordance with the observation that the *int* structure is energetically more stable than the *np* structure during the AIMD simulations (Figure 6.8). Furthermore, the *int* phase can be clearly identified in the experimental patterns for pressures ranging from 0.148 to 0.900 bar and during the evacuation (Figure 6.6 (b)). It should be noted that the MIL-53(Sc)-*int* structure is stable during CO_2 adsorption, as opposed to the metastable MIL-53(Fe)-*int* structure or the soft mode observed in the Cr solid (Millange et al., 2008; Llewellyn et al., 2009; Ghoufi et al., 2010).

Diffraction Peak broadening in the int phase. Whereas Figure 6.9 (c) clearly confirms the presence of the MIL-53(Sc)-*int* phase at the first plateau of the CO_2 adsorption isotherm, it also points to the fact that the XRPD peaks based on the static, AIMD-simulated *int* structure (Figure 6.9 (a)) are markedly stronger, sharper, and narrower than those of the experimental pattern. On the other hand, the magnitude of the XRPD peak broadening in the experimental pattern (at 0.493 bar) is much larger than what would normally be expected from a fully crystalline solid at this low temperature (196 K). Indeed, the high-pressure phase shows very sharp diffraction reflections at the same temperature (Figure 6.6 (b)). In this respect, the AIMD simulation

suggests a possible explanation for the strong and anisotropic broadening of the experimental XRPD peaks, which hindered the application of more conventional approaches to solving the structure.

Figure 6.10 shows that the pattern for the averaged structure (i.e., the energy-minimized, time-averaged *int* structure illustrated in Figure 6.9 (a)) gives all of the characteristic peaks observed in the experimental pattern, but the peaks are too narrow, even though the broadening used in the pattern simulation was the same as used for the *lp* form. Averaging a series of patterns based on the snapshots taken during the AIMD simulation (the individual patterns are given in Appendix A5) yielded an even better agreement with the experimental pattern. Therefore, the anisotropically broadened features of the experimental patterns may be interpreted as a result of the motion and disorder of the adsorbent–adsorbate structure, as identified by the AIMD simulation. Put together, framework dynamics, which often causes a loss of long-range order and hence broad peak shapes, has been shown to make structure determination difficult by diffraction on its own, as reported by Rabone et al. (2010) and Stylianou et al. (2012), for example. Here, the averaged pattern is effectively a more realistic representation of the thermally disordered macroscopic sample and hence is in better agreement with the experimental XRPD pattern. In contrast, the averaged structure is an idealized model – a result of the finite-size unit cell and imposed periodic boundary conditions – that is more "crystalline" than the experimental sample, displaying narrower and sharper peaks.

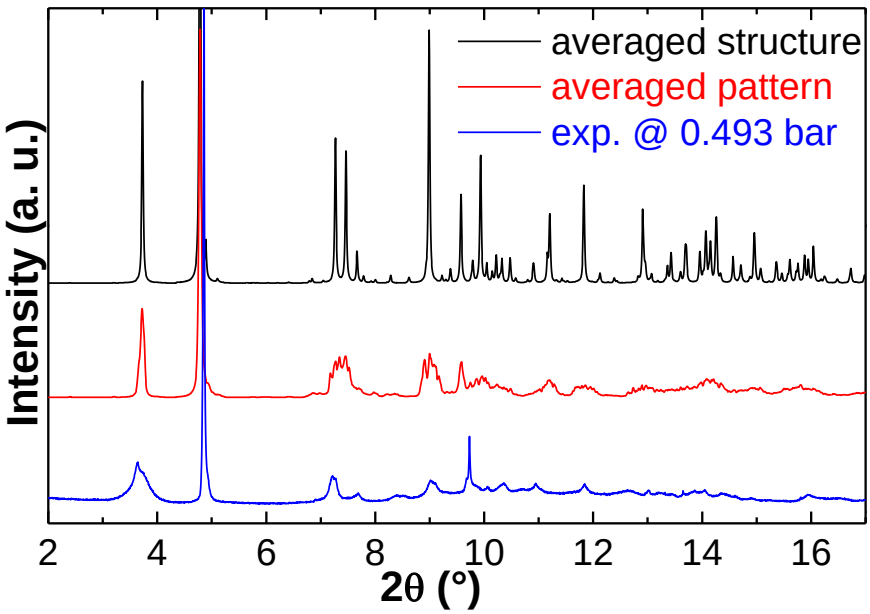

Figure 6.10. Comparison of the experimental XRPD pattern collected at a CO_2 pressure of 0.493 bar with two calculated patterns based on the AIMD-simulated MIL-53(Sc)-*int* form at a CO_2 loading of 2.2 mmol g^{-1}. The "averaged structure" (in black) was calculated on the energy-minimized, time-averaged AIMD structure shown in Figure 6.9 (a), while the "averaged pattern" (in red) was generated by averaging over a series of patterns based on snapshot structures from the same AIMD trajectory used to obtain the averaged structure.

The above explanation for the diffraction peak broadening in the *int* phase, as suggested by the AIMD simulations, is further supported by the investigation of the *lp* form presented below. In brief, the averaged pattern (based on a series of AIMD-simulated structures) for a fully loaded *lp* structure is in very good agreement with the experimental high-pressure XRPD pattern; that is, the experimental peaks are narrow and sharp, so are the ones of the averaged AIMD *lp* pattern. This indicates that the significantly broadened XRPD peaks for the *int* phase indeed result from the molecular motion and long-range disorder of the adsorbent–adsorbate structure at the low CO_2 loading.

Molecular-level interactions in MIL-53(Sc)-int. A close inspection of the conformations of the CO_2 molecules located in the open channels of the *int* structure reveals the microscopic adsorption mechanism, as identified by the

AIMD simulation. Figure 6.9 (a) shows that the CO_2 molecules are aligned with the long diagonal of the rhombic cross section of the channel and are positioned at the centre of the pores, interacting strongly with the hydroxyl groups of the two opposite Sc hydroxide chains corresponding to the short diagonal of the rhombus shape. The CO_2 molecules are closely "stacked" along the channel and are almost parallel to each other, forming a zigzag-like chain of CO_2 along the channel direction as illustrated in Figure 6.11 (a). Every CO_2 molecule is slightly tilted and displaced to favour a conformation in which an oxygen atom of each CO_2 molecule "pulls" the carbon atom of a neighbouring CO_2 molecule.

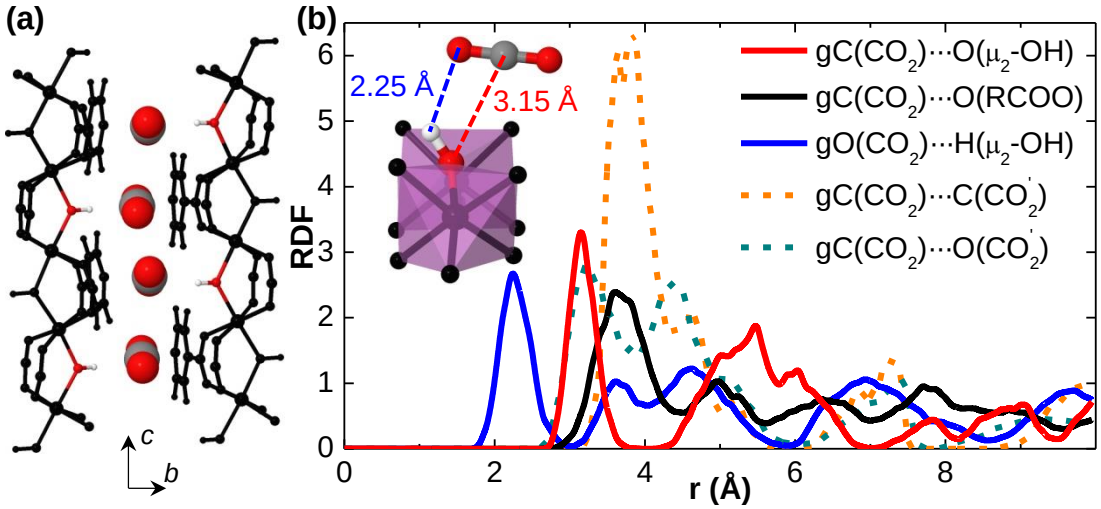

Figure 6.11. AIMD-simulated MIL-53(Sc)-*int* structure for a CO_2 loading of 2.2 mmol g^{-1}. (a) View of the partially open channels, where the CO_2 molecules and hydroxyl groups are colour coded: white, hydrogen; grey, carbon; red, oxygen. (b) Radial distribution functions computed over the last 10 ps of the AIMD simulation. The double interaction between a CO_2 molecule and a hydroxyl group of the framework is shown in the inset in (b).

Radial distribution functions (RDFs) (Levine et al., 2011) were utilized to characterize time-resolved conformational changes of the adsorbed CO_2 molecule with respect to other CO_2 molecules and the framework (Figure 6.11 (b)). The characteristic distance between the carbon atoms of two

adjacent CO_2 molecules, $C(CO_2)\cdots C(CO_2')$, is 3.65 Å, measured by the first distinct peak of the RDF for the pair. Likewise, the RDF plotted for the $C(CO_2)\cdots O(CO_2')$ pair confirms the close proximity by displaying the first peak centred at 3.30 Å. These short distances between adjacent CO_2 molecules along the channel give rise to strong CO_2–CO_2 interactions. These observations from the AIMD simulations performed here are in line with the joint experimental and theoretical investigation of CO_2 adsorption in MIL-53(Cr) reported previously (Serre et al., 2007). However, the distances between neighbouring CO_2 molecules in MIL-53(Sc) are larger than the ones observed in the case of MIL-53(Cr), where $C(CO_2)\cdots C(CO_2')$ and $C(CO_2)\cdots O(CO_2')$ were 3.40 and 3.15 Å, respectively. This might be explained partly by the larger *c* dimension of the MIL-53(Sc) unit cell resulting from the larger ionic radius of Sc^{3+}.

In the adsorption of CO_2 in both MIL-53(Sc) studied here and MIL-53(Cr) reported by Serre et al. (2007), the CO_2 molecules confined in the *np* channels of the MOFs displayed rather short CO_2–CO_2 intermolecular distances: 3.65 and 3.40 Å in the Sc and Cr forms, respectively. These short distances are close to the typical distances (3.24–3.56 Å) observed in the solid-state CO_2 (Yoo et al., 2002). The appearance of such short CO_2–CO_2 distances primarily arises from that each adsorbed CO_2 molecule is "anchored" by one hydroxyl group of the MOF, which is described and discussed in detail below. At one atmosphere, CO_2 deposits directly to a solid at temperatures below 194.65 K, and the solid sublimes directly to a gas above the temperature (i.e., 194.65 K). Considering that the *NPT*-AIMD simulations of CO_2 in MIL-53(Sc) were performed at 1 bar at 196 K, a solidlike CO_2 may thus be expected to be present in the *np* channels. Indeed, a known consequence of an adsorbate confined in a strongly attractive pore is that the in-pore freezing temperature

of the adsorbate can be higher than that of its bulk phase. This implies that in the simulations at 196 K, although higher than 194.65 K, the CO_2 was still possible to be in its solid state. To assess more rigorously a possible crystallization of CO_2 inside the MOF channels, one could apply the so-called Hansen–Verlet criterion (Hansen and Verlet, 1969), an empirical but nevertheless important criterion for freezing. Other criteria for freezing exist, such as the Löwen–Palberg–Simon dynamical freezing criterion (Löwen et al., 1993), the criterion based on the split second peak of the radial distribution function from Ranganathan and Pathak (1992), and the criterion based on the bimodal distribution profile of the shape factor of Voronoi polygons from Moučka and Nezbeda (2005). A detailed study on whether the adsorbate CO_2 is frozen inside the MIL-53(Sc) framework is, however, beyond the scope of the current study.

More significantly, the AIMD simulations show the formation of electron donor–acceptor (EDA) complexes between the adsorbed CO_2 molecules and the framework. As illustrated in Figure 6.11 (a), each adsorbed CO_2 molecule is situated in close proximity to a hydroxyl group of the framework. The CO_2 and the hydroxyl group are "bridged" by a double interaction consisting of the C(CO_2)···O(μ_2-OH) and O(CO_2)···H(μ_2-OH) interactions (see inset in Figure 6.11 (b)), as confirmed by the characteristic peaks centred at 3.15 and 2.25 Å, respectively, in the corresponding RDFs. Moreover, the fact that the C(CO_2)···O(μ_2-OH) distance (3.15 Å) is shorter than the C(CO_2)···O(RCOO) distance (3.55 Å) demonstrates that the carbon atom of the CO_2 molecule interacts preferentially with the oxygen atom of the hydroxyl group over that of the carboxylate group of the framework. In other words, the EDA complex is formed between the C(CO_2) acting as the electron acceptor and the O(μ_2-OH) acting as the electron donor. These observations from the AIMD

simulations thus provide the first evidence concerning the nature of the strong CO_2–framework interactions in the MIL-53(Sc)-*int* structure. The location of the CO_2 molecules relative to the hydroxyl groups of the framework (Figure 6.11) is similar to that for the C(CO_2)···O(μ_2-OH) EDA complexes reported for CO_2 adsorption in MIL-53(Cr) and non-functionalized MIL-53(Fe) (Serre et al., 2007; Vimont et al., 2007; Devic et al., 2012). However, further experimental investigations such as infrared spectroscopic measurements – for example, as demonstrated by Vimont et al. (2007) – are necessary to judge the accuracy of this modelling prediction. The strong CO_2–CO_2 interactions present in the *int* structure are essential for facilitating the observed C(CO_2)···O(μ_2-OH) EDA complexes (see below for further discussion). This EDA-related phenomenon has been explored by several DFT studies on various MIL-53 solids, such as the reports by Serre et al. (2007) and Devic et al (2012). In those studies, the CO_2 molecules were typically placed inside the framework initially by the simulator. Different CO_2 configurations relative to the framework were then examined by energy-minimization calculations at 0 K, in which one would not normally expect to see dramatic steric changes. In contrast, the AIMD simulations performed here arrived at the final configurations starting from a completely different picture, as clearly demonstrated by the structural evolution of MIL-53(Sc)-*int* during the course of the AIMD simulation given in Appendix A4.

In passing, it is worth noting that the dispersion interactions were again found to be crucial for stabilizing the *int* structure. It is clear from Figure 6.12 that the volume of the CO_2-loaded framework increased by more than 60% within 3 ps in the AIMD simulation when dispersion corrections were not applied to the DFT calculations.

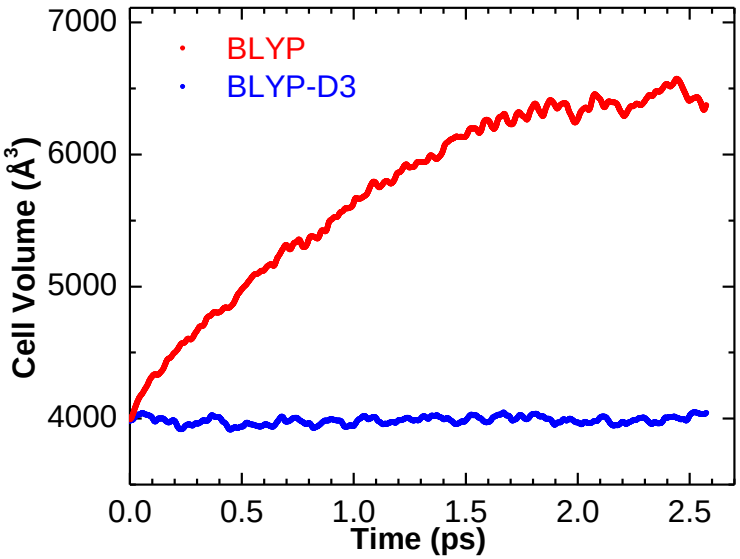

Figure 6.12. Time evolution of the framework volume (corresponding to sixteen $ScO_4(OH)_2$ units) during the AIMD simulations with a CO_2 loading of 2.2 mmol g^{-1} at 196 K. Using the same MIL-53(Sc)-*int* structure as a starting configuration, the two AIMD simulations were performed employing either the BLYP functional (i.e., no dispersion corrections) or the dispersion-corrected BLYP-D3 method.

Molecular-level interactions in MIL-53(Sc)-np. Despite the fact that the presence of the *np* topology cannot be established in any of the experimental XRPD patterns collected during the CO_2 adsorption in MIL-53(Sc), a close look at the AIMD-simulated *np* structure and a comparison with MIL-53(Sc)-*int*, nevertheless, are helpful to understand the important role played by the CO_2–CO_2 interaction in influencing the nature of the CO_2–framework interaction. The results for MIL-53(Sc)-*np* are summarized in Figure 6.13.

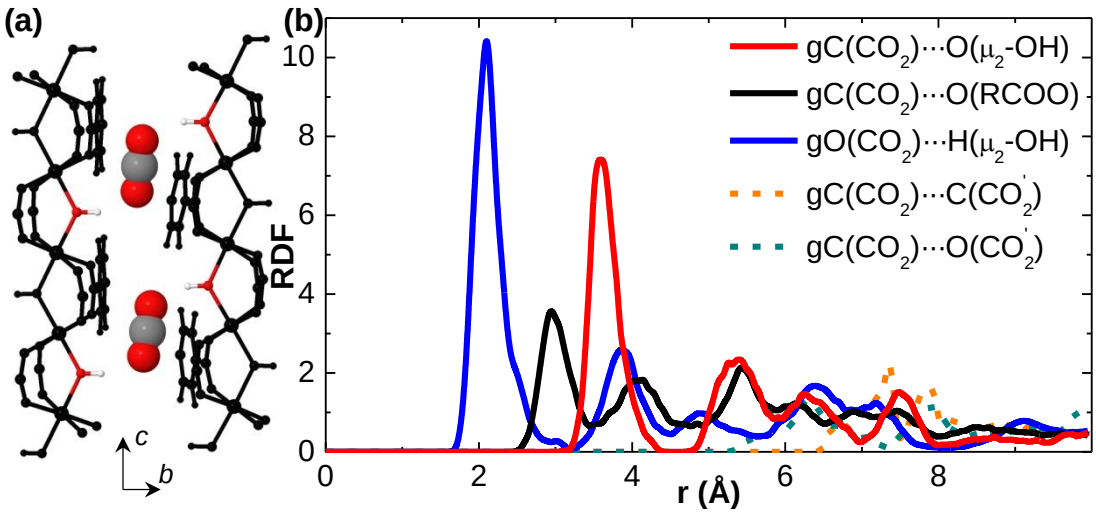

Figure 6.13. AIMD-simulated MIL-53(Sc)-*np* structure for a CO_2 loading of 2.2 mmol g^{-1}. (a) View of the partially open channels, where the CO_2 molecules and hydroxyl groups are colour coded: white, hydrogen; grey, carbon; red, oxygen. (b) Radial distribution functions computed over the last 5 ps of the AIMD simulation.

In contrast to the MIL-53(Sc)-*int* structure (Figure 6.9 (a)) for the same CO_2 loading, the CO_2 molecules are uniformly distributed among all of the channels in the *np* form (Figure 6.9 (b)), resulting in a lower density of CO_2 in each channel compared to that in an open channel of the *int* form. The smaller amount of CO_2 molecules located in each of the channels in the *np* structure helps to relax the steric confinements of the CO_2 molecules along the channel, which are present in the *int* structure (Figure 6.11 (a)). Such steric relaxation is confirmed by the characteristic RDF peaks for the C(CO_2)···C(CO_2′) and C(CO_2)···O(CO_2′) pairs being centred at 7.35 and 6.30 Å, respectively (Figure 6.13 (b)). The lower density of CO_2 in one channel gives rise to a different CO_2–framework conformation compared to the one observed for the *int* form. Figure 6.13 (a) shows that the CO_2 molecules align themselves primarily with the *c* axis (channel direction) and orient so as to "bridge" two hydroxyl groups of the two opposite Sc hydroxide chains corresponding to the short diagonal of the rhombic cross section of the channel. Compared to the double interaction between one CO_2 and one

hydroxyl group in the *int* structure (Figure 6.11), a different type of double interaction in the *np* structure is formed between one CO_2 and two hydroxyl groups, consisting of two hydrogen-bond interactions – the first RDF peak for O(CO_2)···H(μ_2-OH) is at 2.10 Å (Figure 6.13). Moreover, the carbon atom of a CO_2 molecule on longer interacts preferentially with the oxygen atom of a hydroxyl group, but instead forms an EDA complex with the nearest oxygen atom that belongs to a carboxylate group of the framework, as indicated by the characteristic distances of the C(CO_2)···O(μ_2-OH)) and C(CO_2)···O(RCOO) pairs being 3.60 and 3.00 Å, respectively.

In summary, the two structural forms (i.e., *int* and *np*) exhibit remarkably different arrangements of the CO_2 molecules located in the open channels. The ultimate adsorption mechanism is collectively influenced by the natures of the CO_2–framework and CO_2–CO_2 interactions. From the perspective of simulation, these finely distinguished molecular-level interactions in the *int* and *np* forms, especially concerning the different EDA complexes predicted, highlight the power and promise of the AIMD method for the prediction and understanding of the behaviour of flexible MOFs. Predicting the formation of an EDA complex is fundamentally challenging for MD simulations based on classical force fields, mainly because only the electrostatic and vdW interactions are taken into account by such force fields when calculating intermolecular interactions. Nevertheless, Salles et al. (2008) reported that for CO_2 adsorption in MIL-53(Cr) their force-field-based prediction of the double interaction between a CO_2 and a hydroxyl group of the framework agreed well with that determined in a DFT study – this good reproduction, however, may be considered more effective than physically meaningful. On the other hand, when using a DFT-based geometry-optimization method at 0 K, a simulated EDA complex could be biased by human intuition, as initial

configurations, which need specifying by the simulator, do play a role in such calculations. AIMD simulations can be advantageous in these aspects.

6.4.3 MIL-53(Sc) structure at high CO_2 loadings

The structural phase observed at high CO_2 pressures (0.611–0.900 bar) was also determined by AIMD simulations. The maximum number of CO_2 molecules that could be fitted in the pores of the MIL-53(Sc)-*DMF(removed)* structure using GCMC simulations was only 7 CO_2 molecules per unit cell. Higher loadings were realized by progressively adding CO_2 molecules into the framework expanded by AIMD simulations at the current loading, virtually analogous to the adsorption experiment. Note that these supplementary, intermediate structures – i.e., MIL-53(Sc) with a loading of 8, 10, 12, or 14 CO_2 per unit cell of the *DMF(removed)* structure – were not necessarily equilibrated before the new CO_2 molecules were inserted into the framework manually based on chemical intuitions.

The MIL-53(Sc) structure with a loading of 16 CO_2 per unit cell of the *DMF(removed)* structure was found to give a simulated XRPD pattern in very good agreement with the experimental one at 0.900 bar. Therefore, this structure is denoted as MIL-53(Sc)-*lp*, and was equilibrated in the AIMD simulation for 5 ps, followed by a production run of another 5 ps. Averaging the AIMD trajectory of the production run thus gave a time-averaged structure for MIL-53(Sc)-*lp*, which was then energy-minimized at 0 K where the atomic coordinates were fully optimized with respect to the time-averaged AIMD-simulated cell parameters. The resulting MIL-53(Sc)-*lp* structure has an orthorhombic unit cell with lattice parameters a = 7.354 ± 0.100 Å, b = 17.155 ± 0.112 Å, c = 13.442 ± 0.068 Å, α = 90.000 ± 0.383 °, β =

90.000 ± 0.431 °, and γ = 90.000 ± 0.338 °, in very good agreement with the experimentally indexed orthorhombic *Imma* cell with parameters *a* = 7.310(1) Å, *b* = 17.029(2) Å, and *c* = 13.504(1) Å.

In parallel, since the lattice parameters of the *lp* structure were known from the experiment, they were used to identify the atomic positions of the framework atoms by applying a procedure based on molecular energy minimization calculations. Thereafter, the positions of the adsorbed CO_2 molecules were included and optimized using GCMC simulations. This work was carried out by Doctor David Fairen-Jimenez at University of Cambridge. Details about this computational procedure can be found, for example, in the report by Fairen-Jimenez et al (2012).

Figure 6.14 compares the experimental XRPD pattern collected at a CO_2 pressure of 0.900 bar with simulated patterns based on the two computationally anticipated structures (models 1 and 2). It is clear that both modelling approaches – i.e., the AIMD simulation (model 1) and the energy minimization in conjunction with the experimental unit cell (model 2) – were able to assist in determining the structure of the *lp* phase. While the energy-minimization-based approach is computationally much less expensive and is therefore the obvious choice when the cell parameters are known experimentally, the computationally more expensive AIMD method is the only viable option if the experimental cell parameters are not known *a priori*.

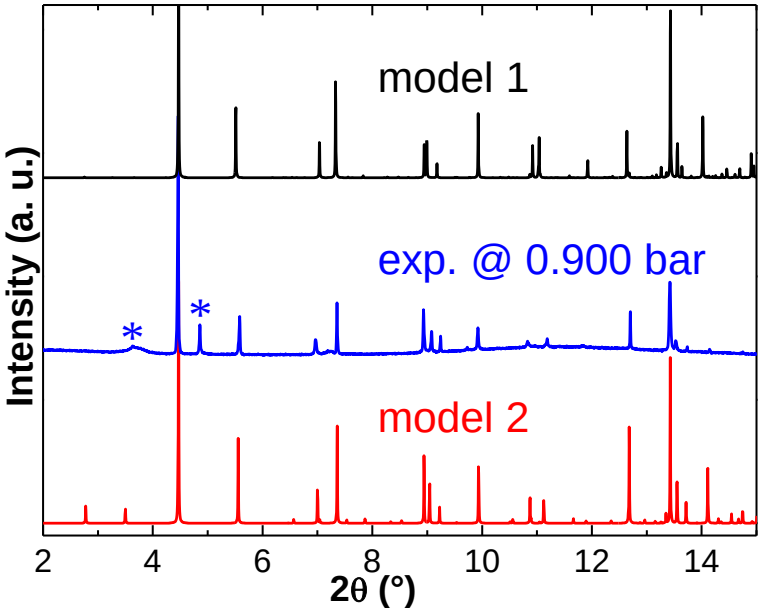

Figure 6.14. Comparison of the experimental XRPD pattern collected at a CO_2 pressure of 0.900 bar with the patterns for two computational *lp* models: model 1 was realized by AIMD simulations, and model 2 was generated through a combination of GCMC simulations and energy minimizations in conjunction with the experimental unit cell. Diffraction peaks marked with * indicate residual MIL-53(Sc)-*int* and were excluded when fitting the MIL-53(Sc)-*lp* pattern and comparing with the simulated patterns. Model 2 results in a slightly better agreement with the experimental pattern, as R_{wp} values of ca. 10% and ca. 8% were obtained for models 1 and 2, respectively.

As mentioned above, the experimental XRPD patterns reported in Figure 6.6 (b) reveal that the high-pressure phase (i.e., the *lp* structure) is highly crystalline with narrow and sharp diffraction peaks, whereas the pattern collected at a CO_2 pressure of 0.493 bar (i.e., the *int* phase) is strongly and anisotropically broadened. The latter is thereby suggested to be a result of the motion and long-range disorder of the adsorbent–adsorbate structure, as identified by the AIMD simulation (Figure 6.10). It is thus interesting to see, in the case of the *lp* form, how the pattern for the time-averaged (static) structure compares with the averaged pattern based on a series of snapshot AIMD structures. In Figure 6.15, the notations of "averaged structure" and "averaged pattern" are in analogy to the ones described previously for Figure 6.10.

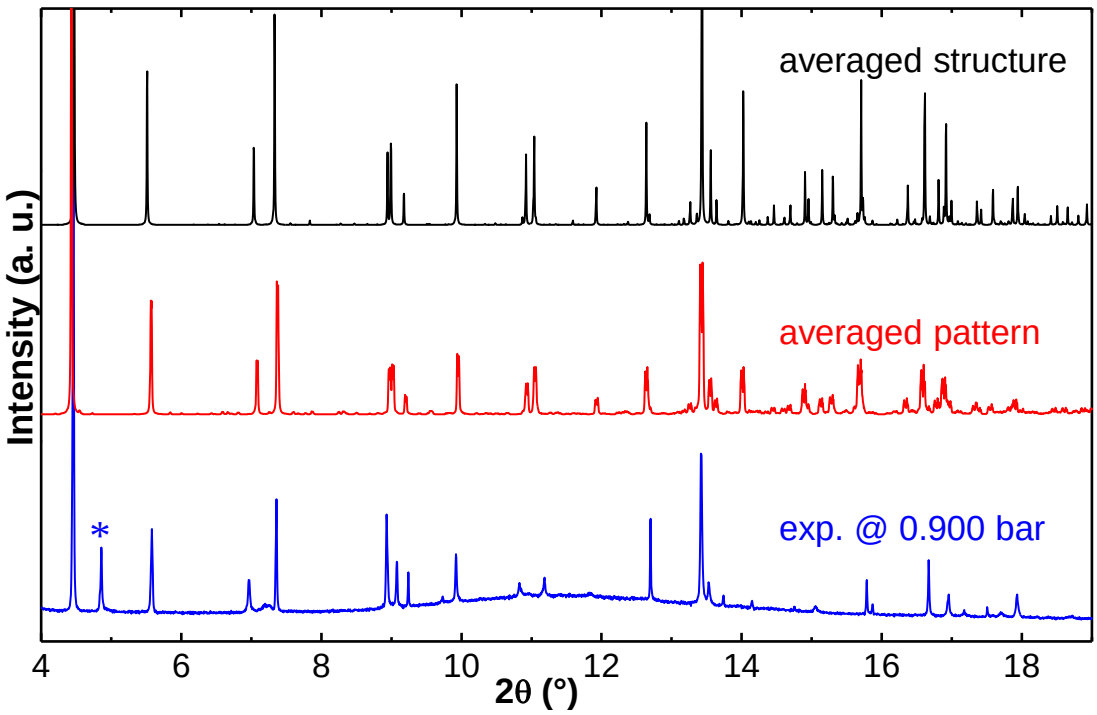

Figure 6.15. Comparison of the experimental XRPD pattern collected at a CO_2 pressure of 0.900 bar with two calculated patterns based on the AIMD-simulated MIL-53(Sc)-*lp* form. The "averaged structure" (in black) was calculated on the energy-minimized, time-averaged AIMD structure (model 1 in Figure 6.14), while the "averaged pattern" (in red) was generated by averaging over a series of patterns based on snapshot structures from the same AIMD trajectory used to obtain the averaged structure.

First, the two simulated XRPD patterns compare very well with the experimental one. Similar to the case of MIL-53(Sc)-*int* (Figure 6.10), the averaged pattern for MIL-53(Sc)-*lp* (the individual patterns are given in Appendix A5) is again in better agreement with experiment compared to the pattern based on the averaged structure, especially in terms of the intensities of the diffraction peaks at, for example, > ca. 13.5 ° 2θ. Second, Figure 6.15 shows that the XRPD peaks of the averaged pattern are broader and less sharp than the corresponding ones of the pattern for the averaged structure. This was expected for the same reasons discussed above for the MIL-53(Sc)-*int* phase – the averaged structure is an idealized model with a higher degree of periodicity than the macroscopic sample, whose long-range disorder may be better represented by the averaged pattern. Comparing the two averaged

patterns for the *int* and *lp* structures (Figures 6.10 and 6.15), it is clear that the magnitude of diffraction-peak broadening is considerably larger in the *int* form than in the *lp* form, in line with the experimental XRPD patterns for the two structural phases. In other words, the AIMD simulations suggest that the *lp* structure exhibits remarkably smaller molecular motion and/or long-range disorder compared to those observed for the *int* structure. This is not difficult to understand, given the fact that the very large loading of 16 CO_2 molecules per unit cell in the *lp* structure prevents the framework and the adsorbed CO_2 from moving substantially.

The AIMD simulations indicate that 16 CO_2 molecules can be accommodated per unit cell of the *lp* structure, while the maximum uptake observed experimentally is ca. 13 mmol g^{-1} (corresponding to ca. 12 CO_2 molecules per unit cell). This suggests that a fraction of the pores in the solid remains closed even at this high uptake, which is in line with the *in situ* XRPD measurements (Figure 6.6 (b)) that suggest the coexistence of *int* and *lp* phases. It can thus be concluded that during CO_2 adsorption two structural transformations occur (i.e., *cp* → *int* and *int* → *lp*) and that MIL-53(Sc) adopts a mixture of two phases over a wide pressure range, probably as a result of kinetic restrictions.

It is worth noting that the molecular-level adsorption mechanism in MIL-53(Sc)-*lp* as identified by the AIMD simulations is markedly different from the one described previously for the *int* phase. In contrast to the clear establishment of C(CO_2)···O(μ_2-OH) EDA complexes in the *int* form, where each CO_2 molecule is strongly "anchored" by a hydroxyl group (Figure 6.11), the *lp* AIMD simulation indicates that C(CO_2) no longer exclusively interacts with O(μ_2-OH) but rather shows more frequent preferential arrangements

with O(RCOO). In addition, the interatomic distances of the pairs defined in Figure 6.11 (b) are consistently smaller than the ones in the *int* form, because of the condensation of CO_2 in the pores at this high loading (16 CO_2 molecules per unit cell). These observations are in line with findings made for the adsorption of small gas molecules in *lp* MIL-53(Cr) and MIL-47 (Bourrelly et al., 2005; Bourrelly et al., 2010; Hamon et al., 2011).

6.4.4 Energetics of the different forms and structural transformations

Potential energies of the various empty MIL-53(Sc) framework structures. Further fundamental insight into the different structural forms of MIL-53(Sc) upon CO_2 adsorption can be obtained by analysing the potential energies of the framework structures. Table 6.4 summarizes the potential energies determined for the empty frameworks; that is, the CO_2 molecules were first removed from the MIL-53(Sc)-*int*, *-np*, and *-lp* structures and then single-point BLYP-D3 calculations using the same exchange–correlation grid were performed to obtain the potential energies for the empty framework structures. On the basis of these results and the potential energies of the *vnp* framework and the *DMF(removed)* as-prepared framework reported in Table 6.3, it is clear that the *cp* structure is indeed the global minimum for a given temperature, as the energy of any other form is greater than that of the *cp* form (i.e., $\Delta E > 0$). It can also be seen that the more open the structure is, the more energetically unfavourable it becomes (Tables 6.3 and 6.4). This decreasing structural stability with expansion of the framework can be largely attributed to the decrease in dispersion interactions as the structure becomes increasingly less dense (Figure 6.16). These observations obtained for MIL-53(Sc) are in agreement with the generally known phenomenon in flexible MOFs that dispersion interactions scale strongly with the density of

the framework, as reported by Nijem et al. (2011), for example. The only outlier in this energy–volume correlation is the *int* structure, which is more stable than the *vnp* structure even though it has a larger cell volume. This can be rationalized by the fact that the *int* structure has one-half of its channels remaining in the *cp* form, which has a much lower energy than the *vnp* form.

Table 6.4. Potential energies and volumes for the empty MIL-53(Sc) structures.

structure	ΔE (kJ mol^{-1})[a]	ΔV (Å^3)[a]
MIL-53(Sc)-*cp*	0.0	0.0
MIL-53(Sc)-*int*[b]	146.6	334.1
MIL-53(Sc)-*np*[b]	318.9	661.6
MIL-53(Sc)-*lp*[b]	644.5	1733.5

[a] Potential energies (ΔE) and volumes (ΔV) for framework structures consisting of eight $ScO_4(OH)_2$ units relative to those of the *cp* structure simulated at 100 K. [b] Prior to the calculation, the CO_2 molecules were removed. All of the energies were determined by single-point calculations in which the same exchange–correlation grid (constant density of grid points) was used.

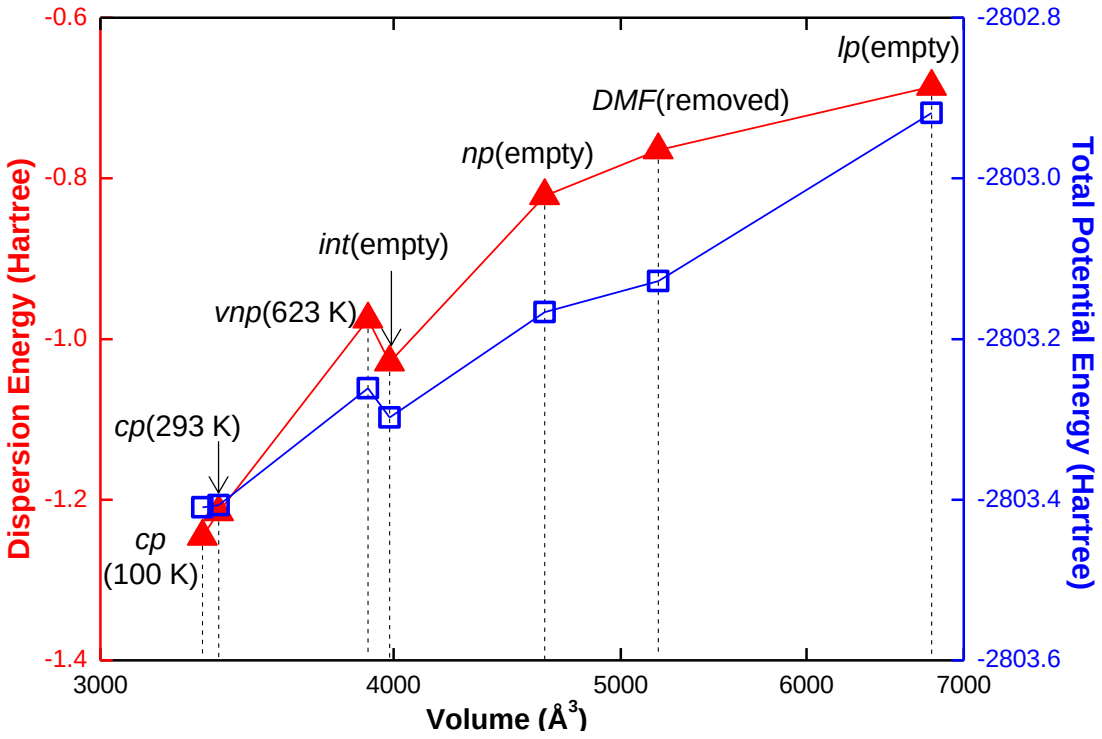

Figure 6.16. Total potential energies, together with the corresponding dispersion contributions according to the DFT-D3 correction, were plotted as a function of the framework volume for all empty MIL-53(Sc) structures generated by the AIMD simulations. Both the energies and the volumes are for frameworks consisting of sixteen $ScO_4(OH)_2$ units, and the energies were calculated using the same exchange–correlation grid (constant density of grid points). Note that the volume is presented on a logarithmic scale and the two vertical axes have the same magnitude (i.e., 0.8 Hartree). The lines were added to guide the eye.

It should be emphasized that the calculated potential energy of a particular form of MIL-53(Sc) is the internal energy at 0 K for the particular framework configuration induced by changes in either temperature or CO_2 uptake. The energetic information of this kind may be indicative of the relative stabilities of the different empty framework structures, but does not necessarily convey information on the actual structural transformations in response to an external stimulus. To be specific, in the absence of guest molecules, increasing the temperature converts the structure from the *cp* form to the *vnp* form rather than the *int* form – this would seem counter intuitive if solely taking into account the energetic data in Tables 6.3 and 6.4. The reason why

the *vnp* form rather than the *int* form is adopted by the solid at 623 K is that the half-closed structure would restrict large motions that are inevitable at this high temperature. This is in essence the same as stating that the *vnp* form is observed in place of the *cp* form at 623 K, even though the *cp* phase has the lower potential energy.

The relative stabilities of the various structural forms therefore allow for an interpretation of the different breathing behaviours of the different MIL-53 solids upon evacuation. Removing guest molecules from the MIL-53(Sc) framework always results in the *cp* structure (or the *vnp* form if the solid is heated up to 623 K), because it is the most energetically favoured. In contrast, outgassed MIL-53(Cr) adopts the *lp* phase, in line with a previous theoretical study in which the dehydrated *lp* structure was found to be lower in energy (more stable) than its *np* counterpart (Coombes et al., 2008).

Up to the completion of this Thesis, there have been considerable efforts devoted to the understanding of adsorption-induced structural deformation and phase transition in flexible MOFs. In general, two key fundamental concepts are called for when interpreting MOF flexibility. First, the adsorption-induced deformation can be viewed as a response of the flexible MOF to an adsorption-induced stress, exerted by the adsorbed fluid on the host solid; for example, see Neimark et al. (2009) and Triguero et al. (2011). Second, an insightful thermodynamic description of the interplay between adsorption and MOF deformation (including phase transitions) can be provided by analysing the free energy profiles. In particular, the osmotic ensemble, a semi-open statistic-mechanical ensemble, has been frequently used, in which the thermodynamic control parameters are the amount of MOF material, the temperature, the gas chemical potential, and the

mechanical pressure on the crystal. The osmotic ensemble has been used by several groups to build theoretical models for studying the influence of adsorption on the equilibrium between metastable host structures, allowing them to rationalize the structural transitions observed experimentally (Coudert et al., 2008; Zang et al., 2011; Ghysels et al., 2013). For example, Ghysels et al. (2013) proposed a generic free energy expression for the osmotic ensemble, consisting of three contributions: one from the host material, one from the guest molecules, and the third one from the host–guest interaction. The authors parameterized an analytical expression for the free energy, which allowed them to construct free energy landscapes as a function of all shapes of the MOF structure and to identify straightforwardly the most stable phase for a given combination of external gas chemical potential and pressure. There are alternative types of applications of free energy to studying structural transitions of MOFs. For example, Sugiyama et al. (2012) combined GCMC simulations (on several rigid structures of a model framework material) with the reconstruction of grand free energy profiles by thermodynamic integration: by choosing both the GCMC-predicted gas loading and the corresponding cell vectors, the free energy landscape was reconstructed directly from the adsorption isotherm in the rigid host. These studies have showcased that when comparing the relative stability of several structural phases or configurations one can determine the free energy difference between them, through an analytical approach or by thermodynamic integration. Additionally, as mentioned in Chapter 2 (Section 2.4) the so-called lattice-switch Monte Carlo method of Wilding and co-workers (Bruce et al., 1997), which was devised to study phase transitions of solid-state crystals, may also be proven a powerful tool for studying

flexible MOFs. For future work, it is of certain interest and importance to examine the structural changes observed for MIL-53(Sc) in free energy terms.

Pore-opening energies of the different structural transformations. For a particular amount of CO_2 molecules adsorbed, the energies required for different structural transformations to accommodate the uptake were determined in order to elucidate the phase evolution in response to CO_2 adsorption (Table 6.5). As a first approximation, the sorption-induced pore-opening energy (ΔE_{open}) can be estimated from the difference between the energies before and after uptake of a certain amount of CO_2 molecules, as given by

$$\Delta E_{\text{open}} = E(\text{MIL} \cdots n_2\text{CO}_2) - E(\text{MIL} \cdots n_1\text{CO}_2) - (n_2 - n_1)E(\text{CO}_2) \qquad (6.1)$$

where E(MIL···n_2CO$_2$) and E(MIL···n_1CO$_2$) are the total energies of the MIL-53(Sc) framework with a loading of n_2 and n_1 CO_2 ($n_2 > n_1$), respectively; and $E(CO_2)$ is the energy of an isolated, geometry-optimized CO_2 molecule in a supercell having the same dimensions as the framework loaded with n_2CO_2.

The energies needed to open the *cp* structure to form the *int* and *np* topologies are -77.3 and +95.8 kJ mol^{-1}, respectively. The negative pore-opening energy in the former case confirms that formation of the *int* structure can be expected as a result of exposure of MIL-53(Sc)-*cp* to CO_2. In contrast, the large positive value in the case of the *np* structure entails the need for a significant amount of external energy to initiate the pore opening, thus providing further evidence that in the experiment only the *int* structure is formed.

To ascertain the preferential structural transformations for further CO_2 adsorption starting from the *int* structure with a loading of 2.2 mmol g^{-1} (four CO_2 per unit cell of the *int* structure), a higher uptake of 3.3 mmol g^{-1} (six CO_2 per unit cell of the *int* structure) was considered (Table 6.5). Two scenarios were investigated: (1) the additional CO_2 adsorption occurred in the already open channels, thus maintaining the *int* topology; and (2) the initially closed channels were opened as a result of the uptake, leading to the *np* topology. A schematic representation of the two structural transformations is given in Figure 6.17. The pore-opening energies were found to be -57.7 and +89.6 kJ mol^{-1} for the *int*(2.2) → *int*(3.3) and *int*(2.2) → *np*(3.3) transformations, respectively. This indicates that upon CO_2 adsorption the MIL-53(Sc) solid favours saturating the open channels over initiating new openings of the closed ones, corroborating the *in situ* XRPD patterns (Figure 6.6 (b)), which suggest the presence of the *int* phase up to high CO_2 partial pressures.

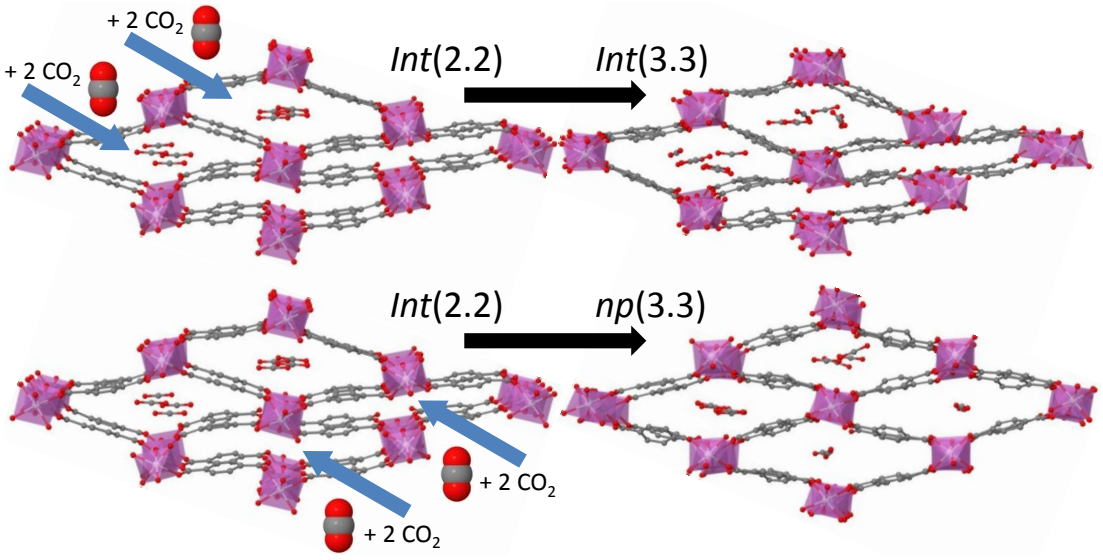

Figure 6.17. Setup of simulations to investigate the structural transformations of MIL-53(Sc) from with a CO_2 loading of 2.2 mmol g^{-1} (eight CO_2 molecules per simulation box) to with a CO_2 loading of 3.3 mmol g^{-1} (twelve CO_2 molecules per simulation box). Hydrogen atoms have been omitted for clarity.

Table 6.5. Pore-opening energies for the different structural transformations.

structural transformation	ΔE_{open} (kJ mol^{-1})[a]
cp(0.0) → *int*(2.2)	-77.3
cp(0.0) → *np*(2.2)	+95.8
int(2.2) → *int*(3.3)	-57.7
int(2.2) → *np*(3.3)	+89.6

[a] Energy required for the particular structural transformation. The framework topology is given in *italic* type, and the CO_2 loading in mmol g^{-1} is given in parentheses. All of the energies were determined by single-point calculations in which the same exchange–correlation grid (constant density of grid points) was used.

6.5 Further Discussions on AIMD Simulations in the *NPT* Ensemble

The AIMD-simulation-based modelling scheme demonstrated in this Chapter can be considered as a valid tool for studying the breathing phenomena of the MIL-53(Sc) solid, on the basis of (1) its accurate reproductions of the experimentally resolved *cp* and *vnp* structures induced by temperature variation, and (2) its successful predictions of the *int* and *lp* phases as a result of CO_2 adsorption, which have been confirmed by the experimental XRPD patterns. The methodology is thus successful with regard to the modelling objectives of this work, which are to assist structure determinations of the different phases of MIL-53(Sc) and to elucidate the structural changes on the molecular level. In addition to validation of the modelling scheme by means of comparing simulation to experiment, detailed analyses of the thermodynamic data obtained from the *NPT*-AIMD simulations are presented in this Section. This is certainly of interest, from a simulation perspective, to more rigorously justify the choices of the

computational settings adopted, particularly concerning the chosen DZVP Gaussian basis set ("DZVP" stands for a double-ζ valence basis set augmented with one set of polarization functions) and 350-Ry cutoff.

In the context of the implementations of the isobaric simulation techniques within the CP2K package, it has been pointed out in the literature that a large Gaussian basis set, in conjunction with a high charge-density cutoff, may be necessary to achieve accurate pressure/stress computations for simulations in ensembles with fluctuating volume (McGrath et al., 2005; Schmidt et al., 2009). For example, using *NPT*-MC simulations, McGrath et al. investigated the effect of charge-density cutoff on the energy–volume (*U*–*V*) curves for liquid water at ambient conditions (McGrath et al., 2005). It was found that a progressively increased cutoff (280 → 1200 Ry), together with a TZV2P basis set (a triple-ζ valence basis set augmented with two sets of polarization functions), systematically decreased the magnitudes of the jumps in the *U*–*V* curves. The study highlights the importance of choosing a basis set and a charge-density cutoff to ensure the accuracy in computations of internal pressures for isobaric simulations.

In light of such findings reported, great attention has been paid to the setup of the *NPT*-AIMD simulations for the MIL-53(Sc) system studied in this work. During the preliminary tests, the influence of several simulation parameters on the performance of the *NPT*-AIMD simulation in reproducing the experimentally known MIL-53(Sc)-*cp* and -*vnp* structures was carefully examined. These tested parameters include DFT functional (BLYP, PBE, B97D), dispersion correction (D2, D3 with/out three-body terms), basis set (size, type), charge-density cutoff, reference-cell treatment, and integration step-size. Among them, the use of a reference cell was found to yield the

most profound improvement of the accuracy in computations of pressure and energy. As an example, Figure 6.18 (a) shows that the *NPT*-AIMD simulation without using a reference cell, in which the grid density was kept constant, exhibits large jumps in the total energy as the volume of the simulation box changes. The discontinuities in energy have been known to be a result of the changing number of grid points as to maintain the grid density with the varying cell volume – they cause numerical problems in *NPT* simulations and, therefore, should be avoided (Schmidt et al., 2009). Indeed, fixing the number of grid points – by means of using a reference cell of constant volume – during the other *NPT*-AIMD simulation of the same system removes almost all of the jumps/discontinuities in the *U*–*V* curve, as shown in Figure 6.18 (b). Therefore, the reference-cell treatment was used throughout this work for all of the AIMD simulations (but not for static DFT calculations). The other simulation parameters were also carefully examined and, on the whole, the parameters finally adopted for the *NPT*-AIMD simulations performed on MIL-53(Sc) have been found to strike a very good balance between computational accuracy and cost.

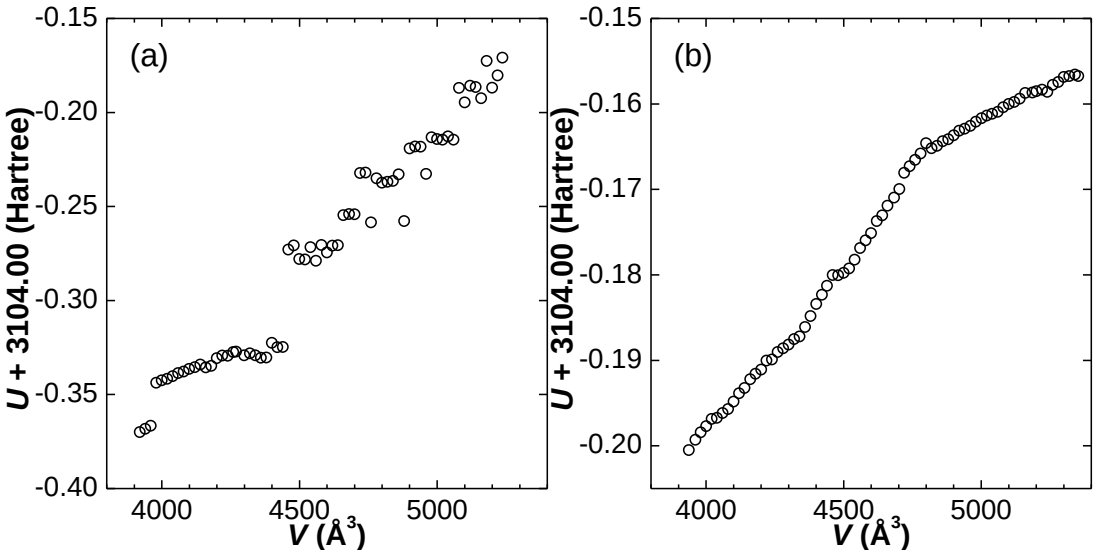

Figure 6.18. Total energy (conserved quantity) of a single snapshot from the *NPT*-AIMD simulations (a) without and (b) with the reference cell was plotted as a function of the volume of the simulation box. Both simulations started with the same system configuration – the MIL-53(Sc)-*DMF(removed)* framework with a CO_2 loading of 2.2 mmol g^{-1} – and used a DZVP basis set and a charge-density cutoff of 350 Ry. For clarity, the spacing between two adjacent data points is approximately 20 $Å^3$ (wherever possible). In both cases, the total energies have been shifted by +3104.00 Hartree for a better illustration.

The large system sizes studied in this work – ranging from 304 to 496 atoms per simulation box – entail the need for using a relatively small basis set and a relatively low charge-density cutoff, in order to allow for tractable AIMD simulations with long enough time frames to develop system dynamics. Despite the use of a DZVP basis set and a 350-Ry cutoff, the *U*–*V* curves (with the reference-cell treatment) obtained from all of the *NPT*-AIMD simulations reported in this work were confirmed to exhibit no significant jumps or discontinuities. For example, Figure 6.18 (b) shows that the *U*–*V* curve is continuous and smooth for a volume change as large as 36%. Note that the 36% volume change is larger than the 24% volume change studied by McGrath et al. (2005), where large jumps in energy were observed when using a TZV2P basis set and a cutoff lower than 600 Ry. The different findings made in this work and by McGrath et al. (2005) may be surprising at

first sight, it, however, needs to be emphasized that the two studies deal with two different systems. That is, the good behaviour ("extra" stability) of the *NPT*-AIMD simulations performed in this work may very well come from the fact that the MIL-53(Sc) system is a solid-state framework, as opposed to the liquid system studied by McGrath et al. Moreover, the focuses here are on using *NPT*-AIMD simulations to anticipate MOF structures, whereas the work of McGrath et al. deals with trying to model liquid densities, which require system dynamics to be stable over considerably longer time scales.

Indeed, for framework systems a DZVP basis set, together with a cutoff in the range of 280–700 Ry, has been shown to allow simulations based upon it to describe accurately a variety of properties – see the articles by Kanoo et al. (2012) and Li et al. (2012), for example – and is normally a good compromise between quality of basis set and speed of computation. Moreover, it is generally known that the choice of simulation parameters is often system-specific. For example, Siepmann and co-workers were able to study several ionic-liquid systems using *NPT*-AIMD simulations with a DZVP basis set and a cutoff of 300 Ry (Mallik and Siepmann, 2010; Mallik et al., 2012).

As a further step to justify the validity of the chosen DZVP basis set and 350-Ry cutoff for *NPT*-AIMD simulations of MIL-53(Sc), the effect of basis-set size and cutoff value on the simulation cell was assessed by means of a sensitivity test. Three *NPT*-AIMD simulations were carried out in parallel, all starting with the same system configuration. Tests 1, 2, and 3 were run using the (DZVP & 350 Ry), (TZV2P & 350 Ry), and (DZVP & 700 Ry) combinations, respectively, while all of the other simulation parameters were kept the same. For the three simulations, the cell parameters were averaged over 1 ps and are summarized in Table 6.6. Note that an intended test with the (TZV2P &

700 Ry) setup was found to be intractable given the computing resources available.

Table 6.6. Comparison of simulated cell parameters from the *NPT*-AIMD simulations with the different combinations of basis set and charge-density cutoff.[a]

test *i*	1	2[b]		3[b]	
sim. variables[c]	DZVP & 350 Ry	TZV2P & 350 Ry		DZVP & 700 Ry	
a (Å)	20.589	20.540	(-0.24)	20.713	(+0.60)
b (Å)	21.304	21.241	(-0.29)	21.296	(-0.04)
c (Å)	14.821	14.879	(+0.39)	14.906	(+0.57)
α (°)	92.656	92.336	(-0.35)	92.621	(-0.04)
β (°)	88.438	88.248	(-0.21)	88.671	(+0.26)
γ (°)	38.377	38.826	(+1.17)	38.384	(+0.02)
V (Å^3)	4010.390	4046.460	(+0.90)	4059.960	(+1.23)
cost (s)[d]	40.0	90.0	(+125.0)	85.0	(+112.5)

[a] All of the three tests started with the same system configuration; that is, a snapshot taken from the *NPT*-AIMD simulation (using DZVP & 350 Ry) of MIL-53(Sc)-*int* at 196 K. The three tests were run for 1 ps, and the cell parameters reported here were obtained by averaging over that period (1 ps). Note, a simulation temperature that is too low (e.g., 100K) would not allow for a meaningful comparison of the simulated cells as a result of the different basis sets and cutoffs, as the structure itself does not change significantly at very low temperatures. On the other hand, a simulation temperature that is too high (e.g., 623 K) would require a much longer simulation time before the time-averaged cell yields a correct representation of the structure. [b] Results are compared to the corresponding ones obtained from test 1. The difference between test *i* (*i* = 2, 3) and test 1 is given in parentheses and is defined as (test *i* - test 1)/test 1 × 100%. [c] All of the other simulation parameters were kept the same. [d] Calculation time for one AIMD step using 512 cores on HECToR (http://www.hector.ac.uk).

It can be clearly seen from Table 6.6 that the three simulations, although with the different combinations of basis set and cutoff, yield mostly identical results. This thus demonstrates that the (DZVP & 350 Ry) setup, which gave the fastest computation, is a valid and sensible choice for *NPT*-AIMD simulations of MIL-53(Sc). Cautions, however, must be applied when

interpreting this sensitivity test on the basis-set/cutoff-dependence of the MIL-53(Sc) system, as these simulations only ran for 1 ps and conclusions cannot be drawn for the behaviour of the system at much longer time scales. Whereas a more rigorous investigation is worth conducting, a comparative, theoretical study for investigating and so understanding the effects of basis set and cutoff on structure prediction is beyond the scope of this work.

Finally, as noted by Schmidt et al. (2009), the conserved quantity is an important quality-indicator for MD simulations in ensembles other than *NVE* (where the total energy is conserved). All of the *NPT*-AIMD simulations performed in this work achieved a very good conservation of energy with almost negligible drift in energy, which can be seen from Figure 6.19 as an example.

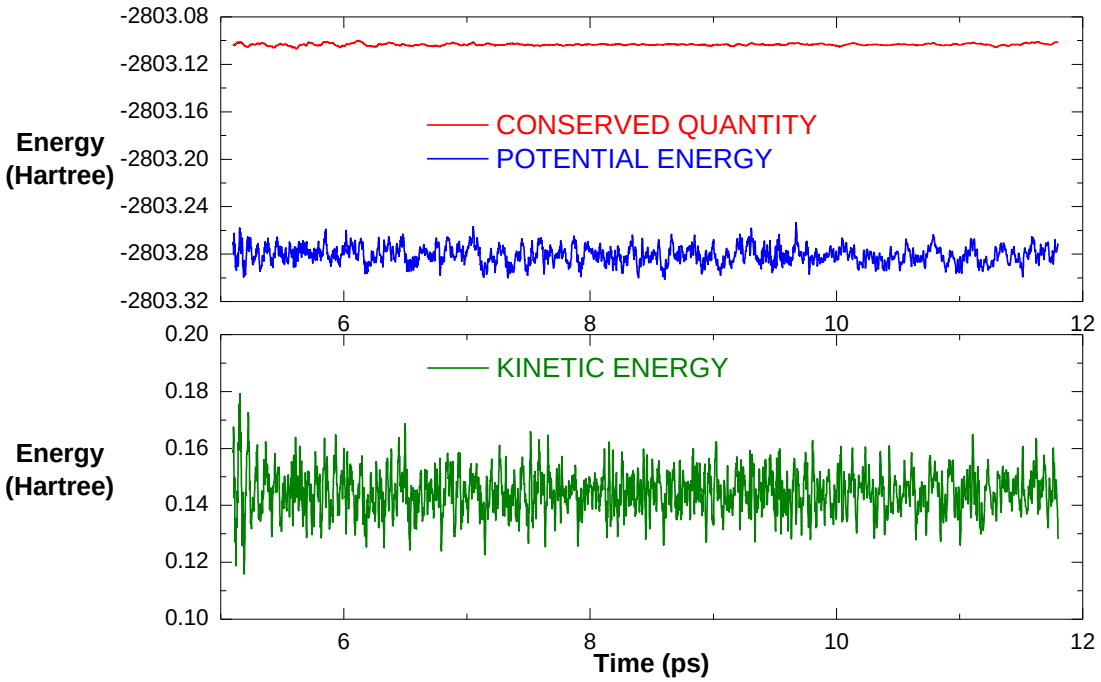

Figure 6.19. Time evolution of the total (conserved quantity), potential, and kinetic energies over the course of the production run of the *NPT*-AIMD simulation performed at 100 K.

Moreover, Figure 6.20 demonstrates that the pressure behaviour of the *NPT*-AIMD simulation performed at 100 K was also fairly good; that is, the cumulative average pressure converged to the externally applied pressure reasonably well with only small fluctuations in an order of 10s of bars. The amplitudes of the fluctuations of the instantaneous pressures are considerably larger, which, however, is known to be mainly a result of the finite system size (Schmidt et al., 2009). Similarly, good pressure behaviours have been observed for the other *NPT*-AIMD simulations done in this work.

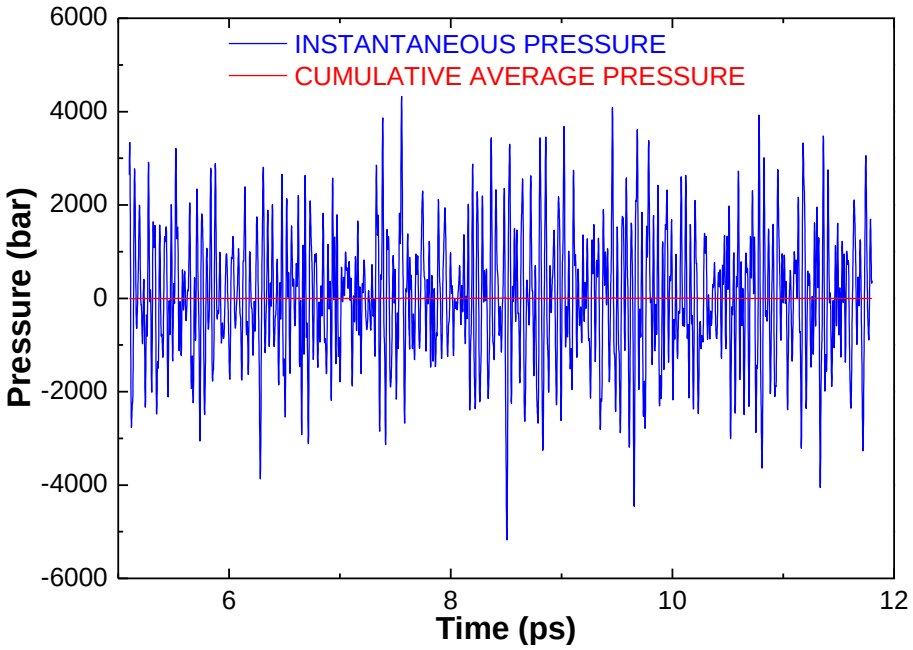

Figure 6.20. Time evolution of the instantaneous and cumulative average pressures over the course of the production run of the *NPT*-AIMD simulation performed at 100 K. The externally applied pressure was 1 bar, and the mean value of the instantaneous pressures is 17 bar.

In Table 6.7, the convergences of the internal pressures in the *NPT*-AIMD simulations performed in this work are compared to those reported in the literature. These data reiterate the general understanding of MD simulations in the *NPT* ensemble; that is, converging of the internal pressure is strongly dependent on the system size and on the simulation duration rather than on

the choice of the basis set or cutoff. Note that, to the best of the personal knowledge, among the very few literature reports on applying AIMD simulations to studying flexible MOFs (Hoffmann et al., 2011; Kanoo et al., 2012), pressure data were not reported when the *NPT* ensemble was used.

Table 6.7. Simulation parameters and corresponding average pressures from *NPT*-AIMD simulations performed in this work and reported in the literature.

system	basis set & cutoff	$\bar{p}$ (bar)[a]
MIL-53(Sc) at 1 bar & 100 K[b]	DZVP & 350 Ry	17 (1330)
MIL-53(Sc) at 1 bar & 623 K[b]	DZVP & 350 Ry	-7 (3715)
liquid water at 1 bar & 330 K[c]	TZV2P & 700 Ry[d]	-30 (3025)
		14 (2752)
		111 (2915)
		46 (3494)
		-57 (3563)
		-175 (3439)
	TZV2P & 1200 Ry[d]	16 (2913)
		22 (3514)

[a] $\bar{p}$ is the average pressure and the corresponding root-mean-square deviation is given in parentheses. Internal pressure can be either positive or negative, as it represents the tendency of the simulation cell to expand or contract (Schmidt et al., 2009). [b] This work. [c] Data were taken from the report by Schmidt et al (2009). [d] Using the same basis set and cutoff, other simulation parameters (i.e., different DFT functionals and reference cells) were varied. It is noteworthy that the standard deviations are given instead of the standard errors, in order to compare the simulation results obtained here with the ones for liquid water reported in the literature. In addition, this Table is aimed at demonstrating that large variations in pressure are a common phenomenon in *NPT* simulations, as observed both here and in the literature. For this purpose, the standard deviation provides a better illustration of the degree to which individual pressure values (during the simulation) differ from the mean value.

In summary, the *NPT*-AIMD simulations performed in this work have been shown to yield very accurate computations and conservations of both

pressure and energy. In addition, the basis-set/cutoff-dependence of the *NPT*-AIMD simulations is almost negligible (at least within the time frames that were investigated), thus justifying the choice of the basis set and cutoff. The applicability of the *NPT*-AIMD methodology, in conjunction with the simulation settings, to studying the breathing of MIL-53(Sc) can be affirmed.

6.6 Conclusions

Ab initio molecular dynamics simulations have been used to probe and elucidate the breathing behaviour of the MIL-53(Sc) solid in response to temperature variation and CO_2 adsorption. The AIMD method has for the first time been shown to predict successfully both temperature-dependent structural changes and the structural response to variable sorbate uptake of a flexible MOF. AIMD employing dispersion-corrected DFT accurately simulated the experimentally observed closure of MIL-53(Sc) upon solvent removal and the transition of the empty MOF from the *cp* phase to the *vnp* phase (symmetry change from $P\,2_1/c$ to $C\,2/c$) with increasing temperature, indicating that it can directly take into account entropic as well as enthalpic effects. Moreover, with the increasing temperature, not only were the cell expansions quantitatively predicted but the subtle differences between the rotations of the Sc hydroxide chains were also correctly captured. Using the same modelling approach, together with the experimental *in situ* XRPD data (provided by Professor Paul A. Wright and co-workers), the structural transformations of MIL-53(Sc) upon CO_2 adsorption were studied. The significantly broadened XRPD peaks of the phase at a CO_2 pressure of 0.493 bar posed a hurdle to structure determination by commonly adopted

methods such as Rietveld refinement or energy minimization. AIMD simulations were therefore carried out to mimic the CO_2 adsorption of MIL-53(Sc) *in silico* by allowing the MIL-53(Sc) framework to evolve freely in response to the CO_2 loading (2.2 mmol g^{-1}) corresponding to the first step in the experimental adsorption isotherm. The resulting structure enabled the determination of the MIL-53(Sc)-*int* phase observed by the *in situ* XRPD experiments. While AIMD simulations were the only viable choice to identify the *int* structure, the *lp* phase with the unit cell indexed experimentally was successfully solved by both the AIMD- and energy-minimization-based approaches. The latter, which was done by Doctor David Fairen-Jimenez, is of course computationally more efficient and, therefore, should be used to predict atomic positions of the structure when the unit-cell parameters are available.

Apart from assisting the structure determinations, the AIMD simulations further provided molecular-level dynamic and energetic information that helped to reveal the nature of the structural responses of MIL-53(Sc) to the external stimuli. The dynamical properties of the system as suggested by the corresponding AIMD trajectories were successfully used to explain, for example, the higher symmetry adopted by the solid at 623 K and the EDA complex formed between the adsorbed CO_2 molecule and the framework. Equally insightful was the energetic information extracted from the AIMD simulations. The calculated framework potential energies provided an indication of the relative stabilities of the various identified structural forms, while the calculated pore-opening energies helped to interpret the experimentally observed phase transitions upon CO_2 adsorption.

This work serves as a systematic demonstration of the application of AIMD simulations to study the flexibility of MOFs upon temperature variation and adsorption uptake. A special focus is on showcasing the applicability of the methodology to assist with structure determinations when the more conventional techniques fail. Since the energies and forces are calculated by a chosen QM method "on the fly", AIMD simulations are likely to permit investigation of a larger number of flexible MOFs than force-field-based approaches. For example, the effect of the nature of the metal on the breathing of the MIL-53 solids with different metals has not yet been fully understood or pursued in parallel by MD simulations. On the basis of correct reproductions of the different breathing behaviours by AIMD simulations, the first-principles descriptions of the MIL-53 variants obtained from such simulations will increase the understanding of the phenomena. Last but not least, as demonstrated by the successful identification of the MIL-53(Sc)-*int* structure in this work, AIMD simulations are predictive and are certainly worth exploring in a wider context in the field of MOFs and other flexible and dynamic microporous solids.

Chapter 7 Conclusions and Outlook

Molecular simulation is undoubtedly an indispensable tool for studying and understanding gas adsorption in metal–organic frameworks. Molecular-level insights gained from simulations – which may also contain time-resolved information as from the molecular dynamics approach – are not always easily accessible with experimental methods. In this respect, molecular simulations provide a valuable complement to experiment and have made substantial contributions toward elucidating underlying adsorption mechanisms of different guest molecules in MOFs. Throughout this Thesis, molecular simulations have been extensively used to predict gas uptakes in MOFs, to understand molecular-level interactions and hence adsorption mechanisms, and to probe structural transformations of a breathing MOF.

Force fields (almost) exclusively determine the accuracy and reliability of the simulation results based upon them. Generic classical force fields (such as DREIDING and UFF) do reasonably well for capturing gas adsorption phenomena in many MOFs. They are, however, less successful at dealing with MOFs with strong, specific interaction sites such as coordinatively unsaturated metal sites. This is a direct result of cus's exhibiting chemical environments that are very different from the ones considered in the development of those generic force fields. In this work (Chapters 3–5) quantum mechanical methods are adopted to provide accurate energetic and geometric information for the adsorbate–cus interactions of interest. Using these data as reference, new force fields are parameterized (Chapters 4, 5), which in turn yield significantly improved predictions of gas adsorption in MOFs with cus's, as compared to generic-force-field-based simulations.

The (urgent) need for tailor-made force fields that accurately describe guest-molecule interactions with MOFs containing cus's, although being repeatedly emphasized in this Thesis, should by no means be interpreted as a lack of importance for commonly used generic force fields. On the contrary, one clear conclusion drawn from this work is that the combined force field approach (Chapter 5) can be both physically sound and computationally efficient for accurate predictions of gas uptakes in MOFs with cus's. From a practical perspective, it is certainly advantageous to augment the application of well-established literature force fields to MOFs with cus's, by means of incorporating a set of *ab initio* force-field parameters that are specifically derived for the adsorbate–cus interactions of interest.

Combining molecular simulation with quantum mechanical calculation is a promising strategy, especially when suitable force fields for the particular fluid–framework systems of interest are unavailable. In addition to the *ab initio* force field approach, information obtained from QM calculations can be used directly in molecular simulations. Chapter 3 gives the first example in the literature, where the fluid–framework interactions calculated by a QM method are directly used in GCMC simulations in the form of a three-dimensional potential-energy grid. In other words, no force field is involved in determining the fluid–framework interactions in the GCMC simulations. The power and promise of combining molecular simulation and QM calculation is further demonstrated in Chapter 6, where the *ab initio* molecular dynamics technique, proposed in the literature (Car and Parrinello, 1985; Kirchner et al., 2012), is used to investigate the breathing behaviour of the flexible MOF MIL-53(Sc).

On the basis of the observations made in this work, molecular simulations, aided by quantum mechanical calculations, can be expected to be highly successful in predicting gas adsorption in MOFs with cus's and in studying the behaviour of flexible MOFs. While this work may have made one or two developments toward furthering the understanding of gas adsorption phenomena in MOFs using molecular simulations, there are certain major aspects in which future improvements and/or continuations can be foreseen.

The direct implementation of an *ab initio* potential energy surface in GCMC simulations (Chapter 3) is a theoretically attractive approach, because it removes much of the ambiguities introduced by approximating the potential energy with semiempirical model potentials. However, it needs to be pointed out that this modelling procedure has two known adverse features that markedly limit its application in a wider context. Firstly, the approach is absolutely system-specific; that is, a new PES is required for every different fluid–framework combination. Moreover, to construct the PES, hundreds (more likely thousands) of *ab initio* calculations are needed, which is too computationally intensive to allow for a simple investigation of several adsorbate species in one MOF, for example. Secondly, an even more restricting factor is that once the orientation dependence of the fluid–framework interaction cannot be ignored (i.e., when involving non-spherical adsorbate molecules such as CO_2), the construction of a PES (or several of them) to represent the *ab initio* potential energies on specific grid points becomes problematic. More effort is needed to resolve such implementation issues, until then the force-field approach will continue to outperform this *ab initio* PES approach in terms of both the ease of application and the potential of transferability.

One main finding coming out of the force-field development (Chapters 4, 5) is that the piecewise MMSV potential, together with the Coulomb potential, is a very good choice for fitting potential energy curves calculated by *ab initio* methods; the combination will presumably be adopted more widely in the future. However, such an approximation to reference *ab initio* energy only can be considered as an effective and physically-motivated (but not exactly physically-meaningful) approach to capturing specific guest-molecule interactions with cus's. The reason is that it is fundamentally important to decompose *ab initio* total energy into explicit contributions – which account separately for the various intermolecular interactions such exchange, electrostatics, induction, and dispersion – and then fit corresponding force-field terms individually. It is of real interest to investigate how (or if) such a more elaborate approach is to ensure the correct description of adsorbate–cus interactions and yield accurate predictions of gas adsorption isotherms and mechanisms in MOFs with cus's.

In Chapter 6, AIMD simulations have been demonstrated to predict successfully both the temperature-dependent structural changes and the structural response to variable sorbate uptake in the case of MIL-53(Sc). Nevertheless, it is worth emphasizing that although the AIMD technique itself is not limited by "difficult" situations such as cations or transition metals, the accuracy of any chosen QM method in describing the chemistry of a particular system needs to be confirmed prior to AIMD simulations, so does the computational setup need to be justified. Put this into context, despite the fact that the GGA-BLYP functional (with dispersion corrections) has been shown in this work to treat MIL-53(Sc) very well, it may be expected to experience difficulties when it comes to, for example, MIL-53(Fe) because of the strongly correlated character of the Fe(3*d*)-orbitals. In general,

DFT functionals based on either LDA or GGA have been known to describe poorly strongly correlated systems such as compounds containing the first-row transition metals (Cohen et al., 2011; Wen et al., 2012). To this end, the so-called "DFT+U" method is one simple approach to overcoming such difficulties of standard exchange–correlation density functionals by empirically correcting self-interaction errors, which are a major source of the deficiency of GGA and LDA in describing strongly correlated systems (Wen et al. (2012) and references therein). Details about the DFT+U method can be found elsewhere (Anisimov et al., 1991; Liechtenstein et al., 1995; Dudarev et al., 1998). Indeed, Combelles et al. (2010) showed that the structural, electronic, and magnetic properties of the MIL-53(Fe) solid could be reproduced very well by employing a DFT+U, or more precisely a GGA+U, approach (with static DFT calculations). This is very encouraging because one can readily apply a GGA+U method, together with dispersion corrections, in AIMD simulations within the CP2K package to studying the breathing behaviour of MIL-53(Fe). It is of interest to see how GGA+U performs when used in the context of AIMD simulations – based on the personal experience, the GGA-BLYP functional appeared to have problems dealing with a flexible MOF containing Manganese. It is worth noting that hybrid DFT functionals, such as the well-known B3LYP functional, are able to provide significantly improved descriptions of strongly correlated systems compared to semilocal density functional approximations (GGA, meta-GGA), as they correct self-interaction errors by incorporating a portion of exact, nonlocal Hartree–Fock exchange into the exchange–correlation functional (Wen et al., 2012). However, hybrid functionals can be prohibitively expensive for extended systems (e.g., solid-state frameworks) even in static single-point energy evaluations, not to mention for (at least) tens of

thousands of such calculations that would be required by an AIMD simulation. Moreover, computation may very well be proven intractable even for AIMD simulations employing the so-called "screened" hybrid DFT functionals (see Henderson et al. (2011) for an example), although such functionals were typically devised to extend the application of hybrid DFT to solids. Put together, it again points to the promise that the GGA+U methods hold for *d*-electron systems such as the Fe and Cr versions of MIL-53.

Despite the apparent advantages of the AIMD approach over the classical flexible force field one, application of the former to the breathing/gate-opening phenomena occurring in flexible MOFs is still severely restricted by the prohibitively large computation associated with the large system size and large time scale that are normally required for simulating a MOF system. To this end, the flexible force field approach, which requires a substantially smaller (by many orders of magnitude) computational effort than AIMD, is an important alternative and undoubtedly merits continuing research inputs. Greathouse and Allendorf (2006) reported one of the first studies in the field, where they combined CVFF (Dauber-Osguthorpe et al., 1988) with a non-bonded parameterization of ZnO for the simulation of the structural deformations of the Zn_4O-based MOF-5. Shortly afterwards, Dubbeldam et al. (2007) first observed the strong negative thermal expansion of the IRMOF family by using a tailor-made flexible force field also based on CVFF. In the meantime, the breathing MOF MIL-53 series also received huge interests, and different flexible force fields were proposed by using experimental and/or quantum mechanical reference data (Coombes et al., 2008; Salles et al., 2008; Vanduyfhuys et al., 2012). As one of the pioneering groups in the field, Schmid and co-workers have invested continuous efforts in developing the so-called MOF-FF, a fully flexible force field for metal–organic frameworks,

in a systematic and consistent fashion from high-level first-principles reference data for a variety of MOFs. They reported in 2007 the first generation of the now termed MOF-FF for MOF-5 (Tafipolsky et al., 2007), with the parameters mostly fitted manually. Later on, the second generation of MOF-FF was made available, featuring a genetic algorithm approach for force-field parameterization; parameters were proposed for the MOF CuBTC (Tafipolsky et al., 2010). By 2013, the third generation of MOF-FF was reported by the group and the force field was extended to a set of inorganic building blocks commonly seen in MOFs (Bureekaew et al., 2013). All of these aforementioned literature studies have demonstrated that a well calibrated or parameterized flexible force field can be a powerful tool for investigating the dynamical properties of flexible MOFs; research is certainly worth carrying out into development of flexible force fields for MOFs.

Ultimately, by introducing robust and generally applicable modelling protocols for accurate predictions of gas adsorption in MOFs with cus's, this work serves as a stepping stone in the pursuit of a holy grail of molecular simulation in the field of MOFs: to computationally identify and to rationally design ideal MOFs for practical applications without resort to time-consuming experiments. Well-defined structure–property correlations that have not yet been apparent can (almost) certainly be revealed when cus-containing MOFs constituent an adequate proportion of the screening MOF collection with their performances correctly evaluated by the simulation method. This will undoubtedly expedite material discovery and design for MOFs. Finally, the challenges and the possible future continuations and improvements outlined above provide new opportunities, in which this work might be viewed as a useful source for information or even as a guide.

References

Ahlrichs, R., Penco, R. and Scoles, G. (**1977**); Intermolecular forces in simple systems; *Chemical Physics* 19(2): 119-130.

Anisimov, V. I., Zaanen, J. and Andersen, O. K. (**1991**); Band theory and Mott insulators: Hubbard U instead of Stoner I; *Physical Review B* 44(3): 943-954.

Atkins, P. and Friedman, R. (**2011**); *Molecular quantum mechanics*; Oxford ; New York, Oxford University Press.

Aziz, R. A., Slaman, M. J., Taylor, W. L. and Hurly, J. J. (**1991**); An improved intermolecular potential for sulfur hexafluoride; *The Journal of Chemical Physics* 94(2): 1034-1038.

Bae, Y.-S. and Snurr, R. Q. (**2011**); Development and Evaluation of Porous Materials for Carbon Dioxide Separation and Capture; *Angewandte Chemie International Edition* 50(49): 11586-11596.

Becke, A. D. (**1988**); Density-functional exchange-energy approximation with correct asymptotic behavior; *Physical Review A* 38(6): 3098-3100.

Becke, A. D. (**1993**); Density-functional thermochemistry. III. The role of exact exchange; *The Journal of Chemical Physics* 98(7): 5648-5652.

Berendsen, H. J. C., Postma, J. P. M., Gunsteren, W. F. v., DiNola, A. and Haak, J. R. (**1984**); Molecular dynamics with coupling to an external bath; *The Journal of Chemical Physics* 81(8): 3684-3690.

Besler, B. H., Merz, K. M. and Kollman, P. A. (**1990**); Atomic charges derived from semiempirical methods; *Journal of Computational Chemistry* 11(4): 431-439.

Blöchl, P. E. (**1994**); Projector augmented-wave method; *Physical Review B* 50(24): 17953.

Bludský, O., Rubeš, M., Soldan, P. and Nachtigall, P. (**2008**); Investigation of the benzene-dimer potential energy surface: DFT/CCSD(T) correction scheme; *Journal of Chemical Physics* 128(11): 114102-114108.

Bourrelly, S., Llewellyn, P. L., Serre, C., Millange, F., Loiseau, T. and Férey, G. (**2005**); Different Adsorption Behaviors of Methane and Carbon Dioxide in the Isotypic Nanoporous

Metal Terephthalates MIL-53 and MIL-47; *Journal of the American Chemical Society* 127(39): 13519-13521.

Bourrelly, S., Moulin, B., Rivera, A., Maurin, G., Devautour-Vinot, S., Serre, C., Devic, T., Horcajada, P., Vimont, A., Clet, G., Daturi, M., Lavalley, J.-C., Loera-Serna, S., Denoyel, R., Llewellyn, P. L. and Férey, G. (**2010**); Explanation of the Adsorption of Polar Vapors in the Highly Flexible Metal Organic Framework MIL-53(Cr); *Journal of the American Chemical Society* 132(27): 9488-9498.

Britt, D., Furukawa, H., Wang, B., Glover, T. G. and Yaghi, O. M. (**2009**); Highly efficient separation of carbon dioxide by a metal-organic framework replete with open metal sites; *Proceedings of the National Academy of Sciences* 106(49): 20637-20640.

Bruce, A. D., Wilding, N. B. and Ackland, G. J. (**1997**); Free Energy of Crystalline Solids: A Lattice-Switch Monte Carlo Method; *Physical Review Letters* 79(16): 3002-3005.

Buckingham, A. D., Fowler, P. W. and Hutson, J. M. (**1988**); Theoretical studies of van der Waals molecules and intermolecular forces; *Chemical Reviews* 88(6): 963-988.

Buckingham, R. A. (**1938**); The Classical Equation of State of Gaseous Helium, Neon and Argon; *Proceedings of the Royal Society of London. Series A. Mathematical and Physical Sciences* 168(933): 264-283.

Bureekaew, S., Amirjalayer, S. and Schmid, R. (**2012**); Orbital directing effects in copper and zinc based paddle-wheel metal organic frameworks: the origin of flexibility; *Journal of Materials Chemistry* 22(20): 10249-10254.

Bureekaew, S., Amirjalayer, S., Tafipolsky, M., Spickermann, C., Roy, T. K. and Schmid, R. (**2013**); MOF-FF – A flexible first-principles derived force field for metal-organic frameworks; *physica status solidi (b)* 250(6): 1128-1141.

Car, R. and Parrinello, M. (**1985**); Unified Approach for Molecular Dynamics and Density-Functional Theory; *Physical Review Letters* 55(22): 2471-2474.

Carra, S. and Konowalow, D. (**1964**); IMPROVED INTERMOLECULAR POTENTIAL FUNCTION; *NUOVO CIMENTO* 34(1).

Caskey, S. R., Wong-Foy, A. G. and Matzger, A. J. (**2008**); Dramatic Tuning of Carbon Dioxide Uptake via Metal Substitution in a Coordination Polymer with Cylindrical Pores; *Journal of the American Chemical Society* 130(33): 10870-10871.

Castillo, J. M., Vlugt, T. J. H. and Calero, S. (**2008**); Understanding Water Adsorption in Cu−BTC Metal−Organic Frameworks; *The Journal of Physical Chemistry C* 112(41): 15934-15939.

Castillo, J. M., Vlugt, T. J. H. and Calero, S. a. (**2008**); Understanding Water Adsorption in Cu−BTC Metal−Organic Frameworks; *The Journal of Physical Chemistry C* 112(41): 15934-15939.

Chen, B. and Siepmann, J. I. (**1999**); Transferable Potentials for Phase Equilibria. 3. Explicit-Hydrogen Description of Normal Alkanes; *The Journal of Physical Chemistry B* 103(25): 5370-5379.

Chen, L., Grajciar, L., Nachtigall, P. and Düren, T. (**2011**); Accurate Prediction of Methane Adsorption in a Metal–Organic Framework with Unsaturated Metal Sites by Direct Implementation of an ab Initio Derived Potential Energy Surface in GCMC Simulation; *The Journal of Physical Chemistry C* 115(46): 23074-23080.

Chen, L., Morrison, C. A. and Düren, T. (**2012**); Improving Predictions of Gas Adsorption in Metal–Organic Frameworks with Coordinatively Unsaturated Metal Sites: Model Potentials, ab initio Parameterization, and GCMC Simulations; *The Journal of Physical Chemistry C* 116(35): 18899-18909.

Chen, L., Mowat, J. P. S., Fairen-Jimenez, D., Morrison, C. A., Thompson, S. P., Wright, P. A. and Düren, T. (**2013**); Elucidating the Breathing of the Metal–Organic Framework MIL-53(Sc) with ab Initio Molecular Dynamics Simulations and in Situ X-ray Powder Diffraction Experiments; *Journal of the American Chemical Society*; DOI: 10.1021/ja403453g.

Chipot, C. and Pohorille, A. (**2007**); *Free energy calculations: theory and applications in chemistry and biology / Ch. Chipot, A. Pohorille (eds.)*, Berlin : Springer-Verlag, 2007.

Chui, S. S. Y., Lo, S. M. F., Charmant, J. P. H., Orpen, A. G. and Williams, I. D. (**1999**); A chemically functionalizable nanoporous material [Cu-3(TMA)(2)(H2O)(3)](n); *Science* 283(5405): 1148-1150.

Clark, S. J., Segall, M. D., Pickard, C. J., Hasnip, P. J., Probert, M. I. J., Refson, K. and Payne, M. C. (**2005**); First principles methods using CASTEP; *Zeitschrift für Kristallographie* 220(5-6-2005): 567-570.

Cohen, A. J., Mori-Sánchez, P. and Yang, W. (**2011**); Challenges for Density Functional Theory; *Chemical Reviews* 112(1): 289-320.

Collins, D. J. and Zhou, H.-C. (**2007**); Hydrogen storage in metal-organic frameworks; *Journal of Materials Chemistry* 17(30): 3154-3160.

Combelles, C., Yahia, M. B., Pedesseau, L. and Doublet, M. L. (**2010**); Design of Electrode Materials for Lithium-Ion Batteries: The Example of Metal−Organic Frameworks; *The Journal of Physical Chemistry C* 114(20): 9518-9527.

Coombes, D. S., Corà, F., Mellot-Draznieks, C. and Bell, R. G. (**2008**); Sorption-Induced Breathing in the Flexible Metal Organic Framework CrMIL-53: Force-Field Simulations and Electronic Structure Analysis; *The Journal of Physical Chemistry C* 113(2): 544-552.

Cornell, W. D., Cieplak, P., Bayly, C. I., Gould, I. R., Merz, K. M., Ferguson, D. M., Spellmeyer, D. C., Fox, T., Caldwell, J. W. and Kollman, P. A. (**1995**); A Second Generation Force Field for the Simulation of Proteins, Nucleic Acids, and Organic Molecules; *Journal of the American Chemical Society* 117(19): 5179-5197.

Coudert, F. o.-X., Jeffroy, M., Fuchs, A. H., Boutin, A. and Mellot-Draznieks, C. (**2008**); Thermodynamics of Guest-Induced Structural Transitions in Hybrid Organic−Inorganic Frameworks; *Journal of the American Chemical Society* 130(43): 14294-14302.

Coudert, F. o.-X., Mellot-Draznieks, C., Fuchs, A. H. and Boutin, A. (**2009**); Prediction of Breathing and Gate-Opening Transitions Upon Binary Mixture Adsorption in Metal−Organic Frameworks; *Journal of the American Chemical Society* 131(32): 11329-11331.

Cui, Y., Yue, Y., Qian, G. and Chen, B. (**2012**); Luminescent Functional Metal–Organic Frameworks; *Chemical Reviews* 112(2): 1126-1162.

Cygan, R. T., Romanov, V. N. and Myshakin, E. M. (**2012**); Molecular Simulation of Carbon Dioxide Capture by Montmorillonite Using an Accurate and Flexible Force Field; *The Journal of Physical Chemistry C* 116(24): 13079-13091.

Dauber-Osguthorpe, P., Roberts, V. A., Osguthorpe, D. J., Wolff, J., Genest, M. and Hagler, A. T. (**1988**); Structure and energetics of ligand binding to proteins: Escherichia coli dihydrofolate reductase-trimethoprim, a drug-receptor system; *Proteins: Structure, Function, and Bioinformatics* 4(1): 31-47.

Deb, K. (**2001**); *Multi-Objective Optimization Using Evolutionary Algorithms*; Chichester, England, John Wiley & Sons.

Della Rocca, J., Liu, D. and Lin, W. (**2011**); Nanoscale Metal–Organic Frameworks for Biomedical Imaging and Drug Delivery; *Accounts of Chemical Research* 44(10): 957-968.

Devic, T., Horcajada, P., Serre, C., Salles, F., Maurin, G., Moulin, B., Heurtaux, D., Clet, G., Vimont, A., Grenèche, J.-M., Ouay, B. L., Moreau, F., Magnier, E., Filinchuk, Y., Marrot, J., Lavalley, J.-C., Daturi, M. and Férey, G. (**2009**); Functionalization in Flexible Porous Solids: Effects on the Pore Opening and the Host−Guest Interactions; *Journal of the American Chemical Society* 132(3): 1127-1136.

Devic, T., Salles, F., Bourrelly, S., Moulin, B., Maurin, G., Horcajada, P., Serre, C., Vimont, A., Lavalley, J.-C., Leclerc, H., Clet, G., Daturi, M., Llewellyn, P. L., Filinchuk, Y. and Férey, G. (**2012**); Effect of the organic functionalization of flexible MOFs on the adsorption of CO2; *Journal of Materials Chemistry* 22(20): 10266-10273.

Dietzel, P. D. C., Besikiotis, V. and Blom, R. (**2009**); Application of metal-organic frameworks with coordinatively unsaturated metal sites in storage and separation of methane and carbon dioxide; *Journal of Materials Chemistry* 19(39): 7362-7370.

Dietzel, P. D. C., Morita, Y., Blom, R. and Fjellvåg, H. (**2005**); An In Situ High-Temperature Single-Crystal Investigation of a Dehydrated Metal–Organic Framework Compound and Field-Induced Magnetization of One-Dimensional Metal–Oxygen Chains; *Angewandte Chemie International Edition* 44(39): 6354-6358.

Dirac, P. A. M. (**1930**); Note on Exchange Phenomena in the Thomas Atom; *Mathematical Proceedings of the Cambridge Philosophical Society* 26(03): 376-385.

Dubbeldam, D., Krishna, R., Calero, S. and Yazaydın, A. Ö. (**2012**); Computer-Assisted Screening of Ordered Crystalline Nanoporous Adsorbents for Separation of Alkane Isomers; *Angewandte Chemie International Edition* 51(47): 11867-11871.

Dubbeldam, D., Krishna, R. and Snurr, R. Q. (**2009**); Method for Analyzing Structural Changes of Flexible Metal−Organic Frameworks Induced by Adsorbates; *The Journal of Physical Chemistry C* 113(44): 19317-19327.

Dubbeldam, D., Walton, K. S., Ellis, D. E. and Snurr, R. Q. (**2007**); Exceptional Negative Thermal Expansion in Isoreticular Metal–Organic Frameworks; *Angewandte Chemie International Edition* 46(24): 4496-4499.

Ducéré, J.-M. and Cavallo, L. (**2007**); Parametrization of an Empirical Correction Term to Density Functional Theory for an Accurate Description of π-Stacking Interactions in Nucleic Acids; *The Journal of Physical Chemistry B* 111(45): 13124-13134.

Dudarev, S. L., Botton, G. A., Savrasov, S. Y., Humphreys, C. J. and Sutton, A. P. (**1998**); Electron-energy-loss spectra and the structural stability of nickel oxide: An LSDA+U study; *Physical Review B* 57(3): 1505-1509.

Düren, T., Bae, Y.-S. and Snurr, R. Q. (**2009**); Using molecular simulation to characterise metal-organic frameworks for adsorption applications; *Chemical Society Reviews* 38(5): 1237-1247.

Düren, T., Millange, F., Férey, G., Walton, K. S. and Snurr, R. Q. (**2007**); Calculating Geometric Surface Areas as a Characterization Tool for Metal−Organic Frameworks; *The Journal of Physical Chemistry C* 111(42): 15350-15356.

Ehrenfest, P. (**1927**); Bemerkung über die angenäherte Gültigkeit der klassischen Mechanik innerhalb der Quantenmechanik; *Zeitschrift für Physik* 45(7-8): 455-457.

Fairen-Jimenez, D., Colon, Y. J., Farha, O. K., Bae, Y.-S., Hupp, J. T. and Snurr, R. Q. (**2012**); Understanding excess uptake maxima for hydrogen adsorption isotherms in frameworks with rht topology; *Chemical Communications* 48(85): 10496-10498.

Fang, H., Kamakoti, P., Zang, J., Cundy, S., Paur, C., Ravikovitch, P. I. and Sholl, D. S. (**2012**); Prediction of CO2 Adsorption Properties in Zeolites Using Force Fields Derived from Periodic Dispersion-Corrected DFT Calculations; *The Journal of Physical Chemistry C* 116(19): 10692-10701.

Férey, G. (**2012**); Swelling Hybrid Solids; *Zeitschrift für anorganische und allgemeine Chemie* 638(12-13): 1897-1909.

Férey, G. and Serre, C. (**2009**); Large breathing effects in three-dimensional porous hybrid matter: facts, analyses, rules and consequences; *Chemical Society Reviews* 38(5): 1380-1399.

Férey, G., Serre, C., Devic, T., Maurin, G., Jobic, H., Llewellyn, P. L., De Weireld, G., Vimont, A., Daturi, M. and Chang, J.-S. (**2011**); Why hybrid porous solids capture greenhouse gases?; *Chemical Society Reviews* 40(2): 550-562.

Fischer, M., Gomes, J. R. B., Fröba, M. and Jorge, M. (**2012**); Modeling Adsorption in Metal–Organic Frameworks with Open Metal Sites: Propane/Propylene Separations; *Langmuir* 28(22): 8537-8549.

Fischer, M., Kuchta, B., Firlej, L., Hoffmann, F. and Fröba, M. (**2010**); Accurate Prediction of Hydrogen Adsorption in Metal−Organic Frameworks with Unsaturated Metal Sites via a Combined Density-Functional Theory and Molecular Mechanics Approach; *The Journal of Physical Chemistry C* 114(44): 19116-19126.

FitzGerald, S. A., Pierce, C. J., Rowsell, J. L. C., Bloch, E. D. and Mason, J. A. (**2013**); Highly Selective Quantum Sieving of D2 from H2 by a Metal–Organic Framework As Determined by

Gas Manometry and Infrared Spectroscopy; *Journal of the American Chemical Society* 135(25): 9458-9464.

Frantz, D. D., Freeman, D. L. and Doll, J. D. (**1990**); Reducing quasi-ergodic behavior in Monte Carlo simulations by J-walking: Applications to atomic clusters; *Journal of Chemical Physics* 93(4): 2769.

Frédéric, L., Mitchell, L. and Richard, M. (**2009**); Non-ergodicity of Nosé–Hoover dynamics; *Nonlinearity* 22(7): 1673.

Frenkel, D. and Smit, B. (**2002**); *Understanding Molecular Simulation: from algorithms to applications*; San Diego, CA 92101-4495, USA, Academic Press.

Frisch, M. J., Trucks, G. W., Schlegel, H. B., Scuseria, G. E., Robb, M. A., Cheeseman, J. R., Scalmani, G., Barone, V., Mennucci, B., Petersson, G. A., Nakatsuji, H., Caricato, M., Li, X., Hratchian, H. P., Izmaylov, A. F., Bloino, J., Zheng, G., Sonnenberg, J. L., Hada, M., Ehara, M., Toyota, K., Fukuda, R., Hasegawa, J., Ishida, M., Nakajima, T., Honda, Y., Kitao, O., Nakai, H., Vreven, T., Montgomery, J., J. A., Peralta, J. E., Ogliaro, F., Bearpark, M., Heyd, J. J., Brothers, E., Kudin, K. N., Staroverov, V. N., Kobayashi, R., Normand, J., Raghavachari, K., Rendell, A., Burant, J. C., Iyengar, S. S., Tomasi, J., Cossi, M., Rega, N., Millam, J. M., Klene, M., Knox, J. E., Cross, J. B., Bakken, V., Adamo, C., Jaramillo, J., Gomperts, R., Stratmann, R. E., Yazyev, O., Austin, A. J., Cammi, R., Pomelli, C., Ochterski, J. W., Martin, R. L., Morokuma, K., Zakrzewski, V. G., Voth, G. A., Salvador, P., Dannenberg, J. J., Dapprich, S., Daniels, A. D., Farkas, Ö., Foresman, J. B., Ortiz, J. V., Cioslowski, J. and Fox, D. J. (**2009**); *Gaussian 09, Revision A.02*; Gaussian, Inc.: Wallingford CT.

Fu, J. and Sun, H. (**2009**); An Ab Initio Force Field for Predicting Hydrogen Storage in IRMOF Materials; *The Journal of Physical Chemistry C* 113(52): 21815-21824.

Furukawa, H., Cordova, K. E., O'Keeffe, M. and Yaghi, O. M. (**2013**); The Chemistry and Applications of Metal-Organic Frameworks; *Science* 341(6149).

Gelb, L. D. and Gubbins, K. E. (**1999**); Pore size distributions in porous glasses: A computer simulation study; *Langmuir* 15(2): 305-308.

Getman, R. B., Bae, Y.-S., Wilmer, C. E. and Snurr, R. Q. (**2012**); Review and Analysis of Molecular Simulations of Methane, Hydrogen, and Acetylene Storage in Metal–Organic Frameworks; *Chemical Reviews* 112(2): 703-723.

Getzschmann, J., Senkovska, I., Wallacher, D., Tovar, M., Fairen-Jimenez, D., Düren, T., van Baten, J. M., Krishna, R. and Kaskel, S. (**2010**); Methane storage mechanism in the metal-organic framework Cu3(btc)2: An in situ neutron diffraction study; *Microporous and Mesoporous Materials* 136(1–3): 50-58.

Ghoufi, A., Maurin, G. and Férey, G. (**2010**); Physics Behind the Guest-Assisted Structural Transitions of a Porous Metal−Organic Framework Material; *The Journal of Physical Chemistry Letters* 1(19): 2810-2815.

Ghoufi, A., Subercaze, A., Ma, Q., Yot, P. G., Ke, Y., Puente-Orench, I., Devic, T., Guillerm, V., Zhong, C., Serre, C., Férey, G. and Maurin, G. (**2012**); Comparative Guest, Thermal, and Mechanical Breathing of the Porous Metal Organic Framework MIL-53(Cr): A Computational Exploration Supported by Experiments; *The Journal of Physical Chemistry C* 116(24): 13289-13295.

Ghysels, A., Vanduyfhuys, L., Vandichel, M., Waroquier, M., Van Speybroeck, V. and Smit, B. (**2013**); On the Thermodynamics of Framework Breathing: A Free Energy Model for Gas Adsorption in MIL-53; *The Journal of Physical Chemistry C* 117(22): 11540-11554.

Goedecker, S., Teter, M. and Hutter, J. (**1996**); Separable dual-space Gaussian pseudopotentials; *Physical Review B* 54(3): 1703-1710.

Goel, S. and Masunov, A. E. (**2008**); Potential energy curves and electronic structure of 3d transition metal hydrides and their cations; *The Journal of Chemical Physics* 129(21): 214302.

Goldberg, D. E. (**1989**); *Genetic Algorithms in Search, Optimization, and Machine Learning*; New York, Addison-Wesley.

Goodbody, S. J., Watanabe, K., MacGowan, D., Walton, J. P. R. B. and Quirke, N. (**1991**); Molecular simulation of methane and butane in silicalite; *Journal of the Chemical Society, Faraday Transactions* 87(13): 1951-1958.

Grajciar, L., Bludský, O. and Nachtigall, P. (**2010**); Water Adsorption on Coordinatively Unsaturated Sites in CuBTC MOF; *The Journal of Physical Chemistry Letters* 1(23): 3354-3359.

Grajciar, L. s., Wiersum, A. D., Llewellyn, P. L., Chang, J.-S. and Nachtigall, P. (**2011**); Understanding CO2 Adsorption in CuBTC MOF: Comparing Combined DFT–ab Initio Calculations with Microcalorimetry Experiments; *The Journal of Physical Chemistry C* 115(36): 17925-17933.

Greathouse, J. A. and Allendorf, M. D. (**2006**); The Interaction of Water with MOF-5 Simulated by Molecular Dynamics; *Journal of the American Chemical Society* 128(33): 10678-10679.

Grimme, S. (**2006**); Semiempirical GGA-type density functional constructed with a long-range dispersion correction; *Journal of Computational Chemistry* 27(15): 1787-1799.

Grimme, S. (**2006**); Semiempirical hybrid density functional with perturbative second-order correlation; *The Journal of Chemical Physics* 124(3): 034108.

Grimme, S., Antony, J., Ehrlich, S. and Krieg, H. (**2010**); A consistent and accurate ab initio parametrization of density functional dispersion correction (DFT-D) for the 94 elements H-Pu; *The Journal of Chemical Physics* 132(15): 154104.

Guo, Z. Y., Wu, H., Srinivas, G., Zhou, Y. M., Xiang, S. C., Chen, Z. X., Yang, Y. T., Zhou, W., O'Keeffe, M. and Chen, B. L. (**2011**); A Metal-Organic Framework with Optimized Open Metal Sites and Pore Spaces for High Methane Storage at Room Temperature; *Angewandte Chemie-International Edition* 50(14): 3178-3181.

Gupta, A., Chempath, S., Sanborn, M. J., Clark, L. A. and Snurr, R. Q. (**2003**); Object-oriented Programming Paradigms for Molecular Modeling; *Molecular Simulation* 29(1): 29 - 46.

Haldoupis, E., Watanabe, T., Nair, S. and Sholl, D. S. (**2012**); Quantifying Large Effects of Framework Flexibility on Diffusion in MOFs: CH4 and CO2 in ZIF-8; *ChemPhysChem* 13(15): 3449-3452.

Hamon, L., Leclerc, H., Ghoufi, A., Oliviero, L., Travert, A., Lavalley, J.-C., Devic, T., Serre, C., Férey, G. r., De Weireld, G., Vimont, A. and Maurin, G. (**2011**); Molecular Insight into the Adsorption of H2S in the Flexible MIL-53(Cr) and Rigid MIL-47(V) MOFs: Infrared Spectroscopy Combined to Molecular Simulations; *The Journal of Physical Chemistry C* 115(5): 2047-2056.

Hamon, L., Llewellyn, P. L., Devic, T., Ghoufi, A., Clet, G., Guillerm, V., Pirngruber, G. D., Maurin, G., Serre, C., Driver, G., Beek, W. v., Jolimaître, E., Vimont, A., Daturi, M. and Férey, G. r. (**2009**); Co-adsorption and Separation of CO2−CH4 Mixtures in the Highly Flexible MIL-53(Cr) MOF; *Journal of the American Chemical Society* 131(47): 17490-17499.

Han, S. S., Kim, D., Jung, D. H., Cho, S., Choi, S.-H. and Jung, Y. (**2012**); Accurate Ab Initio-Based Force Field for Predictive CO2 Uptake Simulations in MOFs and ZIFs: Development and Applications for MTV-MOFs; *The Journal of Physical Chemistry C* 116(38): 20254-20261.

Hansen, J.-P. and Verlet, L. (**1969**); Phase Transitions of the Lennard-Jones System; *Physical Review* 184(1): 151-161.

Hartwigsen, C., Goedecker, S. and Hutter, J. (**1998**); Relativistic separable dual-space Gaussian pseudopotentials from H to Rn; *Physical Review B* 58(7): 3641-3662.

Head-Gordon, M., Pople, J. A. and Frisch, M. J. (**1988**); MP2 energy evaluation by direct methods; *Chemical Physics Letters* 153(6): 503-506.

Henderson, T. M., Paier, J. and Scuseria, G. E. (**2011**); Accurate treatment of solids with the HSE screened hybrid; *physica status solidi (b)* 248(4): 767-774.

Hertzberg, G. (**1945**); *Infrared and Raman Spectra*; New York, van Nostrand Reinhold.

Hoffmann, H. C., Assfour, B., Epperlein, F., Klein, N., Paasch, S., Senkovska, I., Kaskel, S., Seifert, G. and Brunner, E. (**2011**); High-Pressure in Situ 129Xe NMR Spectroscopy and Computer Simulations of Breathing Transitions in the Metal–Organic Framework Ni2(2,6-ndc)2(dabco) (DUT-8(Ni)); *Journal of the American Chemical Society* 133(22): 8681-8690.

Holland, J. H. (**1975**); *Adaptation in natural and artificial systems: an introductory analysis with applications to biology, control, and artificial intelligence*; Cambridge, MA, MIT Press.

Hoover, W. G. (**1985**); Canonical dynamics: Equilibrium phase-space distributions; *Physical Review A* 31(3): 1695-1697.

Horcajada, P., Gref, R., Baati, T., Allan, P. K., Maurin, G., Couvreur, P., Férey, G., Morris, R. E. and Serre, C. (**2012**); Metal–Organic Frameworks in Biomedicine; *Chemical Reviews* 112(2): 1232-1268.

Horike, S., Shimomura, S. and Kitagawa, S. (**2009**); Soft porous crystals; *Nat Chem* 1(9): 695-704.

Jensen, F. (**2006**); *Introduction to computational chemistry*; Chichester, John Wiley & Sons.

Jones, J. E. (**1924**); On the Determination of Molecular Fields. II. From the Equation of State of a Gas; *Proceedings of the Royal Society of London. Series A* 106(738): 463-477.

Jorgensen, W. L., Maxwell, D. S. and Tirado-Rives, J. (**1996**); Development and Testing of the OPLS All-Atom Force Field on Conformational Energetics and Properties of Organic Liquids; *Journal of the American Chemical Society* 118(45): 11225-11236.

Kanoo, P., Reddy, S. K., Kumari, G., Haldar, R., Narayana, C., Balasubramanian, S. and Maji, T. K. (**2012**); Unusual room temperature CO2 uptake in a fluoro-functionalized MOF: insight from Raman spectroscopy and theoretical studies; *Chemical Communications* 48(68): 8487-8489.

Keil, M. and Parker, G. A. (**1985**); Empirical potential for the He+CO[sub 2] interaction: Multiproperty fitting in the infinite-order sudden approximation; *The Journal of Chemical Physics* 82(4): 1947-1966.

Keskin, S., Liu, J., Rankin, R. B., Johnson, J. K. and Sholl, D. S. (**2009**); Progress, Opportunities, and Challenges for Applying Atomically Detailed Modeling to Molecular Adsorption and Transport in Metal−Organic Framework Materials; *Industrial & Engineering Chemistry Research* 48(5): 2355-2371.

Kimmel, G. A., Baer, M., Petrik, N. G., VandeVondele, J., Rousseau, R. and Mundy, C. J. (**2012**); Polarization- and Azimuth-Resolved Infrared Spectroscopy of Water on TiO2(110): Anisotropy and the Hydrogen-Bonding Network; *The Journal of Physical Chemistry Letters* 3(6): 778-784.

Kirchner, B., Dio, P. and Hutter, J. (**2012**); Real-World Predictions from Ab Initio Molecular Dynamics Simulations, in *Multiscale Molecular Methods in Applied Chemistry*; edited by Kirchner, B. and Vrabec, J.; Berlin Heidelberg, Springer, 307: 109-153.

Kitagawa, S., Kitaura, R. and Noro, S.-i. (**2004**); Functional Porous Coordination Polymers; *Angewandte Chemie International Edition* 43(18): 2334-2375.

Kitagawa, S. and Matsuda, R. (**2007**); Chemistry of coordination space of porous coordination polymers; *Coordination Chemistry Reviews* 251(21–24): 2490-2509.

Kitagawa, S. and Uemura, K. (**2005**); Dynamic porous properties of coordination polymers inspired by hydrogen bonds; *Chemical Society Reviews* 34(2): 109-119.

Kizzie, A. C., Wong-Foy, A. G. and Matzger, A. J. (**2011**); Effect of Humidity on the Performance of Microporous Coordination Polymers as Adsorbents for CO2 Capture; *Langmuir* 27(10): 6368-6373.

Klimes, J. and Michaelides, A. (**2012**); Perspective: Advances and challenges in treating van der Waals dispersion forces in density functional theory; *The Journal of Chemical Physics* 137(12): 120901.

Klimeš, J. and Michaelides, A. (**2012**); Perspective: Advances and challenges in treating van der Waals dispersion forces in density functional theory; *The Journal of Chemical Physics* 137(12): 120901.

Krack, M. (**2005**); Pseudopotentials for H to Kr optimized for gradient-corrected exchange-correlation functionals; *Theoretical Chemistry Accounts* 114(1-3): 145-152.

Kreno, L. E., Leong, K., Farha, O. K., Allendorf, M., Van Duyne, R. P. and Hupp, J. T. (**2012**); Metal–Organic Framework Materials as Chemical Sensors; *Chemical Reviews* 112(2): 1105-1125.

Kresse, G. and Hafner, J. (**1993**); Ab initio molecular dynamics for open-shell transition metals; *Physical Review B* 48(17): 13115.

Kristyán, S. and Pulay, P. (**1994**); Can (semi)local density functional theory account for the London dispersion forces?; *Chemical Physics Letters* 229(3): 175-180.

Kuchta, B. (**2003**); MONTE CARLO SIMULATIONS OF THE METASTABILITY IN MOLECULAR CRYSTALS; *Phase Transitions* 76(3): 281-287.

Lee, C., Yang, W. and Parr, R. G. (**1988**); Development of the Colle-Salvetti correlation-energy formula into a functional of the electron density; *Physical Review B* 37(2): 785-789.

Levine, B. G., Stone, J. E. and Kohlmeyer, A. (**2011**); Fast analysis of molecular dynamics trajectories with graphics processing units—Radial distribution function histogramming; *Journal of Computational Physics* 230(9): 3556-3569.

Lewars, E. G. (**2011**); *Computational Chemistry : Introduction to the Theory and Applications of Molecular and Quantum Mechanics*; Dordrecht, Springer Science+Business Media B.V.

Li, J.-R., Sculley, J. and Zhou, H.-C. (**2012**); Metal–Organic Frameworks for Separations; *Chemical Reviews* 112(2): 869-932.

Li, W., Grimme, S., Krieg, H., Möllmann, J. and Zhang, J. (**2012**); Accurate Computation of Gas Uptake in Microporous Organic Molecular Crystals; *The Journal of Physical Chemistry C* 116(16): 8865-8871.

Li, W., Probert, M. R., Kosa, M., Bennett, T. D., Thirumurugan, A., Burwood, R. P., Parinello, M., Howard, J. A. K. and Cheetham, A. K. (**2012**); Negative Linear Compressibility of a Metal–Organic Framework; *Journal of the American Chemical Society* 134(29): 11940-11943.

Liechtenstein, A. I., Anisimov, V. I. and Zaanen, J. (**1995**); Density-functional theory and strong interactions: Orbital ordering in Mott-Hubbard insulators; *Physical Review B* 52(8): R5467-R5470.

Lilienfeld, O. A. v. and Tkatchenko, A. (**2010**); Two- and three-body interatomic dispersion energy contributions to binding in molecules and solids; *The Journal of Chemical Physics* 132(23): 234109.

Lin, L.-C., Berger, A. H., Martin, R. L., Kim, J., Swisher, J. A., Jariwala, K., Rycroft, C. H., Bhown, A. S., Deem, M. W., Haranczyk, M. and Smit, B. (**2012**); In silico screening of carbon-capture materials; *Nat Mater* 11(7): 633-641.

Lippert, G., Hutter, J. and Parrinello, M. (**1997**); A hybrid Gaussian and plane wave density functional scheme; *Molecular Physics* 92(3): 477-488.

Liu, J., Culp, J. T., Natesakhawat, S., Bockrath, B. C., Zande, B., Sankar, S. G., Garberoglio, G. and Johnson, J. K. (**2007**); Experimental and Theoretical Studies of Gas Adsorption in Cu3(BTC)2: An Effective Activation Procedure; *The Journal of Physical Chemistry C* 111(26): 9305-9313.

Liu, J., Thallapally, P. K., McGrail, B. P., Brown, D. R. and Liu, J. (**2012**); Progress in adsorption-based CO2 capture by metal-organic frameworks; *Chemical Society Reviews* 41(6): 2308-2322.

Llewellyn, P. L., Bourrelly, S., Serre, C., Vimont, A., Daturi, M., Hamon, L., De Weireld, G., Chang, J.-S., Hong, D.-Y., Kyu Hwang, Y., Hwa Jhung, S. and Férey, G. r. (**2008**); High Uptakes of CO2 and CH4 in Mesoporous Metal-Organic Frameworks MIL-100 and MIL-101; *Langmuir* 24(14): 7245-7250.

Llewellyn, P. L., Horcajada, P., Maurin, G., Devic, T., Rosenbach, N., Bourrelly, S., Serre, C., Vincent, D., Loera-Serna, S., Filinchuk, Y. and Férey, G. (**2009**); Complex Adsorption of Short Linear Alkanes in the Flexible Metal-Organic-Framework MIL-53(Fe); *Journal of the American Chemical Society* 131(36): 13002-13008.

Loiseau, T., Serre, C., Huguenard, C., Fink, G., Taulelle, F., Henry, M., Bataille, T. and Férey, G. (**2004**); A Rationale for the Large Breathing of the Porous Aluminum Terephthalate (MIL-53) Upon Hydration; *Chemistry – A European Journal* 10(6): 1373-1382.

Löwen, H., Palberg, T. and Simon, R. (**1993**); Dynamical criterion for freezing of colloidal liquids; *Physical Review Letters* 70(10): 1557-1560.

Lucena, S. M. P., Mileo, P. G. M., Silvino, P. F. G. and Cavalcante, C. L. (**2011**); Unusual Adsorption Site Behavior in PCN-14 Metal–Organic Framework Predicted from Monte Carlo Simulation; *Journal of the American Chemical Society* 133(48): 19282-19285.

Ma, S., Sun, D., Simmons, J. M., Collier, C. D., Yuan, D. and Zhou, H.-C. (**2007**); Metal-Organic Framework from an Anthracene Derivative Containing Nanoscopic Cages Exhibiting High Methane Uptake; *Journal of the American Chemical Society* 130(3): 1012-1016.

Mallik, B. S., Kuo, I. F. W., Fried, L. E. and Siepmann, J. I. (**2012**); Understanding the solubility of triamino-trinitrobenzene in hydrous tetramethylammonium fluoride: a first principles molecular dynamics simulation study; *Physical Chemistry Chemical Physics* 14(14): 4884-4890.

Mallik, B. S. and Siepmann, J. I. (**2010**); Thermodynamic, Structural and Transport Properties of Tetramethyl Ammonium Fluoride: First Principles Molecular Dynamics Simulations of an Unusual Ionic Liquid; *The Journal of Physical Chemistry B* 114(39): 12577-12584.

Mark, E. T. (**2002**); Ab initio molecular dynamics: basic concepts, current trends and novel applications; *Journal of Physics: Condensed Matter* 14(50): R1297.

Martyna, G. J., Klein, M. L. and Tuckerman, M. (**1992**); Nosé-Hoover chains: The canonical ensemble via continuous dynamics; *The Journal of Chemical Physics* 97(4): 2635-2643.

Mayo, S. L., Olafson, B. D. and Goddard, W. A. (**1990**); DREIDING: a generic force field for molecular simulations; *The Journal of Physical Chemistry* 94(26): 8897-8909.

McDaniel, J. G. and Schmidt, J. R. (**2013**); Physically-Motivated Force Fields from Symmetry-Adapted Perturbation Theory; *The Journal of Physical Chemistry A* 117(10): 2053-2066.

McDaniel, J. G., Yu, K. and Schmidt, J. R. (**2011**); Ab Initio, Physically Motivated Force Fields for CO2 Adsorption in Zeolitic Imidazolate Frameworks; *The Journal of Physical Chemistry C* 116(2): 1892-1903.

McGrath, M. J., Siepmann, J. I., Kuo, I. F. W., Mundy, C. J., VandeVondele, J., Hutter, J., Mohamed, F. and Krack, M. (**2005**); Isobaric–Isothermal Monte Carlo Simulations from First Principles: Application to Liquid Water at Ambient Conditions; *ChemPhysChem* 6(9): 1894-1901.

Metropolis, N., Rosenbluth, A. W., Rosenbluth, M. N., Teller, A. H. and Teller, E. (**1953**); Equation of State Calculations by Fast Computing Machines; *The Journal of Chemical Physics* 21(6): 1087-1092.

Mie, G. (**1903**); Zur kinetischen Theorie der einatomigen Körper; *Annalen der Physik* 316(8): 657-697.

Millange, F., Guillou, N., Walton, R. I., Greneche, J.-M., Margiolaki, I. and Férey, G. (**2008**); Effect of the nature of the metal on the breathing steps in MOFs with dynamic frameworks; *Chemical Communications*(39): 4732-4734.

Millange, F., Serre, C., Guillou, N., Férey, G. and Walton, R. I. (**2008**); Structural Effects of Solvents on the Breathing of Metal–Organic Frameworks: An In Situ Diffraction Study; *Angewandte Chemie International Edition* 47(22): 4100-4105.

Møller, C. and Plesset, M. S. (**1934**); Note on an Approximation Treatment for Many-Electron Systems; *Physical Review* 46(7): 618-622.

Morse, P. M. (**1929**); Diatomic Molecules According to the Wave Mechanics. II. Vibrational Levels; *Physical Review* 34(1): 57-64.

Moučka, F. and Nezbeda, I. (**2005**); Detection and Characterization of Structural Changes in the Hard-Disk Fluid under Freezing and Melting Conditions; *Physical Review Letters* 94(4): 040601.

Mowat, J. P. S., Miller, S. R., Slawin, A. M. Z., Seymour, V. R., Ashbrook, S. E. and Wright, P. A. (**2011**); Synthesis, characterisation and adsorption properties of microporous scandium carboxylates with rigid and flexible frameworks; *Microporous and Mesoporous Materials* 142(1): 322-333.

Mowat, J. P. S., Seymour, V. R., Griffin, J. M., Thompson, S. P., Slawin, A. M. Z., Fairen-Jimenez, D., Düren, T., Ashbrook, S. E. and Wright, P. A. (**2012**); A novel structural form of MIL-53 observed for the scandium analogue and its response to temperature variation and CO2 adsorption; *Dalton Transactions* 41(14): 3937-3941.

Myers, A. L. and Monson, P. A. (**2002**); Adsorption in Porous Materials at High Pressure: Theory and Experiment; *Langmuir* 18(26): 10261-10273.

Neimark, A. V., Coudert, F.-X., Boutin, A. and Fuchs, A. H. (**2009**); Stress-Based Model for the Breathing of Metal−Organic Frameworks; *The Journal of Physical Chemistry Letters* 1(1): 445-449.

Nijem, N., Thissen, P., Yao, Y., Longo, R. C., Roodenko, K., Wu, H., Zhao, Y., Cho, K., Li, J., Langreth, D. C. and Chabal, Y. J. (**2011**); Understanding the Preferential Adsorption of CO2 over N2 in a Flexible Metal–Organic Framework; *Journal of the American Chemical Society* 133(32): 12849-12857.

Nosé, S. (**1984**); A unified formulation of the constant temperature molecular dynamics methods; *The Journal of Chemical Physics* 81(1): 511-519.

Oh, H., Savchenko, I., Mavrandonakis, A., Heine, T. and Hirscher, M. (**2013**); Highly Effective Hydrogen Isotope Separation in Nanoporous Metal–Organic Frameworks with Open Metal Sites: Direct Measurement and Theoretical Analysis; *ACS Nano* 8(1): 761-770.

Pack, R. T., Piper, E., Pfeffer, G. A. and Toennies, J. P. (**1984**); Multiproperty empirical anisotropic intermolecular potentials. II. HeSF[sub 6] and NeSF[sub 6]; *The Journal of Chemical Physics* 80(10): 4940-4950.

Park, J., Kim, H., Han, S. S. and Jung, Y. (**2012**); Tuning Metal–Organic Frameworks with Open-Metal Sites and Its Origin for Enhancing CO2 Affinity by Metal Substitution; *The Journal of Physical Chemistry Letters* 3(7): 826-829.

Parrinello, M. and Rahman, A. (**1981**); Polymorphic transitions in single crystals: A new molecular dynamics method; *Journal of Applied Physics* 52(12): 7182-7190.

Parson, J. M., Siska, P. E. and Lee, Y. T. (**1972**); Intermolecular Potentials from Crossed-Beam Differential Elastic Scattering Measurements. IV. Ar + Ar; *The Journal of Chemical Physics* 56(4): 1511-1516.

Peng, D.-Y. and Robinson, D. B. (**1976**); A New Two-Constant Equation of State; *Industrial & Engineering Chemistry Fundamentals* 15(1): 59-64.

Perdew, J. P., Burke, K. and Ernzerhof, M. (**1996**); Generalized Gradient Approximation Made Simple; *Physical Review Letters* 77(18): 3865-3868.

Perdew, J. P., Ruzsinszky, A., Constantin, L. A., Sun, J. and Csonka, G. b. I. (**2009**); Some Fundamental Issues in Ground-State Density Functional Theory: A Guide for the Perplexed; *Journal of Chemical Theory and Computation* 5(4): 902-908.

Peterson, K. A. and Puzzarini, C. (**2005**); Systematically convergent basis sets for transition metals. II. Pseudopotential-based correlation consistent basis sets for the group 11 (Cu, Ag, Au) and 12 (Zn, Cd, Hg) elements; *Theoretical Chemistry Accounts: Theory, Computation, and Modeling (Theoretica Chimica Acta)* 114(4): 283-296.

Peverati, R. and Baldridge, K. K. (**2008**); Implementation and Performance of DFT-D with Respect to Basis Set and Functional for Study of Dispersion Interactions in Nanoscale Aromatic Hydrocarbons; *Journal of Chemical Theory and Computation* 4(12): 2030-2048.

Poater, A., Ragone, F., Correa, A. and Cavallo, L. (**2009**); Exploring the Reactivity of Ru-Based Metathesis Catalysts with a π-Acid Ligand Trans to the Ru−Ylidene Bond; *Journal of the American Chemical Society* 131(25): 9000-9006.

Potoff, J. J. and Siepmann, J. I. (**2001**); Vapor–liquid equilibria of mixtures containing alkanes, carbon dioxide, and nitrogen; *Aiche Journal* 47(7): 1676-1682.

Queen, W. L., Brown, C. M., Britt, D. K., Zajdel, P., Hudson, M. R. and Yaghi, O. M. (**2011**); Site-Specific CO2 Adsorption and Zero Thermal Expansion in an Anisotropic Pore Network; *The Journal of Physical Chemistry C* 115(50): 24915-24919.

Rabone, J., Yue, Y.-F., Chong, S. Y., Stylianou, K. C., Bacsa, J., Bradshaw, D., Darling, G. R., Berry, N. G., Khimyak, Y. Z., Ganin, A. Y., Wiper, P., Claridge, J. B. and Rosseinsky, M. J. (**2010**); An Adaptable Peptide-Based Porous Material; *Science* 329(5995): 1053-1057.

Rabuck, A. D. and Scuseria, G. E. (**1999**); Improving self-consistent field convergence by varying occupation numbers; *The Journal of Chemical Physics* 110(2): 695-700.

Ranganathan, S. and Pathak, K. N. (**1992**); Freezing transition of two-dimensional Lennard-Jones fluids; *Physical Review A* 45(8): 5789-5792.

Ranocchiari, M. and Bokhoven, J. A. v. (**2011**); Catalysis by metal-organic frameworks: fundamentals and opportunities; *Physical Chemistry Chemical Physics* 13(14): 6388-6396.

Rappe, A. K., Casewit, C. J., Colwell, K. S., Goddard, W. A. and Skiff, W. M. (**1992**); UFF, a full periodic table force field for molecular mechanics and molecular dynamics simulations; *Journal of the American Chemical Society* 114(25): 10024-10035.

Remy, T., Peter, S. A., Van der Perre, S., Valvekens, P., De Vos, D. E., Baron, G. V. and Denayer, J. F. M. (**2013**); Selective Dynamic CO2 Separations on Mg-MOF-74 at Low Pressures: A Detailed Comparison with 13X; *The Journal of Physical Chemistry C* 117(18): 9301-9310.

Rubeš, M., Grajciar, L., Bludský, O., Wiersum, A. D., Llewellyn, P. L. and Nachtigall, P. (**2012**); Combined Theoretical and Experimental Investigation of CO Adsorption on Coordinatively Unsaturated Sites in CuBTC MOF; *ChemPhysChem* 13(2): 488-495.

Rubeš, M., Kysilka, J., Nachtigall, P. and Bludský, O. (**2010**); DFT/CC investigation of physical adsorption on a graphite (0001) surface; *Physical Chemistry Chemical Physics* 12(24): 6438-6444.

Rubeš, M., Wiersum, A. D., Llewellyn, P. L., Grajciar, L., Bludský, O. and Nachtigall, P. (**2013**); Adsorption of Propane and Propylene on CuBTC Metal–Organic Framework: Combined Theoretical and Experimental Investigation; *The Journal of Physical Chemistry C* 117(21): 11159-11167.

Salles, F., Bourrelly, S., Jobic, H., Devic, T., Guillerm, V., Llewellyn, P., Serre, C., Férey, G. r. and Maurin, G. (**2011**); Molecular Insight into the Adsorption and Diffusion of Water in the Versatile Hydrophilic/Hydrophobic Flexible MIL-53(Cr) MOF; *The Journal of Physical Chemistry C* 115(21): 10764-10776.

Salles, F., Ghoufi, A., Maurin, G., Bell, R. G., Mellot-Draznieks, C. and Férey, G. (**2008**); Molecular Dynamics Simulations of Breathing MOFs: Structural Transformations of MIL-53(Cr) upon Thermal Activation and CO2 Adsorption; *Angewandte Chemie International Edition* 47(44): 8487-8491.

Salles, F., Maurin, G., Serre, C., Llewellyn, P. L., Knöfel, C., Choi, H. J., Filinchuk, Y., Oliviero, L., Vimont, A., Long, J. R. and Férey, G. (**2010**); Multistep N2 Breathing in the Metal−Organic Framework Co(1,4-benzenedipyrazolate); *Journal of the American Chemical Society* 132(39): 13782-13788.

Schmidt, J., VandeVondele, J., Kuo, I. F. W., Sebastiani, D., Siepmann, J. I., Hutter, J. and Mundy, C. J. (**2009**); Isobaric−Isothermal Molecular Dynamics Simulations Utilizing Density Functional Theory: An Assessment of the Structure and Density of Water at Near-Ambient Conditions; *The Journal of Physical Chemistry B* 113(35): 11959-11964.

Schröder, C. A., Baburin, I. A., van Wullen, L., Wiebcke, M. and Leoni, S. (**2013**); Subtle polymorphism of zinc imidazolate frameworks: temperature-dependent ground states in the energy landscape revealed by experiment and theory; *CrystEngComm* 15(20): 4036-4040.

Schwabe, T. and Grimme, S. (**2006**); Towards chemical accuracy for the thermodynamics of large molecules: new hybrid density functionals including non-local correlation effects; *Physical Chemistry Chemical Physics* 8(38): 4398-4401.

Schwabe, T. and Grimme, S. (**2007**); Double-hybrid density functionals with long-range dispersion corrections: higher accuracy and extended applicability; *Physical Chemistry Chemical Physics* 9(26): 3397-3406.

Schwabl, F. (**2006**); *Statistical Mechanics*; Lehrbuch, Springer.

Serre, C., Bourrelly, S., Vimont, A., Ramsahye, N. A., Maurin, G., Llewellyn, P. L., Daturi, M., Filinchuk, Y., Leynaud, O., Barnes, P. and Férey, G. (**2007**); An Explanation for the Very Large Breathing Effect of a Metal–Organic Framework during CO2 Adsorption; *Advanced Materials* 19(17): 2246-2251.

Serre, C., Mellot-Draznieks, C., Surblé, S., Audebrand, N., Filinchuk, Y. and Férey, G. (**2007**); Role of Solvent-Host Interactions That Lead to Very Large Swelling of Hybrid Frameworks; *Science* 315(5820): 1828-1831.

Serre, C., Millange, F., Thouvenot, C., Noguès, M., Marsolier, G., Louër, D. and Férey, G. (**2002**); Very Large Breathing Effect in the First Nanoporous Chromium(III)-Based Solids: MIL-53 or CrIII(OH)·{O2C−C6H4−CO2}·{HO2C−C6H4−CO2H}x·H2Oy; *Journal of the American Chemical Society* 124(45): 13519-13526.

Sieffert, N., Bühl, M., Gaigeot, M.-P. and Morrison, C. A. (**2012**); Liquid Methanol from DFT and DFT/MM Molecular Dynamics Simulations; *Journal of Chemical Theory and Computation* 9(1): 106-118.

Sigfridsson, E. and Ryde, U. (**1998**); Comparison of methods for deriving atomic charges from the electrostatic potential and moments; *Journal of Computational Chemistry* 19(4): 377-395.

Singh, U. C. and Kollman, P. A. (**1984**); An approach to computing electrostatic charges for molecules; *Journal of Computational Chemistry* 5(2): 129-145.

Siska, P. E., Parson, J. M., Schafer, T. P. and Lee, Y. T. (**1971**); Intermolecular Potentials from Crossed Beam Differential Elastic Scattering Measurements. III. He + He and Ne + Ne; *The Journal of Chemical Physics* 55(12): 5762-5770.

Soldan, P. and Hutson, J. M. (**2000**); On the long-range and short-range behavior of potentials from reproducing kernel Hilbert space interpolation; *The Journal of Chemical Physics* 112(9): 4415-4416.

Spackman, M. A. (**1996**); Potential derived charges using a geodesic point selection scheme; *Journal of Computational Chemistry* 17(1): 1-18.

Stavitski, E., Pidko, E. A., Couck, S., Remy, T., Hensen, E. J. M., Weckhuysen, B. M., Denayer, J., Gascon, J. and Kapteijn, F. (**2011**); Complexity behind CO2 Capture on NH2-MIL-53(Al); *Langmuir* 27(7): 3970-3976.

Stock, N. and Biswas, S. (**2012**); Synthesis of Metal-Organic Frameworks (MOFs): Routes to Various MOF Topologies, Morphologies, and Composites; *Chemical Reviews* 112(2): 933-969.

Stylianou, K. C., Rabone, J., Chong, S. Y., Heck, R., Armstrong, J., Wiper, P. V., Jelfs, K. E., Zlatogorsky, S., Bacsa, J., McLennan, A. G., Ireland, C. P., Khimyak, Y. Z., Thomas, K. M., Bradshaw, D. and Rosseinsky, M. J. (**2012**); Dimensionality Transformation through

Paddlewheel Reconfiguration in a Flexible and Porous Zn-Based Metal–Organic Framework; *Journal of the American Chemical Society* 134(50): 20466-20478.

Sugiyama, H., Watanabe, S., Tanaka, H. and Miyahara, M. T. (**2012**); Adsorption-Induced Structural Transition of an Interpenetrated Porous Coordination Polymer: Detailed Exploration of Free Energy Profiles; *Langmuir* 28(11): 5093-5100.

Suh, M. P., Park, H. J., Prasad, T. K. and Lim, D.-W. (**2012**); Hydrogen Storage in Metal–Organic Frameworks; *Chemical Reviews* 112(2): 782-835.

Sumida, K., Her, J.-H., Dincă, M., Murray, L. J., Schloss, J. M., Pierce, C. J., Thompson, B. A., FitzGerald, S. A., Brown, C. M. and Long, J. R. (**2011**); Neutron Scattering and Spectroscopic Studies of Hydrogen Adsorption in Cr3(BTC)2—A Metal−Organic Framework with Exposed Cr2+ Sites; *The Journal of Physical Chemistry C* 115(16): 8414-8421.

Sumida, K., Rogow, D. L., Mason, J. A., McDonald, T. M., Bloch, E. D., Herm, Z. R., Bae, T.-H. and Long, J. R. (**2012**); Carbon Dioxide Capture in Metal–Organic Frameworks; *Chemical Reviews* 112(2): 724-781.

Surble, S., Serre, C., Mellot-Draznieks, C., Millange, F. and Férey, G. (**2006**); A new isoreticular class of metal-organic-frameworks with the MIL-88 topology; *Chemical Communications*(3): 284-286.

Tafipolsky, M., Amirjalayer, S. and Schmid, R. (**2007**); Ab initio parametrized MM3 force field for the metal-organic framework MOF-5; *Journal of Computational Chemistry* 28(7): 1169-1176.

Tafipolsky, M., Amirjalayer, S. and Schmid, R. (**2010**); Atomistic theoretical models for nanoporous hybrid materials; *Microporous and Mesoporous Materials* 129(3): 304-318.

Tafipolsky, M., Amirjalayer, S. and Schmid, R. (**2010**); First-Principles-Derived Force Field for Copper Paddle-Wheel-Based Metal−Organic Frameworks; *The Journal of Physical Chemistry C* 114(34): 14402-14409.

Tan, C., Yang, S., Champness, N. R., Lin, X., Blake, A. J., Lewis, W. and Schroder, M. (**2011**); High capacity gas storage by a 4,8-connected metal-organic polyhedral framework; *Chemical Communications* 47(15): 4487-4489.

Thirumalai, D. and Mountain, R. D. (**1990**); Ergodic convergence properties of supercooled liquids and glasses; *Physical Review A* 42(8): 4574-4587.

Thom H. Dunning, J. (**1989**); Gaussian basis sets for use in correlated molecular calculations. I. The atoms boron through neon and hydrogen; *The Journal of Chemical Physics* 90(2): 1007-1023.

Triguero, C., Coudert, F.-X., Boutin, A., Fuchs, A. H. and Neimark, A. V. (**2011**); Mechanism of Breathing Transitions in Metal–Organic Frameworks; *The Journal of Physical Chemistry Letters* 2(16): 2033-2037.

Triguero, C., Coudert, F.-X., Boutin, A., Fuchs, A. H. and Neimark, A. V. (**2012**); Understanding adsorption-induced structural transitions in metal-organic frameworks: From the unit cell to the crystal; *The Journal of Chemical Physics* 137(18): 184702.

Valenzano, L., Civalleri, B., Sillar, K. and Sauer, J. (**2011**); Heats of Adsorption of CO and CO2 in Metal–Organic Frameworks: Quantum Mechanical Study of CPO-27-M (M = Mg, Ni, Zn); *The Journal of Physical Chemistry C* 115(44): 21777-21784.

Vanderbilt, D. (**1990**); Soft self-consistent pseudopotentials in a generalized eigenvalue formalism; *Physical Review B* 41(11): 7892-7895.

VandeVondele, J. and Hutter, J. (**2007**); Gaussian basis sets for accurate calculations on molecular systems in gas and condensed phases; *The Journal of Chemical Physics* 127(11): 114105.

VandeVondele, J., Krack, M., Mohamed, F., Parrinello, M., Chassaing, T. and Hutter, J. (**2005**); Quickstep: Fast and accurate density functional calculations using a mixed Gaussian and plane waves approach; *Computer Physics Communications* 167(2): 103-128.

Vanduyfhuys, L., Verstraelen, T., Vandichel, M., Waroquier, M. and Van Speybroeck, V. (**2012**); Ab Initio Parametrized Force Field for the Flexible Metal–Organic Framework MIL-53(Al); *Journal of Chemical Theory and Computation* 8(9): 3217-3231.

Vanommeslaeghe, K., Hatcher, E., Acharya, C., Kundu, S., Zhong, S., Shim, J., Darian, E., Guvench, O., Lopes, P., Vorobyov, I. and Mackerell, A. D. (**2010**); CHARMM general force field: A force field for drug-like molecules compatible with the CHARMM all-atom additive biological force fields; *Journal of Computational Chemistry* 31(4): 671-690.

Vimont, A., Travert, A., Bazin, P., Lavalley, J.-C., Daturi, M., Serre, C., Férey, G., Bourrelly, S. and Llewellyn, P. L. (**2007**); Evidence of CO2 molecule acting as an electron acceptor on a nanoporous metal-organic-framework MIL-53 or Cr3+(OH)(O2C-C6H4-CO2); *Chemical Communications*(31): 3291-3293.

Vydrov, O. A. and Van Voorhis, T. (**2012**); Benchmark Assessment of the Accuracy of Several van der Waals Density Functionals; *Journal of Chemical Theory and Computation* 8(6): 1929-1934.

Wang, Q. M., Shen, D., Bülow, M., Ling Lau, M., Deng, S., Fitch, F. R., Lemcoff, N. O. and Semanscin, J. (**2002**); Metallo-organic molecular sieve for gas separation and purification; *Microporous and Mesoporous Materials* 55(2): 217-230.

Weigend, F. and Ahlrichs, R. (**2005**); Balanced basis sets of split valence, triple zeta valence and quadruple zeta valence quality for H to Rn: Design and assessment of accuracy; *Physical Chemistry Chemical Physics* 7(18): 3297-3305.

Wen, X.-D., Martin, R. L., Henderson, T. M. and Scuseria, G. E. (**2012**); Density Functional Theory Studies of the Electronic Structure of Solid State Actinide Oxides; *Chemical Reviews* 113(2): 1063-1096.

Werner, H.-J., Knowles, P. J., G. Knizia, Manby, F. R., M. Schütz, P. Celani, T. Korona, R. Lindh, A. Mitrushenkov, G. Rauhut, Shamasundar, K. R., Adler, T. B., Amos, R. D., A. Bernhardsson, A. Berning, Cooper, D. L., Deegan, M. J. O., Dobbyn, A. J., F. Eckert, E. Goll, C. Hampel, A. Hesselmann, G. Hetzer, T. Hrenar, G. Jansen, C. Köppl, Y. Liu, Lloyd, A. W., Mata, R. A., May, A. J., McNicholas, S. J., W. Meyer, Mura, M. E., A. Nicklass, O'Neill, D. P., P. Palmieri, D. Peng, K. Pflüger, R. Pitzer, M. Reiher, T. Shiozaki, H. Stoll, Stone, A. J., R. Tarroni, T. Thorsteinsson and M. Wang (**2009**); *MOLPRO*, *version 2009.1*; University College Cardiff Consultants Limited: Cardiff, UK.

Whitfield, T. R., Wang, X., Liu, L. and Jacobson, A. J. (**2005**); Metal-organic frameworks based on iron oxide octahedral chains connected by benzenedicarboxylate dianions; *Solid State Sciences* 7(9): 1096-1103.

Wilmer, C. E., Farha, O. K., Bae, Y.-S., Hupp, J. T. and Snurr, R. Q. (**2012**); Structure-property relationships of porous materials for carbon dioxide separation and capture; *Energy & Environmental Science* 5(12): 9849-9856.

Wilmer, C. E., Leaf, M., Lee, C. Y., Farha, O. K., Hauser, B. G., Hupp, J. T. and Snurr, R. Q. (**2012**); Large-scale screening of hypothetical metal–organic frameworks; *Nat Chem* 4(2): 83-89.

Wu, D., Yang, Q., Zhong, C., Liu, D., Huang, H., Zhang, W. and Maurin, G. (**2012**); Revealing the Structure–Property Relationships of Metal–Organic Frameworks for CO2 Capture from Flue Gas; *Langmuir* 28(33): 12094-12099.

Wu, H., Gong, Q., Olson, D. H. and Li, J. (**2012**); Commensurate Adsorption of Hydrocarbons and Alcohols in Microporous Metal Organic Frameworks; *Chemical Reviews* 112(2): 836-868.

Wu, H., Simmons, J. M., Liu, Y., Brown, C. M., Wang, X.-S., Ma, S., Peterson, V. K., Southon, P. D., Kepert, C. J., Zhou, H.-C., Yildirim, T. and Zhou, W. (**2010**); Metal–Organic Frameworks with Exceptionally High Methane Uptake: Where and How is Methane Stored?; *Chemistry – A European Journal* 16(17): 5205-5214.

Wu, H., Simmons, J. M., Liu, Y., Brown, C. M., Wang, X. S., Ma, S., Peterson, V. K., Southon, P. D., Kepert, C. J., Zhou, H. C., Yildirim, T. and Zhou, W. (**2010**); Metal-Organic Frameworks with Exceptionally High Methane Uptake: Where and How is Methane Stored?; *Chemistry-a European Journal* 16(17): 5205-5214.

Wu, H., Simmons, J. M., Srinivas, G., Zhou, W. and Yildirim, T. (**2010**); Adsorption Sites and Binding Nature of CO2 in Prototypical Metal−Organic Frameworks: A Combined Neutron Diffraction and First-Principles Study; *The Journal of Physical Chemistry Letters* 1(13): 1946-1951.

Wu, Y., Kobayashi, A., Halder, G. J., Peterson, V. K., Chapman, K. W., Lock, N., Southon, P. D. and Kepert, C. J. (**2008**); Negative Thermal Expansion in the Metal–Organic Framework Material Cu3(1,3,5-benzenetricarboxylate)2; *Angewandte Chemie International Edition* 47(46): 8929-8932.

Yang, Q., Liu, D., Zhong, C. and Li, J.-R. (**2013**); Development of Computational Methodologies for Metal–Organic Frameworks and Their Application in Gas Separations; *Chemical Reviews*; DOI: 10.1021/cr400005f.

Yang, Q., Wiersum, A. D., Jobic, H., Guillerm, V., Serre, C., Llewellyn, P. L. and Maurin, G. (**2011**); Understanding the Thermodynamic and Kinetic Behavior of the CO2/CH4 Gas Mixture within the Porous Zirconium Terephthalate UiO-66(Zr): A Joint Experimental and Modeling Approach; *The Journal of Physical Chemistry C* 115(28): 13768-13774.

Yazaydın, A. O. z. r., Benin, A. I., Faheem, S. A., Jakubczak, P., Low, J. J., Willis, R. R. and Snurr, R. Q. (**2009**); Enhanced CO2 Adsorption in Metal-Organic Frameworks via Occupation of Open-Metal Sites by Coordinated Water Molecules; *Chemistry of Materials* 21(8): 1425-1430.

Yazaydın, A. O. z. r., Snurr, R. Q., Park, T.-H., Koh, K., Liu, J., LeVan, M. D., Benin, A. I., Jakubczak, P., Lanuza, M., Galloway, D. B., Low, J. J. and Willis, R. R. (**2009**); Screening of Metal−Organic Frameworks for Carbon Dioxide Capture from Flue Gas Using a Combined Experimental and Modeling Approach; *Journal of the American Chemical Society* 131(51): 18198-18199.

Yoo, C. S., Kohlmann, H., Cynn, H., Nicol, M. F., Iota, V. and LeBihan, T. (**2002**); Crystal structure of pseudo-six-fold carbon dioxide phase II at high pressures and temperatures; *Physical Review B* 65(10): 104103.

Yoon, M., Srirambalaji, R. and Kim, K. (**2012**); Homochiral Metal–Organic Frameworks for Asymmetric Heterogeneous Catalysis; *Chemical Reviews* 112(2): 1196-1231.

Yu, D., Ghosh, P. and Snurr, R. Q. (**2012**); Hierarchical modeling of ammonia adsorption in functionalized metal-organic frameworks; *Dalton Transactions* 41(14): 3962-3973.

Zang, J., Nair, S. and Sholl, D. S. (**2011**); Osmotic ensemble methods for predicting adsorption-induced structural transitions in nanoporous materials using molecular simulations; *Journal of Chemical Physics* 134(18): 184103.

Zang, J., Nair, S. and Sholl, D. S. (**2013**); Prediction of Water Adsorption in Copper-Based Metal–Organic Frameworks Using Force Fields Derived from Dispersion-Corrected DFT Calculations; *The Journal of Physical Chemistry C* 117(15): 7519-7525.

Zhang, L., Hu, Z. and Jiang, J. (**2013**); Sorption-Induced Structural Transition of Zeolitic Imidazolate Framework-8: A Hybrid Molecular Simulation Study; *Journal of the American Chemical Society* 135(9): 3722-3728.

Zhou, H.-C., Long, J. R. and Yaghi, O. M. (**2012**); Introduction to Metal–Organic Frameworks; *Chemical Reviews* 112(2): 673-674.

Zhou, W., Wu, H. and Yildirim, T. (**2008**); Enhanced H2 Adsorption in Isostructural Metal−Organic Frameworks with Open Metal Sites: Strong Dependence of the Binding Strength on Metal Ions; *Journal of the American Chemical Society* 130(46): 15268-15269.

Zukal, A., Pulido, A., Gil, B., Nachtigall, P., Bludský, O., Rubeš, M. and Čejka, J. (**2010**); Experimental and theoretical determination of adsorption heats of CO(2) over alkali metal exchanged ferrierites with different Si/Al ratio; *Physical Chemistry Chemical Physics* 12(24): 6413-6422.

Appendices

A1 DFT/CC Method

The DFT/CC method is based on the pairwise representability of the DFT error, ΔE, defined as

$$\Delta E = E_{\mathrm{CCSD(T)}} - E_{\mathrm{DFT}} \tag{A1.1}$$

where $E_{\mathrm{CCSD(T)}}$ and E_{DFT} are the interaction energies, respectively, calculated at the CCSD(T)/CBS and DFT/AVQZ levels of theory. "CBS" stands for complete basis set, and "AVQZ" denotes a mixed basis set of aug-cc-pVQZ-PP (Peterson and Puzzarini, 2005) for Cu and aug-cc-pVQZ (Thom H. Dunning, 1989) for the other atoms (likewise for AVXZ and VXZ, hereafter). Within the DFT/CC method, the DFT error, ΔE, is expressed as the sum of the atom–atom correction functions $\varepsilon_{ij}(R_{ij})$, that is

$$\Delta E = \sum_{ij} \varepsilon_{ij}(R_{ij}) \tag{A1.2}$$

where R_{ij} is the distance between atoms i and j. No explicit functional form for the ε_{ij} correction functions is assumed; instead, a reproducible kernel Hilbert space interpolation is used (Soldan and Hutson, 2000). In addition to the assumption about pairwise representability of the DFT error (Equation A1.2), transferability of the correction functions from the reference system to the system of interest is assumed, which is described for the CH_4 – CuBTC system below.

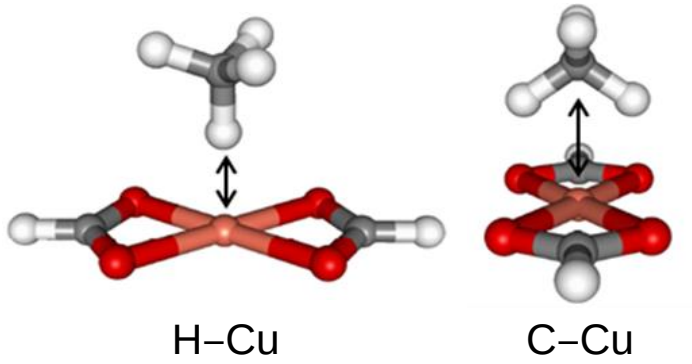

Figure A1.1. The two reference complexes used to obtain the correction functions ε_{HCu} and ε_{CCu}.

To evaluate the DFT/CC corrections (Equation A1.2), the PBE/AVQZ and CCSD(T)/CBS calculations on the reference set were carried out. Figure 3.2 shows the two reference complexes for the CH_4 – Cu system, while the complete reference set can be found in the work of Chen et al (2011). The correction functions $\varepsilon_{HH'}$ $\varepsilon_{HC'}$ $\varepsilon_{CH'}$ $\varepsilon_{CC'}$ $\varepsilon_{HO'}$ $\varepsilon_{CO'}$ and ε_{CCu} (ε_{HCu}) were evaluated from the one-dimensional potential energy curves of $H_2\cdots H_2$, $H_2\cdots C_6H_6$, $CH_4\cdots H_2$, $CH_4\cdots C_6H_6$, $H_2\cdots CO_2$, $CH_4\cdots CO_2$ and $CH_4\cdots Cu(O_2CH)_2$ reference complexes, respectively. The assumption of the DFT/CC correction transferability was tested by calculations carried out for a larger $(CH_4)_2\cdots Cu_2(O_2CH)_4$ cluster model at the CCSD(T)/CBS level (on the PBE/VTZ optimized geometry). The interaction energy of the CH_4 molecule with the $Cu_2(O_2CH)_4$ cluster model was found to be -13.50 kJ mol^{-1} as calculated at the DFT/CC level, which is in excellent agreement with the CCSD(T)/CBS value of -13.48 kJ mol^{-1}.

The periodic DFT calculations of the interaction of a CH_4 molecule with the CuBTC framework were modelled using the experimental rhombohedral primitive cell ($a = b = c = 18.627$ Å, $\alpha = \beta = \gamma = 60.0$ °, and $V = 4570.205$ Å^3) of CuBTC, which includes two small tetrahedral cages and contains 156

framework atoms (of which 12 are copper, 48 oxygen, 24 hydrogen and 72 carbon atoms). The projector augmented wave approximation (Blöchl, 1994) and the plane-wave basis set with a kinetic energy cutoff of 600 eV were used; Brillouin-zone sampling was restricted to the Gamma point. The PBE exchange–correlation functional was employed. Calculations with cluster models and calculations with periodic models were performed using Molpro09 (Werner et al., 2009) and VASP 5.2 (Kresse and Hafner, 1993) programme suites, respectively.

A2 Partial Atomic Charges for the NOTT-140a MOF

Partial atomic charges (Table A2.1) of the NOTT-140a framework were obtained using the cluster shown in Figure A2.1. The cluster was carved out from the experimental crystal structure (Tan et al., 2011) with all dangling bonds saturated by hydrogen atoms. The calculation was performed at the B3LYP/TZVP level of theory – the smaller basis set (compared to the Def2-TZVPP used in most of the other cases) was chosen because of the large size of the cluster. The atomic charges were fitted to the first-principles electrostatic potential of the cluster by the MK method on a grid having a density of ca. 2000 points per atom.

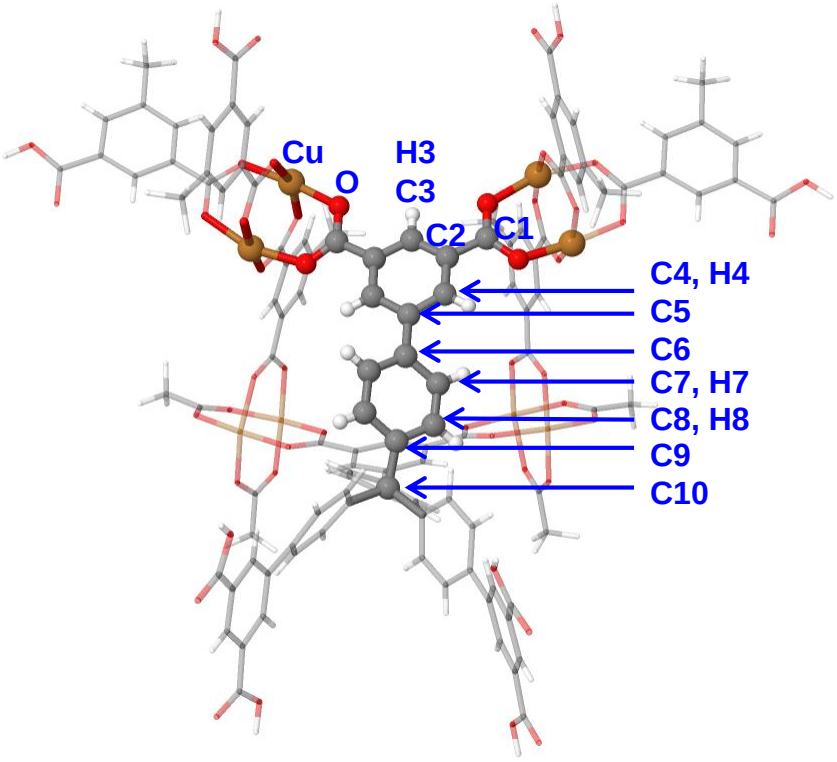

Figure A2.1. Cluster for calculation of partial atomic charges for NOTT-140a.

Table A2.1. Partial atomic charges for the framework of NOTT-140a.

atom	Cu	O	C1	C2	C5	C6	C9	C10
q (e)	1.1130	-0.6657	0.8156	-0.1879	0.0077	0.1354	-0.3419	1.0480
atom	C3	H3	C4	H4	C7	H7	C8	H8
q (e)	-0.0013	0.1347	-0.0709	0.1345	-0.3141	0.1799	0.0645	0.0550

A3 GCMC Simulation Details for CO_2 Adsorption in MIL-53(Sc)

GCMC simulations were performed to generate CO_2 positions in the MIL-53(Sc)-*DMF(removed)* framework, which were used as starting configurations for the AIMD simulations. The atomistic representation of the framework was constructed from the experimental crystallographic data (Mowat et al., 2011) with all of the atoms kept fixed at their positions during the simulation.

The CO_2–framework and CO_2–CO_2 interaction energies were determined according to the Lennard–Jones (LJ) and Coulomb potentials given as:

$$V_{ij} = 4\varepsilon\left[\left(\frac{\sigma}{r_{ij}}\right)^{12} - \left(\frac{\sigma}{r_{ij}}\right)^{6}\right] + \frac{z_i z_j e^2}{4\pi\varepsilon_0 r_{ij}} \quad \text{(A3.1)}$$

where ε and σ are the LJ potential-well depth and hard-sphere diameter, respectively; r_{ij} is the distance between atoms i and j; z_i and z_j are the fractional charges; e is the elementary charge; and ε_0 is the vacuum permittivity.

LJ potential parameters for all of the framework atoms were taken from UFF. The partial atomic charges for the MIL-53(Sc) framework were calculated at the B3LYP/TZVP level of theory and were derived using the MK method, both with the Gaussian 09 program. The model clusters for deriving charges are shown in Figure A3.1. CO_2 molecules were modelled according to a fully flexible model; that is, both the C–O bond and the O–C–O angle can vary, as described in the literature (Cygan et al., 2012). The force-field parameters for the MIL-53(Sc) framework and CO_2 atoms are summarized in Table A3.1, while Table A3.2 lists the partial atomic charges for the framework. The Lorentz–Berthelot combining rules were used to calculate the LJ cross-parameters. Interactions beyond 12.80 Å were neglected. Each GCMC simulation consisted of an equilibration period of 2.0×10^7 iterations, followed by a production run of further 2.0×10^7 iterations. The snapshot taken at the end of the production run was then used as the initial configuration of CO_2 in the AIMD simulation for that particular loading.

Table A3.1. Force-field parameters for the MIL-53(Sc) framework (Mowat et al., 2011) and CO_2 atoms (Cygan et al., 2012).

atom type	σ (Å)	ε/k_B (K)
H	2.571	22.142
C	3.431	52.838
O	3.118	30.193
Sc	2.936	9.561

non-bonded potential			
atom type	σ (Å)	ε/k_B (K)	q (e)
$O(CO_2)$	3.050	80.378	-0.3256
$C(CO_2)$	2.800	28.144	0.6512

bonded potential	
k(C–O)	1015458.633 K
r_0(C–O)	1.162 Å
k(O–C–O)	54351.031 K
θ_0(O–C–O)	180.000 °

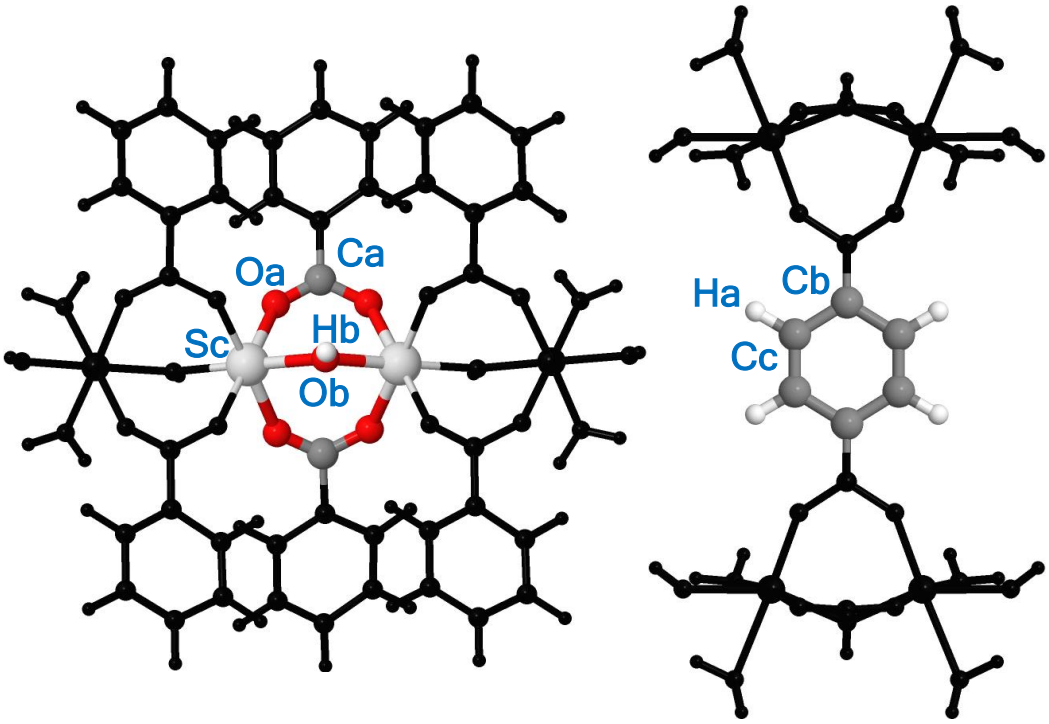

Figure A3.1. Clusters for calculation of partial atomic charges for the MIL-53(Sc) framework.

Table A3.2. Partial atomic charges for the MIL-53(Sc) framework.

atom	Sc	Oa	Ob	Ca	Cb	Cc	Ha	Hb
q (e)	1.8167	-0.7316	-1.0423	0.9471	-0.0511	-0.1647	0.1298	0.4996

A4 Time Evolution of MIL-53(Sc)-*int* during the Course of the AIMD Simulation

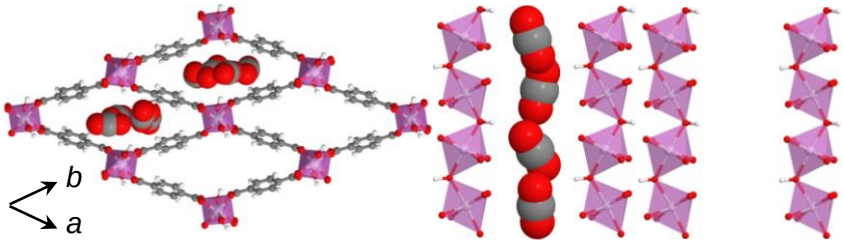

t = 0 ps

a = 21.41 Å, b = 21.41 Å, c = 14.60 Å, α = 90.00 °, β = 90.00 °, γ = 50.78 °, V = 5186.34 Å^3;

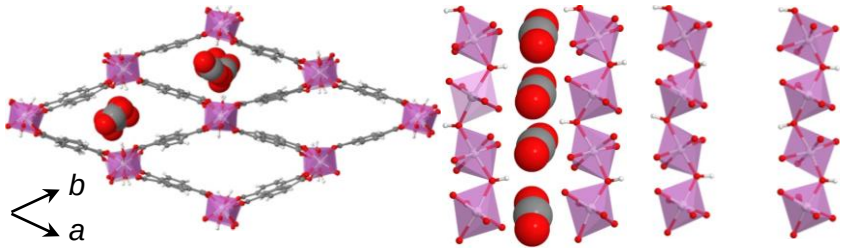

t = 1 ps

a = 21.69 Å, b = 21.79 Å, c = 14.76 Å, α = 90.12 °, β = 89.95 °, γ = 50.14 °, V = 5353.36 Å^3;

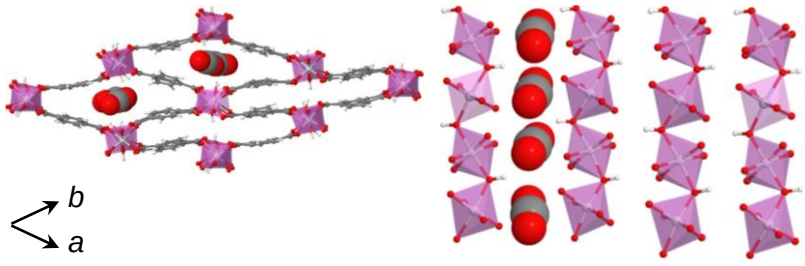

t = 5 ps

a = 20.80 Å, b = 21.39 Å, c = 14.92 Å, α = 87.88 °, β = 87.12 °, γ = 37.49 °, V = 4035.834 Å^3;

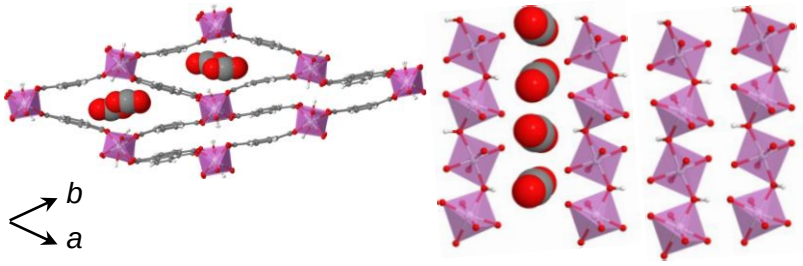

t = 10 ps

a = 20.59 Å, b = 21.38 Å, c = 14.90 Å, α = 90.93 °, β = 87.18 °, γ = 39.01 °, V = 4107.99 Å^3.

A5 Individual Simulated XRPD Patterns Used to Obtain the Averaged Patterns for MIL-53(Sc)-*int* and -*lp* Phases

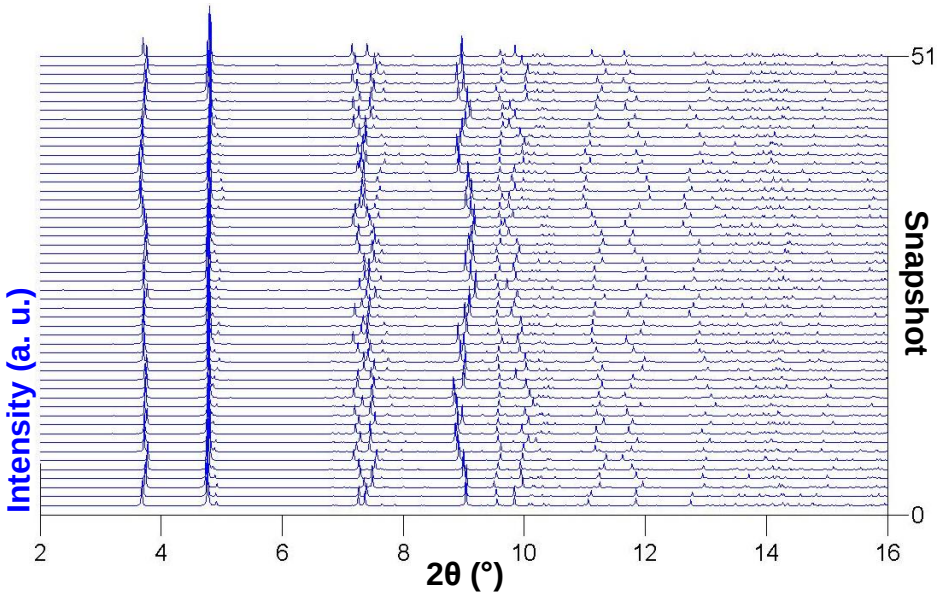

Figure A5.1. A series of simulated patterns based on the snapshots (with an interval of 0.2 ps) taken during the AIMD simulation of the MIL-53(Sc)-*int* structure. These patterns were used to obtain the averaged pattern shown in Figure 6.10.

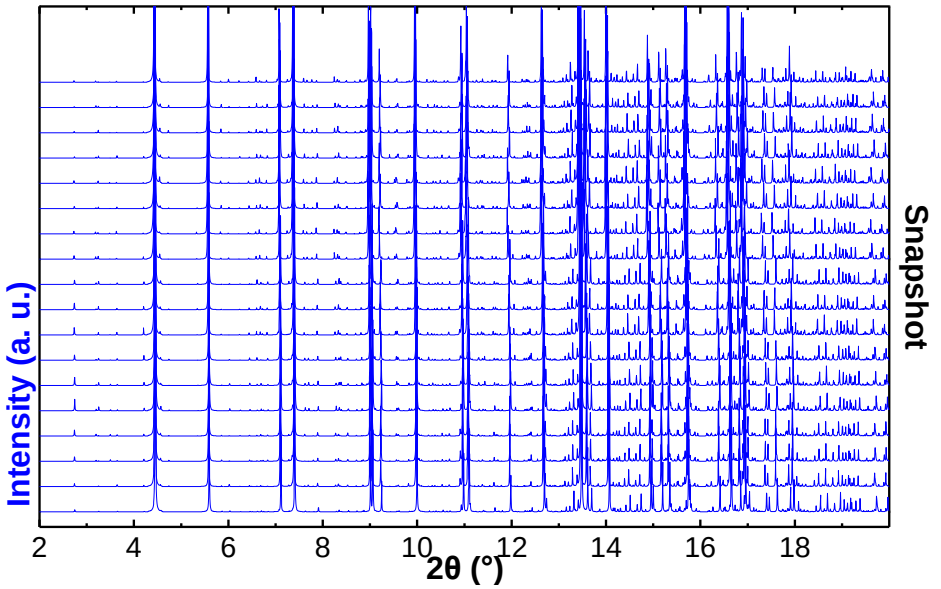

Figure A5.2. A series of simulated patterns based on the snapshots (with an interval of 0.2 ps) taken during the AIMD simulation of the MIL-53(Sc)-*lp* structure. These patterns were used to obtain the averaged pattern shown in Figure 6.15.

A6 A Brief Summary of the Modifications Made to MUSIC

A few modifications and extensions have been made to the standard distribution of the simulation code MUSIC, or multipurpose simulation code. The changes were aimed at (1) allowing GCMC simulations to use predefined fluid–framework interactions supplied externally, in contrast with generating a potential map by the programme itself (Chapter 3), and (2) incorporating additional pairwise non-bonded model potentials into the code (Chapters 4 and 5). MUSIC was written in Fortran 90 in an object-oriented fashion, with its modules functioning as "self-sufficient" entities. New features can be programmed as individual modules that are easily "plugged-in" to the code with only minimal effort. Similarly, necessary changes are made only to the relevant modules, allowing for a better back-tracking and debugging without interfering the rest of the code.

Regarding the first objective of generating a potential-energy grid using externally supplied data, changes were mostly made to the "mapmaker.F90" module. MUSIC has an in-built functionality ("mapmaker.F90") for computing an energy grid to be used in GCMC simulations. The module file was hacked in the following way. When the programme is supposed to call for a calculation of the interaction energy at a specific grid point, it instead reads such information from an external text file where the interaction energy is given for the grid point. In this way, MUSIC takes user-supplied fluid–framework interaction data as input and outputs a potential map that is fully compatible with the programme itself. It is worth noting that when running the map generation simulation MUSIC calculates and stores both the potential energy and its first-, second-, and third-order derivatives (for

interpolation between grid points). In the DFT/CC CH_4–CuBTC potential energy surface (PES) described in Chapter 3, only the potential energy and its first derivative were available for each grid point. The reason for this is that calculation of the higher-order derivatives of the potential energy would be computationally intractable for systems of such a large size. Explicitly, the MUSIC potential map made from the DFT/CC PES included, for each grid point, the potential energy and its first-order derivative, both obtained by the DFT/CC method, while the second- and third-order derivatives were defaulted to the value zero. It is also recommended that one should check carefully the MUSIC-constructed grid (for making the potential map) is exactly the same as the grid supplied by the user (see the "config.F90" module).

To realize the second objective, a separate Fortran 90 module file was written for each of the model potentials investigated in Chapters 4 and 5. Within the module for a particular model potential, the mathematical expressions for the potential energy and for the calculation of the derivatives of the potential energy were specified. A sample file can be made available upon request; modifications necessary for incorporating a new model potential only have to be made where needed while conforming to the format of the sample file. Once this potential-energy module is written, it should be made available to the various functionalities of MUSIC. For example, if the model potential is to be used for pre-computing an energy grid, then it should be called for at various positions within the "mapmaker.F90" module. A simple way to do this is to follow the calls to the "lj.F90" module, in which the Lennard–Jones potential is evaluated; one should then duplicate those calls and replace any keywords related to the Lennard–Jones potential with the corresponding ones for the new potential.